

An X-ray View Of Compact Objects

By

BINAY RAI

Thesis

Submitted to the

University of North Bengal

in partial fulfilment of the

requirements for the degree of

DOCTORATE OF PHILOSOPHY

In

Physics

Under the supervision of

PROF. BIKASH CHANDRA PAUL

Department of Physics

North Bengal University

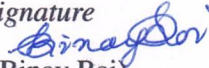
Darjeeling - 734013, West Bengal, India

JULY 2021

Declaration

I, **Binay Rai**, certify that the work embodied in this thesis is my own bonafide work and carried out by me under the supervision of **Prof. (Dr.) Bikash Chandra Paul** from January 2016 to July 2021 at the **Department of Physics**, University of North Bengal (NBU), Darjeeling, Siliguri. The matter embodied in this thesis has not been submitted for the award of any other degree/diploma. I declare that I have faithfully acknowledged and given credits to the research workers whenever and wherever their works have been cited in my thesis. I further declare that I have not willfully copied any others' work, paragraphs, text, data, results, etc., reported in journals, books, magazines, reports dissertations, theses, etc., or available at websites and have not included them in this thesis and have not cited as my own work.

Date 02/07/2021
Place Darjeeling

Signature

(Binay Rai)

Registration no. - Ph.D/Phy.(1256)/427/R-2019

University of North Bengal

Accredited by NAAC with Grade "A"

Dr. B. C. Paul
Professor
Department of Physics
www.nbu.ac.in



সমানো মন্ত্র: সমিতি: সমানী

P.O.NORTH BENGAL UNIVERSITY
Darjeeling, West Bengal
India, PIN 734013
Email: bcpaul@nbu.ac.in

CERTIFICATE OF SUPERVISOR

It is certified that the work contained in the thesis titled "An X-ray view of Compact Objects" by Mr. Binay Rai, has been carried out under my supervision and that this work has not been submitted elsewhere for a degree.

B. C. Paul
01.07.2021

Signature of Supervisor (s)

Name (s) : Dr. Bikash Chandra Paul
Professor
Department of Physics
North Bengal University

July 2021



Professor
Department of Physics
University of North Bengal

Document Information

Analyzed document	Binay Rai_Physics.pdf (D109879460)
Submitted	6/29/2021 8:43:00 AM
Submitted by	University of North Bengal
Submitter email	nbuplg@nbu.ac.in
Similarity	2%
Analysis address	nbuplg.nbu@analysis.orkund.com

Sources included in the report

W	URL: https://ir.nbu.ac.in/bitstream/123456789/2748/22/Full%20thesis%20of%20Pragati%20Pradhan.pdf Fetched: 6/15/2021 1:06:47 AM		10
J	Timing and Spectral Studies of Accretion Powered X ray Pulsars URL: ebe36546-236a-428b-add0-040e1577138b Fetched: 3/16/2019 1:08:25 PM		11
W	URL: https://arxiv.org/pdf/1601.02348 Fetched: 6/15/2021 7:52:53 PM		1
W	URL: http://arxiv.org/pdf/1106.3251 Fetched: 6/15/2021 7:53:07 PM		1
W	URL: https://docplayer.org/154982801-Magnetic-fields-of-accreting-pulsars.html Fetched: 3/13/2021 4:41:51 AM		2
W	URL: https://arxiv.org/pdf/1608.06118 Fetched: 12/18/2020 10:32:19 AM		3
W	URL: https://iopscience.iop.org/article/10.3847/1538-4357/aae309 Fetched: 6/29/2021 8:44:00 AM		1
W	URL: https://arxiv.org/pdf/2004.10452 Fetched: 6/24/2021 7:36:48 AM		1
J	SPECTRAL AND TIMING NATURE OF THE SYMBIOTIC X-RAY BINARY 4U 1954+319: THE SLOWEST ROTATING NEUTRON STAR IN AN X-RAY BINARY SYSTEM URL: ecbbf36d-a643-418b-acc1-f0dca78c806c Fetched: 3/18/2019 11:17:06 PM		1
W	URL: https://www.aanda.org/articles/aa/full_html/2016/10/aa29200-16/aa29200-16.html Fetched: 6/14/2020 2:26:18 PM		3
W	URL: https://heasarc.gsfc.nasa.gov/xanadu/xspec/manual/node162.html Fetched: 6/29/2021 8:44:00 AM		1

Binay Rai
02/07/2021

Binay Rai
02/07/2021



DRC CERTIFICATE

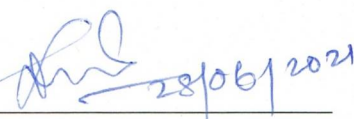
It is certified that the work contained in the thesis titled "An X-Ray View of Compact Objects" by Mr. Binay Rai, have been carried out following University guidelines and have been approved by the Departmental Research Committee for processing by the Board of Research Studies.

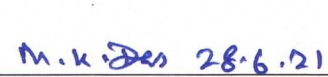
Approved

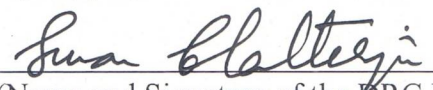
Date

Committee Members:

1. B. C. PAUL  28-06-2021
(Name and Signature of the DRC Member)

2. PROVASH MALI  28/06/2021
(Name and Signature of the DRC Member)

3. Malay Kumar Das  M.K. Das 28.6.21
(Name and Signature of the DRC Member)

4. SUMAN CHATTERJEE

(Name and Signature of the DRC Member)

28/06/2021.

Head
Department of Physics
University of North Bengal

Department of Physics
University of North Bengal



Abstract

AN X-RAY VIEW OF COMPACT OBJECTS

Binay Rai

In this thesis we studied some of neutron star X-ray binaries. A neutron star is a compact object which emits X-rays as a result of accretion when it is in a binary system with a normal or degenerated star. The X-rays originating from these binaries are coming as pulses of X-rays. The study were mainly focused on the timing and spectral analysis. In the timing analysis the light curves, pulse profile etc., are studied whereas in spectral analysis we fit the spectra of X-ray pulsars using different models to understand the different physical processes occurring in the accretion disk, accretion column, magnetosphere and on the surface of neutron star. The cyclotron line present in a spectrum of pulsar is direct indication of presence of magnetic field of the neutron star and one can directly estimate the value of magnetic field from the cyclotron line energy. We have used the data from *RXTE*, *NuSTAR*, *Swift* and *NICER* observations. The sources considered for study are SMC X-1, Swift J1756.9-2508 and 4U 1901+03.

SMC X-1 is a High Mass X-ray binary (HMXB) system and has a pulse period of 0.7 s. The light curves of the source of total observational time ~ 225.5 ks have been analyzed. It is observed that there were presence of a large number of flares due to type II burst in the light curves of SMC X-1. A total of 272 flares were observed with the mean value of FWHM of a flare was ~ 21 s. The shape of the pulse profiles during different observations were same irrespective of the flares which suggest that the geometry of the accretion disk was unchanged during these observations. We also observed that there were no correlation of spectral parameters with flares.

The second source Swift J1756.9-2508 is an accreting mill-second X-ray pulsar having pulse period of ~ 5.5 ms. We have studied the source during its 2018 outburst. The dependence of pulse

profiles and pulse fraction on energy are studied. The pulse profile of the pulsar was observed to deviate from the sinusoidal shaped. The broad 0.3-79 keV spectrum of the pulsar was observed to be hard and flat with a cutoff energy of 74.58 keV. We have also carried out pulse - phase, orbital - phase and time - resolved spectral analysis. We have not observed emission lines or Compton hump in the spectrum of the milli-second X-ray pulsar.

The third source we have studied is a Be/X-ray pulsar 4U 1901+03. It is known that the pulsar went through an outburst in 2019. We have used *Swift*, *NuSTAR* and *NICER* observational data of the pulsar during the outburst for analysis. The pulse profile of the pulsar evolves throughout the outburst. We observed that the 10 keV absorption like feature shows dependence on luminosity and increases with luminosity. In addition to this another absorption like feature near 30 keV were observed in last two *NuSTAR* observations out of the four observations. Fitting this 30 keV feature by GABS model we estimated the line energy to be about 30.51 keV and 30.41 keV respectively for last two observations. We also note that both the 10 keV and 30 keV features shows variation with pulse phases.

Signature : 

Date : 02/07/2021

Acknowledgment

The journey to my Ph. D. degree were full of ups and downs, which makes this journey more memorable. This part of my life won't be such memorable in absence of the people I met during these times. I do not want to lose this opportunity to express my gratitude to all of them.

First of all I would like to thank my supervisor Professor (Dr.) B. C. Paul for introducing me with such an exciting field of astronomy despite of being busy with his classes and academic responsibility as Dean, PG Faculty of Science, NBU. I also thank him for his support and guidance. I do not have a word for his patient and trust on me. I am very thankful to the Head of the Department of Physics and other teachers of the department. I would like to express my gratitude to SERB - DST, Govt. of India, for project fellow during my research, a project of my supervisor EMR/2016/000532. I am thankful to IUCAA Centre for Astronomy Research and Development (ICARD), NBU for providing an excellent research facilities in astronomy and astrophysics.

I thank my parents for the faith shown on me. They were supporting me even during the hard days of our life and also were very patient. I thank my younger brother Pranay who was always there for me whenever I needed. A big thank to Alisha for supporting me by giving her laptop. I am indebted to all my friends - Pranish, Harry, Golay, Tony, Suchitra, Pranesh, Sunny, Pankaj, Vero, Lor, Subarna, and others. I also thank my colleagues - Sagar and Anirban - for the tea we had during the time when I get bored which helped me to refresh myself. I am grateful to Dr. Pragati Pradhan for sharing her knowledge and helping me during the early struggling days of my life and even when she was in abroad at Penn-State, USA. I would also like to express my gratitude to Rajesh Pradhan for helping me in technical aspects related to computers. I thank non-teaching staff - Sarita aunty, Lubai da, Sudip da and others - without whom our department won't function smoothly.

Last but not the least, I am grateful to my university, North Bengal university, for giving me an opportunity to pursue the Ph. D. degree. The environment of the campus being excellent which is full of green trees that blooms during spring or in the monsoon and makes it very refreshing and pleasant.

Dedicated to my loving parents . . .

Preface

The emission of the X-rays from a compact objects is due to very complex processes which occurs in the magnetosphere or in the accretion disk near the compact object. For the neutron star the X-rays are mostly originated from the accretion column formed at the magnetic poles of the neutron star. The compact object considered in this thesis is neutron star, which are in a binary system (X-ray binaries) and sources of X-rays. It is known that X-rays generated from a neutron star in a binary system appears as a pulses of X-rays. The brief outline of the thesis is as follows -

- **Chapter 1** - In this chapter we have given a brief discussion about the history of X-ray astronomy, different types of X-ray binaries, different ways of accretion of matter onto the neutron star. We have mentioned shortly about different mechanism by which X-rays are generated in this chapter. Also we have briefly described about the pulse profile, theoretical study of spectrum of a X-ray pulsar and origin of cyclotron line.
- **Chapter 2** - In this chapter the brief description of the instruments onboard different space observatories from which the observed data were taken up for the study are presented. We have also given a list of the sources used in this thesis and discussed briefly about the discoveries and studies done by others before our study. Finally at the end of this chapter we have given the description of different models used in our study with concluding remarks.
- **Chapter 3** - In this chapter the analysis of NS HMXB SMC X-1 is presented. The RXTE PCA data for the high mass X-ray binary source SMC X-1 between 2003-10 and 2003-12 when the source was in high states are analyzed. The source is found to be frequently bursting which is seen as flares in the light curves, on an average

of one in every 800 s and an average of 4-5 X-ray burst per hour. Typically a burst was short lasting, for few tens of seconds, in addition to that few long bursts of more than hundred seconds were also observed. The flares apparently occupied 2.5% of the total time of observation of 225.5 ks. A total of 272 flares with mean FWHM of the flare ~ 21 s are noted. The r.m.s. variability and the aperiodic variability are found to be independent of flares. As observed the pulse profiles of the lightcurves do not change its shape implying that there is no change in the geometry of accretion disk due to burst. The hardness ratio and the r.m.s. variability of light curves show no correlation with the flares. The flare fraction shows a positive correlation with the peak-to-peak ratio of the primary and secondary peaks of the pulse profile. The observed hardening or the softening of the spectrum cannot be correlated with the flaring rate but may be due to the interstellar absorption of X-rays as evident from the change in the hydrogen column density (n_H). It is found that the luminosity of the source increases with the flaring rate. Considering the viscous timescale equal to mean recurrence time of flares the viscosity parameter is estimated $\alpha \sim 0.16$ for consistency.

- **Chapter 4** - In this chapter timing and spectral the analysis of Accreting Millisecond X-ray Pulsar (AMXP) Swift J1756.9-2508 during 2018 is presented. We have used the data of *Swift* and *NuSTAR* observations. The simultaneous fitting of the *Swift* and *NuSTAR* spectra indicates that the source was in the hard state with a cut-off energy of about 74.58 keV. The pulse profiles of the AMXP and its dependence on energy are also probed. The colour-colour diagram of the source is plotted for investigating how hard colours are distributed with respect to soft colours. The pulse-phase, orbital-phase and time resolved spectral analysis using *NuSTAR* data are carried out. Pulse phase-resolved spectra were fitted with a power-law model and significant changes in the spectral parameters with pulse phase are observed. The

column density and photon index obtained from the orbital phase spectral analysis were found to have some anti-correlation with the flux. Through the time-resolved spectral analysis, we observed that the spectral parameters show positive correlation with each other and also with the flux. We do not observe a softening of the spectrum with time here. No emission lines or Compton hump were observed in the spectrum of the AMXP.

- **Chapter 5** - In this chapter a detail study of pulse profiles and spectra of the source 4U 1901+03 during 2019 outburst is presented. The timing and the spectral properties of the BeXB 4U 1901+03 during 2019 outburst is studied using *NuSTAR*, *Swift* and *NICER* observations. Flares are observed in all the observations which are of tens to hundreds seconds duration. It is observed that the pulse profiles changed significantly with time. It is evident that the single peak of the pulse evolved into double peak having one main peak thereafter to a single peak once again. An increase in the height of the peak of the pulse profiles with energy is observed. The pulse fraction increases with energy and at the end of the outburst. The variation of the pulse profile with time indicates transition from one accretion regime of the pulsar to the other. The absorption like feature at 10 keV found here is connected with positive correlation with the luminosity and along with other spectral parameters. However due to uncertainties in the estimated distance to the source we cannot confirm this feature to be CSRF. Another absorption like feature about 30 keV is observed in the spectra of the last two *NuSTAR* observations in which line energy about 30.51 ± 0.42 and 30.41 ± 0.54 keV respectively. The softening of spectrum along with the increase in pulse fraction at the end of the outburst and absence of pulsation after 58665.09 MJD indicates that the pulsar entered propeller phase, which is also supported by *Swift-XRT* observations

- **Chapter 6** - In this chapter we have summarize the results obtained from the analysis of the observed data for the pulsars. The analysis carried out here will be extended for other pulsars using the data from *ASTROSAT* and other observatories in future.

Table of contents

List of figures	xxv
List of tables	xxxi
Nomenclature	xxxii
1 Introduction	1
1.1 A brief history of X-ray astronomy	1
1.2 Compact Objects	3
1.2.1 X-ray Binaries	7
1.3 Theory of Accretion	9
1.4 Accretion Mechanism	12
1.4.1 Roche-lobe overflow	14
1.4.2 Stellar Wind Accretion	15
1.4.3 Be-disk Accretion	17
1.5 Neutron star X-ray binaries and X-ray pulsars	19
1.5.1 Accretion X-ray millisecond pulsars	23
1.6 Generation of X-rays in Astrophysics	27
1.6.1 Characteristic X-rays	29
1.7 X-ray spectra	29
1.7.1 Cyclotron Resonance Scattering Feature	30

1.8	Pulse Profiles	35
1.9	Objective of the thesis	37
2	Description of the instruments and methods used in study	39
2.1	Rossi X-ray Timing Explorer (<i>RXTE</i>)	41
2.1.1	<i>RXTE</i> -PCA	42
2.1.2	<i>RXTE</i> -HEXTE	42
2.1.3	<i>RXTE</i> -ASM	42
2.2	Nuclear Spectroscopic Telescope Array (<i>NuSTAR</i>)	42
2.3	Swift Observatory (<i>Swift</i>)	43
2.3.1	<i>Swift</i> -BAT	44
2.3.2	<i>Swift</i> -XRT	45
2.3.3	<i>Swift</i> -UVOT	46
2.4	Brief review of the sources considered in the study	46
2.4.1	SMC X-1	46
2.4.2	Swift J1756.9-2508	47
2.4.3	4U 1901+03	48
2.5	Methods of Data Reduction	49
2.6	Timing and Spectral Analysis	51
2.6.1	Timing Analysis	51
2.6.2	Spectral Analysis	53
3	A study of Type II bursts from SMC X-1	59
3.1	Introduction	59
3.2	Observations and Data reduction	60
3.3	Light curves and flares	61
3.4	Pulse profiles	64

3.5	Hardness ratio	65
3.6	Spectral analysis	66
3.7	Variation of flare-fraction with observational time, pulse peak-to-peak ratio and orbital phase	70
3.8	Variation of the spectral parameter with orbital phases and flux	71
3.9	Discussion	72
4	Timing and Spectral properties of Accreting Milli-second X-ray Pulsar Swift J1756.9-2508	77
4.1	Introduction	77
4.2	Observation and data reduction	78
4.3	Analysis and Results	79
4.3.1	Light curves	79
4.3.2	Pulse profiles	80
4.3.3	Spectral analysis	85
4.4	Discussion	93
5	Study of timing and spectral properties of Be/X-ray pulsar 4U 1901+03	97
5.1	Introduction	97
5.2	Observation and Data reduction	98
5.3	Analysis and Results	100
5.3.1	Light curves	100
5.3.2	Pulse Profiles and Pulse Fraction	100
5.3.3	Spectral Analysis	107
5.4	Discussion	116
6	Conclusion and summary	125
6.1	Summary	125

6.2 Future work	127
References	129
Appendix A List of Publication	141
Appendix B Paper Presented in Seminar	143
Appendix C Reprints of papers included in the thesis	145

List of figures

1.1	Classification of X-ray binaries. Image courtesy Reig (2011).	9
1.2	Illustration of equipotential surfaces for binary system having mass ratio $M_2/M_1=0.25$. CM indicates center of mass where as L_1-L_5 indicate Lagrangian points. Equipotential surfaces are labelled by the numeral 1 to 7 in the increasing order of their magnitude. Image credit Frank <i>et al.</i> (1992)	13
1.3	Left: Schematic diagram of a compact object accreting matter through stellar wind. Right: Figure showing the direction of velocities of neutron star and wind.	17
1.4	Illustration of Be/X-ray binary system. The shadow near the Be star represents equatorial disk. The neutron star orbiting around the Be star captures matter from the disc during periastron passage and causes periodic outburst of type I. Image courtesy: (Tauris and van den Heuvel, 2006). . .	18
1.5	Figure showing the accretion powered X-ray pulsar where matter is channeled along the magnetic field lines. The accretion columns are formed inside the the hot spots. Image courtesy : https://astronomy.swin.edu.au/cosmos/X/X-ray+Pulsar	21

- 1.6 The figure on the left represent the super-critical accretion regime where matters fall freely until it encounters a shock above the neutron star surface. From the region below the shock X-rays are emitted in the direction perpendicular to the accretion column to produce fan beam. The figure on the right hand side is in case of luminosity below the critical value. In this case X-ray escapes vertically upward from the hot spots along the accretion column to produce pencil beam pattern. Image courtesy - Schönherr *et al.* (2007) 24
- 1.7 Theoretical spectrum of LMC X-4 computed by Becker and Wolff (2007) 31
- 1.8 An illustration of accretion column of accreting neutron star. Seed photons are produced through blackbody at the thermal mound at the base of the accretion column where as seed photons through bremsstrahlung and cyclotron are produced throughout the accretion column. Image courtesy Becker and Wolff (2007) 31
- 1.9 Variation of scattering cross section with energy for exciting an electron in initial Landau level $n = 0$ to $n = 6$ for given magnetic field about $B = 0.0385B_{crit}$. The fundamental cyclotron line is at 20 KeV. The solid, dashed and dotted lines represents cross section for three viewing angle $\nu = \cos \mu = 0.1, 0.5, 0.9$ respectively. Figure courtesy- Schwarm *et al.* (2017). 35
- 2.1 An image of RXTE spacecraft along with different instruments. Image Courtesy: NASA/GSFC 41
- 2.2 Diagram of the *NuSTAR* observatory. The figures at top and bottom shows the observatory in deployed and stowed configurations respectively. Image courtesy : (Harrison *et al.*, 2013) 44

2.3	Figure of <i>Swift</i> observatory along with different instruments. Image courtesy : (Gehrels <i>et al.</i> , 2004)	45
3.1	<i>RXTE</i> ASM light curve of SMC X-1. The astricks "*" represents the <i>RXTE</i> PCA observations. h1 and h2 indicates the high states.	61
3.2	<i>Upper panel</i> - Light curves for four different <i>RXTE</i> -PCA observations. The down arrow represent flares. <i>Lower panel</i> - Power density spectrum for the corresponding light curves.	63
3.3	<i>Left</i> - Sharp burst observed in SMC X-1. <i>Right</i> - Large flare having duration ~ 300 s. These two large flares are from <i>RXTE</i> observation having Obs Id 80078-01-01-04.	64
3.4	Orbital corrected pulse profiles for four light curves (a), (b), (c) and (d) represented by blue, purple, green and black respectively.	66
3.5	Hardness ratio obtained by dividing the 7-16 keV X-ray count rates by 3-7 keV count rates for four different observations.	67
3.6	The best fitted spectra for four <i>RXTE</i> -PCA spectra in 3-18 keV energy range.	68
3.7	The variation of the flare fraction with the observation time is given by panel figure in panel (a), where as variation of flare-fraction with peak-to-peak ratio and orbital phase are given by figures (b) and (c) respectively. Figure (d) shows the variation of spin with the luminosity where as figure (e) is luminosity of different observations plotted against flare-fraction. Figure (f) is the variation of the photon index with the flare-fraction.	69
3.8	(a), (b) and (c) represents the variation of column density, photon index and flux respectively.	72
4.1	Light curves of J1756.9 during 2018 outburst. Black and red represents the <i>Swift</i> -XRT & BAT light curves respectively. The inset figure represent <i>NuSTAR</i> light curve.	80

4.2	Colour-colour diagram of the AMXP.	81
4.3	Pulse profiles in five different energy range. The fundamental and second harmonic sinusoidal fitting are represented by blue and red respectively. The black line represents the best fitted line.	82
4.4	Variation of normalized amplitude of first (upper panel) and second harmonic (middle panel) with energy. The bottom panel shows the variation of the pulse fraction with energy.	84
4.5	The broad 0.3-79 keV spectral fitting of J1756.9. The points in black represents <i>Swift</i> -XRT spectrum and that one blue and red represent <i>NuSTAR</i> FPMA & B spectra respectively.	86
4.6	Variation of the spectral parameter with the pulse phase. The upper, middle and bottom panels shows variation of column density (n_H), photon index and flux with the pulse phase respectively.	87
4.7	Variation of the best fitted spectral parameter with the orbital phase. The upper panel in red shows the variation of flux with phase. The figures in blue and green indicated the variation of photon index and column density respectively. The lower panel shows the variation of cutoff energy with phase.	89
4.8	Variation of the column density (a), photon index (b) and cutoff energy (c) with flux. Variation of cutoff energy (d) with photon index.	90
4.9	The first upper panel in red indicates the variation of flux with time. The bottom panel indicates the variation of cutoff energy with the time. The two middle panels in blue & green represent the variation of photon index and the column density with time respectively.	91

-
- 4.10 Figures (a), (b) and (c) represents variation of column density, photon index and cutoff energy with flux respectively, whereas that in figure in panel (d) is variation of cutoff energy with the photon index. 92
- 5.1 Upper panel shows *Swift*-BAT light curves of 4U 1901+03 during 2019 outburst in 15-50 keV energy range. The down arrows and vertical lines indicates four *NuSTAR* observations. The middle panel shows variation of *Swift*-XRT flux in 0.5-10 keV energy range. Fluxes are in the order of 10^{-9} and obtained by using the command flux in XSPEC for *Swift*-XRT spectra fitted by POWERLAW model. Bottom panel represents change in Pulse fraction with time, the square and circle symbols are for *Swift*-XRT (0.5-10.0 keV) and NICER (0.2-12 keV) respectively. 101
- 5.2 Light curves showing some of the bursts observed in four *NuSTAR* observations. The burst present in the light curves is indicated by up arrow. . . 102
- 5.3 Pulse profiles for different *NuSTAR* observations and variation of pulse profile with energies. Figures (a), (b), (c) and (d) are for the 58531.12, 58549.31, 58584.95 and 58615.75 MJD respectively. 104
- 5.4 Variation of Pulse profile with time. Pulse profiles from 58532.03 to 58637.08 MJD are obtained by folding *Swift*-XRT lightcurve. For *Swift*-XRT the significant level of pulse periods were greater than 3σ . The broadening of the *Swift*-XRT pulse profiles can be due to the short exposure time of the instrument so that there is not enough photons count rate to fold about the pulse period. The last pulse profile at 58665.09 MJD is obtained by folding NICER lightcurve in 0.2-12 keV energy range (Obs Id - 2200570141). 105

5.5	Variation of the pulse fraction of the pulse profile with energy obtained using <i>NuSTAR</i> observations. The first, second, third and fourth columns are for Obs1, Obs2, Obs3 and Obs4 respectively.	107
5.6	Unfolded spectra of <i>NuSTAR</i> Obs1 and <i>Swift</i> -XRT observation fitted with Model I. The bottom and middle panels shows residuals after without and with the GABS model. Black indicates <i>Swift</i> -XRT spectra, red and green indicates <i>NuSTAR</i> FPMA & B spectra respectively.	110
5.7	Fitted spectra of <i>NuSTAR</i> Obs3 in 3-79 keV energy range. Panel (a) shows residuals for Model I where as panel (b) is residuals for Model I*GABS models and (c) shows residuals for Model I*GABS*GABS models.	111
5.8	Variation of Spectral parameters with pulse phases for four <i>NuSTAR</i> observations. Figures in first, second and third columns are for Obs1, Obs2, Obs3 and Obs4 respectively. α and E_H are photon index and highecut of CUTOFFPL model. E_{Fe} is the energy of Fe line. E_{gabs_1} , σ_{gabs_1} and τ_{gabs_1} are the line energy, width and optical depth of GABS model used for fitting 10 keV feature.	116
5.9	Variation of photon index and pulse fraction with <i>Swift</i> -XRT flux in 0.5-10 keV energy range.	117
5.10	Variation of 30 KeV absorption feature with phase for Obs3 (first column) and Obs4 (second column). E_{gabs_2} , σ_{gabs_2} and τ_{gabs_2} are the line energy, width and the optical depth of the feature.	117

List of tables

3.1	Table showing best fitted spectral parameters for four spectra. χ^2_{ν} is the reduced chi-square for 29 dof. n_H is the hydrogen column density and α is the photon-index of POWERLAW model. E_{cutoff} and E_{fold} are the cutoff energy and e-folding energy of the HIGHECUT model <i>respectively</i>	67
4.1	The best fitted model parameters obtained by fitting <i>Swift</i> and <i>NuSTAR</i> spectra simultaneously.	85
4.2	Values of best fitted spectral parameters.	87
4.3	Best fitted spectral parameters for different orbital phase intervals.	90
4.4	Table showing the variation of the best fitted spectral parameters with time.	92
4.5	The best fitted spectral parameter for different <i>Swift</i> -XRT observation.	93
5.1	Table showing four <i>NuSTAR</i> observations indicated by their observation IDs along with the date of observation, exposure and the pulse period of pulsar.	100
5.2	Variation of pulse fraction (%) with energy four different observations.	108

- 5.3 Best fitted spectral parameters of 4U 1901+03 for four different cases using Model I and Model II. α and E_H are photon index and highcut energy of the CUTOFFPL model. E_{gabs} and E_{Fe} are energy of absorption and Fe lines respectively. τ_{gabs} is the optical depth. σ_{gabs} and σ_{Fe} are the widths of absorption and Fe line. The subscript $gabs_1$ and $gabs_2$ are for two GABS models. The column density (n_H) and flux are in the scale of 10^{22} cm^{-2} and $10^{-9} \text{ erg cm}^{-2} \text{ s}^{-1}$ respectively. T_0 , kT and τ are the spectral parameters of the COMPTT model. Flux were calculated in 3-79 keV energy range. Errors quoted are within 90% confidence interval. . . . 109

Chapter 1

Introduction

1.1 A brief history of X-ray astronomy

X-rays are high-energy electromagnetic waves which spread over electromagnetic spectrum in the wavelength range (1-100 Å) . The energy of X-rays lies between ~ 0.12 -120 keV. X-ray was discovered by W. C. Röntgen in 1895 when he observed a faint glow produced on a fluorescent screen due to some unknown rays coming from the discharge tube. X-rays being high energy radiation can ionize atoms. The interaction of X-rays with matter can cause Compton effect, photo-electric effect, Thomson scattering etc. X-ray are generally produced by the colliding a highly accelerated electrons with a tungsten, the electrons coming from the cathode of a vacuum tube are accelerated by applying high voltage of an order of keV.

There are plenty of X-ray sources in our universe but Earth's atmosphere is opaque to high energy radiations like UV, X-rays and gamma rays. So the ground based observatories which can detect optical and radio waves cannot detect these high energy radiation coming from outer space. So X-ray detector must be placed above the atmosphere and this is done with the the help of rocket flights and balloons. The search for the X-ray sources from outer space began in 1948. In September 1949, a team of researchers from US Naval Research

Laboratory detected weak X-rays coming from the hot corona of sun using German V2 sounding rocket launched in January 28, 1949 from New Mexico. A set of Geiger counters was placed at the nose cone of the rocket. It was after more than a decade a first celestial X-ray source outside the solar system Sco X-1 in the constellation of Scorpius was discovered in 1962 by a team led by Riccardo Giacconi using *Aerobee 150* sounding rocket carrying a small X-ray detector (Giacconi *et al.*, 1962). The presence of galactic X-ray sources was further supported by the two rocket experiments performed in October 1962 and June 1963 from the White Sands Missile Range, New Mexico (Gursky *et al.*, 1963). In this decade numerous X-ray sources were discovered using rocket flights. The first X-ray imaging telescope was made by team led by Riccardo Giacconi at American Science and Engineering in Cambridge, MA which was sent into space on a small sounding rocket in 1963 and was used to make crude images of the hot spots present in sun's atmosphere. The first satellite dedicated to X-ray astronomy was *Uhuru* (Giacconi *et al.*, 1971), launched on December 1970 and was operational for two years. It was also known as Small Astronomy Satellite 1 (*SAS-1*) or Explorer 42. The fourth Uhuru catalog consists of detail of position and intensities of 339 X-ray sources (Forman *et al.*, 1978). After *Uhuru* X-ray satellites namely *SAS 2*, *Ariel*, *SAS 3*, *HEAO-1*, *HEAO-2* and *HEAO-3* were also launched in this decade. The first focusing X-ray telescope was the Apollo Telescope Mount aboard Skylab, US first space station which was launched in May 1973. The first fully imaging X-ray telescope was *HEAO-2* or *Einstein* observatory which was launched in November 1978. In 1980's X-ray satellite like *EXOSAT* and *Ginga* were launched, while in 1990's important missions like *ROSAT*, *ASCA*, *RXTE*, *BeppoSAX*, *XMM* and *Chandra* were launched. The *RXTE* was used to study rapid time variability of X-ray emitted from sources over a wide energy range. The imaging capacity of the *Chandra* observatory is excellent, it is able to detect X-ray sources twice as far away detected by other observatories, which can also produce images five times more prominent. During the first decade of 21st century, X-ray

observatory like *Suzaku*, *Swift*, *INTEGRAL*, *MAXI*, *AGILE* and *Fermi* have been launched, except *Suzaku* all of them are operational till date. The other mission which are under operational at present are *Chandra*, *NuSTAR* and *AstroSat*, the last two observatories were launched in 2012 and 2015 respectively.

1.2 Compact Objects

Compact objects are astronomical objects which are very dense star compared to a typical star. They are stellar remnants as they are formed at the end stage of stellar evolution. There are three types of compact objects - white dwarf, neutron star and black hole. The compact objects are formed as a result of gravitational collapse when the radiation pressure due to nuclear fusion in the star is no longer able to hold the gravitational pressure, as a result a compact core of the star is left behind. In that case the inward gravitational pressure is balanced by the degenerate pressure of fermions, may be electron or neutron. The type of the compact object formed depends on the mass of the proto-star.

- **White dwarfs** - These type of compact objects are formed by the gravitational collapse when the initial mass of the proto-star is less than $8M_{\odot}$, where M_{\odot} is the solar mass. They are found to have small radii and emit thermal energy with the effective temperature greater than normal stars but with low luminosities. The gravitational collapse tears out the electrons from the atom and the degenerate pressure which can be measured due to Pauli's exclusion principle now halts the further collapse of the star. A new star is born which is white dwarf. It was Chandrasekhar who showed that the maximum mass of a white dwarf is $1.24M_{\odot}$. Adams (1915) discovered that the spectral type of Sirius B is similar to its normal companion star Sirius. From the spectral type the estimated effective temperature of Sirius B was 8000 K and from the luminosity the

predicted radius was about 18800 km. Adams (1915) also determined that its density to be $5 \times 10^4 \text{ g cm}^{-3}$. However these prediction are affected because of presence of its companion Sirius. The recent measured temperature of Sirius B is about 27000 K with density about $3 \times 10^6 \text{ g cm}^{-3}$ and radius about four times smaller than predicted earlier. Einstein in 1907 theoretically found that the presence of such highly dense compact object creates strong gravitational field around it which causes redshift of light, Adams (1925) detected the redshift equivalent to $\sim 19 \text{ km s}^{-1}$ for Sirius B, which confirmed that Sirius B is a very high dense object. The magnetic field of the white dwarfs lies between 10^6 to 10^9 G (Schmidt, 1989). The average mass of white dwarf is $0.57M_{\odot}$ (Kepler *et al.*, 2007), where as the minimum estimate mass is $0.17M_{\odot}$ (Kilic *et al.*, 2007) and maximum being $1.33M_{\odot}$ (Kepler *et al.*, 2007). The mean density of white dwarf is around 10^6 gcm^{-3} and radius about $\sim 7000 \text{ km}$.

The cooling of the white dwarf occurs through the loss of the thermal energy in the form of the radiation. For Kramers' law opacity in the envelope the cooling time (t_{cool}) depends on the luminosity such that $t_{cool} \propto L^{-5/7}$ which is also inversely proportional to the mean atomic weight of the interior ions (van Horn, 1971). Other than the thermal cooling the processes responsible for the cooling of white dwarfs are due to neutrino cooling, crystallization and Debye cooling. During the initial and final phases of the evolution of white dwarfs, the degeneracy pressure is not equal everywhere but there exist regions of low degeneracy pressure where contraction still takes place. So there will be release of gravitational energy in the form of radiation which contributes to their observed luminosity. The cooling age of the faintest white dwarf is about 9×10^9 years and the life time of its progenitor is about 0.3×10^9 which together gives an age of the galactic disk to be about 9.3×10^9 . Hot white dwarfs are the

source of UV and soft X-rays. It is known that a white dwarf in binary system with a companion might be a source of X-rays.

- **Neutron star** - In 1934 Baade & Zwicky proposed the formation of a compact object made up of neutrons during supernovae explosion. Oppenheimer & Volkoff in 1939 were first to calculate masses and radii of the neutron stars by assuming that they are composed of neutrons at high density which behave like an ideal gas. They predicted that the maximum mass for neutron stars to be in equilibrium was $\sim 0.7M_{\odot}$, above this the core will collapse further. However this mass limit was below the Chandrasekhar limit of $1.4M_{\odot}$ for white dwarf, the reason behind this was that they did not take the neutron-neutron interaction into account (Ghosh, 2006). By the inclusion of the neutron-neutron interaction the Oppenheimer & Volkoff limit raise to $\sim 2M_{\odot}$ (Cameron, 1959). It was in 1962 when first X-ray source outside solar system was discovered, which brought a wide interest in astronomers about neutron stars as the possible X-ray sources in the sky. X-rays were thought to be originated from cooling of the hot neutron stars. Another very important event was the discovery of quasar in 1963 by Schmidt that raised further interest in exploring neutron stars. The large redshifts of the spectral lines of quasars were thought to be due to large gravitational field of neutron star. However this concept was soon abandoned as the largest observed redshift from the quasars during that time is found to exceed the maximum redshift from the neutron star surface. With the discovery of pulsar in 1967 (Hewish *et al.*, 1968), Gold (1968) proposed that pulsars are nothing but a rotating neutron star. Further evidence for the existence of the neutron star came from the discovery of X-ray pulsars by UHURU in 1971, which were thought to be a binary system between neutron star and a normal companion, where the neutron star accretes matter from the companion.

The mass of the neutron stars were determined using the optical and X-ray observations of some X-ray pulsars. Neutron stars are believed to be formed if the mass of the progenitor is greater than $8M_{\odot}$. In a neutron star the neutron degeneracy pressure balances the star from further collapse due to gravitation. If a star exceeds the theoretical mass limit $3.3M_{\odot}$ (TOV limit) it will further collapse to be a black hole. However, it is known that the mass of the neutron star lies between 1.17 - $2.0M_{\odot}$ and radius in 9.9 - 11.2 km range (Özel and Freire, 2016). The density of a typical neutron star is of the order of 10^{14} g cm⁻³ which is about nuclear density. The magnetic field of the neutron star is found to lie in the range 10^8 - 10^{15} G.

- **Black hole** - In 1795 Laplace using Newtonian gravity discussed the possibility of existence of compact objects having gravitational field so strong that even light cannot escape from their surfaces. In 1915, Albert Einstein proposed general theory of relativity and soon after this Karl Schwarzschild in 1916 was that first to obtain the solution of Einstein field equations for the gravitational field around the spherical object which is the popular vacuum solution. The solution describes a uncharged non-rotating black hole. Hans Reissner in 1916 gave a solution for a charged spherically symmetric non-rotating black hole. The solution describing rotating uncharged black hole was given by Roy Kerr in 1963. Eddington in 1935 discussed that if Chandrasekhar's mass limit is true then the stellar core having mass greater than the limit will go on contracting and radiating until the radius of the core becomes few km and its gravitational field is strong enough to hold the light. In 1939 the formation of the black hole was first demonstrated by Oppenheimer and Snyder when they observed that a homogeneous sphere of pressureless gas becomes cut off from communication from the rest of the universe when it is allowed to collapse in general relativity.

Yakov Zel'dovich and Edwin Salpeter in 1964 independently proposed that quasars were supermassive black holes powered by matter accreting around them. In 1971 astronomers found the massive companion of the X-ray source Cygnus X-1 and estimated the mass of the compact object by studying the motion of the companion (Bolton, 1972; Webster and Murdin, 1972). The mass of the compact object in Cygnus X-1 exceeded the maximum mass of the neutron star and was considered as first the stellar black hole candidate. Today it has been accepted that there are number of black hole candidates in binaries and supermassive black holes that exist at that of the galaxies. Classically black holes are regions in the spacetime that cannot communicate with the rest of the universe. The boundary of this region is called event horizon (Shapiro and Teukolsky, 1983). Inside the event horizon there exist a singularity where laws of physics is not valid. It is now understand that black holes are defined by mass M , electric charge Q and spin angular momentum J in reality.

1.2.1 X-ray Binaries

X-ray binaries (XRBs) are binary system between a compact object and a companion which can be a normal star or another compact object which is a source of X-rays. Depending upon the type of compact objects, XRBs are divided into three groups viz - (1) Black hole binaries (2) Neutron star X-ray binaries (3) White dwarf X-ray binaries. They are the major sources of extraterrestrial X-rays having luminosities in the range of 10^{33} - 10^{39} erg s^{-1} . Depending on the mass of the companion star, Neutron star and black hole X-ray binaries can be of two types- High Mass X-ray Binaries (HMXBs) and Low Mass X-ray Binaries (LMXBs). For HMXBs, the mass of the companion is $\geq 10M_{\odot}$ and for LMXBs the companion mass $M < 2M_{\odot}$. The optical companion of HMXBs is type O or B star where as LMXBs have companion of spectral type after A. The orbital period of HMXBs

varies from few days to a year but in case of LMXBs it ranges from less than a hour to days. Accretion disk is small or absent in HMXBs where as in the case of LMXBs it is always present. Neutron star (NS) HMXBs shows pulsation where as in NS LMXBs pulsation is seen only in some cases. The magnetic field of a NS in HMXBs is of the order of 10^{12} G and in LMXBs its about 10^8 G. HMXBs are comparatively young (age $<10^7$ years) compared to LMXBs having age $\sim 10^9$ years. HMXBs have hard X-ray spectra with $kT \geq 15$ keV where as LMXBs have soft X-ray spectra ($kT \sim 2$ keV) (Jaisawal, 2016). NS HMXBs are further classified into two subgroups - (i) Be/X-ray binaries (BeXBs) and (ii) Super-Giant X-ray Binaries (SGXB), whereas NS LMXBs are divided into two subgroups - (i) Atoll and (ii) Z-sources. Be/X-ray binaries have an optical companion which can be dwarf, subgiant or giant OBe star with luminosity class between III-V. SGXBs have a supergiant companion having luminosity I or II and are bright and persistent. BeXBs are mostly transient in nature having eccentricity, $e \geq 3$ (Reig, 2011). They are observable during an outburst, where outbursts may be a Type I or Type II. Type I outbursts are frequent but Type II outbursts are rare and giant. There are few persistent BeXB rotating slowly ($P > 200$ s) and orbital period $P_{orb} > 200$ days (Reig, 2011). Black hole (BH) X-ray binaries can be persistent or transient in nature. BH HMXBs are persistent in nature but BH LMXBs are mostly transient. The schematic classification of X-ray binaries is shown in Fig. 1.1. The basic process which is responsible for the emission of the X-rays by XRBs is accretion of matter from the companion to the compact objects. There are three ways through which the accretion of matter onto the compact objects occurs, namely (a) Roche-lobe overflow, (b) stellar wind accretion and (c) Be-disk accretion. Accretion in NS LMXBs and BeXBs occurs through Roche-lobe overflow where as in SGXBs there are three disc-fed X-ray binaries where mass transfer occurs through Roche-lobe overflow and there are few tens of SGXBs where mass transfer occurs through stellar wind. In case of black hole, mass accretion in persistent BH HMXB occurs through stellar wind where as

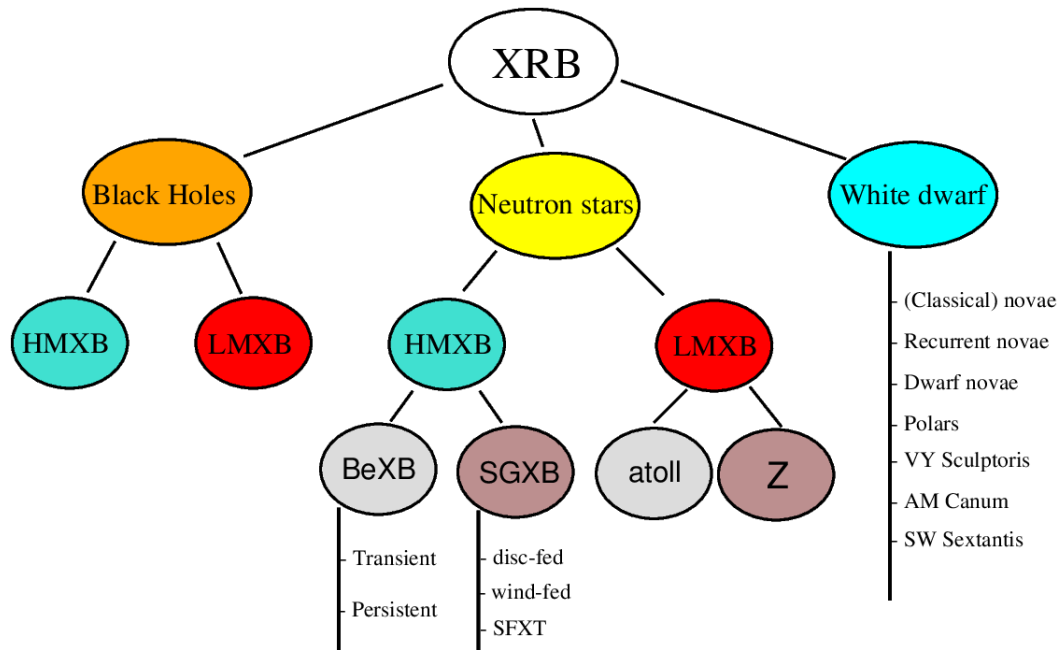


Fig. 1.1 Classification of X-ray binaries. Image courtesy Reig (2011).

in BH LMXB the mass transfer occurs through Roche-lobe overflow. However it is the nature of the compact object which determines the properties of the emitted X-rays.

1.3 Theory of Accretion

In a binary system accretion is a process which powers the most luminous objects in the universe. The gravitational potential energy of the accreting matter in binary system is converted into kinetic energy which subsequently converted into radiation. It is an efficient process for converting the gravitational potential energy into radiation. For understanding accretion theoretically we consider a particle of mass (m) being accreted onto the surface of a body of mass (M) and radius (R), then the gravitation potential energy released will be,

$$E = \frac{GMm}{R} \quad (1.1)$$

where G is the Newton's gravitational constant. Assuming the accreting body to be a neutron star of mass equal to solar mass M_{\odot} and radius $R \sim 10$ km, the energy released E is about 10^{20} erg for $m = 1$ gm. The maximum energy extracted in conversion of unit mass of hydrogen into helium by the process of nuclear fusion is 6×10^{18} erg, which is about 20 times smaller than the energy released during accretion (Frank *et al.*, 1992). The energy released during accretion depends on compactness i.e. M/R ratio of the accreting object, so the efficiency of energy released by accretion will be greater if the object is highly compact. So accretion is efficient way through which energy is released in the case of black holes and neutron star.

The luminosity produced by the accretion of matter onto compact object, which is known as accretion luminosity is given by,

$$L_{acc} = \frac{GM\dot{M}}{R} \quad (1.2)$$

where \dot{M} represents the mass accretion rate. However the total potential energy cannot be released out as the radiation. The efficiency of the accretion process is measured by a dimensionless quantity η , defined as

$$\eta = \frac{L_{acc}}{\dot{M}c^2}. \quad (1.3)$$

In this case for a neutron star of solar mass (M_{\odot}) the calculated efficiency is $\eta \sim 0.15$. From the eq.(1.2) we can see that the accretion luminosity (L_{acc}) of a given star is directly proportional to the mass accretion rate (\dot{M}). So higher the accretion rate higher is the accretion luminosity but there exists upper bound on the accretion luminosity above which the accretion can be halted. This upper limit of the accretion luminosity is known as the Eddington luminosity. To estimate this we consider a steady spherically symmetric accretion of matter, which consists of fully ionized hydrogen gas. Since the cross section of

the Thomson scattering is negligible in the case of proton, so it is the free electrons which experience the force due to radiation and latter undergoes Thomson scattering (Frank *et al.*, 1992). If S be the radiant energy flux and σ_T , the Thomson cross section then the radial force acting outward on each electron is given by $\sigma_T S/c$. The radiant energy flux (S) is related to luminosity (L) which is given by the relation $S=L/4\pi R^2$. The gravitational pull acting on the pair of electron and proton is $\frac{GMm_p+m_e}{R^2} \cong \frac{GMm_p}{R^2}$, where m_p and m_e are proton and electron masses respectively. At Eddington limit the luminosity at which the force due to radiation and gravitation acting on the electron-proton pairs are in equilibrium, is given by

$$\frac{L_{Edd}}{4\pi R^2 c} = \frac{GMm_p}{R^2} \quad (1.4)$$

where c is the speed of light and for electron σ_T is equal to $6.6 \times 10^{-22} \text{ cm}^2$. From the eq. (1.4) it is evident that the Eddington limit and the maximum mass accretion rate is given as,

$$L_{Edd} = \frac{4\pi GMm_p c}{\sigma_T} = 1.3 \times 10^{38} \frac{M}{M_\odot} \text{ erg}^{-1}, \quad (1.5)$$

$$\dot{M} = \frac{4\pi R m_p c}{\sigma_T} = 1.5 \times 10^{-8} \frac{R}{10^6} M_\odot^{-1}.$$

As the above limit is derived by assuming steady accretion onto a spherical geometry, so it is not valid in the case of non-steady accretion in a non-spherical geometry *e.g.* in the case of supernova explosion where the luminosity exceeds the limit. However, the above limiting value is not valid in the presence of higher nuclei other than hydrogen in the accreting material (Frank *et al.*, 1992; Pradhan, 2016). X-rays emitting from a compact

object are mainly due to the accretion of matter from a companion to the compact object. The different accretion mechanisms is discussed in the next section.

1.4 Accretion Mechanism

A binary system consists of two components primary star and secondary star, orbiting around their common center of mass. Before discussing the different accretion mechanisms we need to know about the different potential surfaces formed by the self-gravitational force of the stars and their mutual gravitational interactions. For a star having certain mass and radius spherical equipotential surfaces are formed around it. These equipotential surface no longer remain symmetric in the presence of a second star and gets distorted from the spherical symmetry. The effective gravitational potential (Roche potential) is then determined by the gravitational potential of the individual star and the centrifugal force due to the the motion of stars about the center of mass. The Roche potential ϕ_R is given by

$$\phi_R = -\frac{GM_1}{|r-r_1|} - \frac{GM_2}{|r-r_2|} - \frac{1}{2}(\omega \times r)^2 \quad (1.6)$$

where M_1, M_2 are the masses of two stars, r_1 and r_2 are the position vectors of the star centers. The first two term in the Roche potential represents the individual potentials on a test particle at distance r and in third term ω is the angular velocity of the binary system with respect to the inertial frame represented above. For mass ratio 0.2 the geometry of the equipotential surface is shown in Fig. 1.2. The points where the gradient of the Roche potential vanish are called Lagrangian points denoted by L_1, L_2, L_3, L_4, L_5 in Fig. 1.2. It is evident from the Fig. 1.2 that the three points L_1, L_2 and L_3 are lying on the line joining the centers of two stars where as L_4 and L_5 lying perpendicular to the line. The equipotential surfaces near the stars are almost spherical as it is dominated by the gravitational potential of the individual star but as one moves far away from the stars due

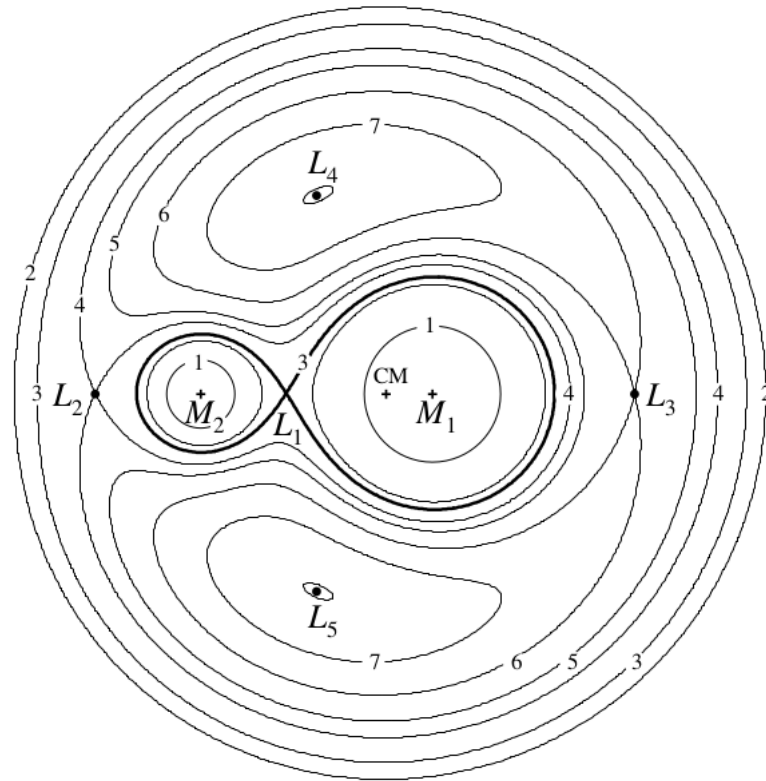


Fig. 1.2 Illustration of equipotential surfaces for binary system having mass ratio $M_2/M_1=0.25$. CM indicates center of mass where as L_1 - L_5 indicate Lagrangian points. Equipotential surfaces are labelled by the numeral 1 to 7 in the increasing order of their magnitude. Image credit Frank *et al.* (1992)

to its tidal effect there is an elongation of the surface of the companion and centrifugal forces flatten them. The nearly circular region surrounding each star is known as Roche lobe. The lobes are connected with each other through an inner Lagrangian point L_1 . The point L_1 is the saddle point which means that the mass in the vicinity of this point moves easily from one lobe to the another. Matter from the companion fills its Roche lobe and after that matter will escape into the Roche lobe of compact object through L_1 . This type of mass transfer is known as Roche lobe overflow. In the following section we discuss about this type of mass transfer along with the other two processes namely, Stellar wind accretion and Be disk accretion .

1.4.1 Roche-lobe overflow

The binary system evolves with time and during the course of its evolution the separation between two stars decreases due to radial expansion of the companion star to the point where the gravitational pull of the compact object is sufficient enough to strip off its outer layer or due to loss of orbital angular momentum of the system in the form of stellar wind or due to gravitational radiation. As the binary separation decreases, the size of the Roche lobes also decreases as a result matter from the Roche lobe of the companion flows into the Roche lobe of the compact object through the inner Lagrangian point L_1 . This process of accretion is known as Roche-lobe overflow. As discussed earlier this type of mass flow is common in LMXBs. Matter from the companion is not accreted directly onto the compact object as it carries some angular momentum due to the rotation of companion. So the accreted matter spiral around the compact object in a circular orbit. Formation of accretion disk around the compact object occurs when the circularization radius (R_{cir}) is greater than the radius of accreting object. At the circularization radius the specific angular momentum (J) of the accreting matter becomes same as that in a circular orbit around the compact object. The circularization radius is given by,

$$R_{cir} = \frac{J^2}{GM} \quad (1.7)$$

where M is the mass of the compact object. The formation of disk begins at this radius. The accreting matter orbiting around the compact object starts losing its angular momentum which transfers due to viscous dissipation and moves inward into the orbit of smaller radius, thus forming an accretion disk. For a typical LMXB the circularization radius is given by

$$R_{cir} \geq 3.5 \times 10^9 M_C^{1/3} P_{hr}^{2/3} \text{ cm}$$

where M_C is the mass of the companion in terms of solar mass and P_{hr} is the orbital period of binary in hours. Thus the circularization radius $R_{cir} > 10^9$ cm which is greater than the radius of the compact object thus the formation of the disk is very obvious in LMXBs, which is supported by observations.

1.4.2 Stellar Wind Accretion

Stellar wind accretion is common in close binary systems having early O or B type star and a compact object (neutron star or black hole). So stellar wind accretion occurs mostly in HMXBs. They are highly luminous object because of this X-ray sources was discovered first in these system. The early type stellar companion throws out matter in the form of stellar wind at the rate of 10^{-6} - $10^{-5} M_{\odot} \text{ yr}^{-1}$ with a very high velocity (Frank *et al.*, 1992). The velocity of the stellar wind (v_w) is given as follow,

$$v_w(r) \sim v_{esc}(R_s) = \left(\frac{2GM_s}{R_s} \right)^{1/2} \quad (1.8)$$

where v_{esc} is the escape velocity at the surface of the star, M_s and R_s are the mass and radius of the star respectively. For the typical values of M_s and R_s the velocity of the stellar wind v_w is few thousand km s^{-1} . If v_n is the orbital velocity of the compact object about its companion then the relative velocity of the wind is $v_{rel} = (v_n^2 + v_w^2)^{1/2} \approx v_w$, as the velocity of the neutron star is relatively small compared to the wind velocity. As the wind passes close to the compact object it will make an angle $\beta \cong \tan^{-1}(v_n/v_w)$ with the line of centers. If the kinetic energy of wind particles passing close to the compact object is less than the gravitational potential energy, then it will get captured and will be accreted by the compact object. The wind capture takes place in the cylindrical region along the wind

direction and will have a radius (r_{acc}) as below,

$$r_{acc} \sim \frac{2GM}{v_{rel}^2} \quad (1.9)$$

where M is the mass of the compact object. The fraction of the mass captured by the compact object from the stellar wind of the companion is,

$$\frac{\dot{M}}{-\dot{M}_w} \cong \frac{\pi r_{acc}^2}{4^2} \cong \frac{1}{4} \left(\frac{M}{M_s} \right)^2 \left(\frac{R_s}{a} \right)^2 \quad (1.10)$$

where \dot{M}_w and \dot{M} are the rate at which companion loses its mass and is captured by the companion respectively and a is the binary separation. For the typical values of the masses of the compact objects and star, radius of the star and binary separation this fraction is about 10^{-3} - 10^{-4} (Frank *et al.*, 1992). Thus the fraction of the mass captured from the stellar wind is very small and seems like wind accretion inefficient compared to Roche lobe overflow but the rate of mass loss by a star in form of the stellar wind is very large because of which the sources appears luminous. The luminosity of the source in terms of \dot{M} and \dot{M}_w can be written as,

$$L \sim 10^{37} \left(\frac{\dot{M}}{10^{-4}\dot{M}_w} \right) \left(\frac{\dot{M}_w}{10^{-5}M_{\odot}yr^{-1}} \right). \quad (1.11)$$

A bow shock wave is formed at a distance r_{acc} from the neutron star due to accretion of highly supersonic stellar wind (see Fig. 1.3). Due to focusing of stellar wind an accretion disk is also formed behind the compact object. In HMXBs an accretion disk is formed if the accreting matter has some angular momentum and the circularization radius R_{cir}^w is greater than radius of the compact object. The R_{cir}^w is defined as,

$$R_{cir}^w \cong 1.3 \times 10^6 M_c^{1/3} P_{10}^{2/3} \quad (1.12)$$

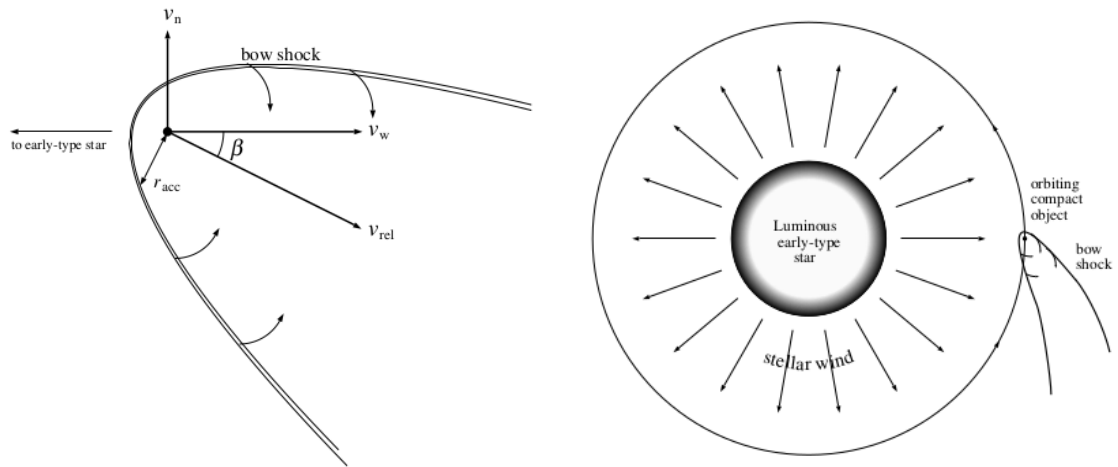


Fig. 1.3 Left: Schematic diagram of a compact object accreting matter through stellar wind. Right: Figure showing the direction of velocities of neutron star and wind.

where P_{10} is the orbital period in the unit of 10 days. However the formation of accretion disk is very rare in the case of HMXBs.

1.4.3 Be-disk Accretion

More than 60% of the HMXBs discovered are Be/X-ray binaries. One of the binary component of this system is an optical Be star, which is non-supergiant B-type star of luminosity class between III-V. The qualifier "e" denotes that spectral lines are observed in the spectrum of the star during some phase of its life which distinguished it from a normal B-star. The prominent spectral lines observed in Be stars are Balmer and Paschen series of the hydrogen but in some cases He and Fe lines are also found to emit (Reig, 2011). These stars also show large IR radiation than from B-star of same spectral type. The presence of the equatorial disk (Fig. 1.4) in BeXBs may be the reason for the origin of the emission lines and the infrared excess observed in the source. However the process through which this disc formed is not known yet but it is proposed that a rapidly rotating Be star expels matter forming the disk (Porter and Rivinius, 2003). The Be stars of the BeXBs are within the Roche lobe as the orbital periods of the system is very long and a

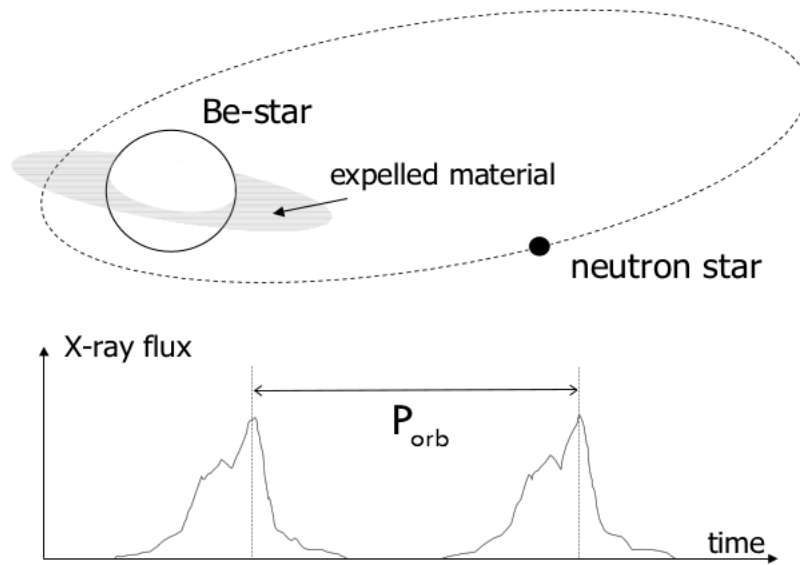


Fig. 1.4 Illustration of Be/X-ray binary system. The shadow near the Be star represents equatorial disk. The neutron star orbiting around the Be star captures matter from the disc during periastron passage and causes periodic outburst of type I. Image courtesy: (Tauris and van den Heuvel, 2006).

Be star being a non-supergiant. Mass is accreted by the neutron star in this system during periastron when the neutron star passage close to or through the equatorial disc of the Be star. The mass transfer occurs through the Roche lobe overflow. Due to accretion of large amount of materials during periastron passage a giant X-ray outburst is observed in these systems. BeXBs have a eccentric orbit with $e \geq 0.3$ and orbital period in $\sim 13-330$ days range.

BeXBs are mostly transient in nature which are observable only during an outburst. The outburst are of two types - Type I and Type II. Type I outburst are frequent and periodic in nature and occurs during periastron passage of the neutron star. The outburst last about $0.2-0.3 P_{orb}$ days, where P_{orb} is the binary orbital period. The luminosities during Type I bursts are found to be below Eddington limit reaching a peak value $L \leq 10^{37} \text{ erg s}^{-1}$. As compared to a Type I outbursts, the Type II outbursts are rare and giant. The luminosities during Type II outburst can reach or even cross the Eddington limit. These outbursts last

longer than Type I outburst and last for a large fraction of the binary orbital period or even cover few orbital periods. This type of outburst is not dependent on orbital phases. It is believed that an accretion disk is formed during the outburst which is also supported by the observations of quasi-periodic oscillations (QPOs) in some BeXBs. The steady spin-up rates in BeXBs during these outbursts are also explained by the presence of accretion disk. The reason behind those outbursts are yet to be known.

1.5 Neutron star X-ray binaries and X-ray pulsars

X-ray binaries consist of neutron star as a compact object. Neutron stars in X-ray binaries can have magnetic field about 10^8 - 10^{13} G. The presence of large magnetic field of the neutron star will affect the accretion of matter onto it. At certain radius disruption of the accretion flow occurs due magnetic field and accreted matter is then channeled by the magnetic field onto the magnetic poles of the neutron star. If we consider the magnetic field (B) of the neutron star to be a dipolar in nature then,

$$B \sim \frac{\mu}{R^3} \quad (1.13)$$

where μ is the magnetic dipole moment and R is the radius of the neutron star. The Alfven radius R_A is then defined as the radius at which the magnetic pressure $\frac{B^2}{8\pi}$ becomes equal to the ram pressure of the infalling matter given by $\frac{1}{2}\rho v^2$. Thus at R_A we have,

$$\frac{B^2}{8\pi} = \frac{1}{2}\rho v^2 \quad (1.14)$$

v is the velocity of the matter and for radial free fall in spherical geometry $v = \sqrt{2GM/R}$ and also $\rho = \dot{M}/4\pi vR^2$. Thus from above equation,

$$R_A = \left(\frac{\mu^4}{2GM\dot{M}^2} \right)^{1/7} = 3.2 \times 10^8 \dot{M}_{17}^{-2/7} \mu_{30}^{4/7} \left(\frac{M}{M_\odot} \right)^{-1/7} \text{ cm}. \quad (1.15)$$

where M_\odot is the solar mass, \dot{M}_{17} is the mass accretion rate in the unit of $10^{17} \text{ gm s}^{-1}$ and μ is in the unit of 10^{30} G cm^3 . The Alfven radius is also called magnetospheric radius, for a distance smaller than this radius, the magnetic field will affect the flow of the infalling matter. The magnetosphere rotates with the same angular velocity as that of the neutron star. For non-spherical geometry the magnetospheric radius is bit modified. The accretion of matter depends on another quantity called co-rotation radius r_{co} which is defined as the radius at which the centrifugal force due to rotation of the neutron star magnetosphere counter balance the gravitational force acting on the accreting matter or in other words it is the radius at which the Keplerian frequency of the disk equals the neutron star spin frequency. Thus r_{co} can be expressed as

$$r_{co} = \left(\frac{GM}{\omega^3} \right)^{1/3}. \quad (1.16)$$

If $r_{co} > r_m$ then the centrifugal force due to rotation of magnetosphere becomes smaller than the gravitational force and there is an accretion of matter onto the neutron star. In this case the Keplerian velocity of the accreting matter is greater than the magnetospheric rotational velocity. The accreting matter is channeled by magnetic field along the neutron star poles. Depending upon the mass accretion rate \dot{M} the accreting matter falling onto the poles is stopped either by radiative shock wave or Coulomb interactions. This causes accumulation of matter on the poles forming an accretion column of cylindrical shape. X-rays are radiated from the accretion column or accretion funnel. However, if $r_{co} < r_m$

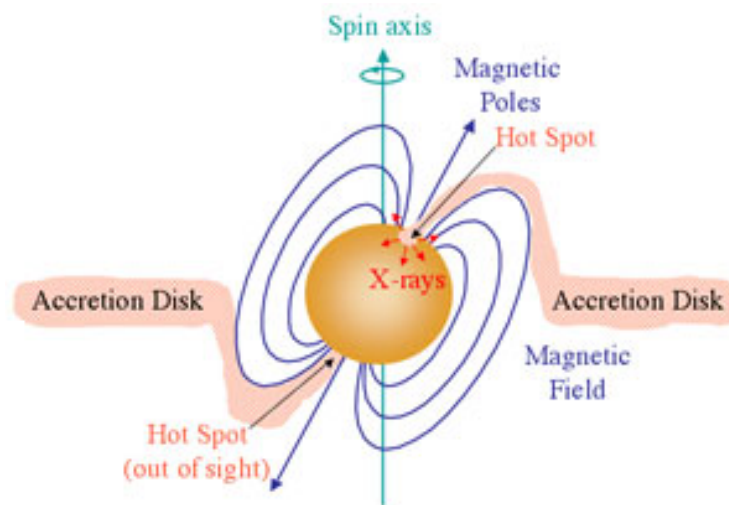


Fig. 1.5 Figure showing the accretion powered X-ray pulsar where matter is channeled along the magnetic field lines. The accretion columns are formed inside the the hot spots. Image courtesy : <https://astronomy.swin.edu.au/cosmos/X/X-ray+Pulsar>

then there exist a centrifugal barrier which prevents the accretion of matter onto the neutron star. This phenomenon of centrifugal inhibition is known as *propeller effect*.

The accretion columns formed at the magnetic poles of a neutron star emits X-rays through different mechanisms. If there exist misalignment between the magnetic axis and rotational axis (Fig. 1.5), then the X-rays emitted from the poles of the rotating neutron will appear as X-ray pulses. Hence the name X-ray pulsars, which are neutron star X-ray binaries that are powered by the accretion. The kinetic energy of the accreting matter moving with the velocity close to that of the light is released as radiation from the poles. The size of the accretion column is about ~ 1 km (Davidson and Ostriker, 1973). However the shape and size of the accretion column along with the physical process behind its formation is not known completely. The emission geometry and the interaction of accreting matter with neutron star surface is determined by the mass accretion rate or the luminosity of the X-rays emitted by the pulsar. When the accretion rate is low thermal X-rays are emitted from the hot spots formed at the poles of the neutron star. However, for a large accretion rate a radiation dominated shock wavefront is formed above the neutron star's

poles. X-ray emission in this case occurs through the shock wavefront and the thermal mound at the bottom of accretion column through thermal and bulk Comptonization processes.

Based upon the luminosity of the pulsar Basko and Sunyaev (1976) proposed two types of accretion regimes. Those regimes were differentiated by a certain value of luminosity called critical luminosity (L_{crit}). If the luminosity of the X-ray pulsars is less than L_{crit} then the pulsars are said to be in sub-critical regime of accretion. For the luminosity greater than L_{crit} the source is in super-critical accretion regime. The critical luminosity depends on the magnetic field of the pulsar and the geometry of accretion disk (Becker *et al.*, 2012). Becker *et al.* (2012) considering the different physical processes that are occurring in the accretion column determined the critical luminosity for X-ray pulsars having cyclotron absorption feature in their spectra, which is given by

$$L_{crit} = 1.49 \times 10_{0.1}^{37-7/5} w^{-28/15} M_{1.4}^{29/30} R_{10}^{1/10} B_{12}^{16/15} \text{ ergs}^{-1} \quad (1.17)$$

where $M_{1.4}$ is the mass of the neutron star in the unit of $1.4M_{\odot}$, R_{10} is the radius of the neutron star in the unit of 10 km and B_{12} is the magnetic field in the unit of 10^{12} G. Λ is a constant which is considered 1 for a spherical accretion but it is less than 1 for a disk accretion. The parameter w lies between 1 – 3, $w = 1$ corresponds to Bremsstrahlung spectrum whereas for $w = 3$ corresponds to Planck spectrum. Considering the typical value of neutron star parameters *i.e.* $M_{1.4} = 1$, $R_{10} = 1$, $\Lambda = 0.1$ and $w = 1$, the critical luminosity becomes,

$$L_{crit} = 1.49 \times 10^{37} B_{12}^{16/15} \text{ erg s}^{-1} \quad (1.18)$$

For low mass accretion rate the X-ray luminosity is smaller than the critical luminosity ($L \ll L_{crit}$). In this case there exist two zone in the accretion column - free falling zone and

shock zone. In free falling zone matter falls freely until it encounters shock near the surface of the neutron star (Basko and Sunyaev, 1976). In the shock zone the deceleration of matter takes place through electrostatic interaction. The X-rays from the hot spot escapes vertically upward along the accretion column. As a result pencil-beam emission pattern is formed which is shown in Fig. 1.6.

A different scenario of accretion formed when the luminosity is close to or equal to the critical luminosity ($L \leq L_{crit}$), in this case the radiation dominated shock wave is formed in the accretion column (Fig. 1.6). Radiation from the accretion column below the shock region is emitted along the direction perpendicular to the column as a result a fan-beam shaped emission pattern is found whereas the radiation above the shock region moves upward in the form of a pencil beam pattern. Thus the resulting beaming pattern is a mixture of pencil and fan beams. Below the shock the plasma is decelerated by electrostatic interaction that sinks slowly toward the neutron star.

For a high accretion rate the luminosity of the source is higher which is greater than the critical luminosity ($L > L_{crit}$), in this case the accreting matter is completely halted by the radiation dominated shock and loses all of its kinetic energy. The shock rises above the surface of the neutron star with an increase in accretion rate and beneath the shock region there exists an extended sinking zone (Basko and Sunyaev, 1976). In this case X-ray emission results only along the side walls of the accretion column and we get a pure fan-beam emission pattern.

1.5.1 Accretion X-ray millisecond pulsars

Accretion X-ray millisecond pulsars (AMXPs) is a subclass of LMXBs which are rotating very fast about few hundreds of times in one second. Soon after the discovery of first millisecond radio pulsar in 1982 (Backer *et al.*, 1982), it was believed that LMXBs are the progenitor of the millisecond radio pulsar. It was suggested that during the course of

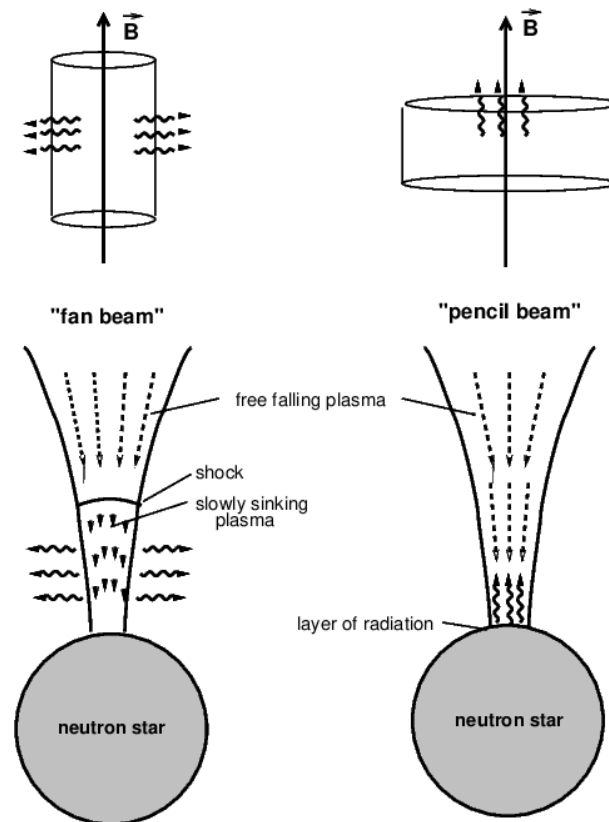


Fig. 1.6 The figure on the left represent the super-critical accretion regime where matters fall freely until it encounters a shock above the neutron star surface. From the region below the shock X-rays are emitted in the direction perpendicular to the accretion column to produce fan beam. The figure on the right hand side is in case of luminosity below the critical value. In this case X-ray escapes vertically upward from the hot spots along the accretion column to produce pencil beam pattern. Image courtesy - Schönherr *et al.* (2007)

evolution of LMXBs the slow rotating neutron stars evolves into the fast rotating neutron stars. The mechanism responsible for the spinning-up of the pulsar is the transfer of angular momentum due to accretion of matter from the companion to the neutron star (Alpar *et al.*, 1982; Radhakrishnan and Srinivasan, 1982). The formation of accreting millisecond X-ray pulsar is explained by what is known as "recycling scenario". A radio pulsar stops emitting radio pulsation after entering a phase called "pulsar-graveyard". After entering this phase the neutron star in a binary with low mass non-collapsed companion be such that during the evolution of the binary system the companion comes in contact with the neutron star through Roche lobe and the transfer of mass from companion to the neutron star occurs. In

addition to transfer of mass there is also a transfer of large amount of angular momentum onto the neutron star resulting in the enhancement of accretion torque which spin-up it. So in a broad sense there is recycling of radio pulsars to AMXPs and hence the name "recycling scenario". At the end when transfer of mass from companion stops the neutron star can no longer emits X-rays but can emit radio waves as recycled millisecond radio pulsar.

The first AMXP discovered was SAX J1808.4-3658 in 1998 by *Rossi X-ray Timing Explorer (RXTE)* (Wijnands and van der Klis, 1998) and provided confirmation of the recycling scenario. Another confirmation of this scenario came through the discovery of a radio millisecond pulsar PSR J1023+0038 with an accretion disk (Archibald and Stairs, 2009). This was the first observed case where a neutron star transforms to a radio pulsar after the X-ray pulsar phase of the star. The model is further supported by the discovery of the millisecond pulsar IGR J18245-2452 (Papitto and Ferrigno, 2013) which shows both an AMXP and radio millisecond pulsar phase. Till date there are 20 AMXPs (Salvo and Sanna, 2020) discovered. Some AMXPs are ultra compact binary systems between neutron star and white dwarf with an orbital period (P_{orb}) less than or equal to 80 min. For compact systems the neutron star companion is a brown dwarf which has an orbital period between 1.5-3 hr. However for wider systems of binary pulsars, the companion may be normal main sequence star with orbital periods between 3.5-20 hr. AMXBs are transient in nature which can be observed during an outburst. Most of the AMXBs have shown only one outburst after their discovery but few of them show recurrent outbursts. The outbursts in most cases last from few days to about three months. NGC 6440 X-2 has shown a recurrence time of one month which is the shortest recurrence time of the outburst observed in AMXPs. The longest duration of an outburst was observed in HETE J1900.1-2455, which lasted for 10 years.

It is known that intermittency of the pulsations can be observed also in AMXPs. This phenomenon was first observed in the AMXP HETE J1900.1-2455 during 2005 outburst when pulsation of 377 Hz was observed during the first 20 days of the outburst and thereafter went in the intermittent phase for next 2.5 years and after that there were appearance and disappearance of pulsations in various instances (Galloway *et al.*, 2007). Another case of intermittency of the pulsation is found in AMXP Aql X-1 where the coherent pulsation is detected only in 150 s data segment with a total exposure time of 1.5 Ms. This phenomenon is particularly important in understanding the absence of pulsations in the major fraction of NS LMXBs. SAX J1748.9-2021 also shows intermittency in pulsation where pulsation is observed in several data segments and it is observed that in three out of four outbursts (Altamirano *et al.*, 2008; Patruno *et al.*, 2009a). This phenomenon is particularly important in understanding the absence of pulsation in the major fraction of the observed time of NS LMXBs. Intermittency in the system is thought to be due to decrease in the magnetic field strength by three order of magnitude on a timescale of few hundreds of days which does not allow disk to truncate and in this case a very small fraction of gas is channeled producing weak pulsation (Patruno and Watts, 2013). However the theory proposed by Patruno and Watts (2013) is not complete and it cannot explain all the phenomenology that are observed in AMXPs.

During an outburst AMXPs have luminosity less than 10% of the Eddington limit and no transition from hard to soft spectral states is observed. The spectral state of AMXPs is similar to that of the NS LMXBs in hard state. The X-ray continuum of AMXPs consist of one or more blackbody components and a Comptonization component having cutoff energies of tens of keV. In few AMXPs fluorescence iron lines are observed in the 6.4-6.7 keV energy range which however are found to smeared out by the Doppler and relativistic effect. In some AMXPs X-ray photons are scattered in the disk producing excess of emission between 10-30 keV which is known as Compton hump (Papitto *et al.*, 2010).

They have long term spin down rate of 10^{-15} - 10^{-16} Hzs⁻¹. The spin down of AMXPs are likely caused by the loss of angular momentum in the form of magnetic dipole radiation which can be used to constraint the magnetic field of the neutron star in AMXP with magnetic field of the order of 10^8 G.

1.6 Generation of X-rays in Astrophysics

It is known that there are four main processes through which continuous X-rays are produced. These are as follows,

- **Blackbody emission** - A body which absorbs radiation emits radiation. The energy of the emitted photon depends on the temperature of the body. A hot body which is above absolute zero temperature emits electromagnetic radiation. So stars can also radiates it energy in the form of electromagnetic radiation like blackbodies. Newly formed neutron stars or hots spot of accretion powered X-ray pulsars which can have a temperature of the order of 10^6 K emits X-rays in the form of blackbody radiation.
- **Bremsstrahlung** - Most of the matters are in the plasma state at a temperature above 10^5 K, so the gas consists of positively charged ions and electrons. These charged particles are also in thermal equilibrium. During a close interaction between an electron and a positive ion, due to strong electric force the electron gets accelerated. This accelerated electron then radiates electromagnetic radiation which is known as Bremsstrahlung (braking radiation). The emitted electromagnetic radiation of electron has continuum shape which depends only on the temperature. With the increase in the temperature the velocity of electrons increases which means that their energy also increase, so energy of radiation emitted by Bremsstrahlung process also increases. At temperature above 10^6 K, photons emitted lies in the X-ray range.

- **Synchrotron radiation** - In the presence of a magnetic field a fast moving electron changes its direction of motion as the field exerts Lorentz force perpendicular to the direction of motion. The change in the velocity the electron is associated with acceleration of electron resulting in emission of electromagnetic radiation. This type of radiation is known as magnetic Bremsstrahlung or synchrotron radiation. The frequency of the emitted radiation depends both on the magnetic field and the energy of the electron. The existence of synchrotron radiation indicates the presence of relativistic electrons as one observes in the synchrotron radiation from a radio emitting shell-like supernova remnants where the energy of the electrons emitting radio waves are about 1 GeV.
- **Inverse Compton scattering** - When low energy photons are scattered by ultra relativistic electrons then photons will gain energy from the relativistic electron, which is the inverse of Compton effect. This process is called inverse Compton effect. For a photon having an energy $h\nu$, the relativistic energy of the scattered photon is $\gamma^2 h\nu$, where $\gamma = \sqrt{1 - \frac{v^2}{c^2}}$ represents the Lorentz factor for electron moving with velocity v which is comparable to the velocity of light c . Thus even a photon of few eV can be scattered by ultra relativistic electron to produce X-ray or γ -ray photon by this process.

The blackbody emission and Bremsstrahlung are the thermal processes where as Synchrotron and inverse Compton scattering are the non-thermal processes that are responsible for the origin of X-rays in the neutron star. Apart from the continuous X-rays spectrum there might exist a discrete X-ray spectrum. This discrete X-ray spectrum is due to the characteristic X-rays.

1.6.1 Characteristic X-rays

The characteristic X-rays appears as sharp peaks in the continuous X-ray spectrum. In principle the de-excitation of excited atoms or ions occurs by the emission of photons which appears as emission lines. There is two main process through which the characteristic X-rays are produced - (1) Fluorescence and (2) Recombination.

1. **Fluorescence** - When a highly energetic X-ray photons hit atoms it can knock the electrons from the inner most orbitals. Electrons from high energy orbitals fills the vacancy so created and the resulting photons having energy equal to the energy difference between two orbitals is emitted. This gives us the fluorescent X-ray lines. The well observed fluorescent X-ray lines in the spectrum of X-ray binaries that of neutral or ionized iron in 6-7 keV energy range.
2. **Recombination lines** - These spectral lines are observed during ion-electron recombination. The recombination of electron with ion usually leaves the ion in an excited state. This excited ion emits photons as the electron jumps successively into the lower energy states and finally to its normal stable state.

1.7 X-ray spectra

X-ray spectra of X-ray binaries (XRB) are almost continuous in shape and which is described by a power law having cutoff energy in 10-30 keV energy range. In some cases there will be blackbody component in soft X-ray range *i.e.* below 5 keV. Along with the continuum shape there exist fluorescence emission lines of iron and other elements in some cases. In some accretion powered X-ray pulsars absorption like feature which is known as cyclotron resonance scattering features (CRSF) are also observed. Although the physical processes responsible for the generation of X-rays in accretion column and in magnetosphere are very complex but the spectra are found to be well predicted by

phenomenological models. It is found that models which fits the spectrum of one XRB well does not fit the other XRBs satisfactorily. There have been several attempts to produce the spectra theoretically (Nagel (1981), Meszaros *et al.* (1983), Burnard *et al.* (1991)) but due to the complexity of the processes a standard model that defines the spectra of X-ray binaries is not known satisfactorily. The absence of knowledge of precise geometry of the accretion column further increases this complexity. The theoretical model proposed by Becker and Wolff (2007) was successful in explaining the continuum shape of Her X-1, LMC X-4 and Cen X-3. This model is based on the bulk and thermal Comptonization of X-ray photons in the accretion column. The fig. 1.7 shows the theoretical spectrum of LMC X-4. Schematically this model is described in fig. 1.8. Soft photons generated by blackbody radiation at the thermal mound located at the bottom of the accretion column act as seed photons for upscattering. The optically thin region above the thermal mound produces bremsstrahlung and cyclotron photons. These photons move upward in the radiation dominated shock in the accretion column and gets upscattered by the electrons in the gas by the process of bulk Comptonization. The thermal Comptonization of photons is responsible for the cut-off and flat soft X-ray spectrum. Another theoretical model COMPMAG (Farinelli *et al.* (2012, 2016)) generally useful for the description of the spectral formation based on the bulk and thermal Comptonization of the photon.

1.7.1 Cyclotron Resonance Scattering Feature

In the spectra of X-ray pulsars the Cyclotron Resonance Scattering Feature (CRSF) which are commonly known as cyclotron lines are observed as absorption like feature in between 10-100 keV energy range. The feature was first observed in Her X-1 (Trümper *et al.*, 1978). The physical mechanism responsible for the cyclotron resonance is the resonant scattering of the X-ray photons by quantized electrons on the surface of the neutron star. These electrons have energy state in the quantized Landau levels. This feature is directly related

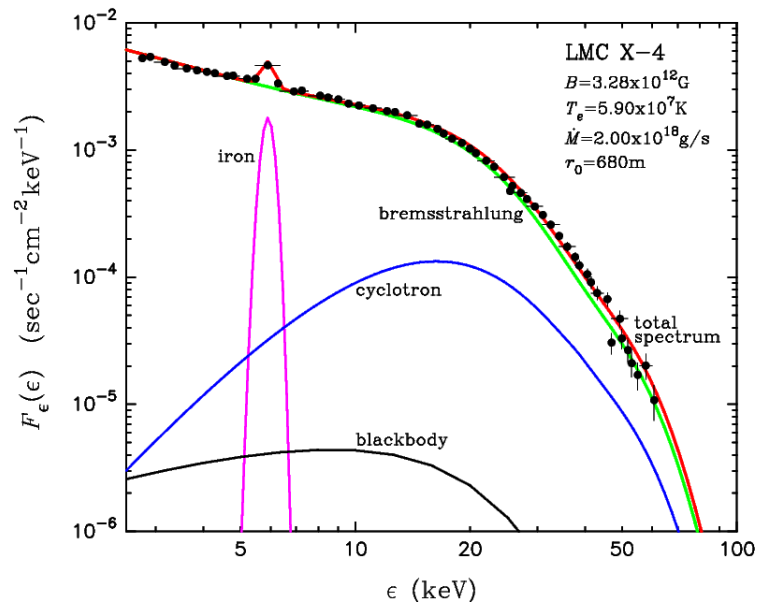


Fig. 1.7 Theoretical spectrum of LMC X-4 computed by Becker and Wolff (2007)

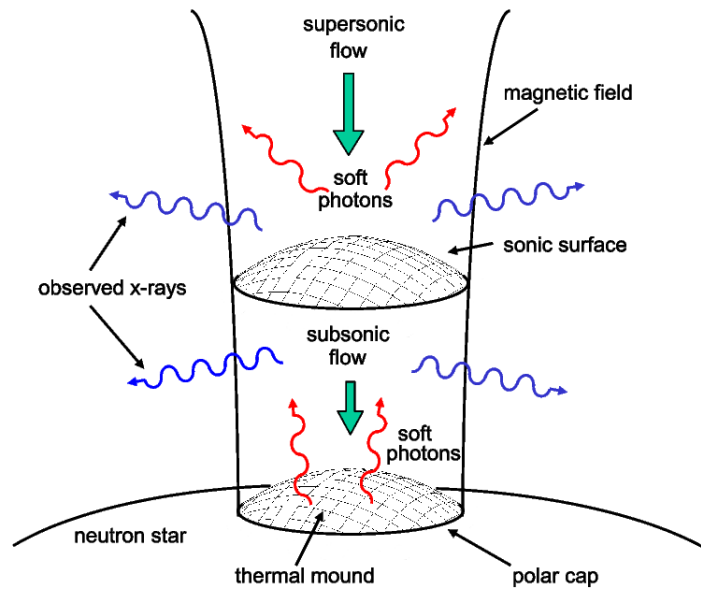


Fig. 1.8 An illustration of accretion column of accreting neutron star. Seed photons are produced through blackbody at the thermal mound at the base of the accretion column where as seed photons through bremsstrahlung and cyclotron are produced throughout the accretion column. Image courtesy Becker and Wolff (2007)

to the magnetic field of the neutron star and the presence of this feature in the spectra of pulsars helps us to estimate the magnetic field of the neutron star.

The origin of the cyclotron line can be explained by quantum electrodynamics. The trajectory of the electrons follows helical path due to the Lorentz force in the presence of magnetic field. The electrons revolves in the helical trajectory with a frequency known as Larmor frequency. The Larmor frequency (ω_b) and radius (r_b) are given by,

$$\omega_b = \frac{eB}{m_e c}, \quad (1.19)$$

$$r_b = \frac{m_e v_{\perp}}{eB} \quad (1.20)$$

where m_e is the mass of the electron, v_{\perp} is the perpendicular component of electron's velocity, e denotes the charge of an electron and B is the magnetic field of the neutron star. Thus the Larmor radius decreases as the magnetic field increases and once it approach the de-Broglie wavelength then the quantum mechanical effect become important for its description. The electron then gets quantized in the direction perpendicular to the magnetic field into the discrete Landau levels. For the Landau levels, the energy of an electron is given by,

$$E_n = \frac{mc^2}{\sin^2 \theta} \left(\sqrt{1 + 2n \frac{B}{B_{crit}} \sin^2 \theta} - 1 \right) \quad (1.21)$$

where θ is the angle between the incident photon and the magnetic field, $B_{crit} = \frac{m_e^2 c^3}{e \hbar} \approx 4.4 \times 10^{13}$ G which is the critical magnetic field at which the kinetic energy of the electron or Landau's energy level becomes equal to the rest mass energy of the electron. Here n is a positive integer such that $n = 1$ corresponds to fundamental cyclotron line and that with $n = 2, 3, 4$ correspond to its harmonics. From eq. (1.21) it is evident that the line energy depends strongly on the angle θ . In case of strong gravitational field the above equation is modified by a factor $(1+z)^{-1}$, where z is redshift parameter. Thus the cyclotron line

corresponds to the internal geometry of the accretion column. When the magnetic field is greater than or equal to the critical B_{crit} i.e. $B \geq B_{crit}$ then the relativistic corrections of path of the electron moving in the magnetic field becomes important (Araya-G'omez and Harding, 2000). In the non-relativistic case when the magnetic field is very small compared to the critical value B_{crit} i.e. $B \ll B_{crit}$, then the energy difference between the quantized states is given by

$$E_{cyc} = \hbar\omega_b = \frac{e\hbar}{m_e c} B = 11.6 B_{12} \text{ keV} \quad (1.22)$$

where B_{12} is the magnetic field in the order 10^{12} G. In the presence of strong gravitational field the above energy is to be modified by redshift correction term $(1+z)^{-1}E_{cyc}$. The above formula in eq. (1.22) is used to estimate the magnetic field of a neutron star for a known value of the cyclotron line energy. Thus in the presence of magnetic field the energy state of electrons are quantized at Landau levels, the photons having energy in the integral multiple of E_{cyc} are absorbed by these electrons. As a result electron gets excited and moves into the higher energy states of Landau levels. These states are very unstable with life time much shorter than that of the time scale of collision de-excitation of electrons. As a result re-emission of the absorbed photon of same energy occurs. Instead of absorption of photon the whole process can be considered as the resonant scattering. As there exist a continuity between absorption and emission processes in plasma, photons having energy in the integral multiple of E_{cyc} will get trapped in the accretion column region. During an inelastic scattering process the energy of these photons changes and it escape the accretion column at suitable energy. As a result of which broad absorption like features are observed in the spectra of X-ray pulsars at the energy close to an integral multiple of E_{cyc} . It is also observed that in some X-ray pulsars fundamental cyclotron line is associated with its harmonics in some cases. The variation of scattering of cross section with energy for exciting an electron in different Landau levels are shown in Fig. 1.9.

Gnedin and Sunyaev (1974) first theoretically demonstrated the presence of the cyclotron resonance scattering features (CRSF) even before the feature was actually discovered by observations. However the origin of this feature is not fully understood. There are three methods by which the formation of the feature can be simulated - (i) Monte Carlo (Araya and Harding, 1999; Araya-Góchez and Harding, 2000), (ii) Feautrier methods (Meszaros and Nagel, 1985) and (iii) analytically (Wang *et al.*, 1993). The Monte Carlo simulation of CRSF based on the interpolation table of mean free path of the scattering photon and the momentum of the scattering electron with a magnetic field B such that $0.01 \leq B/B_{crit} \leq 0.12$ and electron temperature lying between 3-15 keV was considered by Schwarm *et al.* (2017). This method can be used to simulate CRSF for X-ray pulsars having complex accretion geometry for a given magnetic field and viewing angles. The features depend on the geometry of the emission, plasma properties and on the optical depth of the column.

The cyclotron lines are modeled using either Gaussian or pseudo-Lorentzian profiles to obtain its line energy, equivalent width and the strength. The above parameters are found to vary with pulse phase and the luminosity. The line energies either shows correlation or anti-correlation with the luminosity. It has been shown (Basko and Sunyaev, 1976; Becker *et al.*, 2012) that this is because of two accretion regimes depending on the critical luminosity. At super-critical luminosity X-ray pulsars the emission pattern may be fan-shaped which affects the CRSF through Doppler effect on the observation of anti-correlation of CRSF with luminosity. In the sub-critical regime it is observed that the emission pattern is a pencil beam admitting positive correlation of CRSF with energy. However, there are some X-rays pulsars which do not show any correlation with the luminosity. In some cases a wings are observed in the fundamental cyclotron lines which are believed to be due to photon spawning effect.

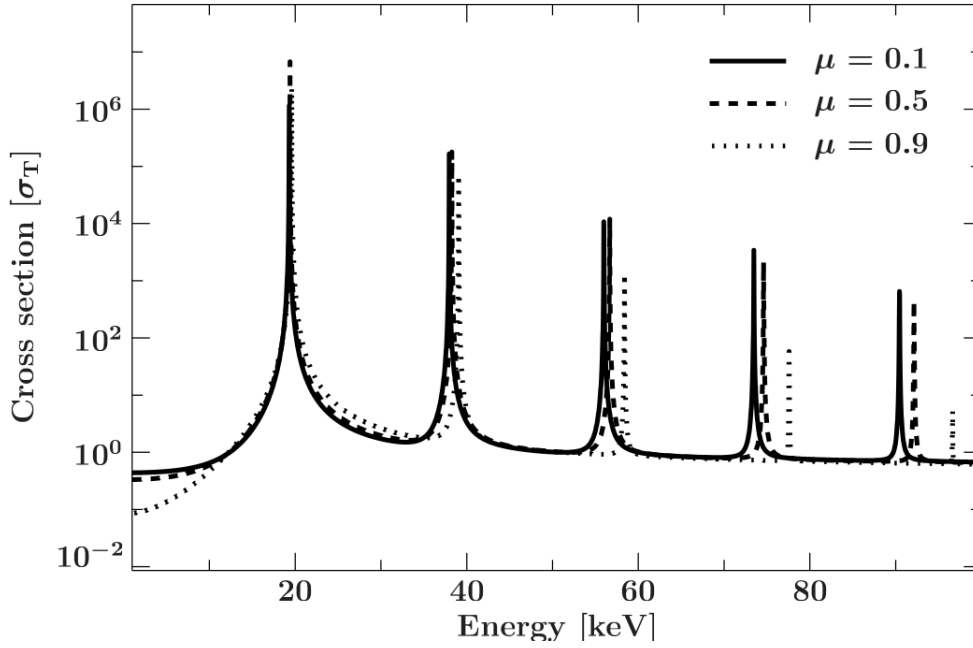


Fig. 1.9 Variation of scattering cross section with energy for exciting an electron in initial Landau level $n = 0$ to $n = 6$ for given magnetic field about $B = 0.0385B_{crit}$. The fundamental cyclotron line is at 20 KeV. The solid, dashed and dotted lines represents cross section for three viewing angle $\nu = \cos \mu = 0.1, 0.5, 0.9$ respectively. Figure courtesy-Schwarm *et al.* (2017).

1.8 Pulse Profiles

The temporal variation of the photon counts per unit time is called light curve. Light curves of X-ray pulsars show periodicity due to the rotation of the neutron stars. By folding these light curves about the spin period of the neutron stars pulse profiles are obtained. Pulse profile of a pulsar shows variation of the X-ray intensities with the pulse phases. Pulse profiles of different X-ray pulsars are different and unique. The shape of the pulse profiles depends on various factors like properties of the accretion column, emission geometry, mass accretion rate, angle between magnetic and rotational axes and bending of light due to gravitation. Considering the beam pattern along with the variation in the geometrical aspect of magnetic axis, geometric axis and the line of sight one can reproduce the pulse profiles. If α and β are the angle which the rotational axis makes with the magnetic axis and the line of sight respectively then both poles are visible if $\alpha + \beta > \pi/2$ and

only one visible if $\alpha + \beta < \pi/2$. A single peaked pulse profiles is thought to be due to emission from a single pole of the neutron star where as the double peaked pulse profiles are due the emission from two poles of the neutron star. In some pulsars multiple peaks are also observed in the soft X-ray energy range. In some cases dips are also observed in pulse profiles at some specific phases this might be due to the eclipsing of the radiation emitted from the hotspot by an optically thick plasma in the accretion column (Cemeljic and Bulik, 1998). It has been observed that at the phases close to the dip the spectrum varies significantly with a large variation in the optical depth, it may be because of an extension of the accretion column only along a direction in these phases (Galloway *et al.*, 2001; Giles *et al.*, 2000). An alternate explanation of the dips is that during these phases the accretion stream comes between the hot spot and our line of sight (Maitra and Paul, 2011; Naik *et al.*, 2011). In some pulsars dips disappear in hard X-ray range. However depending on the density and opacity of matter in accretion column or streams, the dips may be observed at higher energies too. In some pulsars a phase reversal of 180 degree is observed as one moves from soft to hard X-rays range (Beri *et al.*, 2014). It has also been observed that in some pulsars there is sudden change or shift in phase at an energy very close to the cyclotron line energy. Studies of the cyclotron line energy based on the numerical simulations have found that the presence of strong absorption feature due of CSRF can affect the emission of the X-ray beam. Hence the change in pulse profiles are observed at an energy close to the cyclotron line energy (Schönherr *et al.*, 2014).

The X-ray pulsars in which the mass accretion rate and hence the luminosity varies throughout an outburst, the pulse profile is complex in the case where luminosity is above the critical value as a radiative shock wave is formed few kilometers above the neutron star as discussed earlier. If the luminosity is below the critical luminosity then the pencil beam pattern produces a simple pulse profile which is more or less sinusoidal in shape.

1.9 Objective of the thesis

The objective of the thesis is to investigate some of the salient features of neutron star X-ray binaries. The pulse profiles of the star which depends on the mass accretion rate, geometry of accretion disk, magnetic field and its distribution around the neutron star will be studied. The cyclotron lines present in the spectrum of these binaries are the direct source of information of the presence of magnetic field in the source will be use to estimate the magnetic field of the neutron star. To understand the surrounding environment of the neutron star the pulse phase-resolved spectroscopy will be used. The origin of flares in the light curves of some of the X-ray binaries are also analyzed. For the analysis the following types of sources namely, NS LMXB (AMXB) and HMXBs (SGXB & BeXB) are taken up.

Chapter 2

Description of the instruments and methods used in study

In the preceding chapter we have already discussed that the high energy radiations like X-ray, gamma rays etc cannot reach the Earth's surface as they get absorbed high up in the atmosphere. So detectors or observatories are needed to place outside the atmosphere in the space to detect these high energy radiations. This is done with the help of sounding rocket, balloon flight and rockets carrying satellites to catch the X-rays coming from different distance sources. The incoming flux of X-ray from the extraterrestrial sources are extremely low, so detector must either have a large photons collecting area so that enough numbers of X-ray photons can be collected for analysis or there must be some kind of X-ray focusing arrangement such that sufficient numbers of X-rays are focused into the detector having reasonable photon collecting area. An astronomical X-ray detectors can have either imaging or non-imaging capabilities. Non-imaging X-ray detectors in principle uses an ionizing capability of X-rays to detect them like in the case of proportional counters, scintillation detector etc and these were used extensively during the early days of X-ray astronomy. However it is not possible to have non-imaging detectors with large collecting area to have timing, spectral and imaging capabilities simultaneously, so in

order to achieve an excellent spectral and imaging capabilities X-ray focusing technique is used. The instruments with imaging capability consist of two parts the telescope to focuses X-rays and the detector. The telescope collects photons from large area and focus these photons on to the detector. However the normal focusing method using mirror or lens will not work for X-ray detection as X-rays can easily penetrate or even ionize the material used in mirror or lens. For this purpose Wolter telescope is used to focus X-rays which is based on the principle of the grazing incidence. The Wolter telescopic arrangement consists of paraboloid mirror followed by hyperboloid mirror. The necessary condition for reflection of X-rays through the telescope is that the angle of incidence of X-ray photons must be of the order of an arc-minutes. This type of telescope is found in the modern day X-ray missions like *CHANDRA*, *Swift-XRT*, *NuSTAR* etc. The use of X-ray imaging instruments also help in instantaneous estimations of the background radiations which however, is not possible in a non-imaging detector. Another interesting feature is that it is very helpful in morphological study of the extra-terrestrial X-ray sources.

At about 1000 km above the Earth's surface there exist a region where charged particles are trapped as a result of interaction between charged particle in solar wind and Earth's magnetic field. This region is called *van Allen belt*. Due to this region the X-ray detectors are placed well below the van Allen belt. However due to weakening of magnetic field between South America and South Atlantic region the van Allen belt comes closer to the Earth's surface, less than 500 km from the Earth's surface. This phenomenon is known as *South Atlantic Anomaly* (SAA). So the X-ray detectors onboard satellites must be kept switch off while passing through this region to protect the detectors from being damage.

In this thesis we have used observational data from four space based X-ray observatories namely *RXTE*, *Swift-XRT*, *NuSTAR* and *NICER* to study the properties of the neutron star in the X-ray binaries. The brief discussion of the different payloads onboard these observatories are given in the proceeding section.

2.1 Rossi X-ray Timing Explorer (*RXTE*)

The Rossi X-ray Timing Explorer (*RXTE*) is a space borne X-ray observatory named after physicist Bruno Rossi (Fig. 2.1). It was launched on December 30, 1996 which was operational till January 3, 2012. It was designed, built, controlled and managed by NASA Goddard Space Flight Center (GSFC). The mission was able to detect X-rays in 2-250 keV energy range, although its spectral resolution was moderate but it had an excellent time resolution. The two pointed instruments onboard *RXTE* were the Proportional Counter Array (PCA)(Jahoda *et al.*, 1996) and the High Energy X-ray Timing Experiment (HEXTE) (Rothschild *et al.*, 1998), along with these it also consists of a small 1-D coded mask All Sky Monitor (ASM) (Levine *et al.*, 1996).

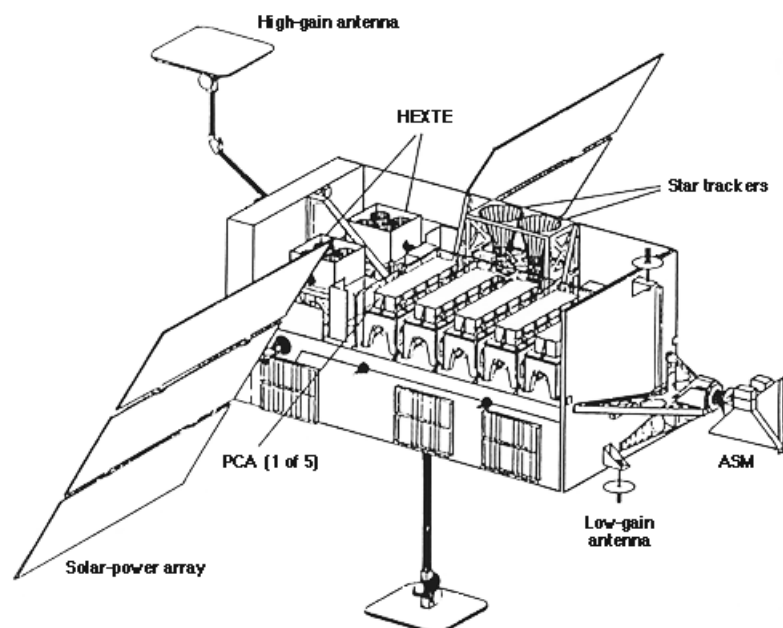


Fig. 2.1 An image of *RXTE* spacecraft along with different instruments. Image Courtesy: NASA/GSFC

2.1.1 *RXTE-PCA*

The Proportional Counter Array (PCA) was operational in 2-60 keV energy range and it had an energy resolution less than 18% at 6 keV with time resolution about 1 μ s. The total collecting area of the PCA was 6500 cm². It consist of five identical Proportional Counter Units (PCU). The net geometric collecting area of each PCU was about \sim 1600 cm². Each detector consists of two veto layer one at the top and the other at the bottom, there were three more xenon layers each divided into two halves in between them.

2.1.2 *RXTE-HEXTE*

The High Energy X-ray Timing Experiment (HEXTE) had two clusters (A and B) of detectors, each cluster consist of four NaI(Tl)/CsI(Na)-Phoswich scintillation counters. Each detector was operational in 15-240 keV and had an energy resolution of 15.4% at 60 keV. The net collecting area of HEXTE was about 1600 cm².

2.1.3 *RXTE-ASM*

The ASM was used to monitor the sky in 1.5-12 keV energy range. It consists of three Scanning Shadow Camera (SSCs), each of them contains a position-sensitive proportional counter (PSPC). With a total collecting area of 90 cm² it was able to scan 80% of the sky in a single revolution. One of the main importance of this instrument was that it was capable of detecting transient X-ray sources in the sky so that the follow-up observation can be carried by the main telescopes of the spacecraft or with other missions.

2.2 Nuclear Spectroscopic Telescope Array (*NuSTAR*)

NuSTAR is the first hard X-ray direct imaging X-ray observatory (Harrison *et al.*, 2013) which was launched successfully on 13 June 2012. It operates in 3-79 keV energy range.

Instead of normal incidence it uses grazing incidence to focus X-rays and this is achieved with the help of two canonical approximation Wolter-I telescopes design optics which focus hard X-rays onto the two solid state detectors placed at the focal plane of the optical device about 10.15 m. away. The two optical devices each contains 133 nested mirror shells, out of these shells the inner 89 shells were coated with depth-graded *Pt/C* multilayers and the remaining with depth-graded *W/Si* multilayers and these multilayers reflect efficiently below 79 keV (*Pt K*-absorption edge). Because of this depth-graded multilayers coating *NuSTAR* it is sensitive to hard X-rays upto 79 keV.

The two telescopes have its own focal plane modulus (FPMA & FPMB) (Fig. 2.2), each focal plane module consists of solid state cadmium zinc telluride (*CdZnTe*) pixel detector surrounded by a *CsI* anti-coincidence shield. The optical modules are separated from the focal plane modules by a deployable mast. Each detector unit contains four detectors in 2×2 array and each *CdZnTe* detector consists of an array of 32×32 , 0.6 mm pixels with each pixel subtending $12.3''$ and thus provides a field of view (FoV) of $12'$ for each focal plane module. The dimension of each *CdZnTe* detector $20\text{mm} \times 20\text{mm}$ with the thickness about 2 mm. The angular resolution (FWHM) of the *NuSTAR* is about $18''$ with energy resolution (FWHM) about 0.4 keV at 10 keV and 0.9 keV at 68 keV. The FoV of the observatory is about $10'$ and $6'$ at 10 and 68 keV respectively. The temporal resolution of the *NuSTAR* is excellent which is about $2 \mu\text{s}$. It has a collecting areas 847 cm^2 at 9 keV and 60 cm^2 at 78 keV.

2.3 Swift Observatory (*Swift*)

Swift which is space based laboratory launched on November 20, 2004 is known as Neil Gehrels *Swift* Observatory (Gehrels *et al.*, 2004). It is mostly dedicated to study Gamma Ray Bursts (GRBs). It operates in different wave bands - optical, ultraviolet, X-ray and gamma ray. The study in these different wave bands are done with the help three different

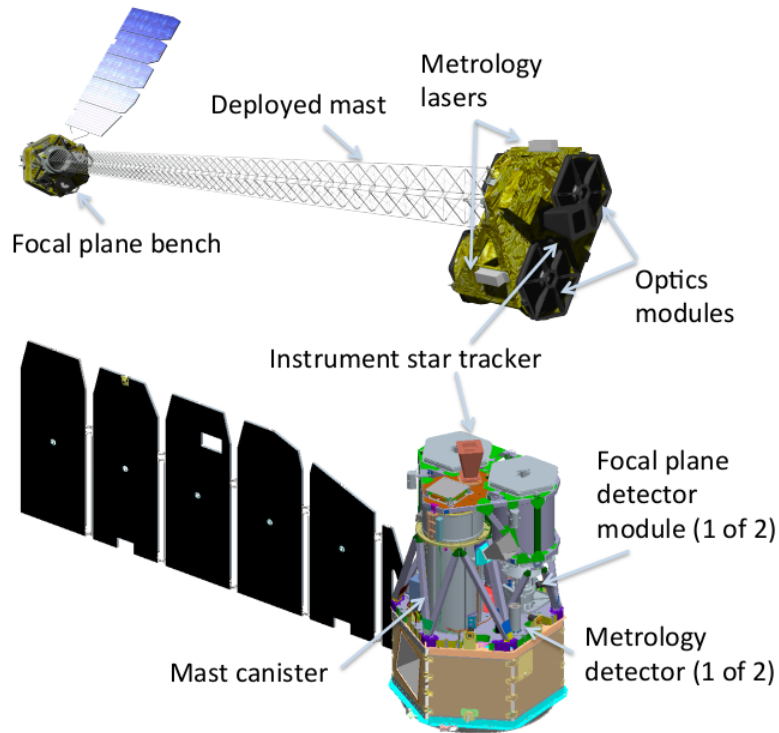


Fig. 2.2 Diagram of the *NuSTAR* observatory. The figures at top and bottom shows the observatory in deployed and stowed configurations respectively. Image courtesy : (Harrison *et al.*, 2013)

instruments - Burst Alert Telescope (BAT), X-ray Telescope (XRT) and Ultraviolet/Optical Telescope (UVOT) (see Fig. 2.3). *Swift*-BAT scans large fraction of sky in search of new GRBs and upon discovery it will trigger the spacecraft to slew automatically to bring burst in the field of views of XRT and UVOT.

2.3.1 *Swift*-BAT

The Burst Alert Telescope (BAT) is one of the three instrument in *Swift* observatory which consists of a detector plane with coded-aperture mask. The detector plane is made up of 32,768 pieces of CdZnTe hard X-ray detectors each having a dimension of $4 \times 4 \times 2$ mm kept 1 m below the coded-aperture mask which is composed of 52,000 pieces of lead each of $5 \times 5 \times 1$ mm in size (Barthelmy *et al.*, 2005). It operates in 15-150 keV energy

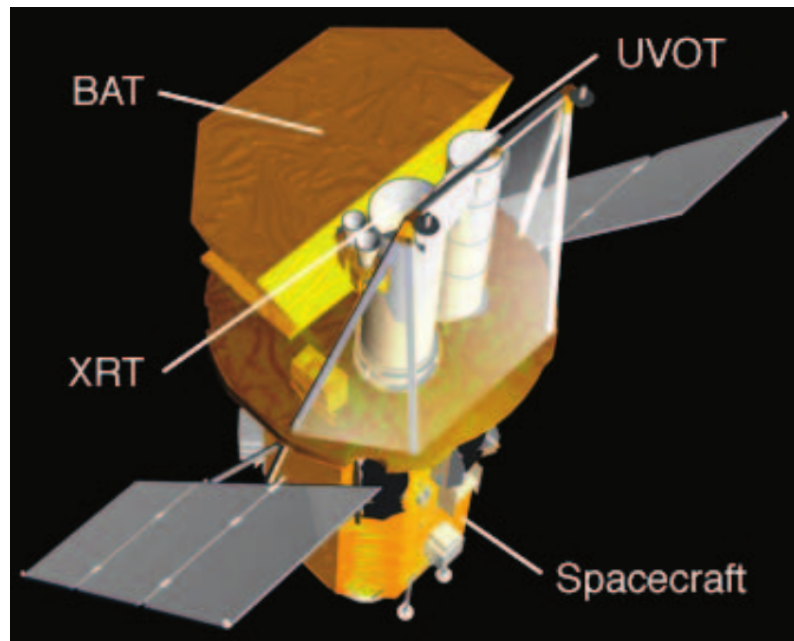


Fig. 2.3 Figure of *Swift* observatory along with different instruments. Image courtesy : (Gehrels *et al.*, 2004)

range having an energy resolution of ~ 6 KeV. The FoV of the instrument is about 1.4 sr (half-coded) with a detecting area 5240 cm^2 .

2.3.2 *Swift*-XRT

The XRT has two components - mirror module and focal plane camera. Mirror module consists of grazing incidence Wolter I telescope, its focal plane camera consists of a single e2v CCD detector (Burrows *et al.*, 2005). X-rays are focused by the telescope onto the CCD which is thermoelectrically cooled down to -100° C . Both the components of the instrument are held in a composite telescopic tube. The XRT can measure the position of the burst with an accuracy of 5 arc-seconds within 100 s of detection of burst by BAT. It operates in 0.2-10 keV energy range and it has an energy resolution of 140 eV at 5.9 keV. The effective area of the instrument is $\sim 125 \text{ cm}^2$ at 1.5 keV and $\sim 20 \text{ cm}^2$ at 8.1 keV. Depending on the XRT readout modes the time resolution is between 0.14 ms to 2.5 s.

The FoV of the instrument is about 23.6×23.6 arc-minutes and its detection sensitivity is $2 \times 10^{-14} \text{ erg cm}^{-2} \text{ s}^{-1}$ in 10^4 s.

2.3.3 *Swift*-UVOT

Swift-UVOT uses a modified Ritchey-Chre'tien telescope of 20 cm diameter¹. The optics and detectors used in it is based on *XMM-Newton*/Optical Monitor (OM). The detectors used in this case are two micro-channel plate intensified CCD (MIC) detectors. These detectors operates in photon counting mode, with its detection capability of very low signal levels which allows UVOT to detect even faint sources over the wavelength 170-650 nm. UVOT has a FoV of 17×17 arcmin having detector element size 2048×2048 pixel.

2.4 Brief review of the sources considered in the study

2.4.1 SMC X-1

SMC X-1 is a 0.71 s X-ray pulsar which is a component of high mass X-ray binary system with a B0 super-giant companion SK 160. The mass of the neutron star companion is about $\sim 17.2M_{\odot}$ (Reynolds *et al.*, 1993). The detection of the pulsar was first reported by Price *et al.* (1971) when SMC region was examined by rocket flight. It has an orbital period of 3.9 days and is eclipsed for a period ~ 0.6 days by its companion (Schreier *et al.*, 1972). The observed luminosity of the source is of the order of $10^{38} \text{ erg s}^{-1}$ (Price *et al.*, 1971), near the Eddington limit. The pulsar shows a secular spin-up with a rate of $\sim 3.279 \times 10^{-11} \text{ Hz s}^{-1}$ (Davison (1977); Wojdowski *et al.* (1998)). The orbital period of the system decayed at a rate of $\sim 3.4 \times 10^{-6} \text{ yr s}^{-1}$ (Levine *et al.* (1993); Wojdowski *et al.* (1998)). The pulsar also shown a superorbital modulation of about 55-60 days which is thought to be due to the obstruction of X-rays by the precessing accretion disk (Wojdowski

¹https://swift.gsfc.nasa.gov/about_swift/uvot_desc.html

et al., 1998). From the spin-up rate the predicted magnetic field of the pulsar is $\sim 10^{11}$ G (Li and van den Heuvel, 1997). It undergone a short burst of few tens of seconds which is different from the thermonuclear burst and it may be caused by the viscous instability in the accretion disk. This type of burst is called Type II burst. Angelini *et al.* (1991) were the first to discover this type of burst in SMC X-1. They also observed an aperiodic variability of 0.1 Hz in SMC X-1. The pulsar also shown soft excess which is modelled by a separate blackbody or thermal-bremsstrahlung-type components (Paul *et al.*, 2002). Using *NuSTAR* observations Pike *et al.* (2019) reported the transient pulsation of SMC X-1 and proposed that it is due to partial obscuration of the pulsar by the precessing accretion disk. The source was observed to be varying on the timescales of less than 1 hr (Moon *et al.*, 2003) and its total duration of flares were $\sim 3\%$ of the total observing time. Also these flares are independent of the orbital phases. There are no significant variation in the properties of the pulsars at normal and flare states. Consequently they pointed out that the flare is nothing but simply an extension of the normal state persistent emission with enhanced accretion rates.

2.4.2 Swift J1756.9-2508

Swift J1756.9-2508 was the eighth accreting millisecond X-ray pulsar (AMXP) discovered in 2007 (Krimm *et al.*, 2007a; Markwardt *et al.*, 2007). Accretion millisecond X-ray pulsars are a subclass of low mass X-ray binaries (LMXB) consisting of neutron star having spin period of few milliseconds. The first AMXP SAX J1808.4-3658 was discovered in 1998 using RXTE (Wijnands and van der Klis, 1998). Swift J1756.9-2508 has a spin period of ~ 5.5 ms and orbital period of 54.7 min. It is a transient in nature and observable during an outburst. The companion of the neutron star is a He-dominated white dwarf having a minimum mass between 0.0067 - $0.0086M_{\odot}$ (Krimm *et al.*, 2007b). After the first outburst in 2007 the second one was observed in 2009 (Patruno *et al.*, 2009b). Patruno

et al. (2010a) observed that the pulse profiles were evolving throughout the outbursts and the pulse fractions of the pulsar are found to increase with the energy even in the hard state. The timing analysis of the 2009 outburst was analyzed by Patruno *et al.* (2010a) and constraint the maximum frequency derivative $\dot{\nu}$ to $3 \times 10^{-13} \text{ Hz s}^{-1}$. Linares *et al.* (2008) reported a strong broad flat topped noise at ~ 0.1 Hz throughout the 2007 outburst similar to the other AMXPs and LMXBs in the high energy state. The spectrum showed a hard-tail extending upto 100 keV. The 2018 outburst of the source was first detected by *INTEGRAL* (Mereminskiy *et al.*, 2018). Bult *et al.* (2018) studied the long term evolution of orbital period of the AMXP using *RXTE* observations in 2007 and 2009 along with Neutron Star Interior Composition Explorer (NICER) 2018 observations of the outburst and estimated the upper limit of orbital period derivative which is $|P_{orb}'| \leq 7.4 \times 10^{-13} \text{ s s}^{-1}$. The estimated magnetic field of the pulsar is of the order of 10^8 G (Patruno *et al.* (2010a); Sanna *et al.* (2018)). During 2018 outburst the source was in hard state with high value of cutoff-energy ~ 70 keV (Sanna *et al.*, 2018).

2.4.3 4U 1901+03

4U 1901+03 is a ~ 2.76 s X-ray pulsar which was discovered in 1970-1971 by Uhuru mission but as a X-ray pulsar it was discovered later. After the discovery it was first observed in 2003 during a giant outburst (Galloway *et al.*, 2005). The *RXTE* observations during 2003 outburst revealed that the source is a X-ray pulsar (Galloway *et al.*, 2005). The pulsar is part of a Be X-ray binary (BeXB) system. BeXBs falls under the High Mass X-ray binary (HMXB) system where the companion of the neutron star is a normal Be star (see section 1.3.4). The binary orbital period of the pulsar is about 22.58 days (Galloway *et al.*, 2005). X-ray flares, pulse frequency broadening and quasi-periodic oscillation (QPO) are studied by James *et al.* (2011). QPOs are basically a quasi-periodic signal found in power spectra of the X-ray binaries which is identified by a broad peak

and generally fitted by Lorentzian model. The flares are 100-300s long which are much stronger and more frequent during the peak of an outburst. The QPO was observed around the frequency of ~ 0.135 Hz having r.m.s. value of 18.5 ± 3.1 %. It was observed that there were negative residuals near 10 keV in the fitted spectrum observed in the 2003 outburst of the source (Galloway *et al.*, 2005; Reig and Milonaki, 2016), which is known as 10 keV feature. When this feature was fitted with Gaussian absorption model the absorption line was found to show positive correlation with the source luminosity. This feature shows a strong dependence on the pulse phases (Reig and Milonaki, 2016) which points that it can be cyclotron scattering resonance feature (CSRF). The pulse profiles of the pulsar was also varied throughout the outburst (Lei *et al.*, 2009; Reig and Milonaki, 2016) which is due to the change in the beam emission pattern with the luminosity. Lei *et al.* (2009) from the phase-resolved spectroscopy of the pulsar during 2003 outburst found that at the beginning of the outburst the optical depth of the Compton scattering is found maximum near the major peak of the pulse profiles where as during the decay the maximum appears away from the main peak. The outburst of the pulsar was once again detected on February 2019 by MAXI/GSC (Nakajima *et al.*, 2019) and Swift/BAT (Kennea *et al.*, 2019). Ji *et al.* (2020) observed that during the flares it was 1.5 times brighter than the persistent emission. Also the pulse profiles during burst differs from that during normal emission but at the comparable luminosities the pulse profiles have similar shape. In addition to the 10 keV feature an additional 30 keV absorption feature was also observed in the residuals of the source (Coley *et al.*, 2019; Nabizadeh *et al.*, 2020).

2.5 Methods of Data Reduction

The observational data for a given source are obtained from NASA data archive HEASARC. The reduction of these data into useful form were done with the help of the software

HEASoft² which is also provided by HEASARC. Along with the software we also need the updated calibration data base (CALDB) files which are downloaded from the archive. The CALDB files contains the information about the calibration of the high energy astrophysical instruments which is different for different instruments.

We have used 2003 observations of SMC X-1 by *RXTE* in our study. We only consider *RXTE*-PCA data in our study. PCA consist of five unit of PCU, from which we only considered the third unit (PCU2) for analysis. For timing analysis we chose GOODXENON data file, these GOODXENON data are then converted into EVENT data files using the script `make_se`. These event files are then used to extract light curve of particular binning using the FTOOL `seextrct`. The FTOOL `seextrct` is a tool or command which is used to extract light curves and spectra from EVENT mode of *RXTE*-PCA data . For the spectral analysis we used PCA data in STANDARD2 mode which have a binning of 16 s. The data from the top Xe-layer of PCU2 were used to obtain spectra here. The spectra were extracted using `saextrct`. `saextrct` is used to create light curves and spectra from *RXTE* SCIENCE ARRAY (SA) data. The background light curves and spectra were obtained using the FTOOL `runpcabackest` taking the bright source model. The response matrices are to be extracted using `pcarsp`. The systematic error of 2% was added to all the spectra while fitting them with suitable models. We only consider those data where the elevation of telescope was greater than 10 degree and 30 minutes after the passage from South Atlantic Anamoly (SAA).

For *NuSTAR* observations the standard data screening and filtering will be done using a mission specific FTOOL `nupipeline`³. Through this task we generate cleaned event files from the unfiltered event files. Each Focal plane modules (FPMA & B) has their own event files. A single Level 1 unfiltered event file generates six different Level 2 event files. Out of these six cleaned event files we chose science observing mode (01) event file to extract

²<https://heasarc.gsfc.nasa.gov/lheasoft>

³https://heasarc.gsfc.nasa.gov/docs/nustar/analysis/nustar_swguide.pdf

light curves and the corresponding spectra. Using the clean event files we extract source and background region files in XSELECT. The image file extracted in the XSELECT is load in DS9 to see the image. The source region file is chosen to be a circular region around the bright region and another same circular region of same area but far away from the bright region is taken as the background region. After the extraction of the suitable region files the Level3 products *i.e.* light curves and spectra are extracted using nuproducts for each focal plane module. Light curves are background corrected using lcmath and the barycentric correction was done using FTOOL barycorr taking the spacecraft orbit file.

For *Swift/XRT* the reprocessing of unfiltered event file is done with the help of standard task xrtpipeline. The source and background region files are extracted using the same method discussed above. The source and background light curves and spectra are obtained using the respective region files in XSELECT. The ancillary response files (arf) are generated using the tool xrtmkarf, however the response matrices files (rmf) are sourced from the calibration data base files. The background and barycentric corrections are applied using lcmath and BARYCORR respectively.

2.6 Timing and Spectral Analysis

2.6.1 Timing Analysis

Timing analysis of the X-ray pulsars includes study of the light curves, pulse profiles, pulse periods, bursts, quasi-periodic oscillations etc. Thus it provides us with the dynamical properties of the X-ray pulsars. Variation of the pulse periods during the orbital motion of the pulsars due to Doppler effect can be fitted with a suitable model to estimate the orbital parameters. Similarly the study of the pulse profile helps us to figure out the accretion process and accretion geometry. The timing analysis were carried out using timing analysis software XRONOS which comes with HEASoft. In timing analysis we search for the pulse

periods, pulse profile, bursts and energy variation of pulse profiles. Some of the extensively used XORNOS tools are given below,

(i) LCURVE

This XRONOS tool is used to produce light curves, its plots and outputs the results. The light curve shows the variation of the intensity of the pulsar with time. The input file format used is FITS using the BINTABLE extension. At a time up to four simultaneous time series can be input and for more than two input series ratios and sums are calculated. Input data can be rebinned and divided into several intervals and frames. The output plot shows variation of count/s with time and for multiple time series we can also determine colour-colour diagram and hardness ratio.

(ii) POWSPEC

For the crude estimation of the pulse period we perform Fourier transformation of the suitably binned light curve. The frequency corresponding to the pulse period of the pulsar appears as the fundamental peak in the power versus frequency distribution of the Fourier transformation. A XRONOS tool powspec is used for this purpose. This task generates power density spectral (PDS) for one input time series, plots and outputs. The PDS is computed using fast Fourier transformation algorithm or direct slow Fourier algorithm. An input file in FITS format with BINTABLE extension is used. We can rebin the input data and divide it into several intervals and frames. PDS from several intervals can be averaged in a single frame and the results can be rebinned. The output shows the variation of power with frequency. The normalization of the PDS can be changed by changing the value of normalization parameter.

(iii) EFSEARCH

EFSEARCH task is used to search for periodicities in a time series by folding data over a period range and determines the χ^2 of the folded light curve and plots the values of χ^2 with periods. The input file is in FITS format with BINTABLE extension. A guess

value of spin period is required to input in this task, this guess value is estimated using the tool `powspec` as discussed above. The value of the period where the χ^2 distribution is maximum represents most likely the pulse period of the X-ray pulsar. The error bars of the χ^2 actually the standard deviation of the relevant χ^2 distribution rescale by the χ^2 value for each period divided by $N-1$, where N is the number of phase bins.

(iv) EFOLD

The `efold` is a timing tool which creates folded light curves for a given period and the number of phases in the period. The output plot of this folded light curves shows variation of the intensity or count rate with respect to the pulse phase which is known as pulse profiles. It is possible to take upto four input time series simultaneously. The input data can be divided into intervals and frames and folded light curves from different intervals can be averaged in one or more frames. The error bars of the average folded light curves from different intervals are determined using standard deviation of the mean values of each phase bin or propagating the error in each phase. One can set different normalizations for the folded light curve by changing the value of the normalization parameter. For the value of normalization parameter set to 0 we will get folded light curve which are normalised to count/s and if it is set to 1 then the folded light curves are normalised by dividing by the average source intensity in the frame.

2.6.2 Spectral Analysis

Spectral analysis mainly focuses on the study of the continuum shape of the energy spectra of the X-ray pulsars by fitting it with the suitable models. It also includes the study of different emission absorption lines present in the energy spectrum. Spectra are fitted in the X-ray spectral fitting package (`XSPEC`) (Arnaud, 1996) which is included in `HEASoft`. Spectra can be fitted also with different models present in the `XSPEC`. One can create a

simple model using an arithmetic or load local models in it. A detector is used to measure and record the spectrum of a source but its not the actual spectrum whereas its photon count remain within some specific channels. So we need an instrument response file which is proportional to the probability that an incoming photon with some energy E will be detected in channel I, however the instrumental response is continuous which is to be converted into discrete function specific for a given instrument. This is called the detector response matrix. The convolution of the spectrum recorded by the detector with the detector response matrix gives us the energy spectrum of the source. The response matrix is incorporated with the ancillary response file which gives the effective area of the detector. Once we obtain the source and background spectra along with the suitable response files we can fit the background corrected spectrum in XSPEC using the χ^2 method. The test statistic χ^2 is defined as,

$$\chi^2 = \sum \frac{(O - M)^2}{\sigma^2}$$

where, O and M are observed and model predicted data photon counts and σ^2 is the variance in the data points. For the goodness of fitting we define reduced χ^2_v such that, $\chi^2_v = \chi^2 / \nu$, where ν is the degrees of freedom which is equal to the number of data points minus the number of model parameters. If $\chi^2_v = 1$ then we can say that the model describe the observed spectrum very well. If $\chi^2_v > 1$ then the model is insignificant where as for $\chi^2_v < 1$ the errors is overestimated.

The basic idea behind the spectral analysis is to obtain the value of physical parameter behind the phenomenon which is responsible for the observed spectra. The spectrum of X-ray pulsars are combination of different physical processes which is quite difficult to model the spectra theoretically. As a result the spectra are fitted with empirical model. However the complete model generally is a combination of two or more components of simple or complex mathematical functional form. The general form of the multi-component model

used in fitting spectra is

$$M(E) = \text{Photoelectric_abs_model} * (\text{cont_model} + \text{emission_line_model}) * \text{cyc_line_model}$$

In the next subsection we describe briefly about the models used in the analysis taken up here.

(i) Power law model

The power-law model which is used for absorption is given,

$$M(E) = KE^{-\alpha}$$

where E is the energy, α is photon index and K is model coefficient

(ii) Blackbody model

The blackbody model is given by,

$$M(E) = \frac{K \times 8.0525E^2 dE}{kT^4 [\exp(E/kT) - 1]}$$

where kT is the temperature in keV and K is the normalization in terms of L_{39}/D_{10}^2 , L_{39} is the luminosity in the units of 10^{39} erg/s and D_{10} is the distance to the source in units of 10 kpc.

(iii) Cutoff power law

It is a continuum model consisting power law with high energy exponential roll-off.

$$M(E) = KE^{-\alpha} \exp(-E/\beta)$$

where α is the photon index of the power law, β is the e-folding energy of exponential rolloff (in keV) and K is the normalization in photons/keV/cm²/s at 1 keV.

(iv) High energy cutoff power law

This continuum model consist of power law multiplied by exponential cut-off. One of the form of exponential cutoff model is highecut (White *et al.*, 1983). The high energy cutoff power law model will be used here is given by,

$$M(E) = KE^{-\tau} \times \begin{cases} 1 & E < E_{cut} \\ \exp\left(\frac{E_{cut} - E}{E_{fold}}\right) & E_{cut} \end{cases}$$

where K and α is the normalization and photon index of the power law model. E_{cut} and E_{fold} are the cutoff energy and e-folding energy in keV of the highecut model.

(v) Gaussian line profile

This model is used to fit the iron line emission in between 6-7 keV energy range. If the width of the model is ≤ 0 then it will be reduced to a delta function. The form of this model is given by,

$$M(E) = K \frac{1}{\sigma\sqrt{2\pi}} \exp\left(-\frac{(E - E_l)^2}{2\sigma^2}\right)$$

where E_l is the line energy in keV, σ is the width of the emission line in keV and K is the normalization which represents the total photons/cm⁻²/s in the line.

(vi) Gaussian absorption line

It is a multiplicative model and widely used to fit the cyclotron absorption line in the spectra of X-ray pulsars. The functional form of the model is given by,

$$M(E) = \exp\left(-\frac{\tau}{\sigma\sqrt{2\pi}} \exp\left(-\frac{(E - E_a)^2}{2\sigma^2}\right)\right) \quad (2.1)$$

where, E_a is the cyclotron line energy, σ is the line width and τ is the line depth. The optical depth is $\frac{\tau}{\sigma\sqrt{2\pi}}$.

(vii) CompTT

This analytic model describes the Comptonization of soft photons in hot plasma, it is developed by Titarchuk (1994). This model also includes relativistic effects and the approximations fits well for both the optically thick or thin regimes. The model has five parameters - redshift, input soft photon temperature (T_0), plasma temperature (kT), plasma optical depth (τ) and geometry switch. For a disk geometry the geometry switch is ≤ 0 and for spherical one the parameter is > 1 . The plasma temperature kT and β parameter which does not depends on the geometry completely determines the shape of the Comptonized spectrum. For a given geometry the optical depth is determined by the function β . For the spherical and disc geometry β is not a direct input which is to be frozen. If geometry switch is ≤ 0 then β is obtained from the optical depth using analytical approximation but for geometry switch < 0 , β is obtained by interpolation from the set of β and τ (Sunyaev and Titarchuk, 1985). The input soft photon spectrum follows Wien law. The plasma temperature lies between 2-250 keV. The model is not valid in the case of simultaneous low temperature and low optical depth or high temperature and high optical depth.

(viii) Photoelectric absorption model

The photoelectric absorption model is described by the function given by,

$$M(E) = \exp[-n_H \sigma(E)] \quad (2.2)$$

where $\sigma(E)$ is the photoelectric cross-section which does not include Thomson scattering. In case of phabs photoelectric absorption model the cross-section can be set by using `xsect` command in XSPEC and the relative abundances are set by the command `abund`, however

in wabs model uses Wisconsin (Morrison 1983) cross-sections along with Anders-Ebihara (Anders and Ebihara, 1982) relative abundance.

Chapter 3

A study of Type II bursts from SMC X-1

3.1 Introduction

SMC X-1 is one of the few disc-fed Super Giant X-ray Binaries (SGXBs). Its frequency of pulsation of the pulsar is ~ 1.41 Hz, which is decreasing regularly at the rate of $\sim 3.279 \times 10^{-11}$ Hz s $^{-1}$ (Davison, 1977; Wojdowski *et al.*, 1998). The orbital period of the neutron star around the companion is about ~ 3.9 days. Along with the periodic modulation like pulse period and orbital period the pulsar also show an aperiodic modulation of $\sim (55-60)$ days (Wojdowski *et al.*, 1998). The pulsar shows Type II bursts (Angelini *et al.*, 1991) which are observed as flares in the light curves. There are no abrupt change in the luminosity of the pulsar and softening of the spectrum as a result of the bursts. Moon *et al.* (2003) showed that the flares occupied 3% of the total observational time. The Type II bursts observed in the pulsar and its pulse profiles as well as the change of its spectra due to the bursts are investigated. We have also estimated the total duration of flare and compared

A part of the chapter is published in *Res. Astron. Astrophys.* 18, 148 (2018)

it with the total observational time. The correlation of the flares with time, peak-to-peak ratio of pulse profile, orbital phase and spectral parameters are also explored.

3.2 Observations and Data reduction

The archived RXTE PCA observations of SMC X-1 between 2003-10 and 2003-12 are considered for analysis. As out of the five PCU units of PCA, PCU 0 suffered propane loss in the year 2000, other units namely, PCU 3 and PCU 4 were given rest regularly to avoid break down. However, PCU 2 was operating all the time and did not went through break down. This PCU unit is also best calibrated counter unit which has been verified by fitting the crab spectrum with power law model.

The reduction of data are done using HEASOFT v 6.11. In order to do timing analysis we used *RXTE* PCA data in GOODXENON mode. The GOODXENON data were converted into EVENT mode using the FTOOL *makeev*. The light curve of desired binning is then extracted using the FTOOL *seextract*. Background files are obtained by using STANDARD 2 data and suitable model with the help of FTOOL *runpcabackest*. The background light curve is then extracted from the background files using *saextract*. The background corrected light curve is then obtained by subtracting the background light curve from the total light curve using the FTOOL *lcmath*. The frame of reference of photon arrival was set to barycentre with the help of *faxbary* using JPL DE400 ephemerides. For our analysis only those data were considered where the elevation of telescope was greater than 10 degree and the data were recorded 30 minutes after the passage of the telescope through South Atlantic anomaly (SAA) region.

For spectral analysis STANDARD 2 *RXTE* PCA data were used which has 129 channels and default binning of 16 s, we have only considered data from top Xe-layer of the PCU 2. In order to obtain response matrix for top layer we used FTOOL *pcarsp*. The background spectrum was extracted from the background file using *saextract*. The background corrected

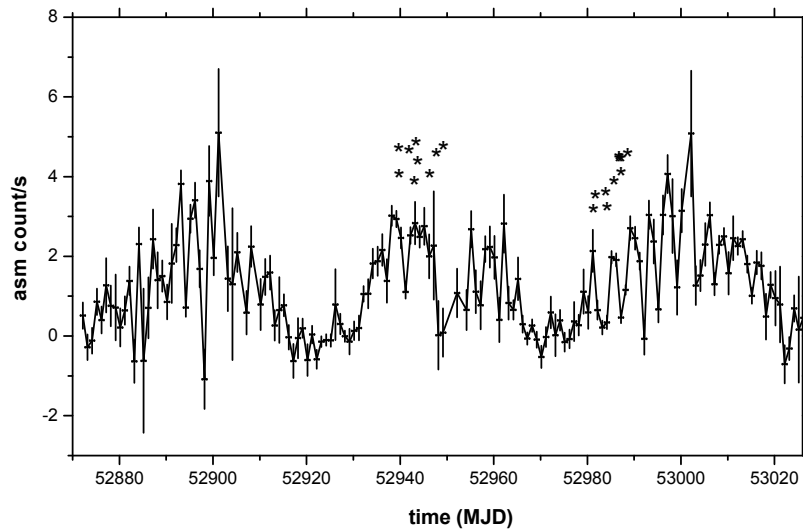


Fig. 3.1 *RXTE* ASM light curve of SMC X-1. The astricks "*" represents the *RXTE* PCA observations. h1 and h2 indicates the high states.

spectrum is obtained by subtracting background spectrum from the total spectrum. Spectra in 3-18 keV energy range were considered for analysis. Spectra above 18 keV were not considered as it is mostly dominated by background and a good fitting not possible. In all the cases a systematic error of 2% have been added to the spectra to cover the uncertainties in the model of the detector response.

3.3 Light curves and flares

SMC X-1 has super-orbital period of ~ 55 -60 days (Wojdowski *et al.*, 1998), the *RXTE* PCA observations of the pulsar lies in the two high states, h1 and h2 as shown in Fig. 3.1. We have used the method followed by Moon *et al.* (2003) to investigate the flares. Flares were taken as a part of light curves where the photon count rates were 3σ level above the mean. The total data were divided into 110 data segments each of mean duration of 2050 s. Light curve of each data segment was plotted and analyzed.

In order to obtain the duration of bursts we fitted them with a GAUSSIAN model. From the width 'w' of the model we can get FWHM of the burst using $FWHM = 2.35482w$, which we considered as a duration of the burst. The reduced χ^2 of the fitting is found between 2.3-3.56. Initially we started with the light curves having 4 s time resolution and searched for flares, after that we looked for flares in the light curves of 2 s, 6 s and 8 s time resolution. A total of 272 flares have been observed with mean FWHM of ~ 21 s and standard deviation of ~ 8 s. So a total of 225.5 ks observational time the source was flaring for 5.7 ks.

Thus the source has undergone through type II bursts for 2.5 % of the time, the value is close to that reported by (Moon *et al.*, 2003). The recurrence time of the flares were observed to vary from few hundreds to thousands of seconds. The average recurrence time between two consecutive flares have been ~ 800 s. The number of flares and the recurrence time are found to be consistent for the light curves of 2 s, 6 s and 8 s time resolutions. The power spectra of the X-ray pulsar are obtained by Fourier transformation of 0.075s time resolution using XRONOS tool *powspec* with normalization=-2. This value of normalization gives us the white noise subtracted normalised power spectra whose integral is related to the r.m.s fractional variability. The r.m.s variability of the four light curves obtained from the power spectra were (a) 30.86%, (b) 31.2 %, (c) 31.2 % and (d) 30%. The source was equally variable in all the four cases. The sharp peak at ~ 1.41 Hz corresponds to the pulse frequency, the other peaks represent the harmonic components (See lower panel of Fig. 3.2).

Large flares where count rate reached few times above the mean have been observed, where in some cases flares had duration of hundreds of seconds. In Fig. 3.3 (*left*) a flare of almost ~ 50 s is shown having two peaks. The first peak arises due to sharp rise in the count rate from the mean value of ~ 300 counts s^{-1} reaching a maximum of ~ 1350 counts s^{-1} . After that count rate falls sharply to ~ 510 counts s^{-1} , followed by sharp increase

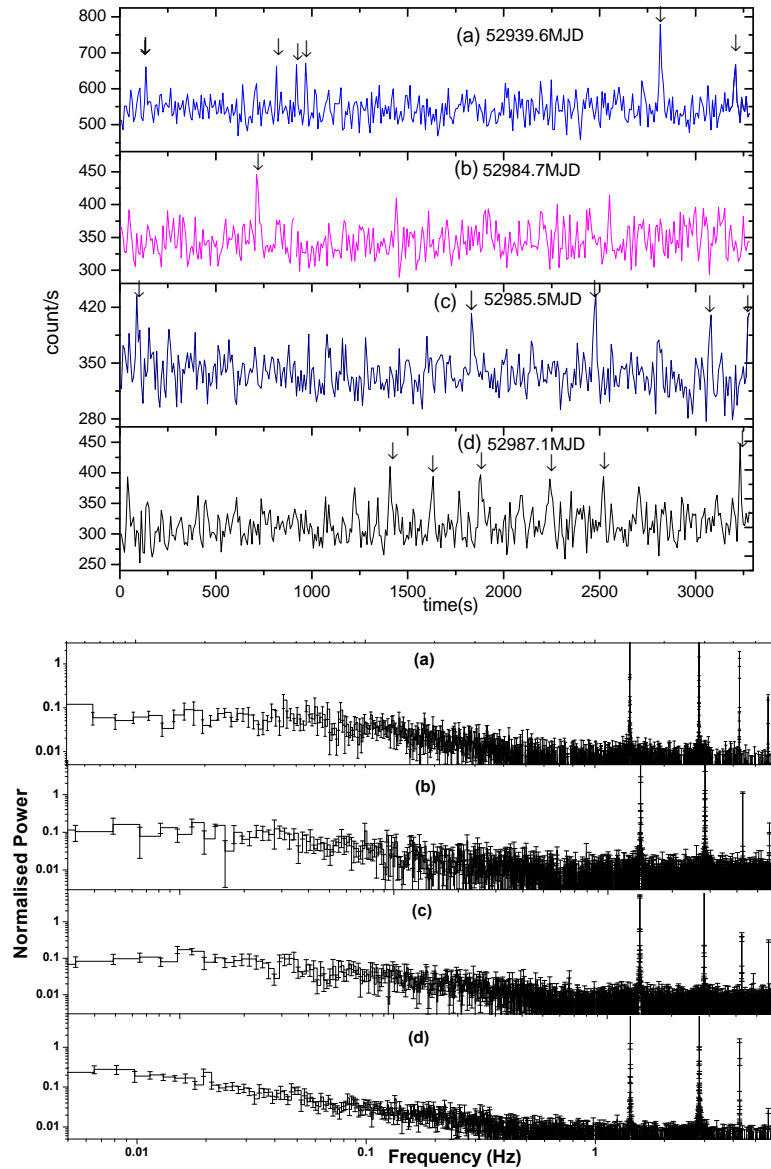


Fig. 3.2 *Upper panel* - Light curves for four different *RXTE*-PCA observations. The down arrow represent flares. *Lower panel* - Power density spectrum for the corresponding light curves.

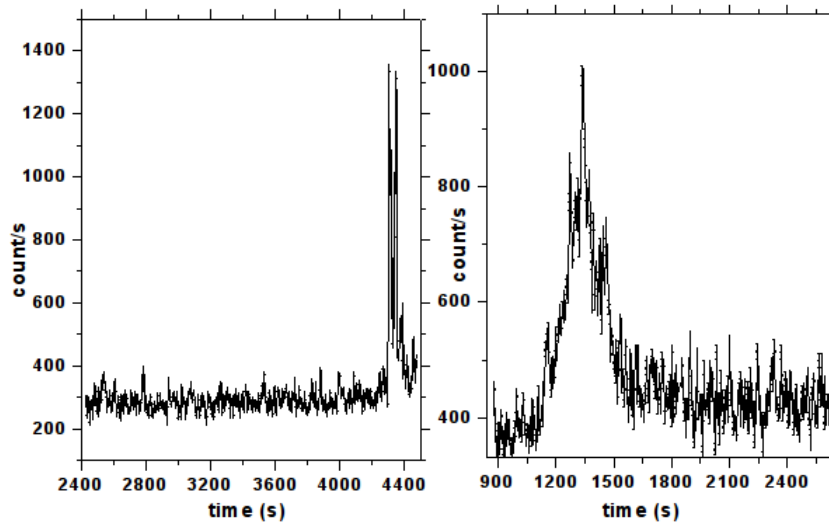


Fig. 3.3 *Left* - Sharp burst observed in SMC X-1. *Right* - Large flare having duration ~ 300 s. These two large flares are from *RXTE* observation having Obs Id 80078-01-01-04.

in count rate giving a second peak of ~ 1320 counts s^{-1} which falls below ~ 500 counts s^{-1} . On the right of the Fig. 3.3 flares having duration of ~ 300 s and accompanying of multiple peaks are found to exist, the highest peak being of ~ 1000 counts s^{-1} . The average number of flares observed per hour in h1 state is 5 and in h2 state is 4 with the average time between two flare being ~ 800 s.

3.4 Pulse profiles

A pulse profile is obtained by folding the light curve of the X-ray pulsar about ~ 0.7 s. As the neutron star moves in a binary orbit there will be delay in pulse arrival time due to orbital modulation *i.e.* when the neutron star is facing the observer the pulse will arrive sooner than when it is away from the observer. So in order to get the correct pulse profile the pulse arrival time of the pulse must be corrected for orbital modulation. The binary orbit of SMC X-1 is almost circular (Levine *et al.*, 1993; Raichur and Paul, 2010; Wojdowski *et al.*, 1998). Let t'_n and t_n be the emission and arrival time of the pulse respectively, which

are related with the each other and the neutron star orbital parameters through the following relations,

$$t'_n = t_0 + nP_s + \frac{1}{2}n^2\dot{P}_sP_s$$

$$t_n = t'_n + f_{orb}(t'_n)$$

where P_s and \dot{P}_s are the spin period and its time derivative respectively. For circular orbit $f_{orb}(t'_n)$ is given by,

$$f_{orb} = a_x \sin i \cos l_n,$$

$$l_n = 2\pi \frac{(t'_n - E)}{P_{orb}} + \frac{\pi}{2}$$

where l_n is known as the mean orbital longitude at time t'_n and E is the epoch when the mean orbital longitude is $\pi/2$, $a \sin i$ is the projected semi-major axis and i is the angle of inclination between the orbital angular momentum vector and the line of sight. The value of the epochs and the other orbital parameters are used from Raichur and Paul (2010). The orbital corrected pulse profiles is shown in Fig. 3.4. The pulse fractions for (a) and (d) is about 20% and for (b) and (c) 30%. It is observed that the secondary peaks of the pulse profile is found to coincide with each other. Except the change in the height of the primary peak and the pulse fraction, there is no significant change in the shape of the pulse profiles.

3.5 Hardness ratio

In order to estimate the hardness ratio we divided the 7-16 keV light curve by 3-7 keV light curve. The hardness ratio for the four observations (a), (b), (c) and (d) are shown in Fig. 3.5. The average values of hardness ratio for the four observations were 0.90, 0.897,

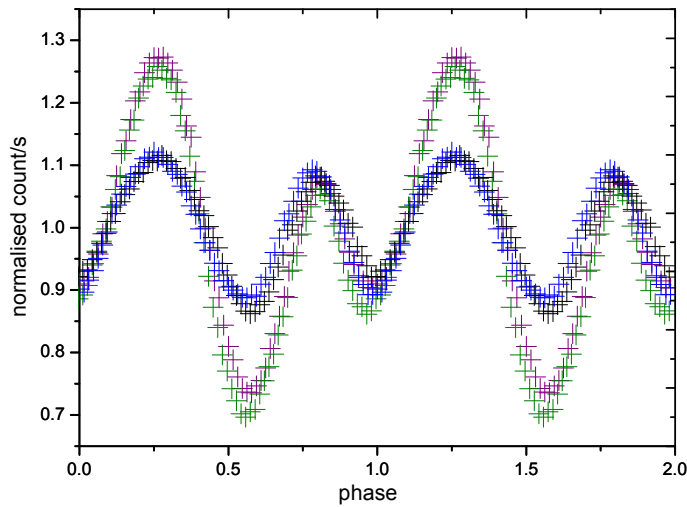


Fig. 3.4 Orbital corrected pulse profiles for four light curves (a), (b), (c) and (d) represented by blue, purple, green and black respectively.

0.856 and 0.837 respectively. No significant change in the hardness ratios are observed in the four light curves during the bursts. Thus the hardness ratio cannot be correlated with flares. We can check these invariance in the hardness ratios by studying the energy spectra of the source.

3.6 Spectral analysis

The energy spectra in 3-18 keV energy range were fitted with PHABS, POWERLAW, HIGHECUT and GAUSSIAN models. The PHABS model is used to estimate the photoelectric absorption of photons by an interstellar medium. The non-thermal emission of the source is estimate by HIGHECUT model, where as the GAUSSIAN model was used to estimate the iron emission line energy. The emission line energy of GAUSSIAN model was fixed at 6.7 keV. The best fitted spectral parameters are shown in Table 3.1

None of the spectral parameters are found to vary significantly for the four spectra. Considering the distance to the SMC X-1 equal to 65 kpc (Keller and Wood, 2006) the

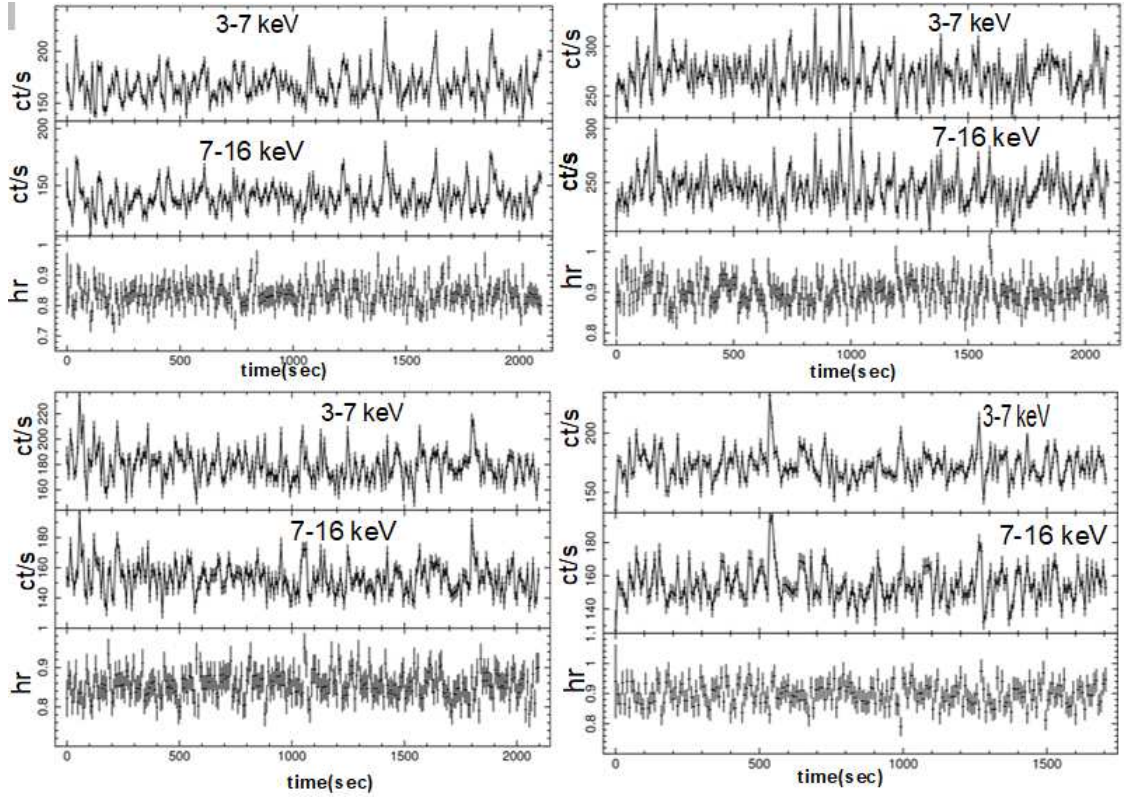


Fig. 3.5 Hardness ratio obtained by dividing the 7-16 keV X-ray count rates by 3-7 keV count rates for four different observations.

observations	a	b	c	d
n_H (10^{22} cm^{-2})	2.062 ± 1.023	1.014 ± 1.06	1.604 ± 1.043	1.968 ± 1.019
α	1.066 ± 0.202	1.004 ± 0.219	1.084 ± 0.218	1.122 ± 0.202
E_{fold} (keV)	17.868 ± 4.726	16.521 ± 4.457	17.723 ± 5.078	17.080 ± 4.143
E_{cutoff} (keV)	5.998 ± 1.045	5.870 ± 1.074	5.837 ± 1.147	6.002 ± 1.218
$flux$ ($10^{-9} \text{ erg cm}^{-2} \text{ s}^{-1}$)	1.345	1.247	1.229	1.160
χ^2_{ν}	1.682	1.375	1.890	1.563

Table 3.1 Table showing best fitted spectral parameters for four spectra. χ^2_{ν} is the reduced chi-square for 29 dof. n_H is the hydrogen column density and α is the photon-index of POWERLAW model. E_{cutoff} and E_{fold} are the cutoff energy and e-folding energy of the HIGHECUT model respectively.

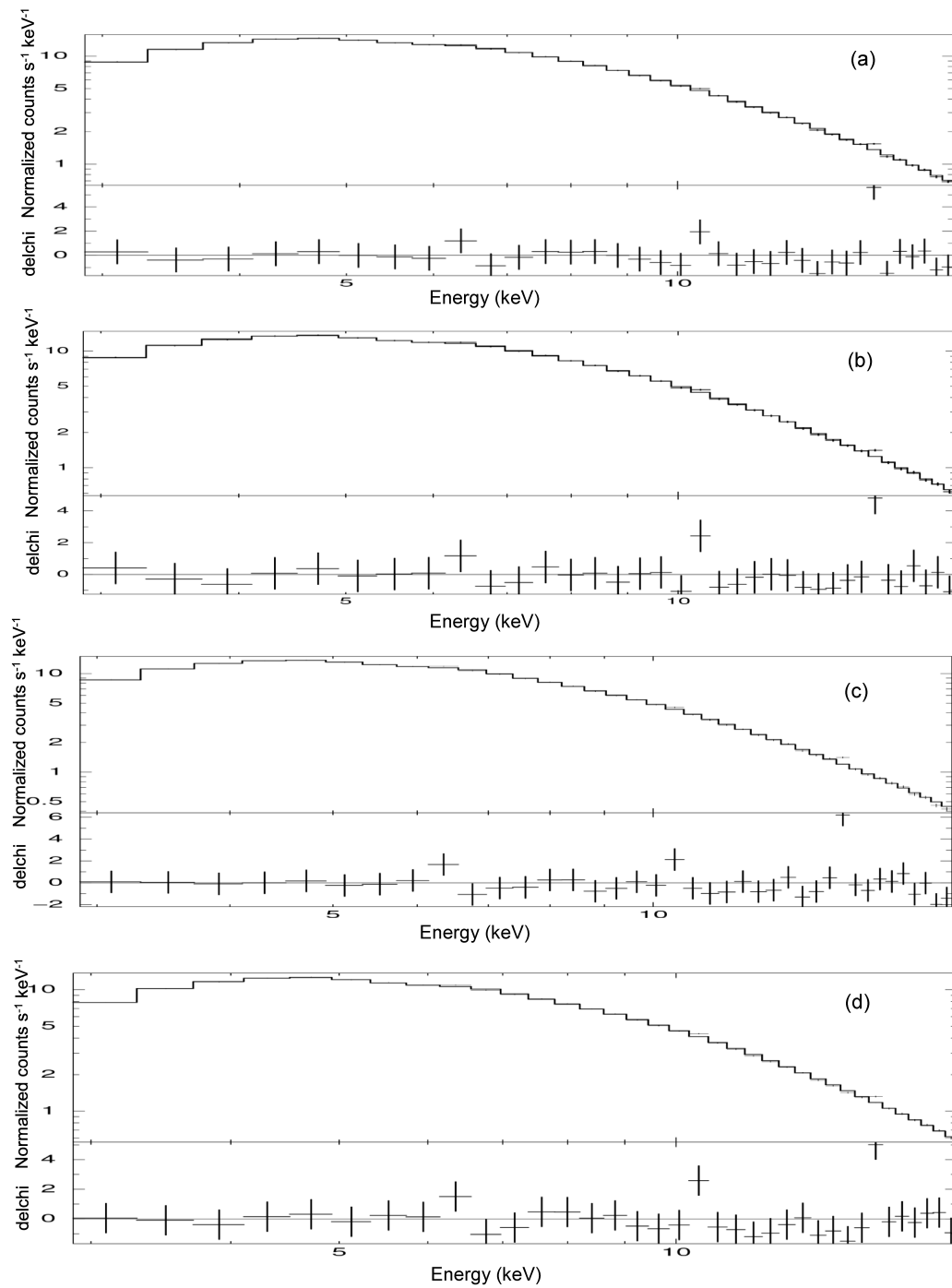


Fig. 3.6 The best fitted spectra for four *RXTE*-PCA spectra in 3-18 keV energy range.

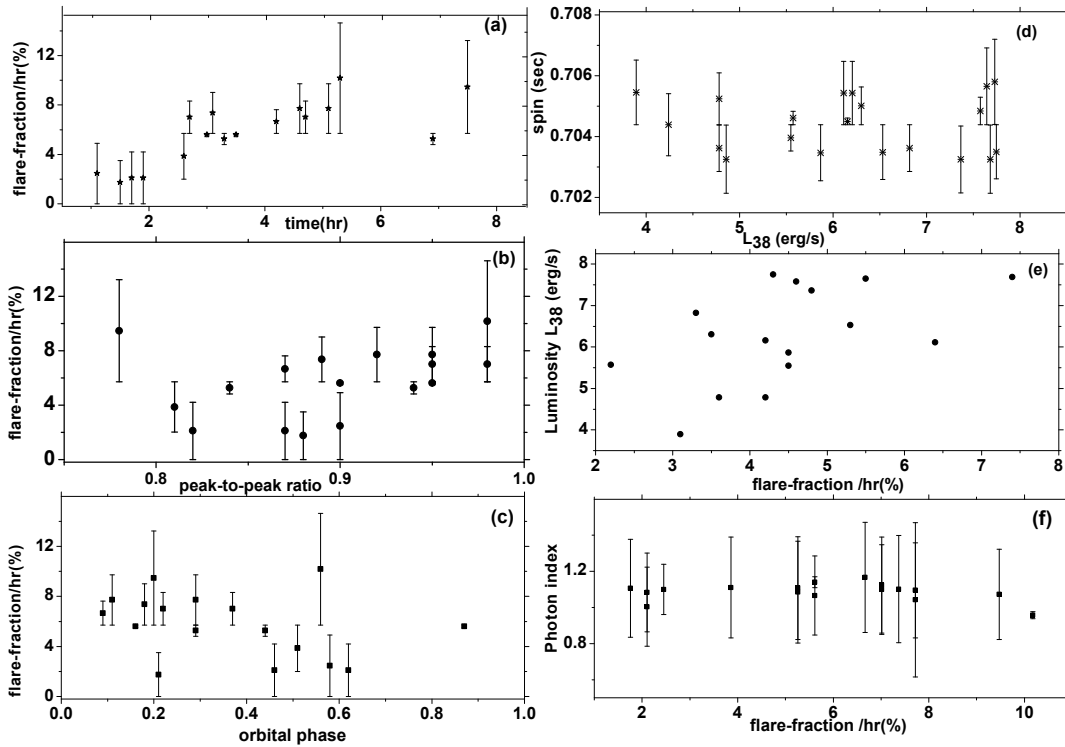


Fig. 3.7 The variation of the flare fraction with the observation time is given by panel figure in panel (a), where as variation of flare-fraction with peak-to-peak ratio and orbital phase are given by figures (b) and (c) respectively. Figure (d) shows the variation of spin with the luminosity where as figure (e) is luminosity of different observations plotted against flare-fraction. Figure (f) is the variation of the photon index with the flare-fraction.

luminosity of the four observations are estimated to be $6.787 \times 10^{38} \text{ erg s}^{-1}$, $6.302 \times 10^{38} \text{ erg s}^{-1}$, $6.211 \times 10^{38} \text{ erg s}^{-1}$ and $5.862 \times 10^{38} \text{ erg s}^{-1}$ respectively. The variation of the column density may be a result of partial obscuration of the neutron star due to the precessing accretion disk or due to X-ray eclipses. The photoelectric absorption being dominated in the soft energy range but as we cannot go below 3 keV energy due to the limitation of the instrument, so its not possible to constrain the value of column density exactly.

3.7 Variation of flare-fraction with observational time, pulse peak-to-peak ratio and orbital phase

It is evident from the Fig. 3.7a that the flare-fraction increases with the increase in the observational time. The flare fraction is defined as the ratio of number of flares present in particular observation to the total number of flares divided by the observational time which is expressed in $\% \text{ hr}^{-1}$. The peak to peak ratio is defined as the ratio of secondary to primary peak. As it is clear from the Fig. 3.7b the flare fraction increases with an increase in the pulse peak to peak ratio. The flare-fraction is high in the orbital phases between 0.0-0.45 and then it decreases (Fig 3.7c). The variation of the flare fraction can be as a result of change in accretion rate which affects the number of bursts observed. The pulse period of the X-ray pulsar is dependent on the luminosity, so in order to study the variation of the pulse period with the luminosity we plotted the pulse period (spin) with the luminosity (Fig. 3.7d). To observe the change in the spectral properties with the flare we plot the variation of the photon index with the flare fraction (Fig.3.7f) for different observations. No correlation of the flare fraction with the photon index is observed. A little bit of hardening of the spectrum is observed when the flare fraction is $\sim 10\%$. As no clear correlation can be set between the flare fraction and the small hardening of the spectrum it may be due to decrease in the photoelectric absorption by the interstellar medium and not due to increase in flare fraction. Also it is evident from the Fig 3.7e the luminosity is found to increase with the increase in flare fraction. So strong positive correlation of the luminosity with the flare fraction is observed here.

The spin period for a given observation is obtained from the orbital corrected light curves using EFSEARCH. The spin period in our observations lies between 0.7033 to 0.707 s, where as the luminosity lies between $3.9\text{-}7.8 \times 10^{38} \text{ erg s}^{-1}$. Theoretically the spin-up rate (\dot{P}) of the X-ray pulsars is found to be proportional to $PL_{38}^{3/2}$ (Ghosh and Lamb, 1979),

where P is the spin period of the neutron star and L_{38} is the luminosity of the pulsar in the order of 10^{38} erg. The SMC X-1 shows secular spin-up and the spin-up rate (\dot{P}) which is about 3.279×10^{-11} Hz s $^{-1}$ (Davison, 1977; Wojdowski *et al.*, 1998). As the separation between the two high states is about 50 days so there will be a negligible spin-up. Hence in this case $PL_{38}^{3/2}$ is a constant *i.e.* $P \propto L_{38}^{-3/2}$. No such variation of the spin with the luminosity is observed as it can be due to the fact that the data considered here are from the observations taken over few months. So it might be possible to study the dependence of the spin on the luminosity for SMC X-1 considering long term observations covering few decades using different mission. However this study is complicated due to superorbital modulation of luminosity due to which the luminosity varies in an aperiodic manner.

3.8 Variation of the spectral parameter with orbital phases and flux

In order to study the variations of different spectral parameters with the orbital phase we have fitted the spectra of different *RXTE* PCA observations taken in different orbital phases. The spectra in 3-18 keV energy range were fitted with the models used above. The variation of the photon index (α), column density (n_H) and flux are shown on the left of Fig. 3.8. As it is evident from the figure no abrupt change in the photon index and column density with the orbital phase are observed. The spectral flux (Fig. 3.8c) is observed to vary significantly with the orbital phase that lies between 9.92×10^{-10} to 1.73×10^{-9} erg cm $^{-2}$ s $^{-1}$. The maximum value of the flux occurs at phase 0.44 and minimum occurs at 0.16. When the flux is maximum then the value of n_H is minimum which is about 1.02×10^{22} cm $^{-2}$. From figs. 3.8(a), 3.8(c) and 3.8(d) we found that at the orbital phase 0.17 the spectrum is a bit softer with the maximum value of the photon index 1.12 along with the maximum value of n_H is $\sim 2.42 \times 10^{22}$ cm $^{-2}$. Also the hardening of spectrum is

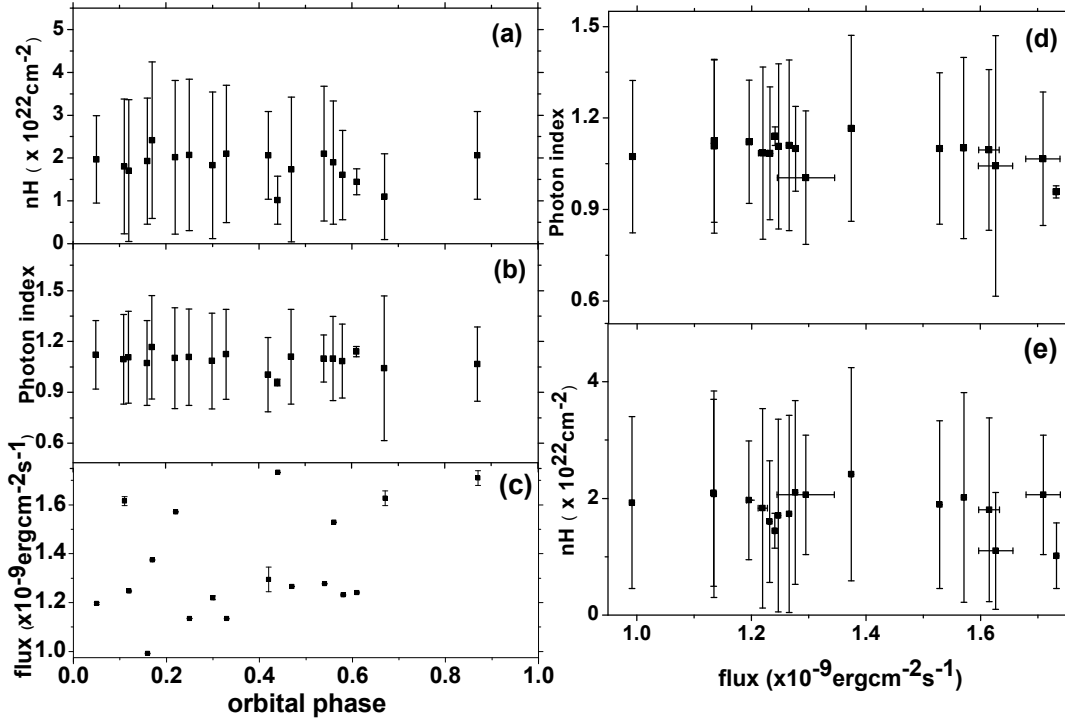


Fig. 3.8 (a), (b) and (c) represents the variation of column density, photon index and flux respectively.

seen when the flux is maximum with photon index 0.96. No clear softening or hardening of the spectra with flux is observed. When the hydrogen column density was minimum the spectrum was a bit harder which can be due to low absorption of hard X-rays in the interstellar medium and it results in maximum flux observed at that phase. In the same way a small softening of the spectra can be as a result of increase in absorption of X-ray by interstellar medium. The variation of flux with the orbital phases may be due to an increase in mass accretion rate.

3.9 Discussion

SMC X-1 exhibits series of type II bursts. The mean recurrence time of the burst was ~ 800 s and almost covers 2.5% of total observing time. The average number of burst per

hour was about 4-5. The type II bursts differs from the type I burst in shape. The type I bursts have sharp rise and falls slowly and gradually in exponential manner where as the type II bursts are recognized by sharp increase and decrease in the count rates in the light curves. Also the origin of the type I burst is due to unstable thermonuclear burning of accreted matter on the surface of the neutron star, where as type II burst are due to increase in accretion rate. During the type I bursts the luminosities of the X-ray pulsars can reach about 10^{39} erg s⁻¹ in few seconds. The type II bursts are thought to be due to Lightman-Eardley instability that developed in the accretion disk. No abrupt change in the luminosity is observed during the type II burst.

Short bursts of few seconds to long burst of few hundreds of seconds are observed study of SMC X-1. The shape of the pulse profiles were almost same for different observations which suggest that the geometry of the accretion disk is unchanged due to bursts. The ratio of the secondary to primary peaks of the pulse profile is found to increase with the increase in flare fraction, which may be due to an increase in the accretion rate along the fainter or colder pole of the neutron star during bursts (Moon *et al.*, 2003). With an increase in accretion rate there is an increase in flare fraction. Accretion of nearly same amount of matter on to the two poles of the neutron star may be the cause for the primary and secondary peak of being nearly of same height. With the increase in the flare fraction the luminosity is found to increase, which can be due to increase in the rate of conversion of accreted matter into radiation.

When the radiation pressure dominates over the total pressure in the inner radius of the accretion disk the Lightman-Eardley instability occurs. The instability will trigger the thermal as well as the surface density instability. The investigation on the global nature of the instability were done by Taam and Li (1984) and Lasota and Pelat (1991) and found that the instability leads to burst with recurrence time of few seconds which are similar to that of the three outburst observed in GRO J1744-28 during 1996 (Cannizzo, 1996),

having duration of ~ 10 s and recurrence time of ~ 1000 s. According to Cannizzo (1996) the fast recurrence of the bursts seen by Taam and Li (1984) and Lasota and Pelat (1991) where due to a given value of the viscosity parameter ' α ' (Shakura and Sunyaev, 1973), which they set equal to 1 and considered the inner radius (r_{inner}) to be equal to the radius of the neutron star. For burst to occur in GRO J1744-28 the accretion rate must be slightly greater than the critical value such the radiation pressure becomes comparable to the gas pressure. Taking the value of α less than 1 and r_{inner} greater than the radius of the neutron star, the viscous timescale at the critical condition is found to be $t_{v,crit} = 1200 r_8^{0.58} m^{0.79}$ s, where r_8 is the inner radius in the order of 10^8 cm, m is the mass of the neutron star in the order of solar mass (M_\odot). Taking the value of $r_{inner} = 10^{7.5}$ cm and $m = 1$ (Cannizzo, 1996) we get $t_{v,crit} \sim 800$ s, which is in good agreement with the recurrence time observed in the burst of GRO J1744-28.

The burst from SMC X-1 is similar to that one observed in GRO J1744-28 but the post-flare dip is absent in the former source. Dips in the GRO J1744-28 are observed after the burst and it is thought to be due to depletion of accreted matter after the burst. The absence of dips in SMC X-1 may be due to slow accumulation of matter after a burst or due to release of energy from small fraction of accumulated matter during the burst such that the intensity is found in the persistent level. Another possible reason for the absence of dips may be an increase in the accretion rate just after the burst.

In the source taken here no correlation of the flare-fraction/hr, column density (n_H) and flux with the orbital phase are found. We do not find any change in the nature of the spectrum due to flares. The small softening or hardening of the spectrum can be due to varying interstellar absorption. The SMC X-1 and GRO J1744-28 shows similar spectral properties, as in the case of GRO J1744-28 there is no spectral softening observed in SMC X-1. The spectrum of both sources are inconsistent with the blackbody, the spectrum of GRO J1744-28 photon index 1.2 with the high cutoff energy of 14 keV (Sazonov *et al.*,

1996). Thus burst in these two X-ray binaries are of the same type and can be due to LE instability.

Due to the low magnetic field of the pulsar the transition region between the radiation dominated region and gas pressure dominated region is located near the inner edge of the disk (Li and van den Heuvel, 1997), such that the instability developed inside the disk cannot propagate any further resulting in the heating of matter because of increase in the viscosity. The heated matter is then accreted onto the neutron star producing short burst. The viscosity parameter (α) in the transition region between the radiation dominated and gas pressure dominated region is given by $\alpha = 216 \frac{\dot{M}_{17}}{t_{visc}^{3/2}}$, where \dot{M}_{17} is the rate of accretion in the order of 10^{17} , t_{visc} is the viscous time scale. The viscous parameter can be estimated by taking the value of $\dot{M}_{17} = 20 \text{ gm s}^{-1}$ and $t_{visc} = 800 \text{ s}$ which is $\alpha \sim 0.16$. Considering the recurrence time of the burst to be equal to the viscous time scale we will get $\alpha \sim 0.16$. A huge accumulation of matter in short time may cause large burst in short time where as if the accumulation of matter takes place slowly causing an instability to develop in a large area for a long time can results in long burst of multiple peaks.

Chapter 4

Timing and Spectral properties of Accreting Milli-second X-ray Pulsar Swift J1756.9-2508

4.1 Introduction

Swift J1756.9-2508 is a 5.5 ms accreting milli-second X-ray pulsar (AMXP) discovered in 2007 (Krimm *et al.* (2007a); Markwardt *et al.* (2007)). The companion of the neutron star in Swift J1756.9-2508 is a He-dominated brown dwarf and has an orbital period of 54.7 min (Krimm *et al.*, 2007b). The estimated magnetic field of the source is about 3.1×10^8 G (Sanna *et al.*, 2018). Bult *et al.* (2018) has done correction on the source coordinates through an astrometric analysis of the arrival time of pulse. The corrected coordinates are R.A. = $17^h 56^m 57.18^s \pm 0.08^s$ and Dec. = $-25^\circ 0' 27.8'' \pm 3.5''$.

A part of the chapter of the thesis is published in *Mon. Not. Roy. Astron. Soc.* 489, 5858-5865 (2019)

The timing and spectral analysis of the pulsar Swift J1756.9-2508 are carried out in detail in this chapter. The source spectrum in a broad 0.3-79 keV energy range are fitted with theoretical models. A detail analysis of the pulse profile is done. We have also studied the variation of pulse profile and pulse fraction with energy using *NuSTAR* observation. The pulse-phase, orbital-phase and time resolved spectral analysis are also obtained.

4.2 Observation and data reduction

We have used one *NuSTAR* and three *Swift*-XRT observations of the source Swift J1756.9-2508 (hereafter J1756.9) for our analysis. Data reduction were performed in HEASOFT v 6.22.1. Out of the seven *Swift* observations the source was clearly visible in four cases. The observation IDs of the *Swift* observations used in our analysis are 00030952018, 00088662001, 00030952019 and 00030952020. The standard data screening and reduction of *Swift*-XRT data are done through *xrtpipeline* (v 0.13.4). The source and background region file are obtained using *xselect*. For the last three observations the count rates are found greater than 0.5 count s^{-1} and therefore, the pile up effect is not-negligible. So to minimize the pile-up effects we took an annular region of radius 3 and 23 pixels around the bright source center for all the observations as a source region, whereas the circular region of radius 20 pixel away from the source was considered as background region. The observation of the source was contaminated with the presence of bright source GX 5-1 in the close proximity, so the background region is so chosen that it includes the maximum contamination. The response matrix files are obtained from the calibration data base whereas the ancillary response files are generated using the tool *xrtmkarf*. During the 2018 outburst *NuSTAR* observed the source twice. The observations IDs are 90402313002 and 90402313004. The source was visible only during the first observation, it was in quiescent state however during the second observation. So we have considered the first *NuSTAR* observational data only for analysis. The standard data reduction along with the products

are obtained using *NuSTAR* data analysis software (*NuSTAR*DAS v 1.9.3). The clean event files from the unfiltered event files for the two focal plane modulus FPMA & B have been obtained using *nupipeline*. The image from the cleaned event files are plotted using *xselect* and *ds9*. From the plotted image the source region were extracted considering a circular radius of $90'$ around the direction of the source and the background region was obtained by taking a circular region of same radius away from the direction of the source. The light curves and spectra are then obtained using these sources and background regions with the help of *nuproducts*. The light curves from the two focal plane modulus were background corrected and combined using the tool *lcmath*. Finally the barycentric correction of the combined light curve was done with the help of the *barycorr* in the analysis.

4.3 Analysis and Results

4.3.1 Light curves

Light curves of the AMXP J1756.9 during 2018 outburst are shown in Fig. 4.1. The light curve in black is from *Swift*-BAT, whereas that in the red colour in the Fig. 4.1 is from *Swift*-XRT. The vertical dotted line represents the *NuSTAR* observation. The inset figure represents the AMXP light curve for a *NuSTAR* observation. From the *NuSTAR* light curve we observed that the count rate decreases quickly by $\sim 3.15 \text{ count s}^{-1}$ or by about 15% in 84.5 ks. Thus the count rate decreases at the rate of $\sim 3.22 \text{ count s}^{-1}$ per day. Fitting the *NuSTAR* light curve with a straight line determined the slope $\sim 3.63 \text{ count s}^{-1}$ per day, considering this to be the decay rate then after six days the count rate is then found to decrease by $\sim 22 \text{ count s}^{-1}$, that is why the source was undetectable during second *NuSTAR* observation. Thus the source was observed once again nearly six days after the first observation.

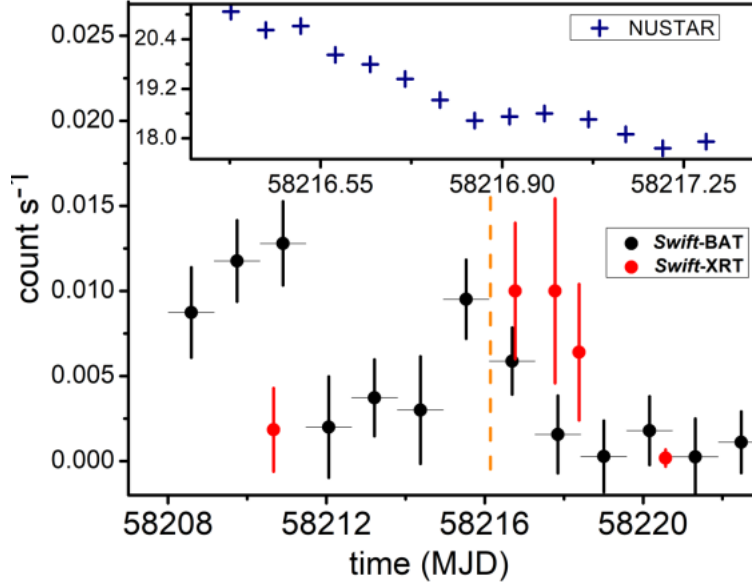


Fig. 4.1 Light curves of J1756.9 during 2018 outburst. Black and red represents the *Swift*-XRT & BAT light curves respectively. The inset figure represent *NuSTAR* light curve.

Colour-colour diagram

The colour-colour diagram gives the variation of the hard colour with respect to soft colour. The soft colour is obtained by dividing the light curve of 5-8 keV energy by light curve of 3-5 keV, whereas the hard colour is analyzed as the ratio of 8-14 keV to 14-22 keV count rates. The colour-colour diagram is found different during this outburst as compared to that reported by Patruno *et al.* (2010a) and it can be due to the fact that this particular *NuSTAR* observation covers only a fraction of the outburst. The soft and hard colours lies between 1.0-2.7 and 1.2-1.8 respectively. The soft colour is more prominent in 1.2-1.8 range corresponding to the hard colour in 0.25-0.40 range.

4.3.2 Pulse profiles

To get the pulse profile we estimated the pulse period of the AMXP. The pulse period was estimated using the ftool *efsearch* which uses χ^2 maximization technique. The estimated pulse period was about 5.4925 ms. Pulse profiles were obtained by folding the light curves

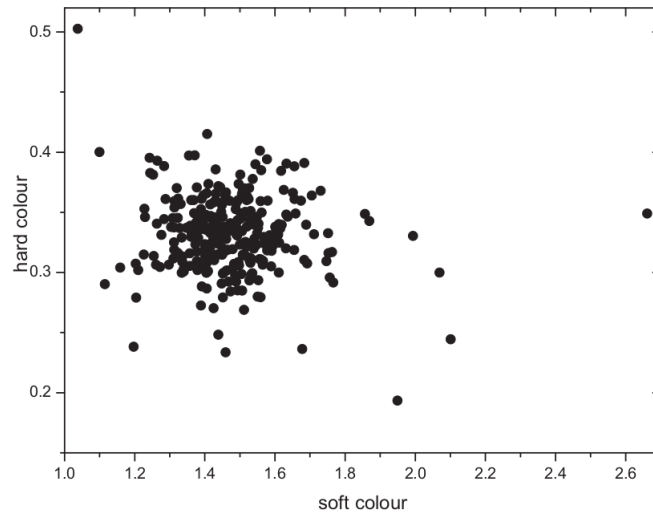


Fig. 4.2 Colour-colour diagram of the AMXP.

about the estimated pulse period using EFOLD. The pulse profiles were folded into 10 phase bins. The pulse profile in the energy range 3-79 keV of the J1756.9 is found to deviate from the sinusoidal shape as the second harmonic component has non-negligible contribution to the pulse profile as observed by Bult *et al.* (2018); Sanna *et al.* (2018). To understand more clearly about the contribution of first and second harmonic components we fitted the pulse profile by two sinusoidal functions (fundamental and second harmonics). The two sinusoidal fittings are represented by the blue (fundamental) and the red (second harmonic) colours in the Fig. 4.3, whereas the black represents the best fitted line.

The pulse profiles variation with the energy is studied by folding the light curves in four different energy ranges namely 3-7 keV, 7-17 keV, 17-35 keV and 35-79 keV, each having 10 phase bins. These pulse profiles were also fitted with two sinusoidal functions. The shape of the pulse profiles were observed to vary with the energy. A significant deviation of the pulse profiles from the sinusoidal shape is observed, which clear indicates about the contribution of the second harmonic component. For hard X-ray range the deviation is much stronger, as it is clear from the Fig. 4.3. For the pulse profiles in 17-35 keV and

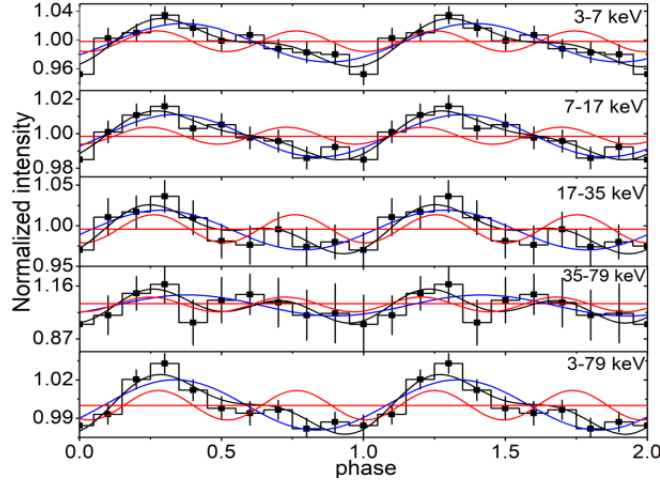


Fig. 4.3 Pulse profiles in five different energy range. The fundamental and second harmonic sinusoidal fitting are represented by blue and red respectively. The black line represents the best fitted line.

35-79 keV the deviation from the sinusoidal shape is much more than the other three cases. The pulse profile in 35-79 keV is found to have nearly double peak.

Patruno *et al.* (2010a) studied the variation of pulse profile with time during 2007 and 2009 outbursts of J1756.9, where it was shown that the pulse profiles were sinusoidal in shape at the beginning of the outburst. Then it gradually evolved into skewed shape during the slow decay phase of the outburst and thereafter became double peaked in the fast decay phase of the outburst. It is also important to note that the variation in the shape of the pulse profile is related with the variation of pulse amplitude and pulse phase with time. They also observed the same kind of variation in pulse profile with time during the two outbursts.

Pulse morphology

To understand in depth about the dependence of the pulse profiles with energy we used the procedure followed by Tendulkar *et al.* (2015). The idea behind this is to decompose the pulses into Fourier harmonics such that we define two Fourier co-efficient a_k and b_k as,

$$a_k = \frac{1}{N} \sum_{j=1}^N p_j \cos\left|\frac{2\pi jk}{N}\right| \quad (4.1)$$

$$b_k = \frac{1}{N} \sum_{j=1}^N p_j \sin \left| \frac{2\pi jk}{N} \right| \quad (4.2)$$

where N represents number of phase bins, j and k are the phase bins and Fourier harmonics respectively and p_j is the count rate of j^{th} phase bin. The strength of each of the Fourier component is defined as $A_k = \sqrt{a_k^2 + b_k^2}$, such that we can define another quantity A which is given by $A = \sqrt{\sum_{k=1}^M A_k^2}$. As the contribution of harmonics other than the second harmonic is negligible on the pulse profiles of AMXPs (Patruno and Watts, 2013) and also the Fourier co-efficient for higher harmonics are very small, so we consider upto first three harmonics in our analysis and therefore consider $M = 3$. In Fig. 4.4 the variation of the normalized amplitude of the fundamental A_1/A and second harmonics A_2/A are shown. For energy upto 40 keV, the normalized amplitude of the fundamental increases after that there is small decrease in its value at ~ 55 keV. The value of normalized amplitude of the second harmonics decreases upto 40 keV and then increases at last at ~ 55 keV. Fitting the normalized amplitudes of the fundamental and harmonics by straight line we observed that there is overall increase in the value of the normalized amplitude of the fundamental with energy whereas the normalized amplitude of the harmonic decreases with energy.

Pulse fraction

The strength of the pulsation is measured in terms of pulse fraction. Here we considered two different definitions of the pulse fraction found in the literature. The root-mean-square (rms) pulse fraction (P_{rms}) in terms of two Fourier coefficients is defined as follows:

$$PF_{rms} = \frac{\sqrt{2 \sum_{k=1}^M [(a_k^2 + b_k^2) - (\sigma_{a_k}^2 + \sigma_{b_k}^2)]}}{a_0} \quad (4.3)$$

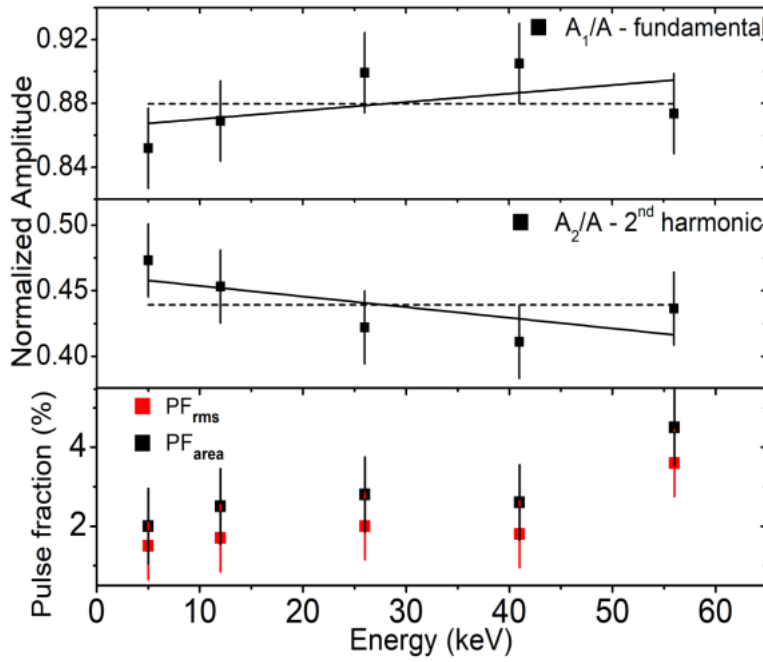


Fig. 4.4 Variation of normalized amplitude of first (upper panel) and second harmonic (middle panel) with energy. The bottom panel shows the variation of the pulse fraction with energy.

where a_k and b_k are the Fourier co-efficient as defined in equation 4.1 and 4.2. σ_{a_k} and σ_{b_k} are the uncertainties linked with a_k and b_k , where

$$\sigma_{a_k}^2 = \frac{1}{N} \sum_{j=1}^N \sigma_{p_j}^2 \cos^2 \left| \frac{2\pi jk}{N} \right| \quad (4.4)$$

$$\sigma_{b_k}^2 = \frac{1}{N} \sum_{j=1}^N \sigma_{p_j}^2 \sin^2 \left| \frac{2\pi jk}{N} \right| \quad (4.5)$$

Another definition of the pulse fraction is as follows (Gonzalez *et al.*, 2010):

$$PF_{area} = \frac{\sum_{j=1}^N (p_j - p_{min})}{\sum_{j=1}^N p_j} \quad (4.6)$$

The variation of the pulse fraction with the energy is plotted in the bottom panel of Fig. 4.4. It is observed that both the pulse fractions increases with the increase in energy.

$n_H (\times 10^{22})$	$8.64 \pm 0.49 \text{ cm}^{-2}$
kT	0.53 ± 0.02
photon index (α)	1.75 ± 0.02
cutoff energy (E_c)	74.58 ± 6.04
χ^2/dof	0.99/4731

Table 4.1 The best fitted model parameters obtained by fitting *Swift* and *NuSTAR* spectra simultaneously.

In 5-26 keV energy range both PF_{rms} and PF_{area} are found to increase slowly with the energy and a small decrease in their values at ~ 42 keV are observed followed by an abrupt increase in their value at 55 keV. However the variation of PF_{area} with energy is found to be steeper than that of the PF_{rms} . This can be due to the fact that the high energy X-ray photons are less in number than the soft X-ray photons, so PF_{area} is found to be biased towards the higher value due to the low statistics in the high energy range (An *et al.*, 2015).

4.3.3 Spectral analysis

A broadband spectral fitting in the energy range 0.3-79.0 was done by fitting simultaneously one of the *Swift*-XRT spectrum in 0.3-10 keV energy range with the 3-79 keV *NuSTAR* spectra. This particular *Swift* observation having Obs ID. 00088662001 was close to the first *NuSTAR* observation. Spectral fittings were done in XSPEC v12.9.1p. The models used in the analysis are CONSTANT, WABS, BLACKBODY and CUTOFFPL. The CONSTANT model is introduced in order to address the issue of the uncertainty of the instrumental calibrations and non-simultaneity of the *Swift* and *NuSTAR* observations.

The column density estimated by the model was about $\sim 8.64 \times 10^{22} \text{ cm}^{-2}$ which is much higher than that of expected value of $\sim 1 \times 10^{22} \text{ cm}^{-2}$ along the direction of the source. The broad 0.3-79 keV energy spectrum was observed to be hard and flat with a high value of cut-off energy 74.58 keV. The source is highly obscured which is indicated by the large absorption column density along the direction of the source. No emission or

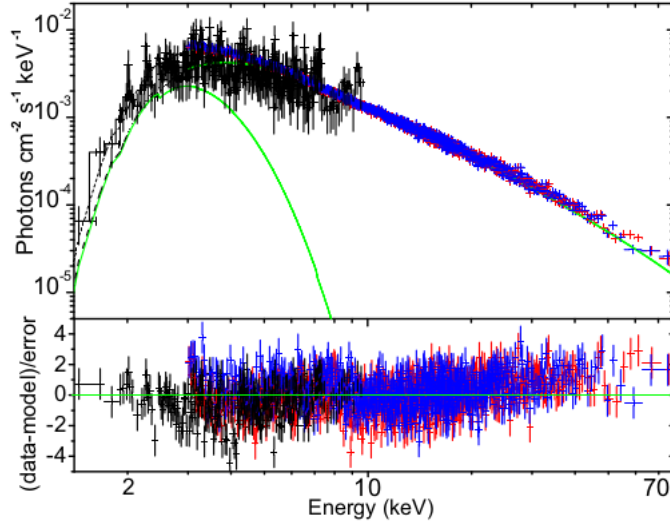


Fig. 4.5 The broad 0.3-79 keV spectral fitting of J1756.9. The points in black represents *Swift*-XRT spectrum and that one blue and red represent *NuSTAR* FPMA & B spectra respectively.

absorption like features were observed in the spectrum. The flux in 0.3-79.0 keV range is found to be $6.48 \times 10^{-10} \text{ erg cm}^{-2} \text{ s}^{-1}$. Considering the distance to the source to be 8 kpc (Krimm *et al.*, 2007b) the luminosity is found to be $4.96 \times 10^{36} \text{ erg s}^{-1}$. The best fitted parameters are shown in Table 4.1.

Pulse phase-resolved spectral analysis

Using *NuSTAR* observation of the J1756.9 we carried out the pulse phase-resolved analysis. For that we took a 5 ks long data segment and divided it into five equal pulse phase interval namely 0.0-0.2, 0.2-0.4, 0.4-0.6, 0.6-0.8 and 0.8-1.0 using the estimated value of pulse period. The necessary good time interval *gti* file for each phase interval was created in *xselect*. Using this *gti* file spectra for each interval are created with the help of *nuproducts*. The 3-79 keV spectra are then analyzed with CONSTANT, WABS and POWERLAW models. The flux is estimated using the model CFLUX. The CONSTANT model parameters were fixed at unity. It is observed that the photon index is maximum in the initial phase interval 0.0-0.2 which decreases in the next phase interval reaching a

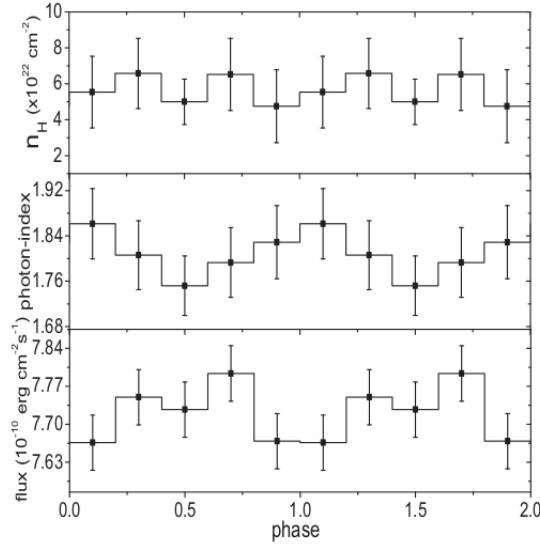


Fig. 4.6 Variation of the spectral parameter with the pulse phase. The upper, middle and bottom panels shows variation of column density (n_H), photon index and flux with the pulse phase respectively.

phase ϕ	n_H cm^{-2}	Photon index α	Flux (\times) $ergcm^{-2}s^{-1}$	χ^2_v
0.0-0.2	5.53 ± 1.99	1.86 ± 0.06	7.666 ± 0.051	0.89
0.2-0.4	6.57 ± 1.95	1.80 ± 0.06	7.750 ± 0.050	0.92
0.4-0.6	4.99 ± 1.26	1.75 ± 0.06	7.727 ± 0.049	0.94
0.6-0.8	6.52 ± 2.01	1.79 ± 0.06	7.794 ± 0.051	0.94
0.8-1.0	4.75 ± 2.03	1.83 ± 0.06	7.669 ± 0.050	0.97

Table 4.2 Values of best fitted spectral parameters.

minimum at 0.4-0.6 and then increases once again in the rest of the phase intervals. No systematic variation of the column density with the pulse phase were observed. The flux is observed to decrease with the phase and it reaches the maximum value in the interval 0.6-0.8 after that it decreases as depicted in Fig. 4.6. The best fitted model parameters are estimated which are displayed in the Table 4.2.

Orbital phase resolved analysis

For orbital phase analysis we used the value of orbital period and epoch obtained by Sanna *et al.* (2018). Using *NuSTAR* observation we divided the total orbital period into ten phase

intervals. For each interval good time interval (*gti*) file was created. Using this good time interval we extracted the spectra for each of the orbital phase interval. Spectra were fitted with CONSTANT, WABS and POWERLAW models. The flux in 3-79 keV energy range was estimated using the convolution model CFLUX. The variation of the spectral parameter with the orbital phase is shown in Fig. 4.7.

It is observed that between the phase interval 0.0-0.2 the flux increases and then it decreases which is followed by an increase and thereafter decrease and once again it increases reaching a maximum value of 5.99×10^{-10} erg cm⁻² s⁻¹ in between 0.5-0.6. After that it is found that the flux decreases continuously between 0.6-0.9, reaching the minimum value of 5.56×10^{-10} erg cm⁻² s⁻¹ and then increase once again in the last phase interval 0.9-1.0. The photon index decreases regularly in between 0.0-0.5 and then increases in the phase interval 0.5-0.7. After that there is a decrease in its value which is followed by an increase and then small decrease in its value. The column density is found to vary similarly with the orbital phase as the photon index. In between 0.0-0.3 the value of column density decreases after that there is a sharp rise and fall. In the interval 0.4-0.7 the value of column density increases which is followed by a decrease and an increase in the values. In between the phase interval 0.8-1.0 the value of column density is almost constant. The cutoff energy decreases between the orbital phase 0.0-0.5 and then increases sharply in 0.5-0.6 phase interval followed by a small increase in its value at 0.6-0.7. After that there is a sharp fall in its value followed by sharp rise. For 0.8-1.0 the value of cutoff energy is almost constant. The value of different spectral parameters are shown in Table 4.3.

The correlation of different spectral parameters with flux is also studied here. For that we have plotted the photon index, column density and cutoff energy against the flux. This is shown in Fig. 4.8. From the figure it is evident that the column density and photon

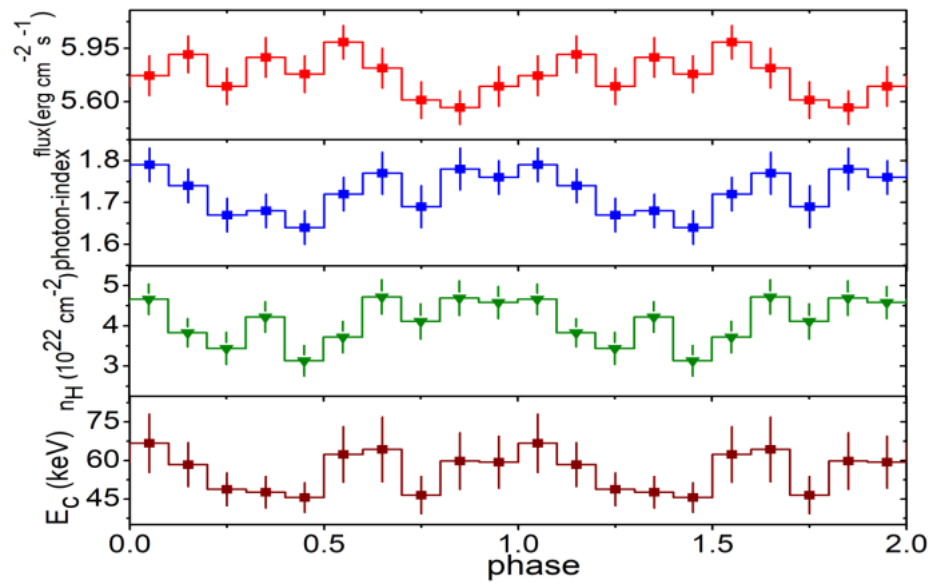


Fig. 4.7 Variation of the best fitted spectral parameter with the orbital phase. The upper panel in red shows the variation of flux with phase. The figures in blue and green indicated the variation of photon index and column density respectively. The lower panel shows the variation of cutoff energy with phase.

index show anti-correlation with the flux whereas the cutoff energy (E_c) shows a positive correlation with both flux and photon index.

Time resolved spectral analysis

To study the variation of the spectrum with time we divided the total exposure time of 39.5 ks into 14 segments. The mean exposure time of each segment being ~ 2.8 ks. For each segment good time interval file created. Using this good time interval file spectra were extracted. Spectra were fitted with the same model as have been used earlier to fit the spectra. The variation of the spectral parameters with the time is shown in Fig. 4.9. From the figure it is evident that the flux is found to decrease with time which is clear from the plot that the outburst is decaying rapidly. However there is no monotonous decrease or increase in the spectral parameters with time. The spectral parameter shows increase and decrease with time. An abrupt increase in the spectral parameters at the last interval is observed. Using GAUSSIAN model we searched for the iron line, first we kept the

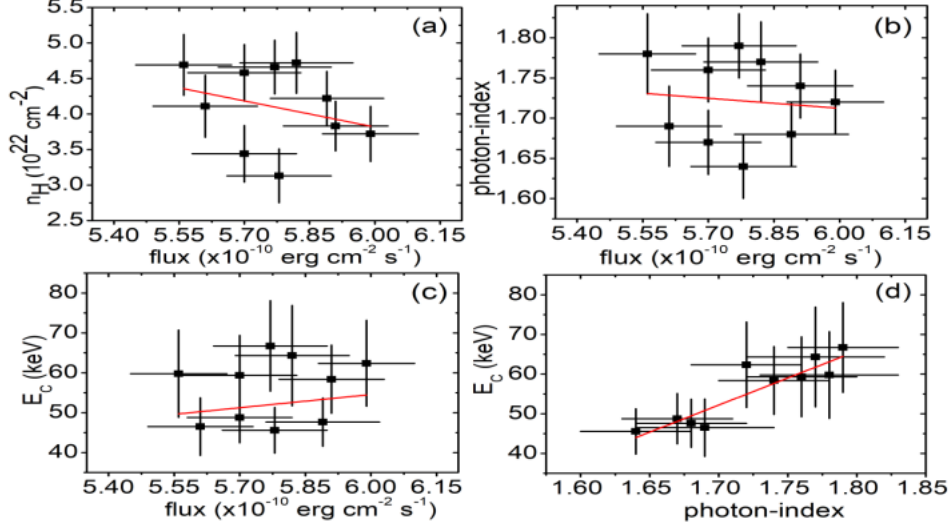


Fig. 4.8 Variation of the column density (a), photon index (b) and cutoff energy (c) with flux. Variation of cutoff energy (d) with photon index.

Phase	n_H (10^{22} cm^{-2})	Photon index α	E_c (keV)	Flux ($10^{-10} \text{ erg cm}^{-2} \text{ s}^{-1}$)	χ^2_ν
0.0-0.1	4.7 ± 0.4	1.79 ± 0.04	66.7 ± 11.4	5.77 ± 0.13	0.97
0.1-0.2	3.8 ± 0.3	1.74 ± 0.04	58.4 ± 8.6	5.91 ± 0.12	0.91
0.2-0.3	3.4 ± 0.4	1.67 ± 0.04	48.8 ± 6.4	5.70 ± 0.12	0.91
0.3-0.4	4.2 ± 0.4	1.68 ± 0.04	47.6 ± 6.1	5.89 ± 0.13	0.88
0.4-0.5	3.1 ± 0.4	1.64 ± 0.04	45.6 ± 5.8	5.78 ± 0.12	0.86
0.5-0.6	3.7 ± 0.4	1.67 ± 0.04	62.4 ± 10.8	5.99 ± 0.11	0.87
0.6-0.7	4.7 ± 0.4	1.77 ± 0.05	64.3 ± 12.6	5.82 ± 0.13	0.83
0.7-0.8	4.1 ± 0.4	1.69 ± 0.05	46.5 ± 7.2	5.61 ± 0.12	0.90
0.8-0.9	4.7 ± 0.4	1.78 ± 0.05	59.8 ± 11.0	5.56 ± 0.11	0.85
0.9-1.0	4.6 ± 0.4	1.76 ± 0.04	59.3 ± 10.1	5.70 ± 0.13	0.90

Table 4.3 Best fitted spectral parameters for different orbital phase intervals.

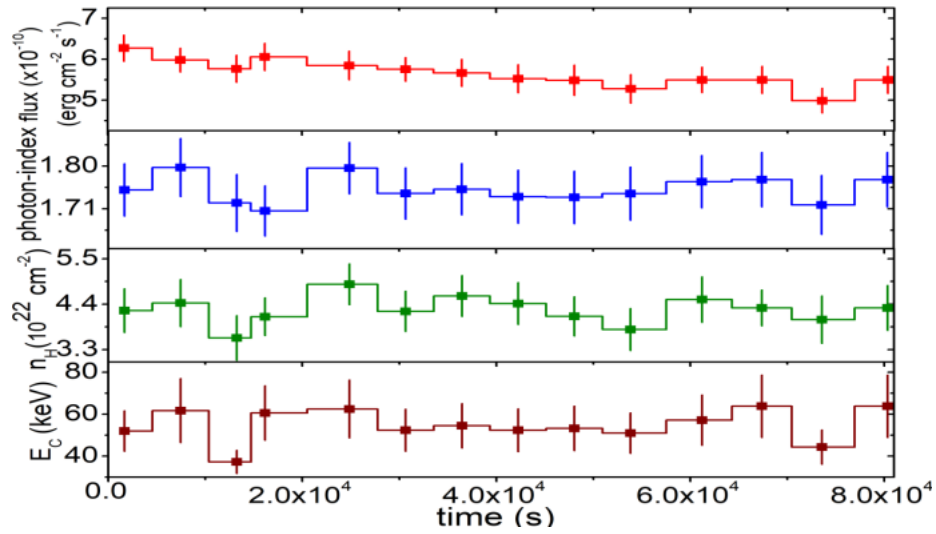


Fig. 4.9 The first upper panel in red indicates the variation of flux with time. The bottom panel indicates the variation of cutoff energy with the time. The two middle panels in blue & green represent the variation of photon index and the column density with time respectively.

Gaussian line fixed at 6.4 keV and then fitted it, after that we set the Gaussian line free and fitted the spectra again. However no iron emission lines are observed. The upcoming mission with high spectral resolution is helpful in finding the presence of iron line in J1756.9 and other AMXPs. No spectral softening or hardening of the spectrum with time is observed. From the Fig. 4.9 it is evident that a correlation is observed between the photon index (α), column density (n_H) and cutoff energy (E_c) as in some part of the figure these parameters follows the same pattern. To check this correlation we have plotted the these parameters with respect to the spectral flux (Fig. 4.10). When the variation is fitted with a linear model we found a straight line having non-zero positive slope, which indicates the existence of correlation. The correlation can be understood in the way that with the generation of high energy X-ray photons there is an increase in their absorption resulting in an increase in column density and softening of spectrum however sufficient number of high energy photons which can still reach the detector. Table 4.4 gives the detail variation of the spectral parameter with time.

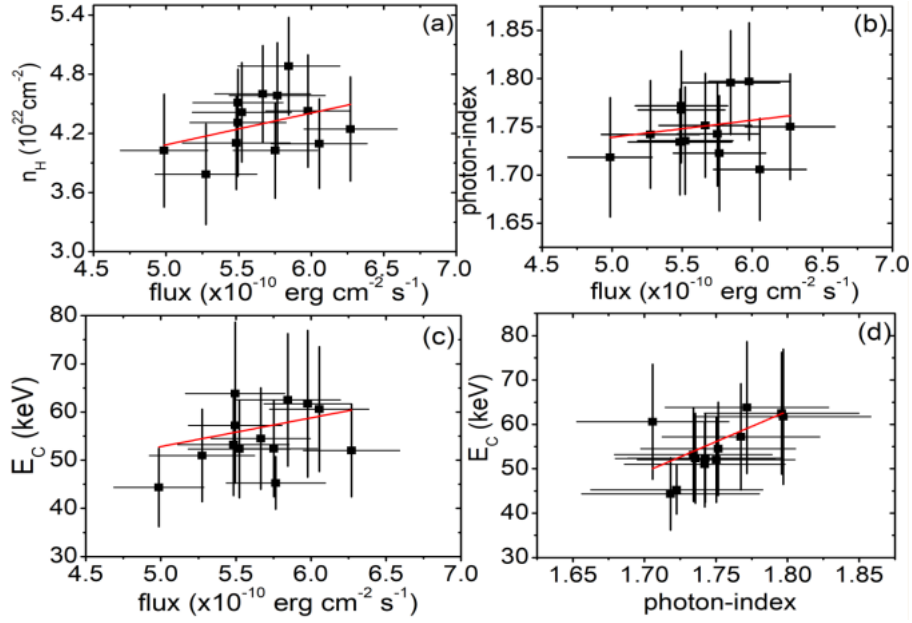


Fig. 4.10 Figures (a), (b) and (c) represents variation of column density, photon index and cutoff energy with flux respectively, whereas that in figure in panel (d) is variation of cutoff energy with the photon index.

Time (ks)	n_H (10^{22} cm^{-2})	Photon index (α)	E_c (keV)	Flux ($10^{-10} \text{ erg cm}^{-2} \text{ s}^{-1}$)	χ^2_ν
0-3.3	4.2 ± 0.5	1.70 ± 0.06	52.0 ± 9.6	6.27 ± 0.32	0.87
6-9	4.4 ± 0.6	1.80 ± 0.06	61.7 ± 15.2	5.98 ± 0.29	0.86
12-15	3.6 ± 0.5	1.63 ± 0.06	37.3 ± 5.5	5.76 ± 0.33	0.90
17-21	4.1 ± 0.4	1.74 ± 0.05	60.6 ± 12.9	6.05 ± 0.33	0.86
23-26	4.9 ± 0.5	1.79 ± 0.05	62.5 ± 13.7	5.84 ± 0.35	0.78
29-32	4.2 ± 0.5	1.74 ± 0.05	52.4 ± 10.0	5.75 ± 0.29	0.90
35-38	4.6 ± 0.5	1.75 ± 0.05	54.5 ± 10.5	5.66 ± 0.33	0.85
41-44	4.4 ± 0.5	1.74 ± 0.06	52.3 ± 10.2	5.52 ± 0.34	0.91
46-50	4.1 ± 0.5	1.73 ± 0.06	53.2 ± 10.6	5.48 ± 0.37	0.86
52-55	3.8 ± 0.5	1.74 ± 0.06	51.0 ± 9.6	5.27 ± 0.35	0.81
58-63	4.5 ± 0.6	1.77 ± 0.06	57.2 ± 12.0	5.49 ± 0.31	0.88
65-70	4.3 ± 0.4	1.77 ± 0.06	63.8 ± 14.9	5.49 ± 0.33	0.78
71-76	4.0 ± 0.6	1.72 ± 0.06	44.3 ± 8.2	4.99 ± 0.30	0.97
76-84	4.3 ± 0.5	1.77 ± 0.06	63.8 ± 14.9	5.49 ± 0.33	0.78

Table 4.4 Table showing the variation of the best fitted spectral parameters with time.

Obs ID	Date of obs (MJD)	n_H (10^{22}cm^{-2})	Photon index (α)	Flux ($\times 10^{-11} \text{ergcm}^{-2} \text{s}^{-1}$)	χ^2_ν
00030952018	58210.67	6.55 ± 2.85	1.52 ± 0.64	13.93	0.85
00088662001	58216.77	6.06 ± 0.59	1.75 ± 0.18	14.96	0.76
00030952019	58217.78	7.99 ± 1.07	2.31 ± 0.30	10.82	0.71
00030952020	58218.38	4.08 ± 1.35	0.94 ± 0.47	6.67	0.73

Table 4.5 The best fitted spectral parameter for different *Swift*-XRT observation.

The *Swift*-XRT spectra in 0.3-10.0 keV were also fitted by a simple POWERLAW model. The best fitted spectral parameter for different observations are shown in Table 4.5 along with their observation IDs. In between 58210.67 and 58217.78 the photon index increases from 1.52 to 2.31 MJD and after that it decreases to 0.94. The flux was observed to increase between 58210.67 and then decreases. So softening of spectrum with an increase in flux is observed as we have observed in the time resolved spectral analysis of the AMXP using *NuSTAR* observation.

4.4 Discussion

From the *NuSTAR* light curve of the AMXP it is clear that the outburst decays very rapidly. In 84.5 ks observation there was about $\sim 15\%$ decrease in the count rate. We presented the detail study of the change in the morphology of the pulse profile with the energy. As we have observed that the 3-79 keV pulse profile of the AMXP shows significant deviation from the sinusoidal shape, which possibly indicates the significant contribution of second harmonics on the pulse profile. It is evident that there was a change in the morphology of the pulse profile with the energy. The pulse profiles in 3-7 keV, 7-17 keV and 17-35 keV are non sinusoidal, whereas in the 35-79 keV pulse profile we found existence of double peak. The deviation are clearly shown by the black line in Fig. 4.3, which corresponds to best fitted line of the two harmonic components.

We have calculated the normalized amplitude of the first and second harmonics in terms Fourier components in the different energy bands. It is observed that the normalized amplitude of the first harmonic increases with energy and for the second harmonic it decreases with the energy. Similar types of variation in the fractional amplitudes of the Swift J1756.9-2508 was observed by Patruno *et al.* (2010a) using RXTE observations and Sanna *et al.* (2018) using *NuSTAR* and XMM-Newton observations. Bult *et al.* (2018) also reported similar variation of the normalized amplitudes with the energy. The variation of pulse profiles and fractional amplitude are observed in all AMXPs, for example the fractional amplitude in case of Aql X-1 (Casella *et al.*, 2008), SAX J1748.9-202 (Patruno *et al.*, 2010b) and IGR J17379-3747 (Bult *et al.*, 2019) increases with the energy. However in some AMXPs decrease in the fractional amplitude with energy is observed as in the case of XTE J0929-314 (Galloway *et al.*, 2007) and HETE J1900.1-2455 (Galloway *et al.*, 2007). In some cases AMXPs show complex variation in fractional amplitude with the energy, where both increase and decrease in its value are observed at different energies (see Patruno *et al.* (2010b); Falanga *et al.* (2005)). The dependence of the pulse fraction of pulse profile on the energy is studied here and found it increases with the energy. The increase in the pulse fraction with the energy can be understand by a simple toy model suggest by Alexander and Sergey (2008). It was interpreted by them that X-ray emitting region becomes smaller and smaller with the increase in energy and hence the X-rays becomes more pulsed. Patruno and Watts (2013) gave similar explanation to explain the observed variation of fractional amplitude of AMXPs with the energy. It was reported that with an increase in energy the amplitude of pulsed blackbody radiation emitted from the hot spots also increases. We have not observed aperiodic signal or broadband noise at ~ 0.1 Hz in the power spectrum of the AMXP as observed by Linares *et al.* (2008).

From broadband 0.3-79.0 keV spectral fitting of *Swift* and *NuSTAR* spectra we observed that the spectrum of Swift J1756.9-2508 was hard and flat having cutoff energy about

74.58 keV, which can be due to Comptonization of soft photons. Sanna *et al.* (2018) also observed the spectra of J1756.9 in hard state with high energy cutoff during the outburst. We have studied both pulse, orbital phase and time resolved spectral analysis. The photon index obtained by fitting the pulse phase resolved spectra of the J1756.9 by POWERLAW model shows the variation of photon index with pulse phase. The photon index decreases in the initial phases (0.0-0.6) and then increases in the rest of the pulse phases. The flux increase in between 0.0-0.8 except at 0.4-0.6 where we observed small decrease in flux (Fig. 4.6) and decreases abruptly at the last phase intervals. However no systematic variation in the photo-electric absorption in the phase is observed. The flux is minimum when the photon index is maximum; this can be as a result of absorption of X-rays during these phases. It can also be due to variation of the optical depth at different viewing angles which accounts for the variation of the flux and the photon index with pulse phase. The variation of spectral parameter with the pulse phase indicates presence of anisotropy in the accretion columns above the hotspots.

With the orbital phase the photon index (α) and column density (n_H) varies in the similar way but it shows anti-correlation with the source flux, however the cutoff energy (E_c) varies differently with orbital phase and flux. It is clear from Fig. 4.8 that n_H and α decreases with an increase in flux. Thus as a result of increase in flux the spectrum becomes more hard. The hardening of the spectrum with the flux can be as a result of an increase in the optical depth with an increase in the flux or mass accretion rate at the different orbital phases. There is no indication of hardening or softening of the spectrum with the time as observed from the time resolved spectral analysis, but the softening of the spectrum with the increase in flux is observed as the photon index increases with an increase in flux. Also the other spectral parameters obtained in the time resolved spectral analysis shows positive correlation with the flux. From the *Swift*-XRT spectral analysis too we observed that the photon index decreases with decrease in flux. This softening of

spectrum with an increase in the flux was also observed by Zhang *et al.* (1998) in Aql X-1. It was suggested that this might be the indication of source entering into propeller phase. The cutoff energy (E_s) shows positive correlation with flux in both the orbital and the phase resolved spectral analyses. The cutoff energy is associated with the temperature of plasma of the X-ray emitting region and in this case an increase in the observed flux indicates an increase in plasma temperature (Soong *et al.*, 1990). Hence an increase in flux results in an increase in cutoff energy E_c .

Sanna *et al.* (2018) also not observed any emission lines in the source spectra. Patruno *et al.* (2010a) observed the presence of emission line like feature in 6-7 keV energy range as a result it was unable to constraint its line energy and width, as the spectral resolution of the RXTE-PCA is very poor. However, Sanna *et al.* (2018) constraint the upper limit of the width of undetected iron line to be 5 eV. We did not observed any emission or absorption like features in the spectra of J1756.9.

Chapter 5

Study of timing and spectral properties of Be/X-ray pulsar 4U 1901+03

5.1 Introduction

The Be X-ray pulsar 4U 1901+03 was discovered by Uhuru in 1970-1971. The pulse period of the pulsar was about ~ 2.76 s. The pulsating nature of the source was discovered in 2003 (Galloway *et al.*, 2005). The orbital period of the pulsar is 22.58 days. Large negative residuals near 10 keV (10 keV feature) have been observed in the spectrum of the source

The objective of the investigation here is to investigate the 10 keV feature present in the spectrum in detail. The variation of 10 keV feature with pulse phase and luminosity are also studied. In addition to that we have also studied the 30 keV feature and its variation with pulse phase. We have discussed in detail the possible reason behind the origin of these features. The detail discussion on the variation of the pulse profiles of 4U 1901+03 with time and energy are also presented.

A part of this chapter is accepted for publication in *Astrophys. Space Sci* ASTR-D-20-00586R2.

5.2 Observation and Data reduction

NuSTAR

The *Nuclear Spectroscopic Telescope Array (NuSTAR)* observed the Be/X-ray pulsar 4U 1901+03 four times during the 2019 outbursts. As discussed earlier *NuSTAR* consists of two focusing telescopes which operates in 3-79 keV energy range, each of them have their own focal plane module consisting of CdZnTe detector. The data reduction were done using HEASOFT v6.26.1. The mission specific FTOOL nupipeline was used to obtain clean event file from the unfiltered event file. From this cleaned event file we have extracted the source and background regions. With the help of xselect, the image obtained from the cleaned event file is plotted in DS9. A circular region of radius 90'' along the direction of the source was considered as a source region and another circular region of same radius but in the direction away from the source was taken as the background region. For both the focal plane modules FPMA & B, the region files were extracted. Using this region files the final product *i.e.* spectra and light curves, were then obtained with the help of *nuproducts*. The background correction of the light curves are done using lcmath. The background corrected light curves from the two focal plane modules were combined using the same tool. After that the barycentric correction were made with the help of barycorr using the telescope orbit file. From hereafter we are going to refer the four *NuSTAR* observations by Obs1, Obs2, Obs3 and Obs4 respectively.

Swift

Swift observed the source multiple times during the outburst. We have used *Swift*-XRT data for our analysis. The standard data processing and screening were done using xrtpipeline. We have only considered the *Swift*-XRT observations done in Window Timing (WT) mode having good timing resolution for the timing analysis. The cleaned event file was extract in

xselect and the image was plotted in DS9. From the plotted clean image a circular region of radius 20 pixel around the optical position of the source is considered as the source region. An another circular region of same radius but far away from the optical center was taken as the background region. Using these region files in xselect we extracted source and background light curves and spectra. The ancillary response file (ARF) required for the spectral analysis of the spectrum was created using the *Swift* mission specific tool `xrtmkarf`. The response matrices file (RMF) was obtained from the latest calibration database files. The background correction was done using `lcmath`. The background corrected light curves have been further corrected from the telescope vignetting and point spread function using the `xrtlccorr`. After 58637.08 MJD *Swift* observations were made in photon counting (PC) mode and the source was visible only in one observation. Finally the barycentric correction was made using `barycorr`.

NICER

To study the variation in the shape of the pulse profiles after 58637.08 MJD we have used data from NICER observations of the pulsar. The standard data screening and filtering in this case was done using the standard NICER pipeline processing tool `nicerl2`. From the clean event file light curves in 0.2-12 keV energy range having a binning of 1 ms are extracted. As NICER is a non-imaging detector so the background light curves cannot be known here consequently the light curves obtained here is not background corrected. However barycentric correction of the light curves can be made here using the tool `barycorr`.

Table 5.1 Table showing four *NuSTAR* observations indicated by their observation IDs along with the date of observation, exposure and the pulse period of pulsar.

obsId	Date of Obs (MJD)	Exposure (ks)	P_s
90501305001	58531.121	17.85	2.764 ± 0.003
90502307002	58549.308	12.25	2.762 ± 0.003
90502307004	58584.946	21.45	2.762 ± 0.001
90501324002	58615.752	45.12	2.760 ± 0.001

5.3 Analysis and Results

5.3.1 Light curves

The four horizontal lines along with the down arrow in Fig. 5.1 represents the four *NuSTAR* observations taken during different stages of the outburst. Flares are seen in the light curves of all the four *NuSTAR* observations. Flare is considered to be a part of the light curve having count rate 3σ level above the mean value. We have found that for the first two observations the mean number of flares per hour was 5-6 and for the last two observations it was 3-4 flares per hour. The duration of the flares were from few tens to hundreds of seconds. To estimate the duration of the flares we have taken the beginning and the end of the flares described by the lowest point of the flares below that of the mean value. For the first observation the mean duration of the burst was ~ 135 s, whereas for the second observation it was ~ 62.18 s. For the last two observations, the mean duration were ~ 98.13 s and 95.35 s (Fig. 5.2).

5.3.2 Pulse Profiles and Pulse Fraction

The pulse periods of the pulsar were estimated crudely making use of the `ftool powspec`, which transforms the light curves into the Fourier components. For the *NuSTAR* observation, we have taken the light curves having binning of 1 ms to estimate the pulse periods and hence obtained the pulse profiles. Using `efsearch` the final estimation of the pulse period was done. The pulse periods of the four *NuSTAR* observations is shown in Table 5.1.

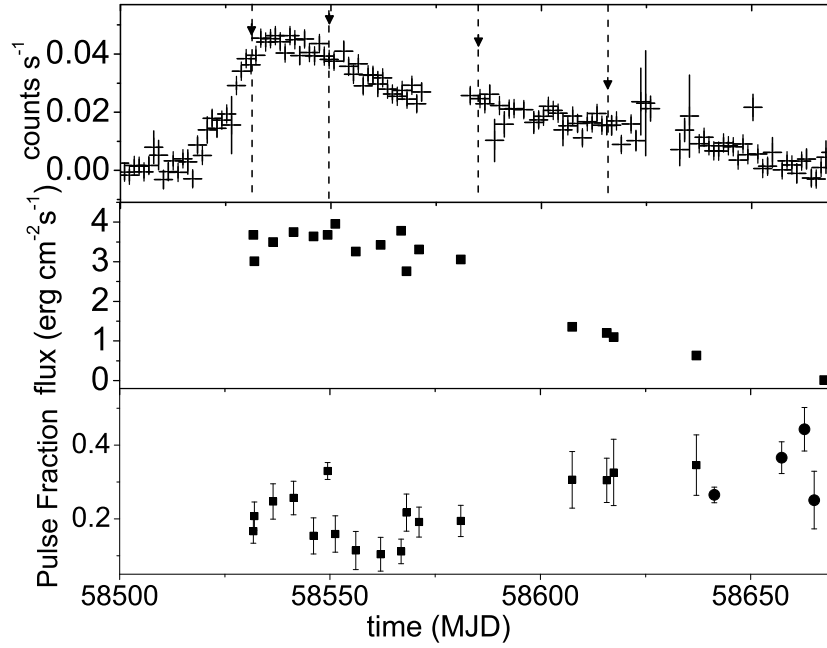


Fig. 5.1 Upper panel shows *Swift*-BAT light curves of 4U 1901+03 during 2019 outburst in 15-50 keV energy range. The down arrows and vertical lines indicates four *NuSTAR* observations. The middle panel shows variation of *Swift*-XRT flux in 0.5-10 keV energy range. Fluxes are in the order of 10^{-9} and obtained by using the command flux in XSPEC for *Swift*-XRT spectra fitted by POWERLAW model. Bottom panel represents change in Pulse fraction with time, the square and circle symbols are for *Swift*-XRT (0.5-10.0 keV) and NICER (0.2-12 keV) respectively.

The uncertainty in the pulse period was determined by the method used in Boldin *et al.* (2013). In this method the errors is determined by the so-called bootstrap method, where we have generated the light curves starting from the initial light curve using the formula $r'_i = r_i + \gamma\sigma_{r_i}$, where r'_i and r_i are the i^{th} count rates of the new and the original light curves respectively, where γ represents a quantity distributed between -1 and +1 and σ_{r_i} represents the error associated with the i^{th} flux measurement. The pulse period from the new light curve is also determined using *efsearch*. The process is repeated for $N = 1000$ times and determined the pulse period (P_i) in each case. The mean pulse period $\langle P \rangle$ corresponds to most probable period and the standard deviation (σ_P) is the associated error of the pulse period. The pulse period of the 4U 1901+03 is found to vary throughout the outburst. The variation of pulse period during the outburst can be due to the transfer of the angular

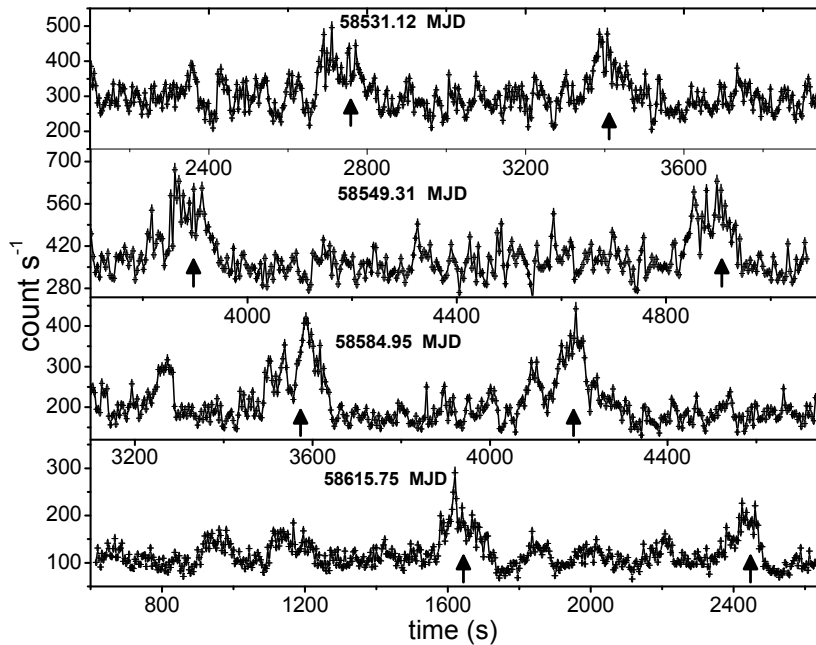


Fig. 5.2 Light curves showing some of the bursts observed in four *NuSTAR* observations. The burst present in the light curves is indicated by up arrow.

momentum onto the neutron star from the accretion disk (Ghosh and Lamb, 1979; Wang, 1987). As a result of transfer of angular momentum there will be an accelerating torque acting on to the neutron star. It is this accelerating torque which causes the intrinsic spin or the pulse period of a X-ray pulsar to vary. Pulse profiles are then obtained by folding the light curve about the given pulse period. For *Swift*-XRT the light curves of binning 1.8 ms are used to extract both the pulse periods and the pulse profiles.

It is evident from the analysis that the pulse profile of the pulsar varies throughout the outburst. The pulse profile during the first *NuSTAR* observation at 58531.121 MJD in the energy range 3-79 keV follow a sinusoidal shape (Fig. 5.3) which later evolved into double peaked at 58549.308 MJD having a main peak. After that it again changed to a single peak with a notch at a phase 0.5 at 58584.946 MJD. During the last *NuSTAR* observation at 58615.752 MJD the pulse profile in 3-79 keV energy range was found to have a single peak similar to that of the first observation but it is little sharper than from that of the first observation. We also studied the temporal variation of the pulse profile using *Swift*-XRT

observations. The variation of the pulse profile is plotted in Fig. 5.4. It is evident that the pulse profile at 58532.03 MJD is double peaked with one major primary peak. The second peak is found to merge with the primary at 58541.33 MJD, which subsequently evolved into single peaked with a notch at 58568.16 MJD later. The pulse profile became broad single peaked at 58581.05 MJD. In between 58607.54-58637.08 MJD the pulse profiles are found having broad single peak. However the pulse profile observed at 58665.09 MJD using NICER observation is found to have single peak which is very sharp compared to that of the *Swift*-XRT. However, no further pulsation observed after 58665.09 MJD.

To study the dependence of the pulse profiles on energy, we have extracted the light curves in different energy bands for the *NuSTAR* observations. The following energy ranges 3-7 keV, 7-12 keV, 12-18 keV, 18-24 keV and 24-32 keV have been chosen for this purpose. For Obs1, the pulse profiles at different energy bands are almost sinusoidal in shape (Fig. 5.3). For this observation the pulse profiles in the energy bands 7-12 keV and 3-79 keV are found almost similar. In the hard X-ray region above 12 keV an increase in the height of the pulse profiles has been observed. For Obs2, pulse profiles in 3-7 keV, 7-12 keV, 12-18 keV and 3-79 keV, we observed existence of double peaks which however differs in shape. It is observed that the second peak was absent in the pulse profiles for the energy ranges 18-24 keV and 24-32 keV. It is observed here that the height of the primary peak has increased in these energy bands. In the energy bands 3-7 keV and 3-79 keV, the pulse profiles for Obs3 are found to have nearly single peak with a notch near ~ 0.5 , however, above 7 keV the pulse profiles are not so smooth, which are associated with large errors. Above 24 keV energy no clear peak was visible. In the case of Obs4, the pulse profiles at different energy bands are found to have almost sinusoidal shape, pulse profiles in the energy bands 7-12 keV and 3-79 keV are almost similar, however, above 18 keV we note large errors associated with each of the normalized count rates.

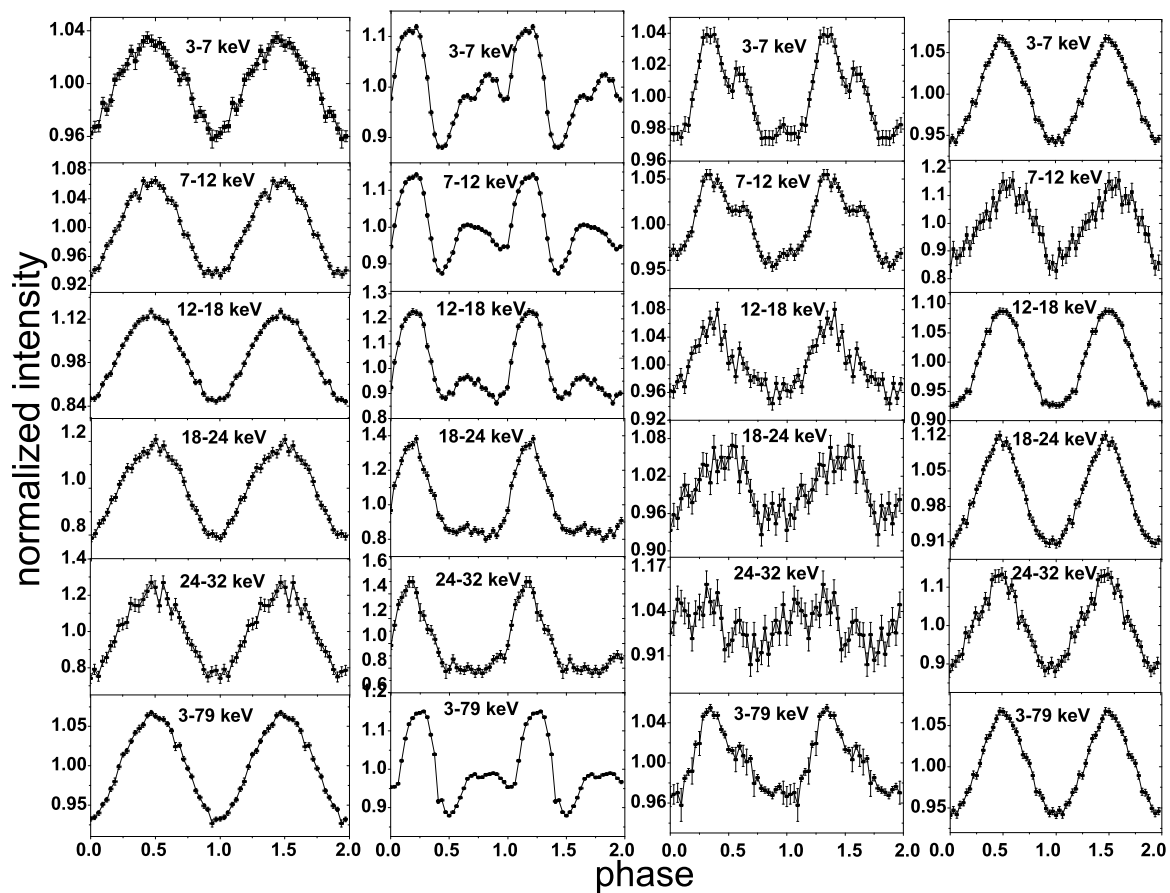


Fig. 5.3 Pulse profiles for different *NuSTAR* observations and variation of pulse profile with energies. Figures (a), (b), (c) and (d) are for the 58531.12, 58549.31, 58584.95 and 58615.75 MJD respectively.

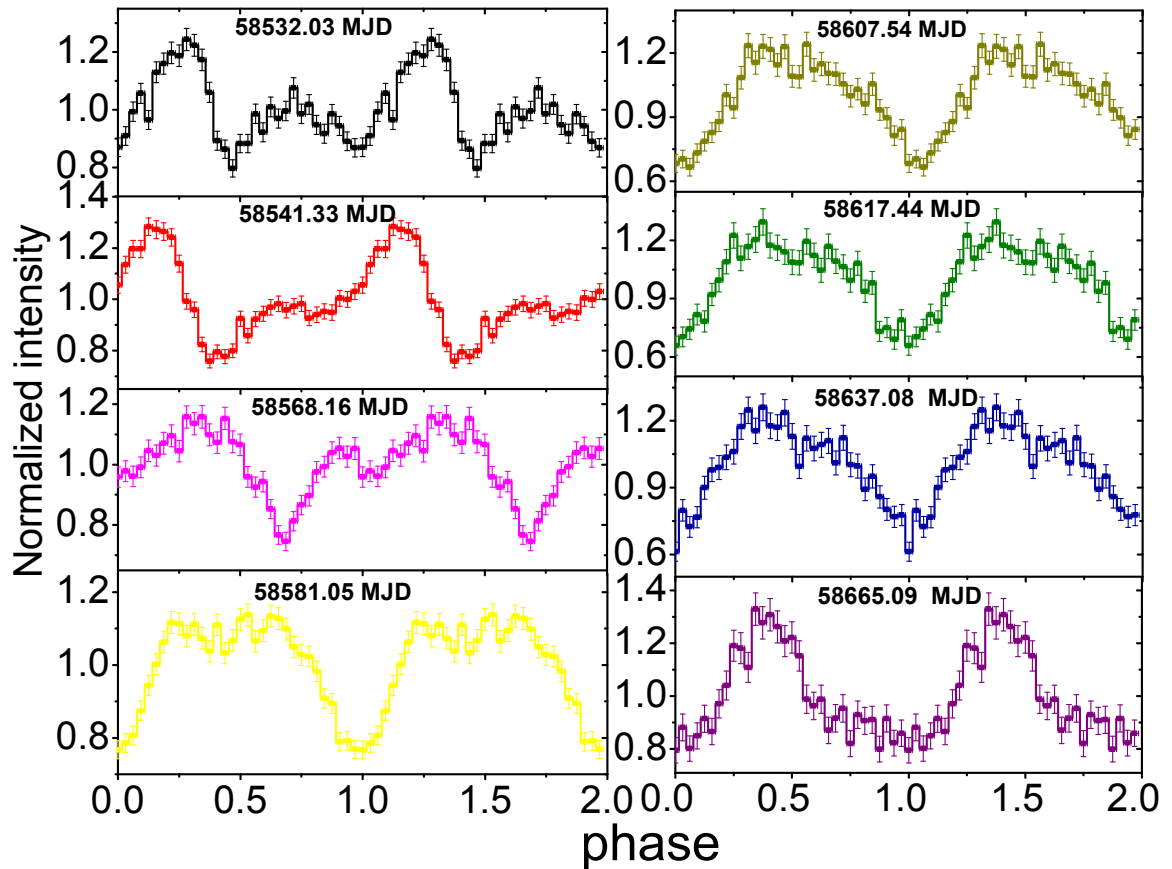


Fig. 5.4 Variation of Pulse profile with time. Pulse profiles from 58532.03 to 58637.08 MJD are obtained by folding *Swift*-XRT lightcurve. For *Swift*-XRT the significant level of pulse periods were greater than 3σ . The broadening of the *Swift*-XRT pulse profiles can be due to the short exposure time of the instrument so that there is not enough photons count rate to fold about the pulse period. The last pulse profile at 58665.09 MJD is obtained by folding NICER lightcurve in 0.2-12 keV energy range (Obs Id - 2200570141).

The pulse fraction (PF) of a pulsar is defined as $PF = \frac{p_{max} - p_{min}}{p_{max} + p_{min}}$, where p_{max} and p_{min} are the maximum and minimum intensities associated with that of the pulse profile respectively. In Fig. 5.5, PF is plotted with respect to energy for the four *NuSTAR* observations. The pulse fraction of the pulsar is found to increase with the energy in all the four *NuSTAR* observations. For Obs1 pulse fraction shows almost a monotonic increase with the increase in energy (black). Pulse fractions increases slowly between 5-15 keV but above 15 keV pulse fraction increases rapidly (red) in the case of Obs2. In the third observation (blue) pulse fractions increases slowly between 5-12 keV and found to have almost constant value between 12-21 keV, above 21 keV pulse fraction is observed to increase once again. In Obs4 pulse fractions increases between 5-25 keV which remains almost constant above 25 keV. From the Fig. 5.5, it is clear that the variation of the pulse fraction with the energy is steep for the first two observations. The luminosity in the case of the first two observations were higher than the last two observations. Thus the pulse fraction in different energy ranges is high if the luminosity is high. The variation of the pulse fraction with energy for different *NuSTAR* observations displayed in Table 5.2.

The variation of the pulse fraction with time and flux are studied using *Swift*-XRT observations. The pulse fraction was found to increase initially between 58531.77-58549.43 MJD from 0.17-0.33 and thereafter decreases to 0.16 at 58551.23 MJD which remains almost constant between 58556.14-58566.91 MJD. However in between 58568.16-58637.08 MJD, the pulse fraction increases from 0.22 to 0.34 (bottom panel of Fig. 5.1). The variation of the pulse fraction with the flux in 0.5-10 keV energy range is shown in the bottom panel of Fig. 5.9. The pulse fraction decreases from 0.34-0.10 as flux increases from $0.64-3.43 \times 10^{-9}$ erg cm⁻² s⁻¹, which is found to increase from 0.11 to 0.33 between $3.43-3.68 \times 10^{-9}$ erg cm⁻² s⁻¹ and then abruptly decreases one again to 0.15 at 3.96×10^{-9} erg cm⁻² s⁻¹. Thus as we study for flux below 3.43×10^{-9} erg cm⁻² s⁻¹, it is found that

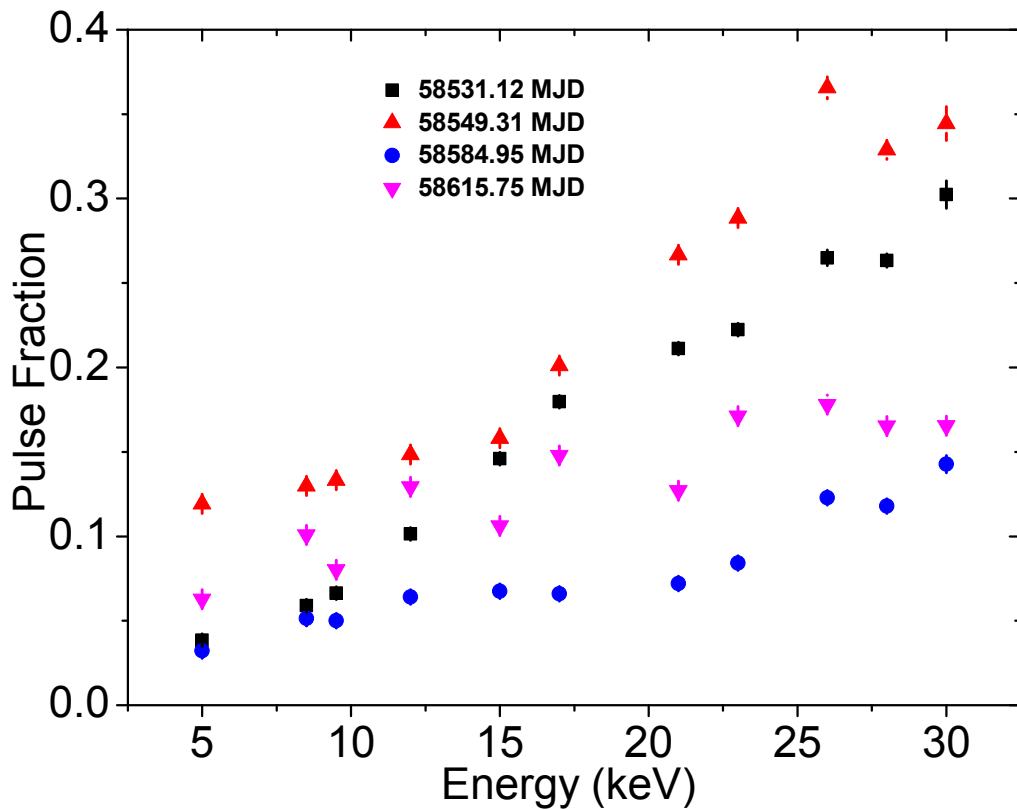


Fig. 5.5 Variation of the pulse fraction of the pulse profile with energy obtained using *NuSTAR* observations. The first, second, third and fourth columns are for Obs1, Obs2, Obs3 and Obs4 respectively.

there is an increase in the pulse fraction. Thus the pulse fraction is found to increase with decay in the outburst.

5.3.3 Spectral Analysis

The three *NuSTAR* observations namely, Obs1, Obs2 and Obs4 were close to three *Swift* observations having Obs Ids 00088846001, 00088849001 and 00088870001 respectively. So we fitted *Swift*-XRT and *NuSTAR* (FPMA & B) spectra simultaneously in the 0.5-79.0 keV energy range, here *Swift* spectra were in 0.5-10 keV energy range and *NuSTAR* in 3-79 keV range. However there is a slight mismatch between the *Swift*-XRT and *NuSTAR* data points while fitting their spectra simultaneously, which has been reported earlier by Bellm *et al.* (2014). A CONSTANT model was used while fitting XRT and *NuSTAR* spectra

Table 5.2 Variation of pulse fraction (%) with energy four different observations.

Energy (keV)	Obs1	Obs2	Obs3	Obs4
5	3.85±0.15	11.92±0.02	3.22±0.01	6.28±0.01
8.5	5.89±0.01	12.98±0.34	5.13±0.01	10.08±0.03
9.5	6.63± 0.01	13.32±0.03	5.01±0.01	8.01±0.02
12	10.14±0.02	14.83±0.05	6.42±0.03	12.92±0.02
15	14.60±0.06	15.81±0.03	6.75±0.03	10.62±0.02
17	17.97±0.09	20.11±0.06	6.59±0.11	14.79±0.07
21	21.12±0.17	26.67±0.02	7.20±0.01	12.70±0.01
23	22.25±0.22	28.86±0.03	8.41±0.01	17.12±0.02
26	26.40±0.46	36.56±0.66	12.28±0.25	16.54±0.03
28	26.34±0.40	32.89±0.51	11.78±0.23	16.54±0.25
30	30.24±0.82	34.44±1.00	14.27±0.52	17.8±0.51

simultaneously to take into account the instrumental uncertainties and non-simultaneity of the observations. The spectra are fitted with two different combination of models. First we used the combination of CONSTANT, PHABS, BLACKBODY, CUTOFFPL and GAUSSIAN and in second case we replaced the CUTOFFPL with the model COMPTT which describes the Comptonization of soft photon in hot plasma. We define Model I to be framed as CONSTANT*PHABS*(CUTOFFPL+GAUSSIAN) and Model II as CONSTANT*PHABS*(COMPTT+GAUSSIAN). The cross section for the PHABS was chosen to be vern and the abundance was set to angr. The optical depth of the Comptonizing region in Model II was obtained using disk geometry. However in both the cases large negative residuals have been found near 10 keV. For this we have incorporated Gaussian absorption model GABS in both the cases. However, the HIGHECUT model did not fit the spectra well and consequently large residuals are observed near the cutoff energy.

When Model I was used to fit Obs1 and Obs2 without GABS model, a wave like feature in the residuals between 3-30 keV energy range have been found to exist with a large negative residuals near 10 keV, causing the fitting to be unacceptable (Fig. 5.6). However, addition of GABS model here fits the spectra well. The reduced χ^2 of the fitting were 1.76

Spectral parameters	Obs1+Swift	Obs2+Swift	Obs3	Obs4+Swift
Model I				
n_H (cm ⁻²)	3.80±0.12	4.03±0.07	2.97±0.43	3.74±0.23
kT (keV)	0.17 ±0.04	0.23±0.02	0.31±0.05	0.15±0.07
α	0.51±0.02	0.46±0.02	0.34±0.01	0.80±0.02
E_H (keV)	7.26±0.12	6.82±0.02	6.21±0.08	6.87±0.02
E_{Fe} (keV)	6.52±0.03	6.52±0.07	6.49±0.02	6.61±0.08
σ_{Fe} (keV)	0.20±0.02	0.32±0.02	0.30±0.07	0.18±0.04
E_{gabs_1} (keV)	10.71±0.11	11.65±0.04	10.14±0.01	7.04±0.33
σ_{gabs_1} (keV)	4.32±0.12	2.49±0.09	4.12±0.14	6.54±0.23
τ_{gabs_1}	0.26±0.05	0.18±0.03	0.33±0.05	0.53±0.07
E_{gabs_2} (keV)	30.37±0.55	30.23±0.62
σ_{gabs_2} (keV)	1.79±0.34	1.04±0.35
τ_{gabs_2}	0.11±0.07	0.07±0.03
$flux$ (erg cm ⁻² s ⁻¹)	6.45 ^{+1.21} _{-0.61}	7.52 ^{+0.80} _{-0.74}	5.01 ^{+0.23} _{-0.1}	2.56 ^{0.90} _{-0.41}
χ^2_v	1.02	1.11	0.98	1.01
Model II				
n_H (cm ⁻²)	2.32±0.02	2.40±0.05	2.70±0.13	3.75±0.45
kT (keV)	0.27 ±0.05	0.39±0.04	0.47±0.02	0.28±0.08
T_0 (keV)	1.27±0.07	1.08±0.08	1.33±0.17	0.75±0.11
kT (keV)	4.81±0.05	4.58±0.05	4.52±0.06	4.63±0.11
τ	4.94±0.05	4.89±0.13	4.81±0.07	4.56±0.15
E_{Fe} (keV)	6.52±0.07	6.45±0.02	6.61±0.07	6.56±0.50
σ_{Fe} (keV)	0.27±0.05	0.23±0.04	0.24±0.04	0.22±0.05
E_{gabs_1} (keV)	11.32±0.36	10.87±0.03	9.57±0.64	10.03±0.27
σ_{gabs_1} (keV)	2.01±0.15	1.57±0.21	3.54±0.50	3.68±0.12
τ_{gabs_1}	0.09±0.04	0.07±0.02	0.17±0.05	0.14±0.07
E_{gabs_2} (keV)	30.09±0.57	31.18±0.48
σ_{gabs_2} (keV)	2.10±0.55	4.04±0.25
τ_{gabs_2}	0.15±0.07	0.10±0.06
$flux$ (erg cm ⁻² s ⁻¹)	6.41 ^{+0.51} _{-0.54}	7.49 ^{+0.61} _{-0.67}	4.15 ^{+0.45} _{-0.70}	2.51 ^{0.51} _{-0.25}
χ^2_v	1.01	1.11	1.00	0.99

Table 5.3 Best fitted spectral parameters of 4U 1901+03 for four different cases using Model I and Model II. α and E_H are photon index and highcut energy of the CUTOFFPL model. E_{gabs} and E_{Fe} are energy of absorption and Fe lines respectively. τ_{gabs} is the optical depth. σ_{gabs} and σ_{Fe} are the widths of absorption and Fe line. The subscript $gabs_1$ and $gabs_2$ are for two GABS models. The column density (n_H) and flux are in the scale of 10^{22} cm²² cm⁻² and 10^{-9} erg cm⁻² s⁻¹ respectively. T_0 , kT and τ are the spectral parameters of the COMPTT model. Flux were calculated in 3-79 keV energy range. Errors quoted are within 90% confidence interval.

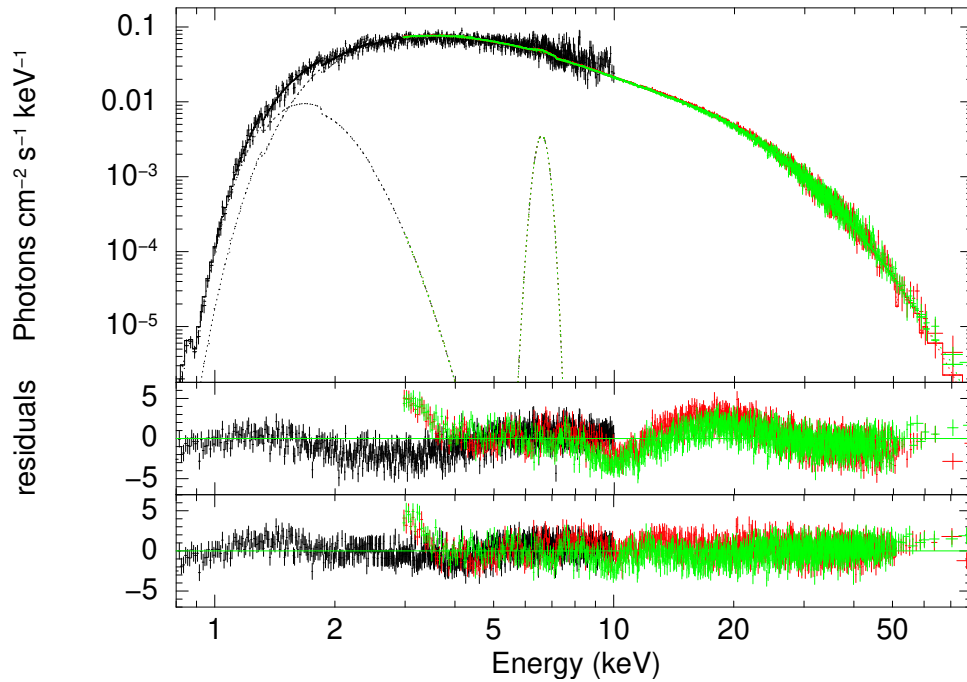


Fig. 5.6 Unfolded spectra of *NuSTAR* Obs1 and *Swift*-XRT observation fitted with Model I. The bottom and middle panels shows residuals after without and with the GABS model. Black indicates *Swift*-XRT spectra, red and green indicates *NuSTAR* FPMA & B spectra respectively.

and 1.52 for the first two cases respectively. However, after the addition of GABS model in the above we note that χ^2 values attained approximately 1.02 and 1.11 respectively.

During the *NuSTAR* Obs3 there was no *Swift* observations close to the *NuSTAR* observation timings, so we only fitted 3-79 keV FPMA & B spectra. The spectra were fitted well with Model I along with the GABS. As observed by Coley *et al.* (2019) we have found negative residuals near 30 keV indicating another absorption like feature and possibly a Cyclotron Resonant Scattering Feature (CSRF). Fitting this absorption like feature with GABS model Coley *et al.* (2019) found that the energy of the line to be at 31 keV with a width of 3.1 keV and optical depth about 1.1. So we have added another GABS model and searched for an absorption feature near 30 keV (see Fig. 5.7), the best fitted value of line energy was 30.37 keV. The width and the depth of the absorption lines are given by 1.79 keV and 0.11 respectively.

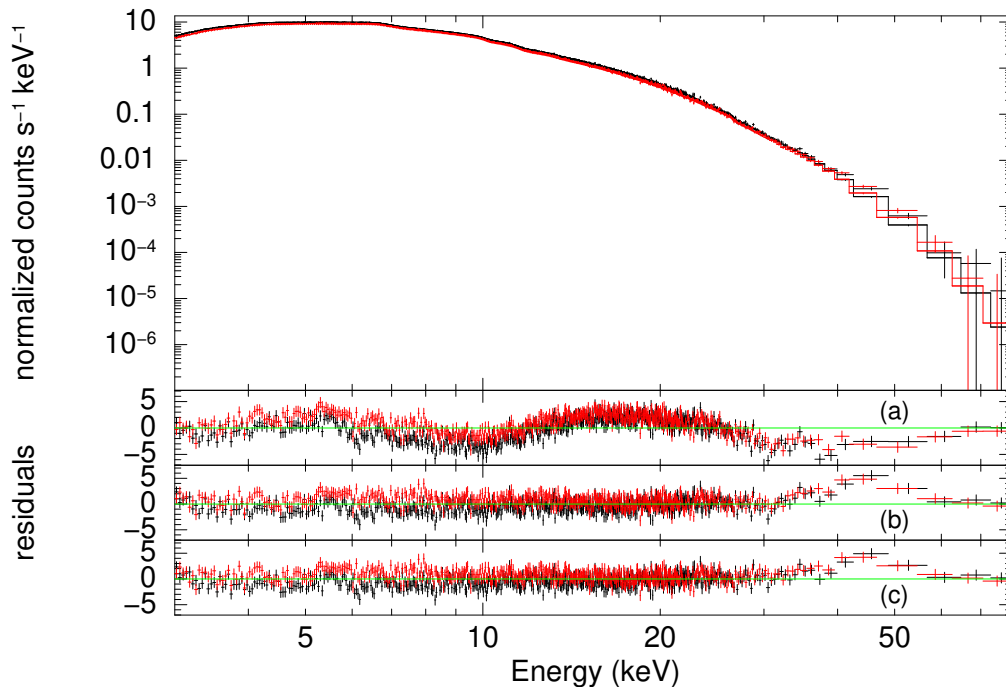


Fig. 5.7 Fitted spectra of *NuSTAR* Obs3 in 3-79 keV energy range. Panel (a) shows residuals for Model I where as panel (b) is residuals for Model I*GABS models and (c) shows residuals for Model I*GABS*GABS models.

The simultaneous fitting of *Swift*-XRT and *NuSTAR* Obs4 using Model I without GABS was not good as wave like feature has been observed with a large negative residuals near 10 keV. So we used two GABS models one for 10 keV and the other for 30 keV absorption like features, the spectra were fitted very well with the reduced $\chi^2 \sim 1.01$. However, the first absorption like feature was observed at 7.04 keV which is much below than what we have observed in the three previous cases. The second feature is observed at 30.23 keV with width and optical depth given by 1.04 keV and 0.07 respectively.

The spectra were also fitted well by Model II along with the GABS model. The column density is found to lie between $2.32\text{-}3.75 \times 10^{22} \text{ cm}^{-2}$ (Table 5.3). The input soft temperature (T_0) of COMPTT model varies between 0.75-1.33 keV. The plasma temperature (kT) and the plasma optical depth (τ) of the model are found to lie between 4.52-4.81 keV and 4.56-4.96 respectively. When the 10 keV feature was fitted with an absorption model the line energy was found at 11.32 keV, 10.87 keV, 9.57 keV and 10.03

keV for the four *NuSTAR* observations respectively. The width and the optical depth of this feature are in the range of 1.57-4.02 keV and 0.07-0.17 respectively. An absorption like feature around 30 keV was also observed in Obs3 and Obs4, so we used another GABS model here and observed that the line energies of the feature are 30.09 and 31.18 keV respectively.

From the spectral fitting by Model I we estimated the blackbody temperature to be about 0.20-0.31 keV. The iron emission line was estimated to lie between 6.52-6.61 keV. For all the four cases the flux were estimated in 3-79 keV energy range. The best fitted spectral parameters are shown in Table 5.3. The thermal component was also observed in the spectra fitted with Model II. The estimated flux were 6.45×10^{-9} , 7.52×10^{-9} , 5.01×10^{-9} and 2.56×10^{-9} erg cm⁻² s⁻¹ respectively. Thus the luminosity of the pulsar in 3-79 keV were $1.24 \times 10^{37} D_4^2$, $1.44 \times 10^{37} D_4^2$, $9.59 \times 10^{36} D_4^2$ and $4.89 \times 10^{36} D_4^2$ erg s⁻¹ for four all the four cases respectively. The 10 keV absorption like feature shows dependence on flux or luminosity and it increases or decreases with an increase or decrease in flux or luminosity, evident from Table 5.3, we noted that as flux decreases from 7.52×10^{-9} to 2.56×10^{-9} erg cm⁻² s⁻¹ the line energy of the feature decreases from 11.65 to 7.04 keV. Thus the line energy of the feature shows positive correlation with the source luminosity. The absorption feature near the 30 keV was only observed in the last two *NuSTAR* observations. This feature was also present in the spectra fitted with Model II. However when the spectra are fitted with Model II, the 10 keV feature does not show similar variation with the flux or the luminosity as seen in the case of spectral fitting with Model I but it shows positive correlation with either flux or luminosity. The observed flux and E_{Fe} were almost same in the two cases. We also fitted the spectra of the last two *NuSTAR* observations with the self-consistent Compton reflection models like PEXRAV, PEXRIV etc., however it is found that these models are not consistent with the observed spectra of the pulsar.

Fitting of Swift-BAT spectra

The 0.5-10 keV *Swift*-BAT spectra were fitted with PHABS and POWERLAW models. The power law model fits the spectra well and no additional models are required. As the pulsar slowly fades, the photon index increase or in other words with the decrease in flux the photon index increases (Fig. 5.9). Thus the spectra were softer near the end of the outburst. As the flux varies between $(0.13-39.60) \times 10^{-10}$ erg cm⁻¹ s⁻¹ the photon index varies between 1.03-2.1. The column density was observed to lie between $(3.20-4.31) \times 10^{22}$ cm⁻². The softening of the spectra of the pulsar at the end of an outburst was also observed by Reig and Milonaki (2016).

Phase Resolved Spectral Analysis

In order to understand the variation of spectral parameters with the pulse phase we have performed phase resolved spectral analysis of the *NuSTAR* observations. For phase resolved spectral analysis we have divided each pulse period into 10 equal segments (Fig. 5.8). For each segment a good time interval (*gti*) is created using XSELECT and then using this (*gti*) file FPMA & B spectra were produced. Each of the spectrum was fitted in 3-79 keV energy range with CONSTANT, PHABS, CUTOFFPL, GAUSSIAN and GABS models. Flux is then determined in 3-79 keV energy band. Spectral parameters are found to vary significantly with the phases. From the phase-resolved spectroscopy of Obs1 we observed that the photon index (α) and the highcut energy (E_H) shows anti-correlation with the flux. The flux varies between $(6.40-7.02) \times 10^{-9}$ erg cm⁻² s⁻¹ where as α and E_H varies between 0.19-0.366 and 6.08-6.64 keV respectively. The column density lies between $(0.80-1.54) \times 10^{22}$ cm⁻². The variation of the Fe emission line (E_{Fe}) follows complex pattern, its value decreases from 6.56 to 6.44 keV and then increases from 6.52 to 6.6 keV in between phase 0.2 to 0.6 and then decreases once again, however, an abrupt increase in its value is observed between 0.9-1.0. The absorption like feature (E_{gabs_1}) was also

observed which indicates anti-correlation with the flux that lies between 10.12-11.02 keV. However the width (σ_{gabs_1}) and optical depth (τ_{gabs_1}) of the line are found to have two peaks and also shows anti-correlation with the E_{gabs_1} and lies between 3.23-5.08 keV and 0.15-0.34 respectively.

From the phase-resolved spectral analysis of Obs2 (second column Fig. 5.8), the photon index and E_H show positive correlation with the flux. In this case the flux decreases in between 0.0-0.3 from 7.89×10^{-9} to 7.79×10^{-9} erg cm⁻² s⁻¹, but in between 0.4-0.8 the the flux increases reaching a maximum value 8.1×10^{-9} erg cm⁻² s⁻¹ at 0.7-0.8. The variation of the Fe line with the phase is found to be complex. The absorption feature E_{gabs_1} in between the phases 0.0-0.1 is 11.38 keV and it reaches a maximum value of 11.6 keV in between 0.1-0.2, thereafter it decreases reaching a minimum of 11.07 keV at 0.9-1.0. σ_{gabs_1} from 2.65 keV at 0.0-0.1 increases to attain a value of 3.12 keV after that it decreases to a minimum value of 2.06 keV in between phase 0.5-0.6, which thereafter increases followed by a decreasing behavior once again. The maximum value of σ_{gabs_1} is 3.50 keV and it was observed at 0.7-0.8. The optical depth (τ_{gabs_1}) decreases from 0.15 at 0.0-0.1 to 0.10 at 0.6-0.7 and then increases abruptly to 0.17, after which it decreases again. The column density varies between 1.14- 1.77×10^{22} cm⁻².

In Obs3 the variation of flux with phase is such that it exhibits two peaks one in between the phase 0.2-0.3 and the other in between 0.7-0.8. The photon index and E_H follows from the flux and it too has two peaks. The Fe line from 6.58 keV decreases to reach a minimum value 6.43 keV in the phase interval 0.2-0.3 and then it increases to climb a first peak value in the interval 0.5-0.6, after that it again decreases and then increases once again to reach a maximum value of 6.61 keV in the interval 0.9-1.0. From the Fig. 5.8 we can see that the variation in E_{gabs_1} is quite different from the two previous cases. The energy of the 10 keV feature E_{gabs_1} decrease from 9.87 keV in between 0.0-0.3 followed by an increase and thereafter a decrease. In the interval 0.4-0.6 the value E_{gabs_1} increases again followed by a

sharp decrease reaching 8.57 keV and after that it increases again. It is evident from the Fig. 5.8 the width of the line σ_{gabs_1} shows negative correlation with the E_{gabs_1} . The optical depth (τ_{gabs_1}) does not vary much in the phase interval 0.0-0.6. In this case the column density varies between $(0.38-1.72)\times 10^{22} \text{ cm}^{-2}$.

From the phase-resolved spectral analysis of the fourth *NuSTAR* observation we found that the flux lies between $(2.53-2.72)\times 10^{-9} \text{ erg cm}^{-2} \text{ s}^{-1}$. The minimum value of photon index 0.39 was observed at phase interval 0.4-0.5 and the maximum value of 1.04 was observed at 0.5-0.6. The cutoff energy (E_H) was within 5.94-7.09 keV energy range. The value of the column density (n_H) lies between $(1.54-3.63)\times 10^{22} \text{ cm}^{-1}$. The iron fluorescence line was lying between 6.45-6.64 keV with its width in 21-380 eV energy range. The 10 keV feature is found to vary between 5.84-8.79 keV. The width and the optical depth of the feature were lying between 1.97-5.59 keV and 0.68-0.99 respectively.

The absorption like feature at 30 keV in Obs3 is found to depend on the pulse phase (Fig. 5.10). The estimated line energy increases from 29.38 to 38.24 keV between the phase interval 0.0-0.4 which decreases to 33.38 keV, after that it increases once again to 33.88 keV and then decreases again to 30.33 keV. In the phase interval 0.7-1.0 the line energy increases as follows 29.89-36.21 keV. The width σ_{gabs_2} and optical depth τ_{gabs_2} of the feature are found to vary with the pulse phase and found to lie between 2.17-7.16 keV and 0.2-0.7 respectively. For the Obs4, the 30 keV feature was found to vary between 27.6-33.51 keV with its width lying between 3.29-6.41 keV and depth varying between 0.17-0.42 (Fig. 5.10).

The phase resolved spectra of Obs1 and Obs2 is fitted with additional GABS model in order to look for the presence of 30 keV absorption like feature. For Obs1 the line energy and the width of the feature were found to vary between 31.24-38.76 keV and 0.75-6.15 keV respectively and it is noted that the feature is not visible in the phase intervals 0.7-0.8 and 0.8-0.9. In the case of Obs2, the energy of the feature lies between 28.90-35.48 keV

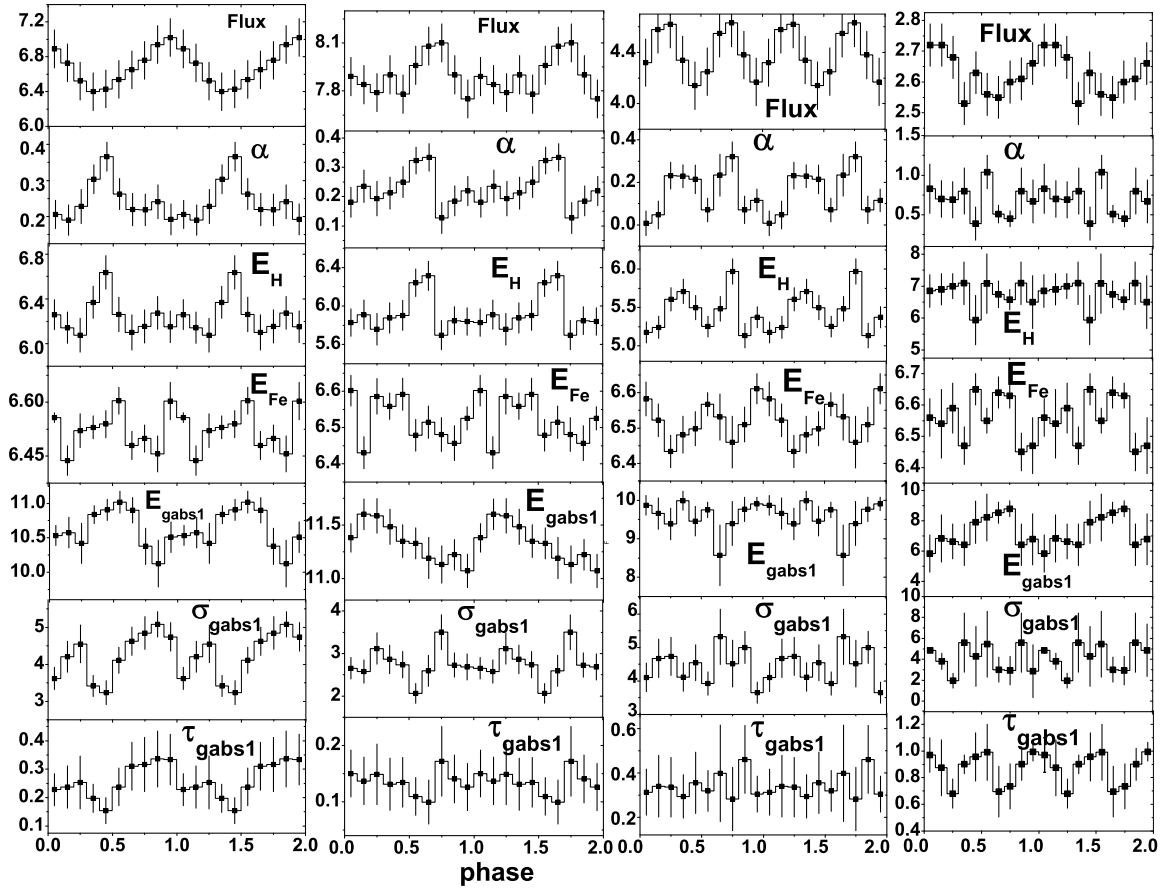


Fig. 5.8 Variation of Spectral parameters with pulse phases for four *NuSTAR* observations. Figures in first, second and third columns are for Obs1, Obs2, Obs3 and Obs4 respectively. α and E_H are photon index and highcut of CUTOFFPL model. E_{Fe} is the energy of Fe line. E_{gabs1} , σ_{gabs1} and τ_{gabs1} are the line energy, width and optical depth of GABS model used for fitting 10 keV feature.

with width between 0.77-6.06 keV. However for phase intervals 0.5-0.6 and 0.8-0.9 of Obs2 as the value of σ_{gabs2} and τ_{gabs2} are unrealistic so we did not consider them here for analysis.

5.4 Discussion

We present the Be X-ray pulsar 4U 1901+03 analysis, which was undergone short bursts of tens to hundreds of seconds. The burst of the X-ray pulsar can be due to instability

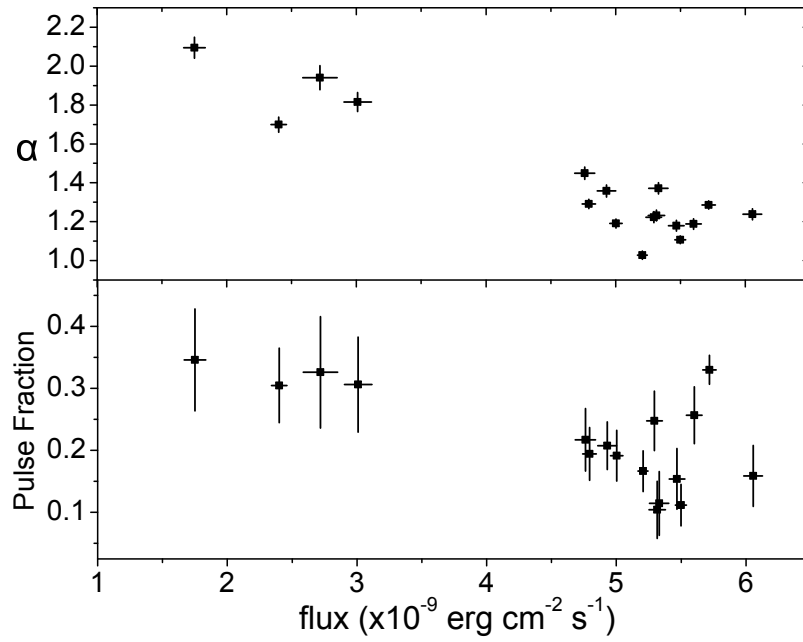


Fig. 5.9 Variation of photon index and pulse fraction with *Swift*-XRT flux in 0.5-10 keV energy range.

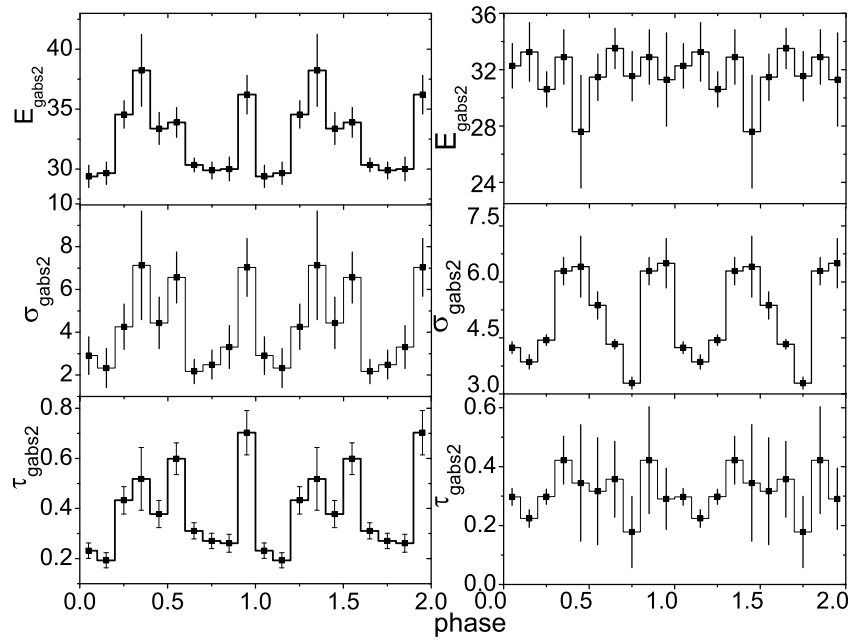


Fig. 5.10 Variation of 30 KeV absorption feature with phase for Obs3 (first column) and Obs4 (second column). E_{gabs2} , σ_{gabs2} and τ_{gabs2} are the line energy, width and the optical depth of the feature.

in accretion disk burst (Taam *et al.* (1988); Lasota and Pelat (1991); Cannizzo (1996)) similar to the burst observed in other sources namely, SMC X-1, GRO J1744-28 and MXB 1730-355 (Moon *et al.* (2003); Rai *et al.* (2018); Briggs *et al.* (1996); Lewin *et al.* (1976)). Pulse profiles shows variation with both the time and the flux, which are similar to that observed by Lei *et al.* (2009), Reig and Milonaki (2016) and Ji *et al.* (2020). The bursts in this case are different from the thermonuclear burst which is characterized by sharp rise and exponential decay. From the *NuSTAR* observations we found that the pulse profile having a single peak evolved into double peak with one main peak and once again become single peaked (Fig 5.3). Similar variations have been observed in *Swift*-XRT pulse profiles (Fig. 5.4). The height of the pulse profile peak increases with the increase in energy. Also the double peaked pulse profile in Obs2 evolved into single peak at the hard energy range. The pulse fraction is found to increase with the increase in energy at the end of the outburst. As the X-ray emitting region shrinks with the increase in energy, it emits more pulses as a result the pulse fraction increases (Alexander and Sergey, 2008). The variation of the pulse profiles may be due to a change in the accretion regimes. The different accretion regimes are set by the critical luminosity (Basko and Sunyaev, 1976; Becker *et al.*, 2012; Mushtukov *et al.*, 2015). The critical luminosity (L_{crit}) is defined as the luminosity above which the radiation pressure is strong enough to stop the accreting matter at a certain distance above the neutron star. The super-critical regime is reached when the luminosity of the pulsar (L_X) is greater than L_{crit} . In this case radiation dominated shock wave is formed which moves up to few kilometers above the neutron star. However for sub-critical regime $L_X < L_{crit}$, accreting material are capable of reaching onto the surface of the neutron star with heating it. In the case of the super-critical regime, X-ray photons escape from the side surface of the accretion column perpendicular to the magnetic field lines thus forming fan shaped beam but for sub-critical regime the emission is parallel to the magnetic field which comes out as a pencil beam pattern consisting of pulsed component

with simple pulse profile. The pulse profile associated with the fan shaped beam pattern is however complex in shape and in some cases it may be a mixture of fan and pencil shape beam as predicted. The abrupt change in the correlation of the photon index with the flux also indicates a transition from super-critical regime to sub-critical regime (Reig and Nespoli, 2013).

From the *NuSTAR* observations we observed that the pulse profile (Fig. 5.3) is sinusoidal in shape at a luminosity of $1.22 \times 10^{37} D_4^2$, which evolved into double-peak pulse profile with one main peak at $1.43 \times 10^{37} D_4^2 \text{ erg s}^{-1}$. The second peak of the pulse profile however disappear and becomes a single-peak with a notch near ~ 0.5 when the luminosity of the pulsar becomes $9.59 \times 10^{36} D_4^2 \text{ erg s}^{-1}$. With the further decrease in luminosity the notch disappears and pulse profile become single peak again which is found at $2.44 \times 10^{36} D_4^2 \text{ erg s}^{-1}$. Similar variations are observed in *Swift*-XRT pulse profiles (Fig. 5.4).

Thus 4U 1901+03 shows luminosity dependent pulse profile having a double peak at high luminosity and single peak at low luminosity. The complex variation of pulse profiles can be due to change in emission beam pattern with luminosity, which may be a mixture of fan and pencil beam pattern (Chen *et al.*, 2008; Ji *et al.*, 2020; Reig and Milonaki, 2016). The mixed contribution of the fan and pencil beam suggest that the source was not in pure super-critical regime during the recent outburst and most of the time it was in the sub-critical regime (Chen *et al.*, 2008; Reig and Milonaki, 2016). In the analysis carried out here no abrupt change in the correlation between the flux and photon index is seen supporting the fact that the source was in the sub-critical regime of accretion.

The 10 keV absorption like feature of the source was observed in all the four *NuSTAR* observations and it increases significantly with the increase in luminosity. Also the width and optical depth of the feature varies for different observations. The energy, width and the optical depth of the feature are found to lie within the range observed by Reig and Milonaki (2016). It was observed that accreting pulsars show positive correlation of the

cyclotron line energy with the luminosity in the sub-critical regime and negative correlation in the super-critical regime (Becker *et al.*, 2012; Mushtukov *et al.*, 2015). If the pulsar was in sub-critical regime most of the time during the outburst as discussed above then the observed positive correlation of the 10 keV feature indicates a cyclotron line. In addition to that the strong dependence of this feature on the viewing angle *i.e.* on the pulse phase like cyclotron line which also shows strong dependence on the pulse phase (Heindl *et al.*, 2004; Isenberg *et al.*, 1998; Reig and Milonaki, 2016), which pointed that this feature is due to a cyclotron line. The width and optical depth of the 10 keV features are within the range given by Coburn *et al.* (2002) for other pulsars. The 10 keV feature are observed in pulsars having CRSF or not at all but it is found to depend on the pulse phase (Coburn *et al.*, 2002). Considering the canonical value of neutron star parameters, the theoretical calculated value of critical luminosity by Becker *et al.* (2012) satisfy $L_{crit} \sim 1.49 \times 10^{37} B_{12}^{16/15}$, thus for this feature to be CRSF it is accepted that the critical luminosity must be $\sim 10^{37} \text{ erg s}^{-1}$. Assuming the distance of the source to be 3 kpc Bailer-Jones *et al.* (2018), the estimated observed luminosity is found to lie between $2.69\text{-}8.04 \times 10^{36} \text{ erg s}^{-1}$ which is however below the critical luminosity. Reig and Milonaki (2016) noted that for the $\frac{L_{peak}}{L_{crit}} \sim 1$, the distance should not be larger than ~ 4 kpc. Thus for the estimated luminosity less than the critical luminosity the distance of the source must be less than 4 kpc. However Strader *et al.* (2019) noted that the distance of the object measured by the Bailer-Jones *et al.* (2018) was not well constraint because of the parallax of the star in Gaia DR2 which was insignificant and considering PS1 reddening maps along the direction of the source (Green *et al.*, 2018) concluded that the distance must be greater than 12 kpc. Recently Tuo *et al.* (2020) with the help of torque model and evolution of pulse profile during outburst the estimated distance of the source is found to be 12.4 kpc. Assuming the distance of the source as 12.4 kpc the observed luminosity can be calculated and which lies between $(4.59\text{-}13.74) \times 10^{37} \text{ erg s}^{-1}$. The measured value is close to or above the critical luminosity and it raises a doubt about

this feature being CRSF. Mushtukov *et al.* (2015) showed that the critical luminosity is not a monotonic function of magnetic field and for the pulsars having cyclotron energy about 10 keV the critical luminosity can reach a minimum value of few 10^{36} erg s^{-1} . If this is the case then even if the source be at a distance of 3 kpc the observed luminosity will be equal or greater than the critical luminosity. In *NuSTAR* spectra weak residuals are observed around 10 keV due to tungsten L-edge of the *NuSTAR* optics (Fürst *et al.*, 2013; Madsen *et al.*, 2015). The 10 keV features were present in the spectra of various X-ray pulsars obtained using different instruments of different satellites (Coburn *et al.*, 2002) like in the case of 4U 1901+03 where this feature has been observed by RXTE (Reig and Milonaki, 2016) and *Insight-HMXT* (Nabizadeh *et al.*, 2020), thus it cleared a doubt about the instrumental origin of the feature. We have also seen that the feature is present even if we used another continuum model COMPTT instead of CUTOFFPL. Nabizadeh *et al.* (2020) showed that when *NuSTAR* Obs3 spectra were fitted by two-components model consisting of two POWERLAW*HIGHECUT along with GAUSSIAN and PHABS models no residuals were left near 10 keV and also no additional absorption model around 10 keV found when this two component model was used to fit *Insight-HMXT* spectra. However the authors also argued that the transition from the typical cutoff power-law spectral shape to two-component spectral shape occurs at low luminosities about $10^{(34-36)}$ erg s^{-1} , which indicates that the source distance must be small. Thus without proper estimation of the distance it is not sure about the feature to be CSRF. It is equally possible that this feature be inherent feature of the accreting X-rays pulsars or due to departure of the phenomenological models used in fitting the spectra Coburn *et al.* (2002).

As observed by Nabizadeh *et al.* (2020) and Coley *et al.* (2019) when Obs3 and Obs4+*Swift* spectra were fitted some negative residuals were observed near 30 keV, fitting the spectra with additional absorption model we have estimated the line energy that lies at 30.37 and 30.23 keV for these observations respectively and these are consistent with

the values estimated by Nabizadeh *et al.* (2020) and Coley *et al.* (2019). However no negative residuals near 30 keV were observed in the first two *NuSTAR* spectra which were having higher flux compared to the last two observations. In Obs3 and Obs4 the line energy of 30 keV feature showed pulse phase variation. Despite the fact that this feature was not observed in the phase-averaged spectra of Obs1 and Obs2 it was observed in the phase-resolved spectra of these observations. However in Obs1 and Obs2 this feature was not observable in some phases. Beri *et al.* (2021) confirmed existence of this feature to be due to cyclotron line by studying the variation of the line energy with the luminosity and the pulse phase. They observed an abrupt change in the pulse profiles around the line energy of the feature. In X-ray pulsars with high mass accretion rate the accretion columns will appear to be confined by the strong magnetic field of the neutron star and supported by the internal radiation pressure. Thus observed cyclotron line can be originated from the accretion column (Schönherr *et al.*, 2014) or due to the X-rays reflected from the neutron star atmosphere (Poutanen *et al.*, 2013). The absence of the cyclotron line in some observed energy spectra of the XRBs can possibly due to large gradient of B-field strength over the visible column height or the latitude on the surface of the neutron star. The appearance of the cyclotron line in certain pulse phases can be due to the partial eclipsing of the accretion column during which an observer is not able to see some parts of the column (Molkov *et al.*, 2019). In such case the magnetic field in the visible part of the accretion column is not so varied and one can observe cyclotron line in these phases like in the case of GRO J2058+42 (Molkov *et al.*, 2019). The appearance of cyclotron line only in some specific phases can be due to the gravitational bending of light too, as it affects the visibility of both the accretion columns and neutron star (see eg. Mushtukov *et al.* (2018)).

When the magnetospheric radius r_m becomes greater than the co-rotational radius r_{co} then the centrifugal force will prevent the material from further falling onto the neutron star, this is known as *Propeller Effect* (Illarionov and Sunyaev, 1975; Stella *et al.*, 1986)).

As the propeller effect sets in there will be an abrupt decrease in the flux leading to an absence of pulsation and even cause non-detection of source. Here the co-rotational radius is defined as the radius where the Keplerian angular velocity is equal to the spin angular velocity of the neutron star. The magnetospheric radius depends on the mass accretion rate, during the bright phase of an outburst the magnetospheric radius is less than the co-rotational radius consequently matter can cross the magnetospheric region and reach the neutron star. As the mass accretion rate decreases the magnetospheric radius increase thereby it can reach a point when its radius equal to the co-rotational radius, the propeller phase sets in at this stage. From the NICER observations it was detected that there does not exist pulsation after 58665.09 MJD, and the flux abruptly decreases from 6.37×10^{-10} at 58637.08 MJD to 1.31×10^{-11} erg s⁻¹ at 58667.45 MJD which indicates that the pulsar entered into the propeller phase. The increase in pulse fraction and the softening of the spectrum at the end of the outburst also supports our argument (Reig and Milonaki, 2016; Tsygankov *et al.*, 2016; Zhang *et al.*, 1998). As the accretion of matter onto the neutron star ceases at $r_m = r_{co}$, the magnetic field in this case can be determined, which is given by $B = 4.8 \times 10^{10} P^{7/6} \left(\frac{flux}{10^{-9} \text{ ergs}^{-1}} \right)^{1/2} \times \left(\frac{d}{1 \text{ kpc}} \right) \left(\frac{M}{1.4 M_{\odot}} \right)^{1/3} \left(\frac{R}{10^6 \text{ cm}} \right)^{-5/2}$ G (Cui, 1997)), where *flux* represents the minimum bolometric X-ray when the pulsation was still detectable and *d* represents the distance to the source. Using *Swift*-XRT *flux* 6.37×10^{-10} erg cm⁻² s⁻¹ in 0.5-10.0 keV observed at 58637.08 MJD and it was the minimum flux estimated in *Swift*-XRT observations when the source was still pulsating, assuming the distance to the source to lie between 3-12.5 kpc, the estimated magnetic field of the neutron star lies $(0.38-1.56) \times 10^{12}$ G, making use of the canonical values of mass and radius. However, the estimated magnetic field is entangled with uncertainties because the bolometric correction of the flux was not done and the minimum flux measured in the observation was not exactly known.

Chapter 6

Conclusion and summary

6.1 Summary

In the thesis neutron stars compact objects mainly neutron stars are taken up to investigate its features from X-ray detection of the sources from different observatories. The binary systems formed between neutron star and its companion are the typical sources of X-rays. The companion of the neutron star may be a normal star or a white dwarfs. The sources we have taken here are different from one another in terms of their mass accretion process and the types of their companion. The X-ray emitting from these sources are the valuable tools in understanding the objects at the extreme conditions namely, high temperature, high magnetic field, more than nuclear density which cannot be attained in the terrestrial laboratory. In the thesis we consider the following source SMC X-1, Swift J1756.9-2508 and 4U 1901+03, the observed data taken from the RXTE, NuSTAR, Swift and NICER were used for the analysis.

The source SMC X-1 was bursting frequently which is observed as flares that are detected in the light curves of the source. The average interval between the two bursts is almost 800 s and the average number of bursts per hour is 4-5. The bursts observed in the source is of Type II, when an instability in the accretion column is observed. The bursts

were of short duration covering few tens of seconds however few of the burst were large having duration of more than a hundred of second. The flares covered 0.025 fraction of the total observational time of 225.5 ks. It is noted here that a total of 272 flares with mean FWHM of ~ 21 s can be observed. The variability of the light curves are independent of flares. The shape of the pulse profiles for different observations are unchanged with almost similar feature indicating that the accretion geometry were unchanged during those observations. No correlation of hardness ratio and r.m.s. variability of the light curves with the flares are seen. The flare fraction however exhibits positive correlation with the peak-to-peak ratio of the primary and that of the secondary peaks of the pulse profiles. There was no indication of the hardening or softening of the spectrum being caused by flares but possibly can be due to the absorption of X-rays by interstellar medium as it is supported by the change in hydrogen column density (n_H). The luminosity of the source is found to increases with the increase in the flaring rate. Taking the viscous time scale equal to that of the mean recurrence time of the flares, the viscosity parameter α is estimated which is nearly equal to 0.16.

The accreting millisecond X-ray pulsar Swift J1756.92508 undergone through a outburst in 2018 for almost ten days. It was observed by different X-ray observatories like Swift, NICER, NuSTAR, ASTROSAT and XMM-Newton. The source is studied using the Swift and the NUSTAR observations. The simultaneous fitted spectra of the Swift in 0.3-10 keV and NUSTAR in 3-79 keV indicate that the source was in the hard state with a high cut-off energy 74.58 keV. The pulse profile of the AMXP and its relation with energy are investigated. We performed phase and time-resolved spectroscopy of the source using NUSTAR observations. From the pulse phase resolved spectroscopy it is observed that a significant variation exists in the spectral parameters with the pulse phase. The orbital phase and the time-resolved spectra were fitted by cut-off power-law model. From the orbital phase resolved spectral analysis it is found that the column density and photon

index shows some anti-correlation with the flux. In the case of the time-resolved spectral analysis, we found that the spectral parameters show a bit positive correlation with one another and that with the flux also. We do not find presence of emission lines or Compton hump in the spectrum of the AMXP.

The X-ray source BeXB 4U 1901+03 went through a large outburst during 2019. Flares were observed in all the NuSTAR observations which were of tens to hundreds seconds in duration. Change in the pulse profiles are observed with time and the luminosity of the source. As the one moves from the soft to hard X-ray ranges the height of the peak of pulse is found to increase. The pulse fraction of the pulse profiles increases with the energy and that at the end of the outburst. The variation of the pulse profiles during different observations can be as a result of the change in the accretion regime. The absorption like feature at 10 keV were observed in the spectra of all the NuSTAR observations and show positive correlation with the luminosity. This feature is also pulse phase dependent. Another absorption like feature at 30 keV were observed in the last two NuSTAR observations. Fitting with the absorption models we found that the line energy of the feature were about 30.51 ± 0.42 and 30.41 ± 0.54 keV for that last two observations respectively. This feature is confirmed to be CRSF by Beri *et al.* (2021). The softening of the spectrum along with an increase in the pulse fraction is also observed near the end of the outburst. Also it is found that the pulsation of the source was absent after 58665.09 MJD which indicate that the source has entered into a propeller phase. This fact is also correlated with the abrupt change in the flux at the end of the outburst.

6.2 Future work

Study of burst storm from a magnetar SGR 1935+2154 - A magnetars is a neutron star having very high magnetic field - about an order of 10^{15} G. They frequently undergone through short bursts of duration $\sim 0.1-1$ s and intermediate bursts of \sim

1-40 s. During a short burst the luminosity can reach about $\sim 10^{39}$ - 10^{41} erg s⁻¹, whereas during intermediate burst the peak luminosity lies between $\sim 10^{41}$ - 10^{43} erg s⁻¹. It is known that some the magnetars show giant burst where the luminosity can reach $\sim 10^{43}$ - 10^{47} erg s⁻¹. These bursts are powered by the magnetic energy (for review see Turolla *et al.* (2015)). SGR 1935+2154 was discovered during burst in the year 2014 (Stamatikos *et al.*, 2015) with Swift-BAT. The magnetic nature of the source was confirmed later with the help of X-ray observations along with its spin period of $P = 3.25$ s (Israel *et al.*, 2016). The spin-down rate is $\dot{P} = 1.43 \times 10^{-11}$ s s⁻¹ from which the magnetic field is estimated to be 2.2×10^{14} G (Israel *et al.*, 2016). The magnetar again went through a burst storm with the emission of tens of burst in between 27-28 April (Fletcher and Team, 2020). In future the analysis will be extended to study the burst.

Observations of X-ray pulsars using ASTROSAT - ASTROSAT is India's first multi-wavelength observatory. It consist of Large Area X-ray Proportional Counters (LAXPC), Soft X-ray telescope (SXT), Cadmium Zinc Telluride Imager (CZTI), Ultra-Violet Imaging Telescope (UVIT) and Scanning Sky Monitor (SSM). LAXPC operates in 3-80 keV and has an excellent timing resolution is good for the timing analysis of pulsars. SXT (0.3-8.0 keV) has good spectral resolution and helpful in understanding the phenomena which occurs in soft energy range. The SMC X-1 was observed once in high state using ASTROSAT, it is important to work in future with the source. It is also interesting to look for other X-ray pulsars like LMC X-4, Cen X-3, Vela X-1 using the ASTROSAT data.

References

- Adams, W. S. (1915). The Spectrum of the Companion of Sirius. *Pub. Astron. Soc. Pac.*, 27:236.
- Adams, W. S. (1925). The Relativity Displacement of the Spectral Lines in the Companion of sirius. *Proc. Nat. Acad. Sci.*, 11:382.
- Alexander, L. and Sergey, T. (2008). X-ray pulsars through the eyes of INTEGRAL. preprint, arxiv:0808.2034v1.
- Alpar, M., Cheng, A., Ruderman, M., and Shaham, J. (1982). A new class of radio pulsars. *Nature*, 300:728.
- Altamirano, D., Casella, P., Patruno, A., Wijnands, R., and van der Klis, M. (2008). INTERMITTENT MILLISECOND X-RAY PULSATIONS FROM THE NEUTRON STAR X-RAY TRANSIENT SAX J1748.9-2021 IN THE GLOBULAR CLUSTER NGC 6440. *Astrophys. J.*, 674:L45.
- An, H., Archibald, R. F., Kaspi, R. H. V. M., Beloborodov, A. M., Archibald, A. M., Beardmore, A., Boggs, S. E., Christensen, F. E., Craig, W. W., Gehrels, N., Hailey, C. J., Harrison, F. A., Kennea, J., Kouveliotou, C., Stern, D., Younes, G., and Zhang, W. W. (2015). DEEP NuSTAR AND SWIFT MONITORING OBSERVATIONS OF THE MAGNETAR 1E 1841045. *Astrophys. J.*, 807:93.
- Anders, E. and Ebihara, M. (1982). Solar-system abundances of the elements. *Geochimica et Cosmochimica Acta*, 46:2363–2380.
- Angelini, L., Stella, L., and White, N. (1991). The Discovery of an X-Ray Burst and a Study of Aperiodic Variability from SMC X-1. *Astrophys. J.*, 371:332.
- Araya, R. A. and Harding, A. K. (1999). Cyclotron line Features from Near-critical Magnetic Fields: The Effect of Optical Depth and Plasma Geometry. *Astrophys. J.*, 517:334.
- Araya-G'ochez, R. A. and Harding, A. K. (2000). Cyclotron-Line Features from Near-critical Fields. II. On the Effect of Anisotropic Radiation Fields. *Astrophys. J.*, 544:1067–1080.
- Araya-Góchez, R. A. and Harding, A. K. (2000). Cyclotron-Line Features from Near-critical Fields, II, On the Effect of Anisotropic Radiation Fields. *Astrophys. J.*, 544:1067.
- Archibald, A. and Stairs, I. (2009). A millisecond pulsar in an x-ray binary system. *Science*, 324:1411.

- Arnaud, K. A. (1996). *Astronomical Data Analysis Software and Systems V*, eds. Jacoby G. and Barnes J., p17, ASP Conf. Series volume 101.
- Backer, D., Kulkarni, S., Heiles, C., Davis, M., and Goss, W. (1982). A millisecond pulsar. *Nature*, 300:615.
- Bailer-Jones, C. A. L., Rybizki, J., Fouesneau, M., Mantelet, G., and Andrae, R. (2018). Estimating Distance from Parallaxes. IV. Distances to 1.33 Billion Stars in Gaia Data Release 2. *Astrophys. J.*, 156:58.
- Barthelmy, S. D., Barbier, L. M., Cummings, J. R., Fenimore, E. E., Gehrels, N., Hullinger, D., Krimm, H. A., C. B. Markwardt, D. M. P., Parsons, A., Sato, G., Suzuki, M., Takahashi, T., Tashiro, M., and Tueller, J. (2005). The Burst Alert Telescope (BAT) on the SWIFT Midex Mission. *Space Science Review*, 120:143–164.
- Basko, M. M. and Sunyaev, R. A. (1976). The limiting luminosity of accreting neutron stars with magnetic fields. *Mon. Not. Roy. Astron. Soc.*, 175:395–417.
- Becker, P. A., Klochkov, D., Schönherr, G., Nishimura, O., Ferrigno, C., Caballero, I., Kretschmar, P., Wolff, M. T., Wilms, J., and Staubert, R. (2012). Spectral formation in accreting x-ray pulsars: bimodal variation of the cyclotron energy with luminosity. *Astron. Astrophys.*, 123:544.
- Becker, P. A. and Wolff, M. T. (2007). Thermal and bulk comptonization in accretion-powered x-ray pulsars. *Astrophys. J.*, 654:435–457.
- Bellm, E. C., Fürst, F., Pottschmidt, K., Tomsick, J. A., Boggs, S. E., Chakrabarty, D., Christensen, F. E., Craig, W. W., Hailey, C. J., Harrison, F. A., Stern, D., Walton, D. J., Wilms, J., and Zhang, W. W. (2014). CONFIRMATION OF A HIGH MAGNETIC FIELD IN GRO J100857. *Astrophys. J.*, 792:108.
- Beri, A., Girdhar, T., Iyer, N. K., and Maitra, C. (2021). Evolution of timing and spectral characteristics of 4U 1901+03 during its 2019 outburst using the Swift and NuSTAR observatories. *Mon. Not. Roy. Astron. Soc.*, 500:1350.
- Beri, A., Jain, C., Paul, B., and Raichur, H. (2014). Torque reversals and pulse profile of the pulsar 4U 1626-67. *Mon. Not. Roy. Astron. Soc.*, 439:1940–1947.
- Boldin, P. A., Tsygankov, S. S., and Lutovinov, A. A. (2013). On timing and spectral characteristics of the x-ray pulsar 4U 0115+63 : Evolution of the pulsation period and the cyclotron line energy. *Astron. Lett.*, 39:375–388.
- Bolton, C. T. (1972). Identification of Cygnus X-1 with HDE 226868. *Nature*, 235:271–273.
- Briggs, M. S., Harmon, B. A., van Paradijs, J., Kouveliotou, C., Fishman, G. J., Kommers, J., and Lewin, W. H. G. (1996). Gro j1744-28. IUA Circ. 6290, 2.
- Bult, P., Altamirano, D., Arzoumanian, Z., Chakrabarty, D., Gendreau, K. C., Guillot, S., Ho, W. C. G., Jaisawal, G. K., Lentine, S., Markwardt, C. B., Ngo, S. N., Pope, J. S., Ray, P. S., Saylor, M. R., and Strohmayer, T. E. (2018). On the 2018 Outburst of the Accreting Millisecond X-Ray Pulsar Swift J1756.9–2508 As Seen with NICER. *Astrophys. J.*, 864:14.

- Bult, P., Markwardt, C. B., Altamirano, D., Arzoumanian, Z., Chakrabarty, D., Gendreau, K. C., Guillot, S., Jaisawal, G. K., Ray, P. S., and Strohmayer, T. E. (2019). On the Curious Pulsation Properties of the Accreting Millisecond Pulsar IGR J17379–3747. *Astrophys. J.*, 887:70.
- Burnard, D. J., Arons, J., and Klein, R. I. (1991). Accretion powered pulsars - Continuum spectra and light curves of settling accretion mounds. *Astrophys. J.*, 367:575–592.
- Burrows, D. N., Hill, J. E., Nousek, J. A., Kennea, J. A., Wells, A., Osborne, J. P., Abbey, A. F., Beardmore, A., Mukerjee, K., Short, A. D. T., Chincarini, G., Campana, S., Citterio, O., Moretti, A., Pagani, C., Tagliaferri, G., Giommi, P., Capalbi, M., Tamburelli, F., Angelini, L., Cusumano, G., Braeuninger, H. W., Burkert, W., and Hartner, G. D. (2005). The Swift X-ray Telescope. *Space Science Review*, 120:165–195.
- Cameron, A. G. W. (1959). Neutron star models. *Astrophys. J.*, 130:884.
- Cannizzo, J. K. (1996). The Nature Of the Gaint Outbursts in the Bursting Pulsar GRO J1744-28. *Astrophys. J.*, 466:L31–L34.
- Casella, P., Altamirano, D., Patruno, A., Wijnands, R., and van der Klis, M. (2008). Discovery of Coherent Millisecond X-Ray Pulsations in Aquila X-1. *Astrophys. J.*, 674:L41.
- Cemeljic, M. and Bulik, T. (1998). The Influence of Reprocessing in the Column on the Light Curves of Accretion Powered Neutron Stars. *Acta Astronomica*, 48:65–75.
- Chen, W., Qu, J. L., Zhang, S., Zhang, F., and Zhang, G. B. (2008). A study on the pulse profiles of the hmx b 4u 1901+03. *Chin. Astron. Astrophys.*, 32:241.
- Coburn, W., Heindl, W. A., Rothschild, R. E., Gruber, D. E., Kreykenbohm, I., Wilms, J., Kretschmar, P., and Staubert, R. (2002). Magnetic Fields of Accreting X-ray Pulsars with the Rossi X-Ray Timing Explorer. *Astrophys. J.*, 580:394.
- Coley, J. B., Fuerst, F., Hemphill, P., Kretschmar, P., Pottschmidt, K., Jaisawal, G. K., Malacaria, C., Vasilopoulos, G., Wilms, J., and Wolff, M. (2019). Possible discovery of a cyclotron line in 4U 1901+03 with NuSTAR. *The Astronomers Telegram*, 12684:1.
- Cui, W. (1997). Evidence for "propeller" effects in x-ray pulsars gx 1+4 and gro j1744–28. *Astrophys. J.*, 482:L163.
- Davidson, K. and Ostriker, J. P. (1973). Neutron Star Accretion in a Stellar Wind : Model for a Pulsed X-ray source. *Astrophys. J.*, 179:585–598.
- Davison, P. J. N. (1977). Spin-up in SMC X-1. *Mon. Not. Roy. Astron. Soc.*, 179:15–20.
- Falanga, M., Kuiper, L., Poutanen, J., Bonning, E. W., Hermsen, W., Salvo, T. D., Goldoni, P., Goldwurm, A., Shaw, S. E., and Stella, L. (2005). INTEGRAL and RXTE observations of accreting millisecond pulsar IGR J00291+5934 in outburst. *Astron. Astrophys.*, 444:15–24.
- Farinelli, R., Ceccobello, C., Romano, P., and Titarchuk, L. (2012). Numerical solution of the radiative transfer equation: X-ray spectral formation from cylindrical accretion onto a magnetized neutron star. *Astron. Astrophys.*, 538:A 67.

- Farinelli, R., Ferrigno, C., Bozzo, E., and Becker, P. A. (2016). A new model for the X-ray continuum of the magnetized accreting pulsars. *Astron. Astrophys.*, 591:A29.
- Fletcher, C. and Team, F. G. (2020). Fermi gbm observation of a bright flare from magnetar sgr 1935+2154. *GRB Coordinates Network*, 27659:1.
- Forman, W., Jones, C., Cominsky, L., Julien, P., Murray, S., Peters, G., Tananbaum, H., and Giacconi, R. (1978). THE FOURTH UHURU CATALOG OF X-RAY SOURCES. *Astrophys. J. Supplement*, 38:357–412.
- Frank, J., King, A., and Raine, D. (1992). *Accretion Power in Astrophysics*.
- Fürst, F., Pottschmidt, K., Wilms, J., Tomsick, J. A., Bachetti, M., Boggs, S. E., Christensen, F. E., Craig, W. W., Grefenstette, W. W., Hailey, C. J., Harrison, F., Madsen, K. K., Miller, J. M., Stern, D., Walton, D. J., and Zhang, W. (2013). NuSTAR DISCOVERY OF A LUMINOSITY DEPENDENT CYCLOTRON LINE ENERGY IN VELA X-1. *Astrophys. J.*, 780:133.
- Galloway, D., Morgan, E. H., Krauss, M. I., Kaaret, P., and Chakrabarty, D. (2007). INTERMITTENT PULSATIONS IN AN ACCRETION-POWERED MILLISECOND PULSAR. *Astrophys. J.*, 654:L73.
- Galloway, D. K., Giles, A. B., Wu, K., and Greenhill, J. G. (2001). Accretion column eclipses in the X-ray pulsars GX 1+4 and RX J0812.4-3114. *Mon. Not. Roy. Astron. Soc.*, 325:419–425.
- Galloway, D. K., Wang, Z., and Morgan, E. H. (2005). Discovery of pulsations in the X-ray transient 4U 1901+03. *Astrophys. J.*, 635:1217–1223.
- Gehrels, N., Chincarini, G., Giommi, P., Mason, K. O., Nousek, J. A., Wells, A. A., White, N. E., Barthelmy, S. D., Burrows, D. N., Cominsky, L. R., Hurley, K. C., Marshall, F. E., Mészáros, P., Roming, P. W. A., Angelini, L., Barbier, L. M., Belloni, T., Campana, S., Caraveo, P. A., Chester, M. M., Citterio, O., Cline, T. L., Cropper, M. S., Cummings, J. R., Dean, A. J., Feigelson, E. D., Fenimore, E. E., Frail, D. A., Fruchter, A. S., Garmire, G. P., Gendreau, K., Ghisellini, G., Greiner, J., Hill, J. E., Hunsberger, S. D., Krimm, H. A., Kulkarni, S. R., Kumar, P., Lebrun, F., Lloyd-Ronning, N. M., Markwardt, C. B., Mattson, B. J., Mushotzky, R. F., Norris, J. P., Osborne, J., Paczynski, B., Palmer, D. M., Park, H.-S., Parsons, A. M., Paul, J., Rees, M. J., Reynolds, C. S., Rhoads, J. E., Sasseen, T. P., Schaefer, B. E., Short, A. T., Smale, A. P., Smith, I. A., Stella, L., Tagliaferri, G., Takahashi, T., Tashiro, M., Townsley, L. K., Tueller, J., Turner, M. J. L., Vietri, M., Voges, W., Ward, M. J., Willingale, R., Zerbi, F. M., and Zhang, W. W. (2004). THE SWIFT GAMMA-RAY BURST MISSION. *Astrophys. J.*, 611:1005–1020.
- Ghosh, P. (2006). *Rotation and Accretion Powered Pulsars*.
- Ghosh, P. and Lamb, F. K. (1979). Accretion by rotating magnetic neutron stars. III. accretion torques and period changes in pulsating X-ray sources. *Astrophys. J.*, 234:296–316.
- Giacconi, R., Gursky, H., Paolini, F. R., and Rossi, B. B. (1962). Evidence for x Rays From Sources Outside the Solar System. *Physical Review Letters*, 9:439–443.

- Giacconi, R., Kellogg, E., Gorenstein, P., Gursky, H., and Tananbaum, H. (1971). X-Ray Scan of the Galactic Plane from UHURU. *Astrophys. J.*, 165:L27.
- Giles, A. B., Galloway, D. K., Greenhill, J. G., Storey, M. C., and Wilson, C. A. (2000). Pulse Profiles, Accretion Column Dips, and a Flare in GX 1+4 During a Faint State. *Astrophys. J.*, 529:447–452.
- Gnedin, I. N. and Sunyaev, R. A. (1974). Polarization of optical and x-radiation from compact thermal sources with magnetic field. *Astron. Astrophys.*, 36:379.
- Gold, T. (1968). Rotating Neutron Stars as the Origin of the Pulsating Radio Sources. *Nature*, 218:731.
- Gonzalez, M. E., Dib, R., Kaspi, V. M., Woods, P. M., Tam, C. R., and Gavrii, F. P. (2010). LONG-TERM X-RAY CHANGES IN THE EMISSION FROM THE ANOMALOUS X-RAY PULSAR 4U 0142+61. *Astrophys. J.*, 716:1345.
- Green, G. M., Schlafly, E. F., Finkbeiner, D., Rix, H.-W., Martin, N., Burgett, W., Draper, P. W., Flewelling, H., Hodapp, K., Kaiser, N., Kudritzki, R., Magnier, E. A., Metcalfe, A., Tonry, J. L., Wainscoat, R., and Waters, C. (2018). Galactic reddening in 3D from stellar photometry - an improved map. *Mon. Not. Roy. Astron. Soc.*, 478:651.
- Gursky, H., Giacconi, R., Paolini, F. R., and Rossi, B. B. (1963). Further Evidence for the Existence of Galactic x Rays. *Physical Review Letters*, 11:530–535.
- Harrison, F. A., Craig, W. W., Christensen, F., Hailey, C., Zhang, W., Boggs, S., Stern, D., Cook, W., Forster, K., Giommi, P., Grefenstette, B., Kim, Y., Kitaguchi, T., Koglin, J., Madsen, K., Mao, P., Miyasaka, H., Mori, K., Perri, M., Pivovarov, M., Puccetti, S., Rana, V., Westergaard, N., Willis, J., Zoglauer, A., An, H., Bachetti, M., Barrière, N., Bellm, E., Bhalerao, V., Brejnholt, N., Fuerst, F., Liebe, C., Markwardt, C., Nynka, M., Vogel, J., Walton, D., Wik, D., Alexander, D., Cominsky, L., Hornschemeier, A., Hornstrup, A., Kaspi, V., Madejski, G., Matt, G., Molendi, S., Smith, D., Tomsick, J., Ajello, M., Ballantyne, D., Baloković, M., Barret, D., Bauer, F., Blandford, R., Brandt, W., Brenneman, L., Chiang, J., Chakrabarty, D., Chenevez, J., Comastri, A., Dufour, F., Elvis, M., Fabian, A., Farrah, D., Fryer, C., Gotthelf, E., Grindlay, J., Helfand, D., Krivonos, R., Meier, D., Miller, J., Natalucci, L., Ogle, P., Ofek, E., Ptak, A., Reynolds, S., Rigby, J., Tagliaferri, G., Thorsett, S., Treister, E., and Urry, C. (2013). The Nuclear Spectroscopic Telescope Array (NuSTAR) High-energy X-Ray Mission. *Astrophys. J.*, 770:103.
- Heindl, W. A., Rothschild, R. E., Coburn, W., Staubert, R., Wilms, J., Kreykenbohm, I., and Kretschmar, P. (2004). Timing and Spectroscopy of Accreting X-ray Pulsars: the State of Cyclotron Line Studies. *AIP Conf. Proc.*, 714:323. *X-ray Timing 2003 : Rossi and Beyond*, edited by P. Kaaret, F. K. Lamb and J. H. Swank.
- Hewish, A., Bell, S. J., Pilkington, J. D. H., Scott, P. F., and Collins, R. A. (1968). Observation of a Rapidly Pulsating Radio Source. *Nature*, 218:709.
- Illarionov, A. F. and Sunyaev, R. A. (1975). Why the Number of Galactic X-ray Stars is so Small? *Astron. Astrophys.*, 39:185.

- Isenberg, M., Lamb, D. Q., and Wang, J. C. L. (1998). EFFECTS OF THE GEOMETRY OF THE LINE-FORMING REGION ON THE PROPERTIES OF CYCLOTRON RESONANT SCATTERING LINES. *Astrophys. J.*, 505:688.
- Israel, G. L., Esposito, P., Rea, N., Zelati, F. C., Tiengo, A., Campana, S., Mereghetti, S., Castillo, G. A. R., G'otz, D., Burgay, M., Possenti, A., Zane, S., Turolla, R., Perna, R., Cannizzaro, G., and Pons, J. (2016). The discovery, monitoring and environment of SGR J1935+2154. *Mon. Not. Roy. Astron. Soc.*, 457:3448–3456.
- Jahoda, K., Swank, J. H., Giles, A. B., Stark, M. J., Strohmayer, T., Zhang, W., and Morgan, E. H. (1996). In-orbit performance and calibration of the Rossi X-ray Timing Explorer (RXTE) Proportional Counter Array (PCA). *Society of Photo-Optical Instrumentation Engineers (SPIE) Conference Series*, 2808:59–70.
- Jaisawal, G. K. (2016). Timing and Spectral Studies of Accretion Powered X-ray Pulsars. PhD thesis, MOHANLAL SUKHADIA UNIVERSITY.
- James, M., Paul, B., Devasia, J., and Indulekha, K. (2011). Flares, broadening of the pulse-frequency peak and quasi-periodic oscillations in the transient x-ray pulsar 4U 1901+03. *Mon. Not. Roy. Astron. Soc.*, 410:1489–1495.
- Ji, L., Ducci, L., Santangelo, A., Zhang, S., Suleimanov, V., Tsygankov, S., Doroshenko, V., Nabizadeh, A., Zhang, S. N., Ge, M. Y., Tao, L., Bu, Q. C., Qu, J. L., Lu, F. J., Chen, L., Song, L. M., Li, T. P., Xu, Y. P., Cao, X. L., Chen, Y., Liu, C. Z., Cai, C., Chang, Z., Chen, G., Chen, T. X., Chen, Y. B., Chen, Y. P., Cui, W., Cui, W. W., Deng, J. K., Dong, Y. W., Du, Y. Y., Fu, M. X., Gao, G. H., Gao, H., Gao, M., Gu, Y. D., Guan, J., Guo, C. C., Han, D. W., Huang, Y., Huo, J., Jia, S. M., Jiang, L. H., Jiang, W. C., Jin, J., Jin, Y. J., Kong, L. D., Li, B., Li, C. K., Li, G., Li, M. S., Li, W., Li, X., Li, X. B., Li, X. F., Li, Y. G., Li, Z. W., Liang, X. H., Liao, J. Y., Liu, B. S., Liu, G. Q., Liu, H. X., Liu, H. W., Liu, X. J., Liu, Y. N., Lu, B., Lu, X. F., Luo, Q., Luo, T., Ma, X., Meng, B., Nang, Y., Nie, J. Y., Ou, G., Sai, N., Shang, R. C., Song, X. Y., Sun, L., Tan, Y., Tuo, Y. L., Wang, C., Wang, G. F., Wang, J., Wang, P. J., Wang, W. S., and X. Y. Wen, Y. S. W., Wu, B. Y., Wu, B. B., Wu, M., Xiao, G. C., Xiao, S., Xiong, S. L., X., H., Yang, J. W., Yang, S., Yang, Y.-J., Yang, Y.-J., Yi, Q. B., Yin, Q. Q., You, Y., Zhang, A. M., Zhang, C. M., Zhang, F., Zhang, H. M., Zhang, J., Zhang, P., Zhang, T., Zhang, W., Zhang, W. C., Zhang, W. Z., Zhang, Y., Zhang, Y. F., Zhang, Y. J., Zhang, Y. H., Zhang, Y., Zhang, Z., Zhang, Z., Zhang, Z. L., Zhao, H. S., Zhao, X. F., Zheng, S. J., Zhou, D. K., Zhou, J. F., Zhu, Y. X., Zhu, Y., and Zhuang, R. L. (2020). Switches between accretion structures during flares in 4U 1901+03. *Mon. Not. Roy. Astron. Soc.*, 493:5680–5692.
- Keller, S. C. and Wood, P. R. (2006). BUMP CEPHEIDS IN THE MAGELLANIC CLOUDS: METALLICITIES, THE DISTANCES TO THE LMC AND SMC, AND THE PULSATION-EVOLUTION MASS DISCREPANCY. *Astrophys. J.*, 642:834.
- Kennea, J. A., Krimm, H. A., Page, K. L., and Tohuvavohu, A. (2019). Swift detection of 4U 1901+03. *GRB Coordinates Network*, 23882:1.
- Kepler, S. O., Kleinman, S. J., Nitta, A., Koester, D., Castanheira, B. G., Giovannini, O., Costa, A. F. M., and Althaus, L. (2007). White dwarf mass distribution in the SDSS. *Mon. Not. R. Astron. Soc.*, 375:1315.

- Kilic, M., Prieto, C. A., Brown, W. R., and Koester, D. (2007). The lowest mass white dwarf. *Astrophys. J.*, 660:1451.
- Krimm, H. A., Barthelmy, S. D., Barbier, L., Cummings, J. R., Fenimore, E., Gehrels, N., Markwardt, C., Palmer, D., Parsons, A., Sakamoto, T., Sato, G., Stamatikos, M., and Tueller, J. (2007a). SwiftBAT discovers a new galactic transient: SWIFT J1756.9-2508. *The Astronomers Telegram*, 1105:1.
- Krimm, H. A., Markwardt, C., Deloye, C. J., Romano, P., Chakrabarty, D., Cummings, J. R., Galloway, D. K., Gehrels, N., Hartman, J. M., Kaaret, P., Morgan, E. H., and Tueller, J. (2007b). DISCOVERY OF THE ACCRETION-POWERED MILLISECOND PULSAR SWIFT J1756.9-2508 WITH A LOW-MASS COMPANION. *Astrophys. J.*, 668:L147–L150.
- Lasota, J. P. and Pelat, D. (1991). Variability of accretion discs around compact objects. *Astron. Astrophys.*, 249:574–580.
- Lei, Y.-J., Chen, W., Qu, J.-L., Song, L.-M., Zhang, S., Lu, Y., Zhang, H.-T., and Li, T.-P. (2009). PHASE-RESOLVED SPECTRAL ANALYSIS OF 4U 1901+03 DURING ITS OUTBURST. *Astrophys. J.*, 707:1016–1022.
- Levine, A., Rappaport, S., Deeter, J. E., Boynton, P. E., and Nagase, F. (1993). Discovery of orbital decay in SMC X-1. *Astrophys. J.*, 480:327.
- Levine, A. M., Bradt, H., Cui, W., Jernigan, J. G., Morgan, E. H., Remillard, R., Shirey, R. E., and Smith, D. A. (1996). First Results from the All-Sky Monitor on the Rossi X-Ray Timing Explorer. *Astrophys. J.*, 469:L33.
- Lewin, W. H. G., Doty, J., Clark, G. W., Rappaport, S. A., Bradt, H. V. D., Doxsey, R., Hearn, D. R., Hoffman, J. A., Jernigan, J. G., Li, F. K., Mayer, W., McClintock, J., Primini, F., and Richardson, J. (1976). The discovery of rapidly repetitive X-ray bursts. *Astrophys. J.*, 207:L95.
- Li, X. D. and van den Heuvel, E. P. J. (1997). On the nature of SMC X-1. *Astron. Astrophys.*, 321:L25.
- Linares, M., Wijnands, R., van der Klis, M., Krimm, H., Markwardt, C. B., and Chakrabarty, D. (2008). Timing and Spectral Properties of the Accreting Millisecond Pulsar SWIFT J1756.9–2508. *Astrophys. J.*, 677:515.
- Madsen, K. K., Harrison, F. A., Markwardt, C. B., An, H., Grefenstette, B. W., Bachetti, M., Miyasaka, H., Kitaguchi, T., Bhalerao, V., Boggs, S., Christensen, F. E., Craig, W. W., Forster, K., Fuerst, F., Hailey, C. J., Perri, M., Puccetti, S., Rana, V., Stern, D., Walton, D. J., Westergaard, N. J., and Zhang, W. W. (2015). CALIBRATION OF THE NuSTAR HIGH-ENERGY FOCUSING X-RAY TELESCOPE. *Astrophys. J. Supplement*, 220:8.
- Maitra, C. and Paul, B. (2011). Pulse-phase-resolved Spectroscopy of Vela X-1 with Suzuka. *Astrophys. J.*, 763:79.
- Markwardt, C. B., Krimm, H. A., and Swank, J. H. (2007). SWIFT J1756.9-2508 is a 182 Hz Millisecond X-ray Pulsar. *The Astronomers Telegram*, 1108:1.

- Mereminskiy, I. A., Grebenev, S. A., Krivonos, R. A., and Sunyaev, R. A. (2018). New X-ray outburst of accreting millisecond pulsar SWIFT J1756.9-2508 detected by INTEGRAL. *The Astronomers Telegram*, 11497:1.
- Meszaros, P., Harding, A. K., Kirk, J. G., and Galloway, D. J. (1983). Accreting X-ray pulsar atmospheres heated by Coulomb deceleration of protons. *Astrophys. J.*, 266:L33–L37.
- Meszaros, P. and Nagel, W. (1985). X-ray pulsar models, I - Angle-dependent cyclotron line formation and comptonization. *Astrophys. J.*, 298:147.
- Molkov, S., Lutovinov, A., Tsygankov, S., Mereminskiy, I., and Mushtukov, A. (2019). Discovery of a Pulse-phase-transient Cyclotron Line in the X-ray pulsar GRO J2058+42. *Astrophys. J.*, 883:L11.
- Moon, D.-S., Eikenberry, S. S., and Wasserman, I. M. (2003). SMC X-1 as an Intermediate-Stage Flaring X-Ray Pulsar. *Astrophys. J.*, 582:L91–L94.
- Mushtukov, A. A., Suleimanov, V. F., Tsygankov, S. S., and Poutanen, J. (2015). The critical accretion luminosity for magnetized neutron stars. *Mon. Not. Roy. Astron. Soc.*, 447:1847.
- Mushtukov, A. A., Verhagen, P. A., Tsygankov, S. S., van der Klis, M., Lutovinov, A. A., and Larchenkova, T. I. (2018). On the radiation beaming of bright x-ray pulsars and constraints on neutron star mass–radius relation. *Mon. Not. Roy. Astron. Soc.*, 474:5425.
- Nabizadeh, A., Tsygankov, S. S., Ji, L., Doroshenko, V., Molkov, S. V., Tuo, Y., Zhang, S.-N., Lu, F.-J., Zhang, S., and Poutanen, J. (2020). Spectral evolution of X-ray pulsar 4U 1901+03 during 2019 outburst based on insight-HXMT and NuSTAR observations. *arXiv preprint arXiv:2005.14555*.
- Nagel, W. (1981). Radiative transfer in a strongly magnetized plasma I - Effects of anisotropy. II - Effects of Comptonization. *Astrophys. J.*, 251:278–296.
- Naik, S., Paul, B., Kachhara, C., and Vadawale, S. V. (2011). Suzaku observation of the transient x-ray pulsar GRO J1008-57. *Mon. Not. Roy. Astron. Soc.*, 413:241–248.
- Nakajima, M., Negoro, H., Mihara, T., Serino, M., Sakamaki, A., Maruyama, W., Aoki, M., Kobayashi, K., Nakahira, S., Yatabe, F., Takao, Y., Matsuoka, M., Sakamoto, T., Sugita, S., Hashimoto, T., Yoshida, A., Kawai, N., Sugizaki, M., Tachibana, Y., Morita, K., Oeda, M., Shiraishi, K., Ueno, S., Tomida, H., Ishikawa, M., Sugawara, Y., Isobe, N., Shimomukai, R., Midooka, T., Ueda, Y., Tanimoto, A., Morita, T., Yamada, S., Ogawa, S., Tsuboi, Y., Iwakiri, W., Sasaki, R., Kawai, H., Sato, T., Tsunemi, H., Yoneyama, T., Asakura, K., Ide, S., Yamauchi, M., Hidaka, K., Iwahori, S., Kawamuro, T., Yamaoka, K., Shidatsu, M., and Kawakubo, Y. (2019). MAXI/GSC detection of the outburst from binary x-ray pulsar 4U 1901+03. *The Astronomers Telegram*, 12498:1.
- Özel, F. and Freire, P. (2016). Masses, Radii, and the Equation of State of Neutron Stars. *Annu. Rev. Astron. Astrophys.*, 54:401–440.
- Papitto, A. and Ferrigno, C. (2013). Swings between rotation and accretion power in a binary millisecond pulsar. *Nature*, 501:517.

- Papitto, A., Riggi, A., Salvo, T. D., Burderi, L., Dai, A., Iaria, R., Bozzo, E., and Menna, M. T. (2010). The X-ray spectrum of the newly discovered accreting millisecond pulsar IGR J175113057. *Mon. Not. Roy. Astron. Soc.*, 407:2575.
- Patruno, A., Altamirano, D., Hessels, J., Casella, P., Wijnands, R., and van der Klis, M. (2009a). PHASE-COHERENT TIMING OF THE ACCRETING MILLISECOND PULSAR SAX J1748.92021. *Astrophys. J.*, 690:1856.
- Patruno, A., Altamirano, D., and Messenger, C. (2010a). The long-term evolution of the accreting millisecond X-ray pulsar Swift j1756.92508. *Mon. Not. Roy. Astron. Soc.*, 403:1426–1432.
- Patruno, A., Hartman, J. M., Wijnands, R., Chakrabarty, D., and van der Klis, M. (2010b). ACCRETION TORQUES AND MOTION OF THE HOT SPOT ON THE ACCRETING MILLISECOND PULSAR XTE J1807–294. *Astrophys. J.*, 717:1253.
- Patruno, A., Markwardt, C. B., Strohmayer, T. E., Swank, J. H., Smith, S. E., and Pereira, D. (2009b). RXTE PCA and Swift-BAT detects the Millisecond Pulsar Swift J1756.9-2508 in Outburst. *The Astronomers Telegram*, 2130:1.
- Patruno, A. and Watts, A. L. (2013). Accreting Millisecond X-ray Pulsars. *arXiv preprint arXiv:1206.2727*.
- Paul, B., Nagase, F., Endo, T., Dotani, T., Yokogawa, J., and Nishiuchi, M. (2002). Nature of the Soft Spectral Component in the X-Ray Pulsars SMC X-1 and LMC X-4. *Astrophys. J.*, 579:411–421.
- Pike, S. N., Harrison, F. A., Bachetti, M., Brumback, M. C., Fürst, F. S., Madsen, K. K., Pottschmidt, K., Tomsick, J. A., and Wilms, J. (2019). Observing the Transient Pulsations of SMC X-1 with NuSTAR. *Astrophys. J.*, 875:144.
- Porter, J. M. and Rivinius, T. (2003). Classical be stars. *Pub. Astron. Soc. Pac.*, 115:1153–1170.
- Poutanen, J., Mushtukov, A. A., Suleimanov, V. F., Tsygankov, S. S., Nagirner, D. I., Doroshenko, V., and Lutovinov, A. A. (2013). A REFLECTION MODEL FOR THE CYCLOTRON LINES IN THE SPECTRA OF X-RAY PULSARS. *Astrophys. Astron.*, 777:115.
- Pradhan, P. (2016). Pulse profile studies and hard x-ray properties of neutron stars. PhD thesis, North Bengal Universtiy.
- Price, R. E., Groves, D. J., Rodrigues, R. M., and Seward, F. D. (1971). X-RAYS FROM THE MAGELLANIC CLOUDS. *Astrophys. J.*, 168:L7.
- Radhakrishnan, V. and Srinivasan, G. (1982). On the origin of the recently discovered ultra-rapid pulsar. *Current Science*, 51:1096.
- Rai, B., Pradhan, P., and Paul, B. C. (2018). A report on Type II X-ray bursts from SMC X-1. *Res. Astron. Astrophys.*, 18:148.

- Raichur, H. and Paul, B. (2010). Effect of pulse profile variation on the measurement of eccentricity in the orbits of Cen X-3 and SMC X-1. *Mon. Not. Roy. Astron. Soc.*, 401:1532–1539.
- Reig, P. (2011). Be/x-ray binaries. *Astrophys. Space Sci.*, 332:1–29.
- Reig, P. and Milonaki, F. (2016). Accretion regimes in the X-ray pulsar 4U 1901+03. *Astron. Astrophys.*, 594:A45.
- Reig, P. and Nespoli, E. (2013). Patterns of variability in be/x-ray pulsars during giant outbursts. *Astrophys. Astron.*, 551:A1.
- Reynolds, A. P., Hilditch, R. W., Bell, S. A., and Hill, G. (1993). Optical spectroscopy of the massive X-ray binary SMC X-1/Sk 160. *Mon. Not. Roy. Astron. Soc.*, 261:337.
- Rothschild, R. E., Blanco, P. R., Gruber, D. E., Heindl, W. A., MacDonald, D. R., Marsden, D. C., Pelling, M. R., Wayne, L. R., and Hink, P. L. (1998). In-Flight Performance of the High-Energy X-Ray Timing Experiment on the Rossi X-Ray Timing Explorer. *Astrophys. J.*, 496:538–549.
- Salvo, T. D. and Sanna, A. (2020). Accretion Powered X-ray Millisecond Pulsars. *arXiv preprint arXiv:2010.09005*.
- Sanna, A., Pintore, F., Riggio, A., Mazzola, S. M., Bozzo, E., Salvo, T. D., Ferrigno, C., Gambino, A. F., Papitto, A., Iaria, R., and Burderi, L. (2018). SWIFT J1756.92508: spectral and timing properties of its 2018 outburst. *Mon. Not. Roy. Astron. Soc.*, 481:1658–1666.
- Sazonov, S., Sunyaev, R., and Swank, J. (1996). *IAU Circ.*, 6291.
- Schmidt, G. D. (1989). Magnetic Fields in White Dwarfs. page 305. White Dwarfs. Proceedings of IAU Colloquium No. 114, held at Dartmouth College, Hanover, New Hampshire, USA, August 15-19, 1988. Editor, G. Wegner; Publisher, Springer-Verlag, Berlin; New York, 1989.
- Schönherr, G., Schwarm, F. W., Falkner, S., Dauser, T., Ferrigno, C., Köhnel, M., Klochkov, D., Kretschmar, P., Becker, P. A., Wolff, M. T., Pottschmidt, K., Falanga, M., Kreykenbohm, I., Fürst, F., Staubert, R., and Wilms, J. (2014). Formation of phase lags at the cyclotron energies in the pulse profiles of magnetized, accreting neutron stars. *Astron. Astrophys.*, 564:L8.
- Schönherr, G., Wilms, J., Kretschmar, P., Kreykenbohm, I., Santangelo, A., Rothschild, R. E., Coburn, W., and Staubert, R. (2007). A model for cyclotron resonance scattering features. *Astron. Astrophys.*, 472:353–365.
- Schreier, E., Giacconi, R., Gursky, H., Kellogg, E., and Tananbaum, H. (1972). DISCOVERY OF THE BINARY NATURE OF SMC X-1 FROM UHURU. *Mon. Not. Roy. Astron. Soc.*, 178:L71.

- Schwarm, F. W., Schönherr, G., Falkner, S., Pottschmidt, K., Wolff, M. T., Becker, P. A., Sokolova-Lapa, E., Klochkov, D., Ferrigno, C., Fürst, F., Hemphill, P. B., Marcu-Cheatham, D. M., Dauser, T., and Wilms, J. (2017). Cyclotron resonant scattering feature simulations. I. Thermally averaged cyclotron scattering cross sections, mean free photon-path tables, and electron momentum sampling. *Astron. Astrophys.*, 597:A3.
- Shakura, N. I. and Sunyaev, R. A. (1973). Black holes in Binary Systems. Observational Appearance. *Astron. Astrophys.*, 24:337.
- Shapiro, S. L. and Teukolsky, S. A. (1983). *Black holes, white dwarfs, and neutron stars : the physics of compact objects*.
- Soong, Y., Gruber, D. E., Peterson, L. E., and Rothschild, R. E. (1990). Spectral Behavior of Hercules X-1: Its Long-Term Variability and Pulse Phase Spectroscopy. *Astrophys. J.*, 348:641.
- Stamatikos, M., Malesani, D., Page, K. L., and Sakamoto, T. (2015). Grb 140705a: Swift detection of a short burst. *GRB Coordinates Network*, 16520:1.
- Stella, L., White, N. E., and Rosner, R. (1986). Intermittent stellar wind acceleration and the long-term activity of population i binary systems containing an x-ray pulsar. *Astrophys. J.*, 308:669.
- Strader, J., Chomiuk, L., Swihart, S., and Aydi, E. (2019). Optical Spectroscopy of the Candidate Be Star Counterpart to 4U 1901+03. *The Astronomers Telegram*, 12554:1.
- Sunyaev, R. A. and Titarchuk, L. G. (1985). Comptonization of low-frequency radiation in accretion disks: angular distribution and polarization of hard radiation. *Astron. Astrophys.*, 143:374–388.
- Taam, R. E., Fryxell, B. A., and Brown, D. A. (1988). A Model for the Recurrent Flares in EXO 2030+375. *Astrophys. J.*, 331:L117.
- Taam, R. E. and Li, D. N. C. (1984). THE EVOLUTION OF THE INNER REGIONS OF VISCOUS ACCRETION DISKS SURROUNDING NEUTRON STARS. *Astrophys. J.*, 287:761.
- Tauris, T. M. and van den Heuvel, E. P. J. (2006). Formation and evolution of compact stellar x-ray sources. pages 623–665. Edited by W Lewin and M. van der Klis.
- Tendulkar, S. P., Hascöet, R., Yang, C., Kaspi, V. M., Beloborodov, A. M., An, H., Bachetti, M., Boggs, S. E., Christensen, F. E., Craig, W. W., Guillot, S., Hailey, C. A., Harrison, F. A., Stern, D., and Zhang, W. (2015). PHASE-RESOLVED NuSTAR AND SWIFT-XRT OBSERVATIONS OF MAGNETAR 4U 0142+61. *Astrophys. J.*, 808:32.
- Titarchuk, L. (1994). Generalized Comptonization Models and Application to the Recent High-Energy Observations. *Astrophys. J.*, 493:434–570.
- Trümper, J., Pietsch, W., Reppin, C., Voges, W., Staubert, R., and Kendziorra, E. (1978). Evidence for strong cyclotron line emission in the hard X-ray spectrum of Hercules X-1. *Astrophys. J. Lett.*, 219:L105 – L110.

- Tsygankov, S. S., Lutovinov, A. A., V. Doroshenko, A. A. Mushtukov, V. S., and Poutanen, J. (2016). Propeller effect in two brightest transient x-ray pulsars: 4U 0115+63 and V 0332+53. *Astron. Astrophys.*, 593:A16.
- Tuo, Y. L., Ji, L., Tsygankov, S. S., Mihara, T., Song, L. M., Ge, M. Y., Nabizadeh, A., Tao, L., Qu, J. L., Zhang, Y., Zhang, S., Zhang, S. N., Bu, Q. C., Chen, L., Xu, Y. P., Cao, X. L., Chen, Y., Liu, C. Z., Cai, C., Chang, Z., Chen, G., Chen, T. X., Chen, Y. B., Chen, Y. P., Cui, W., Cui, W. W., Deng, J. K., and Y. Y. Du, Y. W. D., Fu, M. X., Gao, G. H., Gao, H., Gao, M., Gu, Y. D., Guan, J., Guo, C. C., Han, D. W., Huang, Y., Huo, J., Jia, S. M., Jiang, L. H., Jiang, W. C., Jin, J., Jin, Y. J., Kong, L. D., Li, B., Li, C., Li, G., Li, M. S., Li, T. P., Lia, W., Lia, X., Li, X. B., Li, X. F., Li, Y. G., Li, Z. W., Liang, X. H., Liao, J. Y., Liu, B. S., Liu, G. Q., Liu, H. W., Liu, X. J., Liu, Y. N., Lu, B., Lu, F. J., Lu, X. F., Luo, Q., Luo, T., Ma, X., Meng, B., Nang, Y., Nie, J. Y., Oua, G., Sai, N., Shang, R. C., Song, X. Y., Suna, L., Tan, Y., Wang, C., Wang, G. F., Wang, J., Wang, W. S., Wang, Y. S., Wen, X. Y., Wu, B. Y., Wu, B. B., Wu, M., Xiaoa, G. C., Xiaoa, S., Xiong, S. L., Yang, J. W., Yang, S., Yang, Y. J., Yang, Y. J., Yia, Q. B., Yin, Q. Q., You, Y., Zhang, A. M., Zhang, C. M., Zhang, F., Zhang, H. M., Zhang, J., Zhang, T., Zhang, W., Zhang, W. C., Zhang, W., Zhang, Y., Zhang, Y. F., Zhang, Y. J., Zhang, Y., Zhang, Y., and Z. Zhang, Z. Z., Zhang, Z. L., Zhao, H. S., Zhao, X. F., Zheng, S. J., Zheng, Y. G., Zhoua, D. K., Zhou, J. F., Zhua, Y. X., Zhua, Y., and Zhang, R. L. (2020). Insight-hxmt insight into switch of the accretion mode: The case of the x-ray pulsar 4u 1901+03. *Journal of High Energy Physics*, 27:38.
- Turolla, R., Zane, S., and Watts, A. L. (2015). Magnetar : the physics behind observations. *Rep. Prog. Phys.*, 78:11690.
- van Horn, H. M. (1971). Cooling of white dwarfs. page 97. White Dwarfs, Proceedings from IAU Symposium no. 42. Edited by Willim Jacob Luyten. International Astronomical Union. Symposium no. 42, Springer-Verlag, Dordrecht.
- Wang, J. C. L., Wasserman, I., and Lamb, D. Q. (1993). A semi-analytic model for cyclotron line formation. *Astrophys. J.*, 414:815.
- Wang, Y. M. (1987). Disc accretion by magnetized neutron stars : a reassessment of the torque. *Astron. Astrophys.*, 183:257.
- Webster, B. L. and Murdin, P. (1972). Cygnus X-1—a Spectroscopic Binary with a Heavy Companion ? *Nature*, 235:37–38.
- White, N. E., Swank, J. H., and Holt, S. S. (1983). Accretion powered X-ray pulsars. *Astrophys. J.*, 270:711–734.
- Wijnands, R. and van der Klis, M. (1998). A millisecond pulsar in an x-ray binary system. *Nature*, 394:344.
- Wojdowski, P., Clark, G. W., Levine, A. M., Woo, J. W., and Zhang, S. N. (1998). Quasi-periodic Occultation by a Precessing Accretion Disk and Other Variabilities of SMC X-1. *Astrophys. J.*, 541:963.
- Zhang, S. N., Yu, W., and Zhang, W. (1998). Spectral State Transitions in Aquila X-1: Evidence for “Propeller” Effects. *Astrophys. J.*, 494:L71.

Appendix A

List of Publication

1. A report on Type II X-ray bursts from SMC X-1
Binay Rai, Pragati Pradhan and Bikash Chandra Paul
Research in Astronomy and Astrophysics (RAA), Vol. 18 No. 12, 148 (2018).
2. NuSTAR and Swift observations of AMXP Swift J1756.9-2508 during its 2018 outburst
Binay Rai and Bikash Chandra Paul
Monthly Notice Royal Astronomical Society (MNRAS) 489, 5858-5865 (2019)
3. Timing and spectral properties of Be/Xray pulsar 4U 1901+03 during 2019 outburst
Binay Rai and Bikash Chandra Paul
Accepted in *Astrophysics and Space Science*, ASTR-D-20-00586R2, 2021

Appendix B

Paper Presented in Seminar

1. Spectral analysis of 2S 1417-624 during and after its 2018 outburst (2020), Exploring the Cosmos (A National Conference on Relativistic Universe), High Energy and Cosmic Ray Research Centre (HECRRC), North Bengal University, Siliguri, West Bengal-734013.
2. NuSTAR and Swift observations of X-ray binary 4U 1901+03 (2020), 1st International e-Conference on Recent Advances in Physics & Materials Science, Kurseong College, Darjeeling, West Bengal, India-734203.

Appendix C

Reprints of papers included in the thesis

A report on Type II X-ray bursts from SMC X-1

Binay Rai¹, Pragati Pradhan^{2,3} and Bikash Chandra Paul¹

¹ Dept. of Physics, North Bengal University, Darjeeling, West Bengal, 734013, India; binayrai21@gmail.com

² Department of Astronomy and Astrophysics, Pennsylvania State University, Pennsylvania, 16802, USA

³ St. Joseph's College, Darjeeling-734104, West Bengal, India

Received 2018 March 20; accepted 2018 May 28

Abstract We study *RXTE* PCA data for the high mass X-ray binary source SMC X-1 between 2003–10 and 2003–12 when the source was in its high states. The source is found to be frequently bursting which can be seen as flares in lightcurves that occur at a rate of one every 800 s, with an average of 4–5 Type II X-ray bursts per hour. We note that typically a burst was short, lasting for a few tens of seconds in addition to a few long bursts spanning more than a hundred seconds that were also observed. The flares apparently occupied 2.5% of the total observing time of 225.5 ks. We note a total of 272 flares with mean FWHM of the flare ~ 21 s. The rms variability and aperiodic variability are independent of flares. As observed, the pulse profiles of the lightcurves do not change their shape, implying that there is no change in the geometry of an accretion disk due to a burst. The hardness ratio and rms variability of lightcurves exhibit no correlation with the flares. The flare fraction shows a positive correlation with the peak-to-peak ratio of the primary and secondary peaks of the pulse profile. The observed hardening or softening of the spectrum cannot be correlated with the flaring rate but may be due to the interstellar absorption of X-rays as evident from the change in hydrogen column density (n_H). It is found that the luminosity of the source increases with the flaring rate. Considering that the viscous timescale is equal to the mean recurrence time of flares, we fixed the viscosity parameter $\alpha \sim 0.16$.

Key words: accretion — accretion discs — pulsar: individual (SMC X-1) — stars: neutron — X-rays: binaries — X-ray: burst

1 INTRODUCTION

SMC X-1 is a high mass X-ray binary (HMXB) system in the Small Magellanic Cloud (SMC). A Type II X-ray burst from the source was discovered by Angelini et al. (1991) along with aperiodic variability of 0.01 Hz. It was discovered while comparing the burst with MXB 1730–355, which is known as a “Rapid Burster” (Lewin et al. 1976). The burst is considered to be due to viscous instability in the accretion disk characterised by a sharp rise and decay in the count rate of the lightcurve, with recurrence time ranging from ~ 10 s to 1 h.

It may be pointed out here that a Type I X-ray burst (Lewin & Joss 1983) arises from a thermonuclear origin and displays a sharp rise and exponential decay in the intensity observed in the lightcurve along with a recurrence time of hours or days. The spectrum of a Type I burst is

consistent with that of a blackbody followed by spectral softening in the burst decay. It was observed that in a “Rapid Burster” the average fluxes emitted in Type II X-ray bursts were 120 times larger than the average fluxes emitted in Type I X-ray bursts (Hoffman et al. 1978). The observed ratio of time-averaged persistent flux to time-averaged Type I X-ray burst flux lies between 10 and 10^3 (Lewin et al. 1993).

SMC X-1 is an HMXB system with a neutron star (Price et al. 1971) and the B0 supergiant SK 160 with mass $\sim 17.2 M_\odot$ having an orbital period of ~ 3.9 days (Schreier et al. 1972). The X-ray source is eclipsed by the companion for 0.6 days. The source is found to have a regular spin up state $\sim 3.279 \times 10^{-11} \text{ Hz s}^{-1}$ (Davison 1977; Wojdowski et al. 2000) with no spin down state as has been recorded in the source. The source is observed to have an orbital decay rate of $\sim 3.4 \times 10^{-6} \text{ yr}^{-1}$

(Levine et al. 1993; Wojdowski et al. 2000). It has been reported that SMC X-1 shows an aperiodic variation of $\sim (55 - 60)$ d due to obstruction of X-rays coming from the source by its tilted precessing accretion disk (Wojdowski et al. 2000). It is also regarded as an “intermediate-stage source” (Moon et al. 2003) between low-mass X-ray binaries (LMXBs) and X-ray pulsars along with some interesting intermediate-stage sources having a magnetic field from 10^8 to 10^{11} G and which undergoes either Type I or II X-ray bursts, or both, and may or may not have coherent pulsation. Examples of these types of sources are “the Bursting Pulsar” GRO J1744–28 (Fishman et al. 1995) which shows Type II characteristic bursts along with coherent pulsation, “the Rapid Burster” MXB 1730–355 (Lewin et al. 1976) undergoing both Type I and Type II X-ray bursts and “the Accreting Milli-second pulsar” SAX J1808.4–3658 (in in ’t Zand et al. 1998) which undergoes Type I X-ray bursts with coherent pulsation.

SMC X-1 and GRO J1744–28 have some properties in common, namely both of them undergo Type II bursts with coherent pulsation (Li & van den Heuvel 1997). Their spin periods are also very small; for SMC X-1 it is ~ 0.71 s and that for GRO J1744-28 is ~ 0.47 s. They have steady spin up in their spin with the measured magnetic field value $\sim 10^{11}$ G (Bildsten & Brown 1997) and luminosity below an Eddington limit. However in the case of GRO 1744–28, bursts occur at a higher rate than SMC X-1, although they also differ in burst pattern. The analysis of *Rossi X-ray Timing Explorer (RXTE)* Proportional Counter Array (PCA) data targeting SMC X-1 by Moon et al. (2003) found that the flare occupies 3% of the total observing time and is spread over different orbital phases, and is strongly correlated with variability in the lightcurve. The flare fraction is found to increase with the peak to peak ratio of the pulse profile. The properties of SMC X-1 do not differ very much during the flaring period from those of the normal state. Here, we study detailed properties of Type II X-ray bursts from SMC X-1 by making use of *RXTE* PCA data between 2003–10 and 2003–12. The organization of the paper is as follows: In Section 2 we discuss the data reduction to analyze the source. In Section 3 study of lightcurves with flares is presented. Section 4 is concerned with study of the pulse profile, hardness ratio and spectrum of the source. Section 5 deals with study of the correlation between bursts with different parameters and also investigates the relation of luminosity with flaring rate. Finally a discussion is given in Section 6.

2 DATA SELECTION AND REDUCTION

To investigate the source SMC X-1, we used *RXTE* PCA data. PCA has an array of five proportional counter units (PCUs), namely PCU 0, PCU 1, PCU 2, PCU 3 and PCU 4 (Jahoda et al. 2006). PCU 0 suffered propane loss in the year 2000. PCU 3 and PCU 4 were regularly rested to avoid breakdown. Out of the above mentioned counter units, data from PCU 2 will be employed here for analysis as it was the only PCU unit that did not suffer any breakdown and was operating all the time. PCU 2 is the best calibrated counter unit as verified by fitting the Crab spectrum simply with a power law (PL).

The data reduction was done using *HEASOFT* ver 6.11. For spectral analysis, standard 2 mode of *RXTE* PCA data was used which has 129 channels and default binning of 16 s. The data from only the top X-layer of PCU 2 were considered. The response matrix for the top layer has been obtained using *FTOOL PCARSP*. The background spectra were extracted using the tool *RUNPCABACKEST* taking a bright source background model. The source spectra were then produced by subtracting these background spectra with the total spectra in *XSPEC*. Here the energy range for a spectrum under consideration lies in the range 3–18 keV. We have not considered data above 18 keV as the spectrum in that case is dominated by background and good fitting may not be possible. A systematic error of 2% was added to all spectra.

Timing analysis was carried out using the *GOODXENON* mode of *RXTE* PCA data. The lightcurves were extracted from the *GOODXENON* data using the mission specific tool *SEEXTRCT* for the whole available energy range and all layers of PCU 2 with background correction. Background correction was applied by subtracting the background lightcurve from the total lightcurve using *lcmath*. The background lightcurve was extracted using the background model for the bright source. The reference frame of photon arrival time was transformed to the barycentre with the help of *FTOOL FAXBARY* using JPL DE400 ephemeris. The set of data where the elevation of the telescope was $<10^\circ$ and 30 min after the passage from the South Atlantic Anomaly (SAA) has been considered in this paper for data reduction and analysis.

3 LIGHTCURVES AND FLARES

For our analysis, in addition to flares, we searched for all *RXTE* PCA data available for SMC X-1 between 2003–

10 and 2003–12. The data we have considered lie in two high states, h1 and h2, as observed in the *RXTE* ASM lightcurve of the source, as shown in Figure 1. The technique used by Moon et al. (2003) to search for flares is followed in this work. All the photon counts which were 3σ above the mean are considered to be a flare in a lightcurve. The data were divided into 110 data segments, with each segment having duration ~ 2050 s. Hence, we have 110 lightcurves, each of which has been plotted and analyzed.

The time spent by a burst varies from burst to burst where some of them last for a few tens of seconds to much more than that. To determine the duration of a burst, we fit each flare with a Gaussian model to obtain the width ‘ w ’ of the flare. Consequently the full width at half maximum (FWHM) of a flare may be obtained by using the relation $\text{FWHM} = 2.35482w$, which we take as the duration of a burst. The reduced χ^2 of the fitting varies from 2.3 to 3.56. We began with the lightcurves that have a 4 s time resolution. We found 272 such cases of flares with mean FWHM of ~ 21 s and mean standard deviation of ~ 8 s. Therefore out of 225.5 ks, we note 5.7 ks as the time of flaring. Thus it is clear that the source is flare active for $\sim 2.5\%$ of the total time which is close to the value reported earlier by Moon et al. (2003). The left panel of Figure 2 shows the lightcurves for four different observations, with a time resolution of 4 s and the corresponding normalised power spectra on the right. It is observed from the plot that the recurrence time between flares varies from a few hundred to a few thousand. The average value of recurrence time between flares from the above analysis is ~ 800 s. The number of flares, width of flares and recurrence time are found to be the same for the lightcurves having time resolutions of 2 s, 6 s and 8 s.

For power spectra we use data with the time resolution of 0.075 s and we plot them using the XRONOS tool *POWSPEC* with normalization = -2 . The value of normalization gives us the white noise normalised power spectra with their integral yields fractional root mean square (rms) variability. The power spectra corresponding to four lightcurves (left Fig. 2) are displayed in the right panel of Figure 2. The rms variabilities of the four lightcurves obtained from the power spectra are estimated to be (a) 30.86%, (b) 31.2%, (c) 31.2% and (d) 30.6%. Thus during all four observations the source is found to show the same variability, i.e. the source was equally variable.

Along with the coherent peak at frequency equal to the frequency of rotation of the pulsar (~ 1.41 Hz), peaks are also observed in frequencies which are integral multiples of the rotational frequency. Due to presence of aperiodic components some rise in power spectra is seen at low frequency range. For the power spectrum (d) it is noted that as we go to the low frequency region (from 1 to 0.005 Hz), power rises moderately and at ~ 0.019 Hz a broad peak exists. A similar rise is seen in the right of Figure 2(c) at the same frequency as the flat top.

It is observed that during some flares the count rate reached up to many times the mean value, while, in some cases, flares were found to last for more than hundreds of seconds (Fig. 3). Generally, the bursts are single peaked (Fig. 2), however large bursts were found to have multiple peaks before they finally decayed to the mean value as shown in Figure 3. The left panel of Figure 3 shows a lightcurve with a flare of duration ~ 50 s consisting of two sharp peaks. The first peak arises because of a sharp increase in the count rate, reaching $\sim 1350 \text{ s}^{-1}$ then sharply falls to $\sim 510 \text{ s}^{-1}$, followed once again by an increase in count rate giving a second peak of $\sim 1320 \text{ s}^{-1}$ which falls rapidly below 500 s^{-1} . The situation is such that one burst is followed by another one immediately. However, the flare shown in the right panel of Figure 3 is long, ~ 300 s, and has multiple peaks; the highest peak has a count rate of $\sim 1000 \text{ s}^{-1}$, signalling the instability lasts for a long time and comes to a normal stable state with slow rise and decay in intensity with multiple peaks. The burst per hour per observation for the first high state (h1) as shown in Figure 1 is $\sim 5 \text{ h}^{-1}$ and for the second (h2) we note $\sim 4 \text{ h}^{-1}$. However, for the complete observation, the average number of bursts per hour was ~ 5 and the average time between two bursts may be set as ~ 800 s.

4 PULSE PROFILE, HARDNESS RATIO AND ENERGY SPECTRA

The binary orbit of SMC X-1 is found to be nearly circular (Levine et al. 1993; Wojdowski et al. 2000; Raichur & Paul 2010). As the neutron star moves in its circular binary orbit there are delays in the pulse arrival time because of orbital modulation, i.e. when the neutron star is close to an observer, the pulse will arrive sooner than when the neutron star is away from the observer. In order to get a correct pulse profile, the arrival time of a pulse must be corrected so that we get an arrival time which also includes the effect of orbital modulation. If t'_n and t_n are the times of emission and arrival respectively then

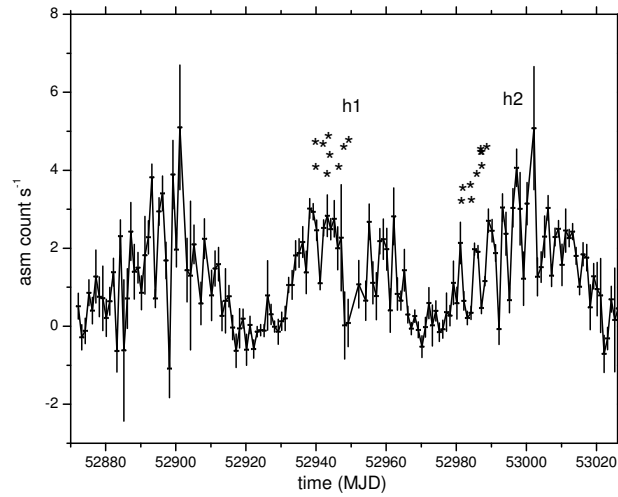


Fig. 1 A segment of the *RXTE* ASM lightcurve of SMC X-1 with rebinning of 1 day. The star symbols indicate the dates of the observations. Our observations of the source occurred during two high states as indicated by h1 and h2.

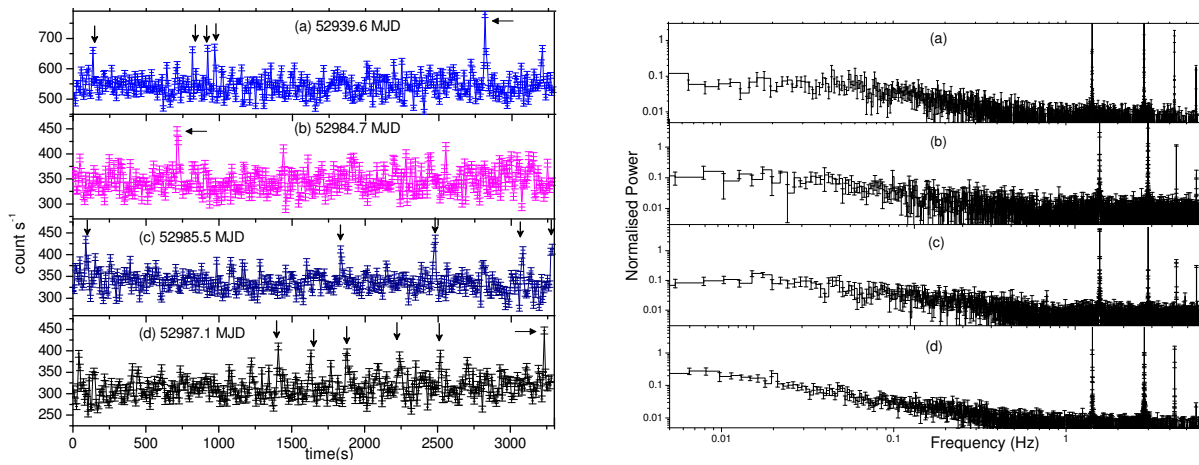


Fig. 2 The left panel of the figure displays the lightcurves of four different observations as indicated by lower case letters (a), (b), (c) and (d) with the date in MJD. The right panel shows their corresponding power spectra. The flares are indicated by *arrows* in the lightcurves. The power in power density spectra is expressed in the unit of $(\text{rms})^2 \text{ Hz}^{-1}$.

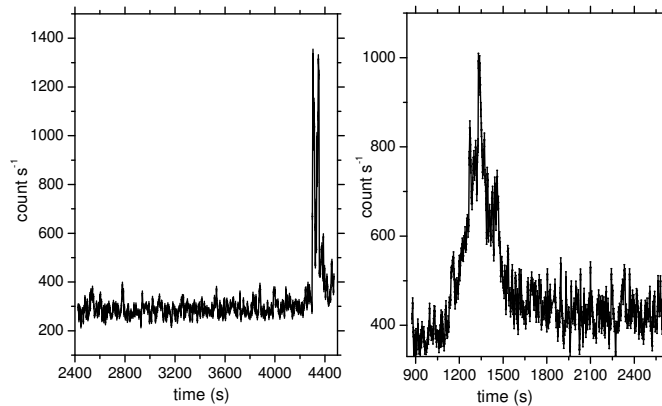


Fig. 3 Two large bursts observed in SMC X-1. The Obs.Id for the observation is 80078-01-01-04. The left panel shows the burst where the count rate rises up to ~ 4 times above the mean value and in the right one the burst lasts for ~ 300 s. Both of the bursts have multiple peaks.

they are related to each other and to the orbit of the neutron star through $f_{\text{orb}}(t'_n)$ (Deeter et al. 1981) as

$$\begin{aligned} t'_n &= t_0 + nP_s + \frac{1}{2}n^2\dot{P}_sP_s, \\ t_n &= t'_n + f_{\text{orb}}(t'_n), \end{aligned}$$

where P_s and \dot{P}_s are respectively the spin period and time derivative of the spin period for the neutron star. For a circular orbit, $f_{\text{orb}}(t'_n)$ takes the form

$$\begin{aligned} f_{\text{orb}} &= a_x \sin i \cos l_n, \\ l_n &= 2\pi(t'_n - E)/P_{\text{orb}} + \pi/2, \end{aligned}$$

where l_n is the mean orbital longitude at time t'_n , E is the epoch when the mean orbital longitude is equal to $\pi/2$ and $a_x \sin i$ is the projected semi-major axis with ‘ i ’ being the angle of inclination between the line of sight and orbital angular momentum vector.

We have used the value of epochs and other orbital parameters from Raichur & Paul (2010) for the orbital correction. The orbital corrected pulse profiles are shown in Figure 4. The pulse fraction of (a) and (d) is 20% whereas for (b) and (c) it is 30%. All the pulse profiles have their secondary peak at a phase ~ 0.78 and primary at ~ 0.28 . The secondary peaks of all four lightcurves coincide with each other. Except for the change in pulse fraction, there is no significant change in the pulse profiles.

The hardness ratios for the four observations were obtained by dividing the 7–16 keV energy X-ray photon count rate by the 3–7 keV energy X-ray photons count rate. The average hardness ratios for the four lightcurves are 0.9 ± 0.03 , 0.897 ± 0.035 , 0.8563 ± 0.031 and 0.837 ± 0.031 respectively, as displayed in Figure 5(a), 5(b), 5(c) and 5(d). The average hardness ratios for the four observations do not vary significantly. Also there is no noticeable change in hardness ratio in any of the four lightcurves during a burst. Therefore, the hardness ratio may not be correlated with flares from the source. We can check this invariance in the hardness ratio by studying the energy spectra of the source.

The energy spectra for four observations are shown in Figure 6. The models we have used for fitting these spectra are PHABS to estimate the photoelectric absorption of the photon by an interstellar medium, POWERLAW, HIGHECUT for the non-thermal emission of the source and GAUSSIAN for the iron line. The Gaussian peak for an iron line is fixed at 6.7 keV. The best fit parameters of the fit are shown in Table 1. For all observations, the PL indices are nearly the same; for the

first three it is ~ 1 , as displayed in Figure 6(a), 6(b) and 6(c) whereas it is ~ 1.1 for Figure 6(d). None of the best fit parameters changed significantly for the four spectra. Considering the distance of SMC X-1 from the observing point at 65 kpc (Keller & Wood 2006; Naik & Paul 2004) the luminosity of the source is measured, which for the four observations are 6.787×10^{38} , 6.302×10^{38} , 6.211×10^{38} and 5.862×10^{38} erg s^{-1} respectively for Figure 6(a), 6(b) 6(c) and 6(d). The variation of the n_{H} value may be due to partial obscuration of the neutron star by the precessing accretion disk or X-ray eclipses. Another possibility for the variation may be an artifact of a simple POWERLAW model or the tails of the soft excess components affecting our result (Inam et al. 2010). The photoelectric absorption by interstellar matter is dominant in the lower energy range but as we cannot go below an energy of 3 keV due to the limitation of our instrument, it is not possible to constrain the n_{H} value precisely.

4.1 Variation of the Spectral Parameter with Orbital Phase and Flux

To study the variation of different spectral parameters over the binary orbit, the available spectra in the energy range 3–18 keV are fitted with the models discussed above, and the reduced χ^2 of the fitting lies between 1 and 2. We plotted the hydrogen column density (n_{H}) and photon index with orbital phase. Spectral flux between the energy range 3–18 keV was also plotted with phase. From the left panel of Figure (7), we can see that there is no abrupt change in the photon index or n_{H} value with orbital phase. It is evident from Figure 7(c) that the flux lies between $0.992 \pm 0.001 \times 10^{-9}$ and $1.7326 \pm 0.001 \times 10^{-9}$. The maximum flux is at an orbital phase of 0.44 and the minimum at 0.16. The minimum of the n_{H} value is $1.01662 \times 10^{22} \text{ cm}^{-2}$ and it happens when the flux is maximum. As is evident from Figure 7(a), 7(c) and 7(d), the spectrum is a bit softer at phase 0.17 with the maximum value of the photon index, i.e. 1.16604 ± 0.3048 , along with the maximum value of hydrogen density column 2.4156×10^{22} . The spectrum becomes harder with photon index 0.9574 ± 0.02 as the flux becomes maximum. From Figure 7(b) and 7(d) we can see there is no correlation of spectral softening or hardening with either phase or flux. The small hardening of the spectrum with minimum hydrogen density column may be because of the low absorption of hard X-ray by the interstellar medium, which also results in maximum flux observed

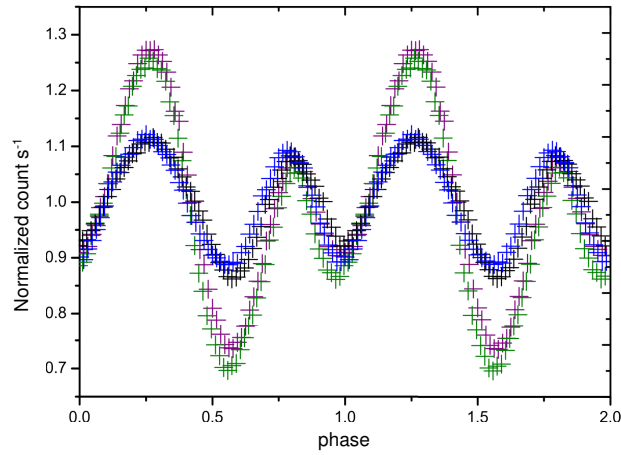


Fig. 4 Orbital corrected pulse profiles of the four lightcurves displayed in the left panel of Figs. 2(a), (b), (c) and (d) folded at ~ 0.7 s; blue (a), purple (b), green (c) and black (d).

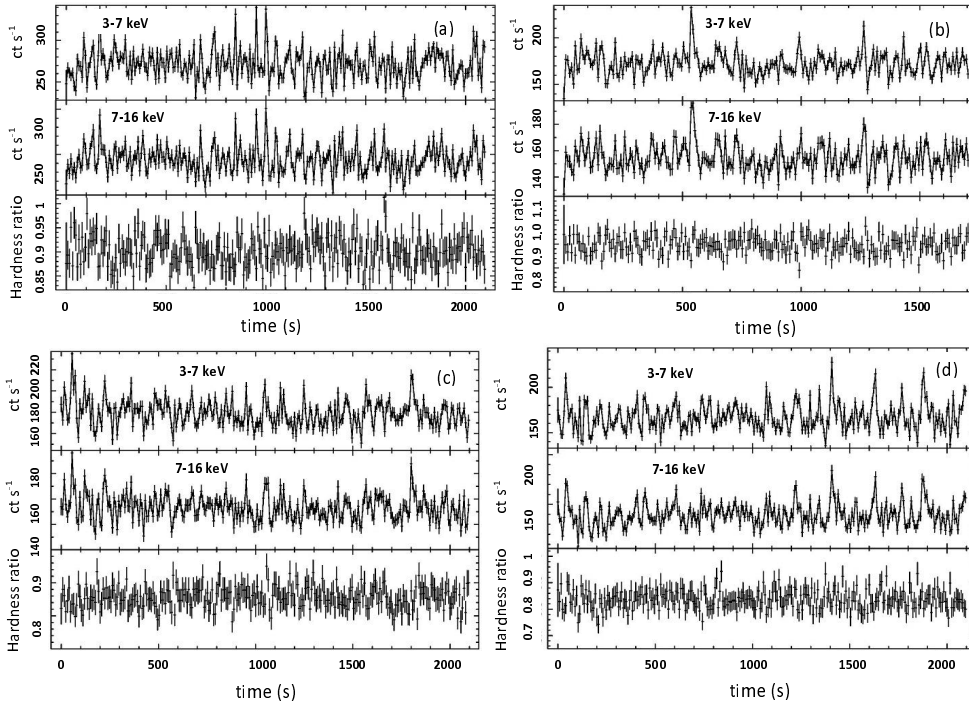


Fig. 5 Hardness ratio of four observations (a), (b), (c) and (d) obtained by dividing the X-ray photon count rate of 16 keV by 3-7 keV plotted with the time resolution of 8 s.

Table 1 The best-fit parameters of the fit. χ^2_{ν} is the reduced chi-square of the fit for 29° of freedom. n_{H} is the hydrogen column density of intervening interstellar matter. α is the PL index. E_{cutoff} and E_{fold} are the cutoff energy and e-folding energy of the model HIGHCUT expressed in keV respectively. The measured flux is for energy range 3–18 keV and in the unit 10^{-9} erg s^{-1} cm^{-2} .

Observation	a	b	c	d
n_{H}	2.062 ± 1.023	1.014 ± 1.06	1.604 ± 1.043	1.968 ± 1.019
α	1.066 ± 0.202	1.004 ± 0.219	1.084 ± 0.218	1.122 ± 0.202
E_{fold}	17.868 ± 4.726	16.521 ± 4.457	17.723 ± 5.078	17.080 ± 4.143
E_{cutoff}	5.998 ± 1.045	5.870 ± 1.074	5.837 ± 1.147	6.002 ± 1.218
flux	1.345	1.247	1.229	1.160
χ^2_{ν}	1.682	1.375	1.890	1.563

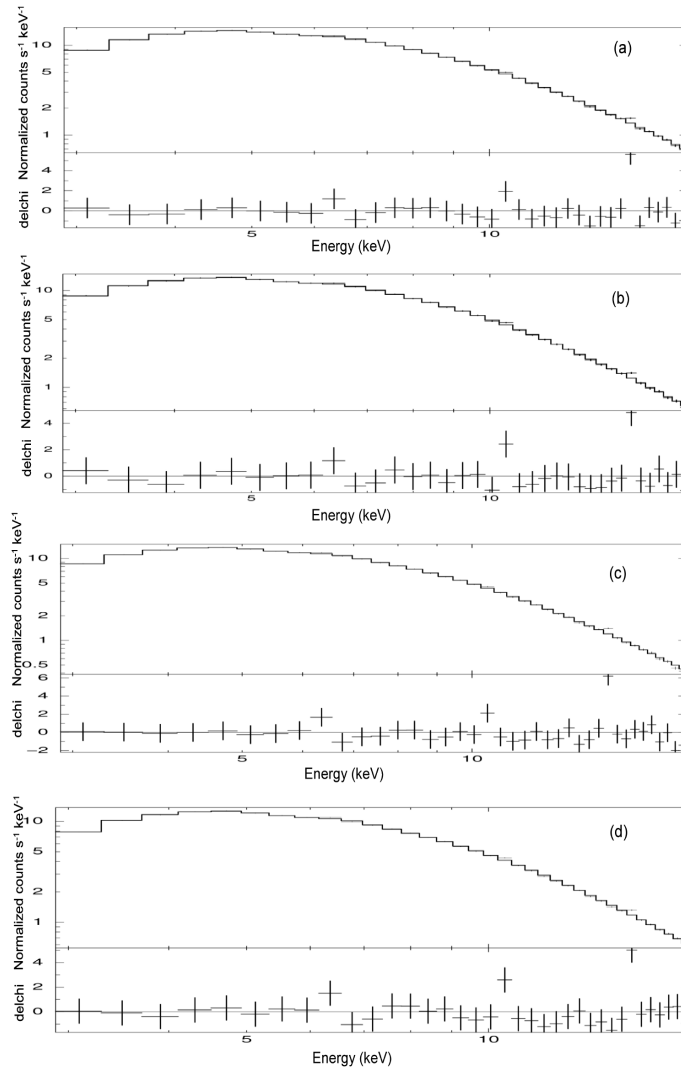


Fig. 6 Energy spectra (d) along with their best-fit spectra. The lower panel of each spectrum is the $\Delta\chi^2$ of the fit, which is the ratio of the difference of the observed data and the model value to the corresponding error.

at that phase. Similarly, the small softening of the spectrum may result from an increase in absorption of X-rays by the interstellar medium. The overall variation of the flux may be due to variation in the accretion rate of the neutron star.

5 CORRELATION OF THE FLARES WITH TIME, PHASE PEAK TO PEAK RATIO AND ORBITAL PHASE

The number of flares observed depends on the total observation time as shown in Figure 8(a). Thus it may be concluded that if the observation time is longer, greater numbers of flares may be observed. We did not find any correlation of the flare fraction with rms variability of the lightcurve of the source. The rms variability was found to

lie between $\sim 30\% - 33\%$ with an average of $\sim 31\%$. To investigate the correlation of the flares with pulse profile peak-to-peak ratio, we divide the flare fraction of a particular observation by time so the flare fraction is now measured in $\% \text{ h}^{-1}$ and plotted with the peak-to-peak ratio of secondary to primary peaks of the pulse profiles. The flare fraction per hour shows some correlation with the peak-to-peak ratio (Fig. 8b), as there is a relative increase in the flare fraction per hour. However it is evident from Figure 8(c) that no correlation of the flare fraction with orbital phase exists. The flare fraction/h is constant from ~ 0.05 to ~ 0.3 then starts decreasing except near 0.2 where a change is observed; it is noted that near 0.56 an increase in the flare fraction is also observed. This variation of flare fraction with orbital phase

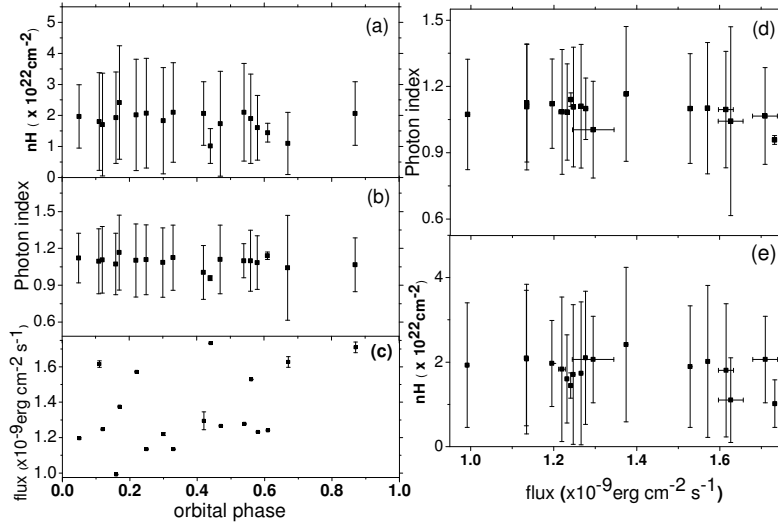


Fig. 7 The variations of n_H , photon index of PL and flux are displayed in panels (a), (b) and (c) respectively, whereas panels (d) and (e) give the variation of photon index and n_H with flux respectively.

may be due to the varying accretion rate of the neutron star, which changes the number of bursts observed. To know whether flaring is the reason behind the change in photon index, which results in the softening or hardening of the spectrum, we plotted the photon index of the spectrum with respect to the flare fraction/h of different observations (Fig. 8f). As observed in Figure (8f), one cannot correlate the change in photon index with the change in flare fraction, however the spectrum looks harder when the flare fraction/h(%) is ~ 10 . As there is no correlation of photon index with flare fraction, one can conclude that the hardening of the spectrum in this case may be due to a decrease in absorption by the interstellar medium, not due the increase in flaring rate.

The variation of spin period of the neutron star with luminosity of the source is depicted in Figure 8(d). The spin periods were obtained by using the timing tool EFSEARCH in orbitally corrected data obtained by following the method described in Section 4. The spin period in our observations lies between ~ 0.7033 and ~ 0.7057 with the luminosity ranging from 3.9×10^{38} to $7.8 \times 10^{38} \text{ erg s}^{-1}$. The spin-up rate is found to be directly proportional to $PL_{38}^{3/2}$ where (P) is the spin of the neutron star and (L_{38}) is the luminosity of the source. As the spin up rate \dot{P} is small, about $\sim 3.279 \times 10^{-11} \text{ Hz s}^{-1}$ (Davison 1977; Wojdowski et al. 2000) and the two high states are separated by ~ 50 d, there is negligible spin up. Hence the variation of the spin (P) with luminosity (L_{38}) is $PL_{38}^{3/2} = \text{constant}$ (Ghosh & Lamb 1979). In our case, we do not see such variation of spin for the source

with its luminosity, which may be because of the fact that the data we have considered span a few months of observations of the source. It can be possible to find the relation between luminosity and spin, and also possibly the relation between spin-up rate, spin and luminosity with the help of long term study of the source. But in a source like SMC X-1, it is harder to study the spin-luminosity relation because of superorbital modulation of luminosity which causes the luminosity to vary in an aperiodic manner. The luminosity of the source increases with the increase in flares as evident from Figure 8(e), i.e. the luminosity of the source has a strong positive correlation with flares.

6 DISCUSSION

The source SMC X-1 emits Type II bursts with the mean recurrence time of ~ 800 s and for 2.5% of the observed time the source was bursting. The Type II bursts are due to Lightman-Eardley (LE) instability, which develops in the viscous accretion disk. The average number of bursts per hour is found to be $\sim 4 - 5$. Thus SMC X-1 is an HMXB “bursting pulsar.” We notice a large burst of very short duration and one with long duration with multiple peaks. However, the observed pulse profiles do not change their shape despite the fact that the different observations were carried out in different bursting states, signalling that the accretion disk geometry has not changed because of the burst. The peak-to-peak ratio of the spin-phase increases with the increase in flaring

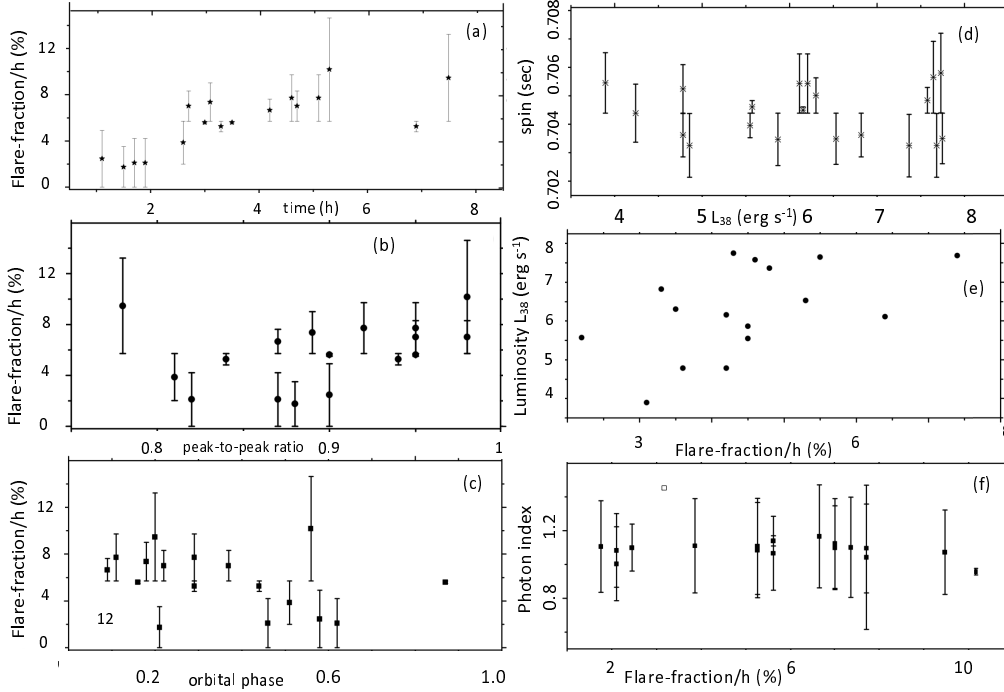


Fig. 8 The variation of flare fraction with the time of observation (a), with the pulse profile peak-to-peak ratio (b) and with the orbital phase (c). For (b) and (c), the average flare fraction, i.e. flare fraction per hour, is plotted against peak-to-peak ratio and orbital phase respectively. The variation of spin with luminosity is plotted in (d) and in (e) the variation of luminosity with flare fraction is shown. Panel (f) displays the variation in photon index of the spectrum with flare fraction per hour.

rate which may be due to the greater rate of accretion of matter at the cooler pole as compared to the hotter pole of the neutron star during bursts (Moon et al. 2003). We suspect that the increase in accretion rate above leads to the associated instability, so the increase in accretion rate may cause nearly equal accretion of matter at both the poles, resulting in nearly equal primary and secondary peaks as observed in the pulse profile. The luminosity of the source is found to increase with the increase in flaring rate as the conversion of matter into radiation takes place at a higher rate than during a normal state.

LE instability is seen when the radiation pressure becomes dominant and is a major contributor to the total pressure. The instability is followed by thermal and surface density instability. The global nature of the instability was investigated by Taam & Lin (1984) and Lasota & Pelat (1991) who found that the instability results in bursts which recur after a few seconds. This phenomenon was similar to the three outbursts observed in the lightcurve of GRO J1744–28 during 1996 (Cannizzo 1996), which had outbursts of ~ 10 s and recurrence times of ~ 1000 s. According to Cannizzo, the fast timescale seen by Taam & Lin (1984) and Lasota & Pelat (1991) was because they set the viscosity pa-

rameter ‘ α ’ (Shakura & Sunyaev 1973) equal to one and considered the inner radius (r_{inner}) of the accretion disk equal to the neutron star radius. ($R \sim 10$ km). It has been pointed out that for outbursts to occur in GRO J1744–28, the accretion rate must exceed the critical value by a small amount at which the radiation pressure is comparable to the gas pressure. Taking a reasonable value of α (less than 1 and r_{inner} greater than R), the viscous timescale at the critical condition has been found to equal $t_{\nu, \text{crit}} = 1200 r_8^{0.58} m^{0.79}$ s, where $r_8 = r_{\text{inner}}/10^8$ cm, $m = M/M_{\odot}$ and M is the mass of the neutron star which is in good agreement with the recurrence time of the burst in GRO J1744–28 provided by $r_{\text{inner}} = 10^{7.5}$ cm and $M = 1.4 M_{\odot}$ (Cannizzo 1996), $t_{\nu, \text{crit}} \sim 800$ s. The burst from SMC X-1 is similar to that of GRO 1744–28 but we note that the post-flare dip is absent in the former. The absence of the dip in the former may be due to the slow accumulation of matter after the burst or because of the release of only a certain amount of accumulated matter during the burst so that after the burst intensity is found at the persistent level. Another possibility for there being no dip observed in the SMC X-1 after the burst may be due to the increase in accretion rate just after the burst.

There was no correlation between flare fraction/h, n_H and flux with the orbital phase. There is no evidence of a change in the nature of the spectrum because of flares. The small softening or hardening of the spectrum was not due to flares but may be due to varying interstellar absorption. The spectrum of the burst for SMC X-1 shows similar properties to GRO J1744–28 as there is no spectral softening, but it is also inconsistent with the associated blackbody, and the photon index is ~ 1.2 and the high cutoff energy is 14 keV (Sazonov et al. 1996). We may conclude that the bursts in the two X-ray binaries are due to LE instability with a comparable magnetic field. Due to the presence of a low magnetic field, the transition region (between the radiation dominated and gas pressure dominated region) is located near the inner edge of the disk (Li & van den Heuvel 1997), therefore, the instability develops inside the disk which is not carried far and heats the surrounding matter because of increasing viscosity. The heated matter is then accreted onto the neutron star producing a burst. From Moon et al. (2003), in the transition region between the radiation dominant and pressure dominant regions, the viscous timescale is

$$\alpha = 216 \dot{M}_{17} / t_{\text{visc}}^{\frac{3}{2}},$$

where \dot{M}_{17} is the accretion rate on the order of 10^{17} and t_{visc} is the viscous timescale. Taking the typical value of $\dot{M}_{17} = 20 \text{ g ms}^{-1}$ and $t_{\text{visc}} = 800 \text{ s}$, $\alpha \sim 0.16$. If the recurrence of the burst occurs on the same timescale as that of the viscous timescale then we can say $\alpha \sim 0.16$. The accumulation of a huge amount of matter during a short time may lead to large bursts in a short time. However, if accumulation of matter happens slowly it results in instability that develops in a large area for a long time over the disk, causing long bursts with multiple peaks.

The aperiodic variability of the power spectra can be a possible low frequency quasi-periodic oscillation (QPO) because of interaction of the magnetosphere of the pulsar with the inner edge of the accretion disk as observed in EXO 2030+375 and Cen X-3 or “peaked low frequency noise” seen in LMXRB’s Sco X-1 and GX 17+2 (Angelini et al. 1991). Our observation suggests that the flaring activity of the pulsar bears no correlation with this aperiodic variability as seen in Figure 2, in which the aperiodic variability exists whether the number of flares increases or decreases. The rms variability of the lightcurves of the sources is observed to be independent of the flares, implying the source was varying equally all the time.

Acknowledgements This research has made use of data obtained through the High Energy Astrophysics Science Archive Research Center (HEASARC) Online Service, provided by NASA’s Goddard Space Flight Center. BCP would like to acknowledge SERB-DST for the research grant EMR/2016/005734. The authors would like to thank the anonymous reviewer for his/her valuable comments and suggestions.

References

- Angelini, L., Stella, L., & White, N. E. 1991, *ApJ*, 371, 332
 Bildsten, L., & Brown, E. F. 1997, *ApJ*, 477, 897
 Cannizzo, J. K. 1996, *ApJ*, 466, L31
 Davison, P. J. N. 1977, *MNRAS*, 179, 15P
 Deeter, J. E., Boynton, P. E., & Pravdo, S. H. 1981, *ApJ*, 247, 1003
 Fishman, G. J., Kouveliotou, C., van Paradijs, J., et al. 1995, *IAU Circ.*, 6272
 Ghosh, P., & Lamb, F. K. 1979, *ApJ*, 234, 296
 Hoffman, J. A., Marshall, H. L., & Lewin, W. H. G. 1978, *Nature*, 271, 630
 in ’t Zand, J. J. M., Heise, J., Muller, J. M., et al. 1998, *A&A*, 331, L25
 Inam, S. Ç., Baykal, A., & Beklen, E. 2010, *MNRAS*, 403, 378
 Jahoda, K., Markwardt, C. B., Radeva, Y., et al. 2006, *ApJS*, 163, 401
 Keller, S. C., & Wood, P. R. 2006, *ApJ*, 642, 834
 Lasota, J. P., & Pelat, D. 1991, *A&A*, 249, 574
 Levine, A., Rappaport, S., Deeter, J. E., Boynton, P. E., & Nagase, F. 1993, *ApJ*, 410, 328
 Lewin, W. H. G., Doty, J., Clark, G. W., et al. 1976, *ApJ*, 207, L95
 Lewin, W. H. G., & Joss, P. C. 1983, in *Accretion-Driven Stellar X-ray Sources*, ed. W. H. G. Lewin & E. P. J. van den Heuvel, 41
 Lewin, W. H. G., van Paradijs, J., & Taam, R. E. 1993, *Space Sci. Rev.*, 62, 223
 Li, X.-D., & van den Heuvel, E. P. J. 1997, *A&A*, 321, L25
 Moon, D.-S., Eikenberry, S. S., & Wasserman, I. M. 2003, *ApJ*, 582, L91
 Naik, S., & Paul, B. 2004, *A&A*, 418, 655
 Price, R. E., Groves, D. J., Rodrigues, R. M., et al. 1971, *ApJ*, 168, L7
 Raichur, H., & Paul, B. 2010, *MNRAS*, 401, 1532
 Sazonov, S., Sunyaev, R., & Swank, J. 1996, *IAU Circ.*, 6291
 Schreier, E., Giacconi, R., Gursky, H., Kellogg, E., & Tananbaum, H. 1972, *ApJ*, 178, L71
 Shakura, N. I., & Sunyaev, R. A. 1973, *A&A*, 24, 337
 Taam, R. E., & Lin, D. N. C. 1984, *ApJ*, 287, 761
 Wojdowski, P. S., Clark, G. W., & Kallman, T. R. 2000, *ApJ*, 541, 963

NUSTAR and *Swift* observations of AMXP *Swift* J1756.9–2508 during its 2018 outburst

Binay Rai[★] and Bikash Chandra Paul[★]

Department of Physics, North Bengal University, Darjeeling, West Bengal 734013, India

Accepted 2019 September 4. Received 2019 August 19; in original form 2019 March 13

ABSTRACT

We present here the timing and spectral analysis of the accreting millisecond pulsar (AMXP) *Swift* J1756.9–2508 during its recent outburst in 2018 using *Swift* and *NUSTAR* observations. The simultaneous fitting of the *Swift* and *NUSTAR* spectra indicates that the source was in the hard state with a cut-off energy of about 74.58 keV. We also study in detail the pulse profile of the AMXP and its dependence on energy. The colour–colour diagram of the source is different from those previously reported. We performed phase- and time-resolved spectral analysis using *NUSTAR* data. Pulse phase-resolved spectra were fitted with a power-law model and significant changes in the spectral parameters with pulse phase were observed. The orbital phase and time-resolved spectra were fitted with a cut-off power-law model. The column density and photon index obtained from orbital phase spectral analysis were found to show some anticorrelation with the flux. Through time-resolved spectral analysis, we observed that the spectral parameters show positive correlation with each other and with the flux. We do not observe a softening of the spectrum with time. No emission lines or Compton bump were observed in the spectrum of the AMXP.

Key words: stars: neutron – pulsars: general – pulsars: individual: *Swift* J1756.9–2508 – X-rays: binaries – accretion.

1 INTRODUCTION

Accreting millisecond X-ray pulsars (AMXPs) belong to a subgroup of low-mass X-ray binaries (LMXBs) which contain a neutron star rotating at a speed of a few milliseconds. The first AMXP, SAX J1808.4–3658, was discovered by Wijnands & van der Klis (1998) using the *Rossi X-ray Timing Explorer* (*RXTE*). *Swift* J1756.9–2508 (hereafter J1756.9) was the eighth accreting millisecond X-ray pulsar discovered in 2007 (Krimm et al. 2007a) using the *Swift* Burst Alert Telescope (BAT). After the detection of the source, further observations were carried out by the *Swift* X-ray telescope and *RXTE* missions and further analysis confirmed that it is an accreting millisecond pulsar with a spin period of 5.5 ms (182 Hz) and an orbital period of 54.7 min (Markwardt & Krimm 2007; Krimm et al. 2007b). The source is transient in nature and only visible during an outburst: a very fast rise and subsequent exponential decay in count rate are observed during its outbursts. The minimum mass of the companion of the neutron star in the AMXP lies between 0.0067 and 0.0086 M_{\odot} , which is He-dominated (Krimm et al. 2007b).

The source was once again detected by the *Swift* BAT and *RXTE* PCA during its second outburst in 2009 after the first outburst in 2007 (Patruno et al. 2009b). The long-term spin behaviour

of J1756.9 was studied by Patruno, Altamirano & Messenger (2010b), Bult et al. (2018b) and Sanna et al. (2018b). The long-term spin and orbital evolution of the AMXP studied by Bult et al. (2018b), using previous *RXTE* observations of the 2007 and 2009 outbursts combined with Neutron star Interior Composition Explorer (NICER) observations of the 2018 outburst, estimated the upper limit of the orbital period derivative as $|\dot{P}_b| < 7.4 \times 10^{-13} \text{ s s}^{-1}$. The long-term spin rate helped us to constrain the magnetic field, which was estimated to be $3.1 \times 10^8 \text{ G}$ (Sanna et al. 2018b). The result of the timing analysis during its second outburst reveals an upper limit in frequency derivative within an outburst of $3 \times 10^{-13} \text{ Hz s}^{-1}$ (Patruno et al. 2010b). Bult et al. (2018b) corrected the coordinates of the source through astrometric analysis of the pulse arrival time: the corrected coordinates are R.A. = $17^{\text{h}}56^{\text{m}}57.18^{\text{s}} \pm 0.08^{\text{s}}$, Dec. = $-25^{\circ}0'27.8'' \pm 3.5''$. The pulse profiles are found to depend on different outburst phases (Patruno et al. 2010b).

The 2018 outburst was first discovered by the *International Gamma-Ray Astrophysics Laboratory* (*INTEGRAL*) while observing the weak X-ray burster IGR J17379–374 during April 1–2 and the Galactic centre region during 2018 April 2–3 (Mereminskiy et al. 2018). No outbursts were reported after 2009 until 2018. From the NICER observation on 2018 April 3, it was claimed that the source is J1756.9 with 182-Hz pulsation (Bult et al. 2018a). A new outburst from J1756.9 was detected by NICER and *Swift*–XRT while preparing this manuscript (Sanna et al. 2019): the NICER

[★] E-mail: binayrai21@gmail.com (BR); bcpaul@associates.iucaa.in (BCP)

light curve showed a decay in count rate of 2.5 count s^{-1} per day and the 0.3–10 keV unabsorbed flux was $3.78 \times 10^{-10} \text{ erg cm}^{-2} \text{ s}^{-1}$.

Linares et al. (2008) found strong broad-band flat-topped noise at $\sim 0.1 \text{ Hz}$ throughout the outburst that happened during 2007, which is similar to all other AMXPs and to other LMXBs in the hard state. They found a hard tail in the energy spectrum, which extended up to 100 keV. Sanna et al. (2018b) investigated the source using *XMM-Newton*, *NICER* and *NUSTAR* observations and reported that the source is in a hard state with non-thermal emission. The absence of a Compton hump or emission line was observed by them in the spectrum of the AMXP. The orbital parameters of J1756.9 during the 2018 outburst have been given by Bult et al. (2018b) and Sanna et al. (2018b) and hence we use the values of orbital parameters given in Table 3 of Sanna et al. (2018b) for the *NUSTAR* observation in our analysis.

2 OBSERVATIONS AND DATA REDUCTION

Data reduction was performed using *HEASOFT* (v 6.22.1). For the spectral analysis of the *Swift*–XRT data, we reduced the data using *xrtpipeline* (v 0.13.4). Then spectra and light curves were generated using the photon-counting mode level 2 clean event file. For three observations with observation IDs 00088662001, 00030952019 and 00030952020, the count rate is greater than 0.5 count s^{-1} and thus pile-up effects are not negligible. In order to minimize pile-up effects, we extracted the source event from an annular region with inner and outer radii of 3 and 23 pixels, respectively, around the source centre, ignoring a circular region of 3 pixels around the source centre for all observations. A circular region of radius 20 pixels away from the source was used to extract the background event. As the source is contaminated by bright source GX 5–1, the background region is therefore chosen in such way that it includes maximum contamination. The ancillary response file has been generated using the tool *xrtmkarf*. Out of seven *Swift* observations during 2018 April, the source is clearly visible for four different observations.

During the recent outburst, *NUSTAR* observed the source twice with observation IDs 90402313002 and 90402313004. From analysis of the *NUSTAR* data, we found that the source is only visible in the former observation, as the source has returned to the quiescent state in the latter case. The data from the first observation were taken for further analysis. For *NUSTAR*, standard screening and filtering are carried out by the *NUSTAR* data analysis software (*NUSTARDAS*) version 1.9.3. We have selected a circular region of radius 90 arcsec to extract source and background event files. The final products, i.e. spectra and light curves, were generated using *NUPRODUCTS*. The light curves were then background-corrected using *lcmath*. We then combined background-corrected light curves from FPMA (Focal Plane module A) and FPMB (Focal Plane Module B) using *lcmath*. The barycentric correction of the light curves was then performed using *barycorr*.

3 DATA ANALYSIS AND RESULTS

3.1 Light curve

The light curves of the AMXP during the outburst are shown in Fig. 1; blue indicates *NUSTAR*, whereas black and red represent *Swift* BAT¹ and XRT light curves, respectively, which shows that

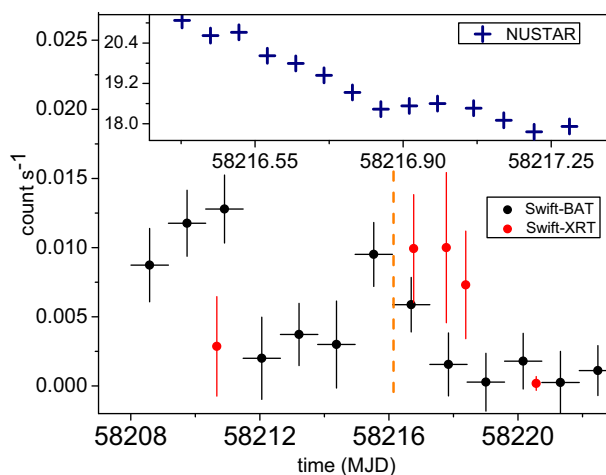


Figure 1. Light curves of AMXP *Swift* J1756.9–2508: black represents the *Swift*–BAT count rates and red represents *Swift*–XRT count rates. As the *Swift*–XRT count rate is greater than that for BAT, in order to plot both *Swift*–XRT and BAT light curves in a single panel, we rescaled the XRT count rate by a factor of 0.0132. The vertical dashed line indicates the date of the *NUSTAR* observation, 90402313002. The inset shows the light curve of the *NUSTAR* (blue) observation.

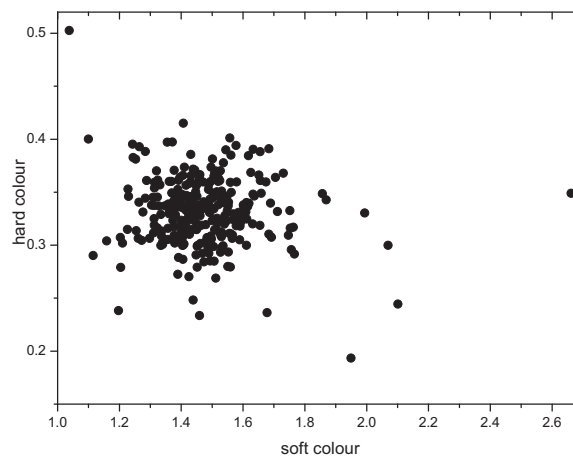


Figure 2. The colour–colour diagram of AMXP *Swift* J1756.9–2508 using *NUSTAR* observations.

the source approaches a quiescent state quickly. From the *NUSTAR* light curve, we observed that the count rate decreases by $\sim 3.15 \text{ count s}^{-1}$ or by 15 per cent in $\sim 84.5 \text{ ks}$, so the count rate decreases at a rate of $\sim 3.22 \text{ count s}^{-1}$ per day. The *NUSTAR* light curve can be fitted linearly and the slope of the fitted line was estimated to be $\sim 3.63 \text{ count s}^{-1}$ per day; if we consider a constant decay rate of $3.63 \text{ count s}^{-1}$, then after six days the count rate will reduce by $\sim 22 \text{ count s}^{-1}$, which is why the source is undetectable in the second *NUSTAR* observation, as the second observation was made nearly six days after the first. The light curve of J1756.9 observed by Patruno et al. (2010b) during the 2007, 2009 outburst was found to have two different phases: the first is the slow decay phase, which lasts for ~ 5 days, and then the fast decay phase, which has a time-scale of ~ 2 days.

¹<http://swift.gsfc.nasa.gov/results>

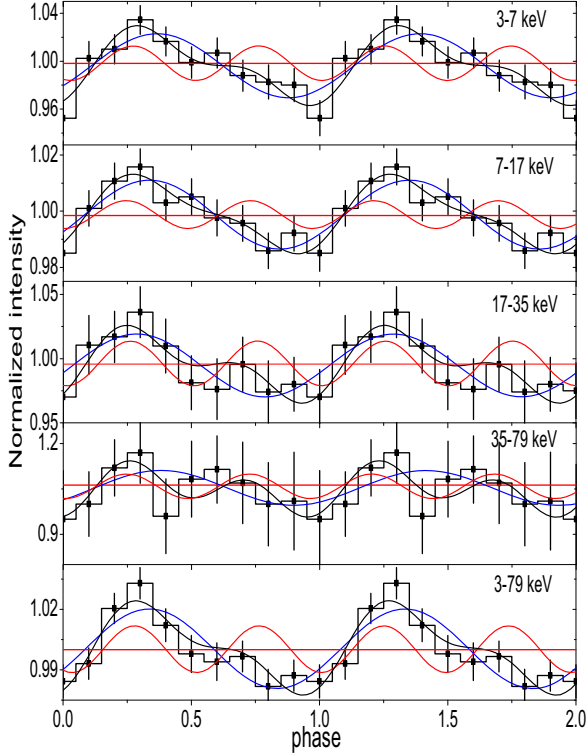


Figure 3. Pulse profile of *Swift* J1756.9–2508 in five different energy ranges during its 2018 outburst. The pulse profiles were fitted with two harmonic components and black represented the best-fitting line. Blue and red lines represent the fundamental and second harmonic components of the pulse profiles.

3.1.1 Colour–colour diagram

The colour–colour diagram (Fig. 2) was obtained by plotting hard colour with respect to soft colour. The soft colour is defined as the ratio of 5–8 keV to 3–5 keV count rates, whereas hard colour is the ratio of 8–14 keV to 14–22 keV count rates. The colour–colour diagram differs from that reported earlier by Patruno et al. (2010b). The soft colour ranges from $\sim(1.0\text{--}2.7)$, whereas the hard colour ranges from $\sim(0.2\text{--}0.5)$, but most of the soft colour lies in range $\sim(1.2\text{--}1.8)$, corresponding to hard colour that lies in range $\sim(0.25\text{--}0.4)$.

3.2 Pulse profiles

We estimated the pulse period using the χ^2 maximization technique with the help of task *efsearch* and folded the 3–79 keV energy range light curve into 10 phase bins about the estimated spin period, i.e. $P_s \sim 5.4925$ ms. The 3–79 keV pulse profile of J1756.9 is found to deviate from sinusoidal, due to the non-negligible contribution of the second harmonic (Fig. 3), as observed by Bult et al. (2018b) and Sanna et al. (2018b). The pulse profiles are fitted with two sinusoidal functions (fundamental and second harmonic) to understand in depth the contribution of the first two harmonic components; the black line in Fig. 3 is the best-fitting line. In order to understand the dependence of the pulse profile on energy, we folded the light curves of four different energy bands, namely 3–7, 7–17, 17–35 and 35–79 keV, each having 10 phase bins, as shown in Fig. 3. From the figure, we can see that the pulse profile varies in shape with energy. Pulse profiles were observed to deviate significantly from

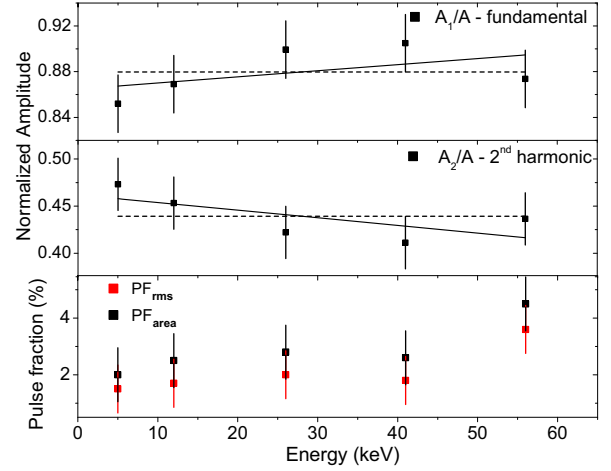


Figure 4. The normalized amplitudes of fundamental and second harmonics of the pulse profile as a function of energy are shown in the upper and middle panels, respectively. The bottom panel shows the variation of pulse fraction with energy. Two different definitions of pulse fraction are used: PF_{rms} and PF_{area} . PF_{rms} and PF_{area} are represented by red and black points, respectively, in the figure, with 1σ error bars. The dashed line represents best-fitting constant line and the black line represents the best-fitting straight line.

a sinusoidal shape, which indicates the presence of the second harmonic component. Pulse profiles in 17–35 and 35–79 keV ranges are seen to deviate much more from sinusoidal than the other three, while the pulse profile in range 35–79 keV is observed to be double-peaked. The variation of pulse profiles with time during the 2007 and 2009 outbursts of J1756.9 was studied by Patruno et al. (2010b). The above study by Patruno et al. (2010b) leads to the fact that the pulse profiles were sinusoidal at the beginning of the outburst, evolved into a skewed shape during a slow decay and thereafter became double-peaked during a fast decay. It is further found that the variation in pulse shape is related to the variation of pulse amplitude and the variability of pulse phase with time. The pulse profiles in the two outbursts had similar evolution, with similar shapes for similar orbital phases.

3.2.1 Pulse morphology

To understand in detail the dependence of the pulse profile on energy, we followed the procedure described by Tendulkar et al. (2015). The basic idea is to decompose the pulses into Fourier harmonics: for that, we define two Fourier coefficients a_k and b_k such that

$$a_k = \frac{1}{N} \sum_{j=1}^N p_j \cos \left[\frac{2\pi jk}{N} \right], \quad (1)$$

$$b_k = \frac{1}{N} \sum_{j=1}^N p_j \sin \left[\frac{2\pi jk}{N} \right], \quad (2)$$

where N is the number of phase bins, j and k denote the phase bins and Fourier harmonics, respectively, and p_j is the count rate of the j th phase bin. The strength of each Fourier component is defined by $A_k = \sqrt{a_k^2 + b_k^2}$. We define another quantity A , such that $A = \sqrt{\sum_{k=1}^M A_k^2}$. Since the contribution of higher overtones is negligible in the pulse profile of AMXPs (Patruno & Watts 2012),

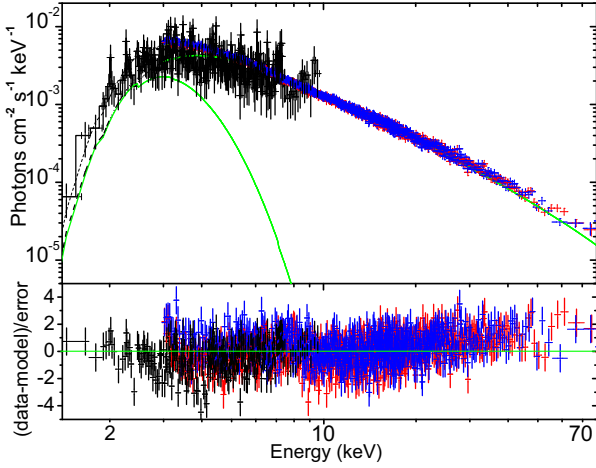


Figure 5. The simultaneously fitted spectra of J1756.9 as observed by *NUSTAR* (FPMA – red and FPMB – blue) and *Swift* (black) are shown in the upper panel and the bottom panel shows the residue of the fitting.

the Fourier coefficients for higher harmonics are very small, so we consider only up to three harmonics in this analysis, such that $M = 3$. The variation of the normalized amplitude of first harmonic A_1/A and second harmonic A_2/A is shown in Fig. 4. The normalized amplitude of the first harmonic increases at first up to 26 keV and thereafter shows a small increase up to 42 keV, finally decreasing in value at ~ 55 keV, whereas the normalized amplitude of the second harmonic decreases with increasing energy, between 26–42 keV a small decrease in its value is observed and at ~ 55 keV an increase in its value can be seen. The overall variation of the normalized amplitude of the first and second harmonics is fitted by a constant and straight line: we found that the normalized amplitude of the first harmonic shows a slow increase in value with energy, whereas that of the second harmonic shows a slow decrease in value with energy.

3.2.2 Pulse fraction

The pulse fraction (PF) is used to measure the strength of the pulsation and can be defined in different ways. We use two different definitions: the first one is the root-mean-square (rms) pulse fraction, which uses the two Fourier coefficients we have described earlier and is defined as

$$PF_{\text{rms}} = \frac{\sqrt{2 \sum_{k=1}^M [(a_k^2 + b_k^2) - (\sigma_{a_k}^2 + \sigma_{b_k}^2)]}}{a_0}, \quad (3)$$

where a_k and b_k are Fourier coefficients defined by the above equations and σ_{a_k} and σ_{b_k} are the uncertainties associated with a_k and b_k , which are given by

$$\sigma_{a_k}^2 = \frac{1}{N^2} \sum_{j=1}^N p_j^2 \cos^2 \left[\frac{2\pi jk}{N} \right], \quad (4)$$

$$\sigma_{b_k}^2 = \frac{1}{N^2} \sum_{j=1}^N p_j^2 \sin^2 \left[\frac{2\pi jk}{N} \right]. \quad (5)$$

In the second definition, the pulse fraction is defined as per Gonzalez et al. (2010) and is given by

$$PF_{\text{area}} = \frac{\sum_{j=1}^N (p_j - p_{\min})}{\sum_{j=1}^N p_j}. \quad (6)$$

Table 1. The best-fitting model parameter obtained by simultaneous fitting of *Swift* and *NUSTAR* (FPMA and FPMB) spectra.

$n_{\text{H}} (\times 10^{22})$	$8.64 \pm 0.49 \text{ cm}^{-2}$
kT	$0.53 \pm 0.02 \text{ keV}$
photon index (α)	1.75 ± 0.02
cut-off energy (E_c)	$74.58 \pm 6.04 \text{ keV}$
χ^2_{ν}/dof	0.993/4731

The variation of the pulse fraction with energy is shown in the bottom panel of Fig. 4. Both PF_{rms} and PF_{area} increase slowly with energy in range 5–26 keV and decrease a bit at ~ 42 keV, before increasing abruptly at 55 keV. The variations of PF_{area} are steeper than those of PF_{rms} . As high-energy photons are less than low-energy photons, PF_{area} is found to be biased towards high values, due to low statistics in the high-energy range, as argued by An et al. (2015).

3.3 Spectral analysis

Spectral fittings were performed in XSPEC v12.9.1p (Arnaud et al. 1996). We simultaneously fitted 3.0–79.0 keV spectra of *NUSTAR* (FPMA and FPMB) observations with those of the 0.3–10.0 keV *Swift* (XRT) observation (obs Id-00088662001), which is close to the *NUSTAR* observation (Figure 5). In order to fit spectra simultaneously, we include cross-calibration constants using a model CONSTANT, which accounts for the uncertainty in the instrument calibrations and also the lack of simultaneity of observations by *Swift* and *NUSTAR*. The spectra were fitted with CONSTANT, WABS, BLACKBODY and CUT-OFFPL.

The estimated value of the column density was $\sim 8.64 \times 10^{22} \text{ cm}^{-2}$, which is much higher than the expected value of the column density in the direction of the source,² $\sim 1 \times 10^{22} \text{ cm}^{-2}$. The column density value is close to that obtained by Sanna et al. (2018b). We found that the spectrum is hard and flat with a cut-off energy of about 74.58 keV, which is in agreement with the value of cut-off energy given by Sanna et al. (2018b) after performing simultaneous fitting of *NUSTAR* and *XMM-Newton* spectra of the source. As observed earlier (Krimm et al. 2007b; Bult et al. 2018a; Sanna et al. 2018b), the source is highly obscured along the line of sight, which is predicted by the large value of column density. We do not find any emission or absorption lines in the spectra. Sanna et al. (2018b) reported the upper limit on the width of the iron line to be 5 eV. The best-fitting spectral parameters are given in Table 1. The 0.3–79.0 keV flux was found to be $6.48 \times 10^{-10} \text{ erg cm}^{-2} \text{ s}^{-1}$; taking the distance of the source to be 8 kpc (Krimm et al. 2007b), we found the luminosity to be $4.96 \times 10^{36} \text{ erg s}^{-1}$. The value of the photon index (α) is higher than reported by Sanna et al. (2018b), with cut-off energy E_c close to the value they have reported, which is ~ 75 keV. The blackbody temperature is found to be about 0.53 keV. Fitting only the 3–79 keV *NUSTAR* spectra using WABS and CUT-OFFPL gave us α and E_c of about 1.68 and 68.17 keV, respectively, with $\chi^2_{\nu} \sim 0.97$.

3.3.1 Pulse phase-resolved spectral analysis

Phase-resolved spectral analysis is carried out with the *NUSTAR* observation of J1756.9. We took a 5-ks long segment of data and,

²<https://heasarc.gsfc.nasa.gov/cgi-bin/Tools/w3nh/w3nh.pl?>

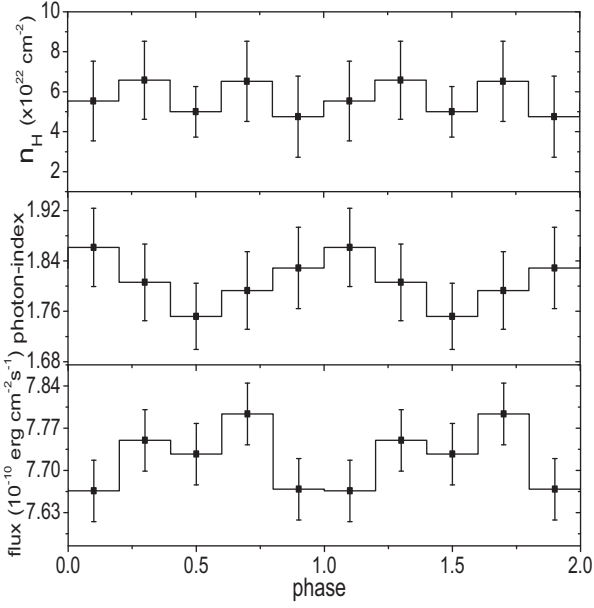


Figure 6. Variation of n_{H} (upper), photon index (bottom) and flux (lower) with respect to phase.

Table 2. Table showing the spectral parameters in different phases. χ^2_{ν} is the reduced chi-square.

Phase ϕ	$n_{\text{H}} (\times 10^{22})$ cm^{-2}	Photon index α	Flux ($\times 10^{-10}$) $\text{erg cm}^{-2} \text{s}^{-1}$	χ^2_{ν}
0.0–0.2	5.53 ± 1.99	1.86 ± 0.06	7.666 ± 0.051	0.89
0.2–0.4	6.57 ± 1.95	1.80 ± 0.06	7.750 ± 0.050	0.92
0.4–0.6	4.99 ± 1.26	1.75 ± 0.06	7.727 ± 0.049	0.94
0.6–0.8	6.52 ± 2.01	1.79 ± 0.06	7.794 ± 0.051	0.94
0.8–1.0	4.75 ± 2.03	1.83 ± 0.06	7.669 ± 0.050	0.97

Note. *The flux is calculated in the 3–79 keV energy range.

after that, energy spectra for five equal phase bins, i.e. $\phi = 0.0\text{--}0.2$, $0.2\text{--}0.4$, $0.4\text{--}0.6$, $0.6\text{--}0.8$, $0.8\text{--}1.0$, were extracted using a good time interval (gti) created using the observed spin period of J1756.9. We fit the 3–79 keV spectrum with CONSTANT, WABS and POWERLAW models. The flux was determined using the model CFLUX. The two constants C_{FPMA} and C_{FPMB} were kept frozen to unity. The variation of the spectral parameters with phase is given in Fig. 6. The photon index is found to be maximum during the initial phase 0.0–0.2 and then decreases, reaching a minimum at 0.4–0.6 before once again increasing. The column density value does not show systematic variation with phase, but seems to follow a repeated pattern of rise and fall. The flux increases with phase, reaching a maximum in region 0.6–0.8, then decreases. The values of spectral parameters at different phases are shown in Table 2.

3.3.2 Orbital phase-resolved spectral analysis

Using the values of the orbital period and epoch given by Sanna et al. (2018b), we studied the orbital phase-resolved spectra of the source produced using *NUSTAR* data. For this, we divided the orbit into 10 phases and then created good time interval (gti) files. With the help of the gti files, we extracted the spectrum for each phase then simultaneously fitted the *NUSTAR* FPMA and FPMB spectra using WABS (to estimate the photoelectric absorption) and CUT-OFFPL (to

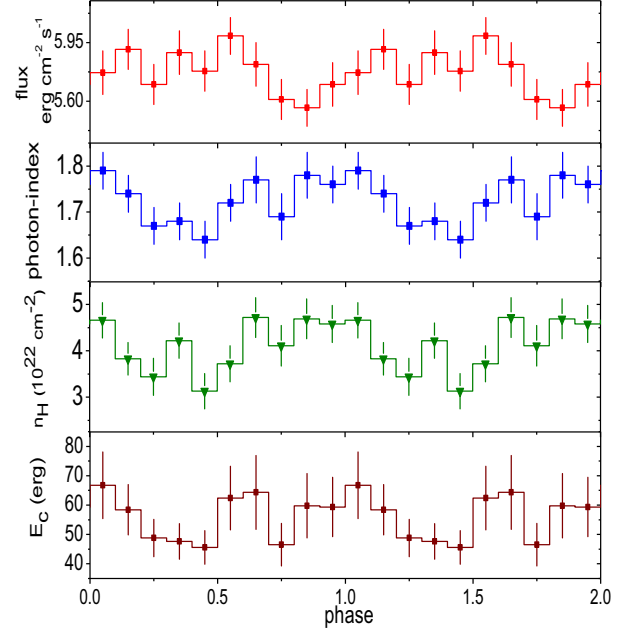


Figure 7. Variation of spectral parameters with orbital phase. The flux on a scale of 10^{-10} is shown in the upper panel (red). The bottom panel shows the variation of cut-off energy E_c . The variation of photon index α and column density n_{H} are shown in blue and green, respectively.

estimate the contribution of non-thermal components in the spectrum) models. The flux was calculated using the convolution model CFLUX. The variation of spectral parameters with phase is given in Fig. 7. The spectral parameters at different phases are displayed in Table A1. The flux first increases then decreases and again follows the same pattern, reaching a maximum of $5.99 \times 10^{-10} \text{ erg cm}^{-2} \text{ s}^{-1}$ between phases 0.5 and 0.6 and decreasing to reach a minimum value of $5.56 \times 10^{-10} \text{ erg cm}^{-2} \text{ s}^{-1}$ between 0.8 and 0.9. The variation of photon index (α) is such that it decreases first from a maximum value of 1.79, then increases. Similarly, column density (n_{H}) first decreases from a maximum value of $4.7 \times 10^{22} \text{ cm}^2$, then rises sharply between 0.3 and 0.4, falls quickly, increases and becomes almost constant between 0.6 and 1.0. E_c also decreases from a maximum value of 66.7 keV between 0.0 and 0.5. In order to understand the correlation of spectral parameters with flux, we plot spectral parameters with flux. As is evident from Fig. 8, the column density and photon index show an anticorrelation with the flux, however E_c shows a correlation with both flux and photon index.

3.3.3 Time-resolved spectral analysis

To know the detailed variation of the spectrum with time, we perform a time-resolved spectrum analysis. For this, a total exposure of 39.5 ks was divided into 14 segments each of ~ 2.8 ks. The spectrum from each segment was then extracted and fitted. Each spectrum was fitted using CUT-OFFPL to estimate the contribution of non-thermal emission to the energy spectra. For estimation of photoelectric absorption, we used WABS in both cases. To determine the flux, we used the convolution model CFLUX. The constants were kept fixed at unity. The best-fitting parameters are given in Table A2. The variation of different spectral parameters is shown in Fig. 9. If we look at the figure, the flux is decreasing with time, which is obvious. The spectral parameters do not increase or decrease

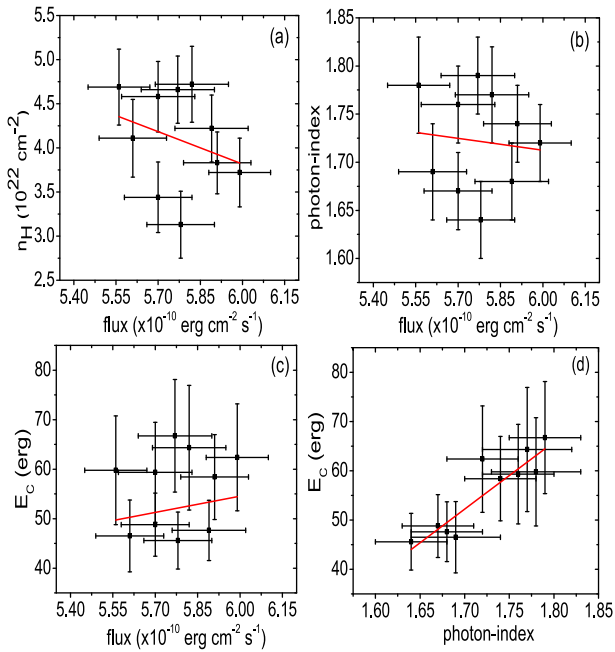


Figure 8. Figure showing variation of the spectral parameters with flux. The red line represents the best-fitting straight line. Panels (a), (b) and (c) show the variation of column density, photon index and cut-off energy with flux, respectively, and the bottom panel (d) shows the variation of cut-off energy with photon index.

Table 3. The best-fitting model parameters for different observations from *Swift*–XRT.

Obs ID	Date of obs (MJD)	n_{H} ($\times 10^{22} \text{ cm}^{-2}$)	Photon index* (α)	Flux** (erg $\text{cm}^{-2} \text{ s}^{-1}$)	χ^2_{ν}
00030952018	58210.67	6.55 ± 2.85	1.52 ± 0.64	13.93	0.85
00088662001	58216.77	6.06 ± 0.59	1.75 ± 0.18	14.96	0.76
00030952019	58217.78	7.99 ± 1.07	2.31 ± 0.30	10.82	0.71
00030952020	58218.38	4.08 ± 1.35	0.94 ± 0.47	6.67	0.73

Notes. * χ^2_{ν} is the reduced chi-square.

** Flux is on a scale of 10^{-11} .

regularly, but show a series of increases and decreases with time. At the last segment, however, there is an abrupt increase in spectral parameters. We searched for the iron line using the GAUSSIAN model: we first fitted the spectra keeping the Gaussian peak fixed at 6.4 keV; after that, we set it free to take any value and again fitted the spectra, but did not find any iron emission lines. It will be only possible through upcoming missions with very high spectral resolution to make it clear whether an iron line is present or not in J1756.9 and other AMXPs. We did not find any softening or hardening of the spectrum of J1756.9 with time. The photon index (α), n_{H} and E_{c} show some variation with flux, which can be seen in Fig. 10. Also, in some segments they follow the same pattern, so there could be some correlations between n_{H} , α and E_{c} (Fig. 10d), which indicates the fact that with the generation of high-energy X-ray photons in the source there is an increase in their absorption, resulting in softening of the spectrum and an increase in n_{H} value, but a significant number of high-energy X-ray photons can still reach the detector.

We also fitted the 0.3–10.0 keV spectra of J1756.9 observed by *Swift*–XRT using the simple POWERLAW model. The spectral parameters of different observations are given in Table 3, along with their observation IDs with the date. The photon index is found to increase from 1.52 to 2.31 between 58210.67 and 58217.78

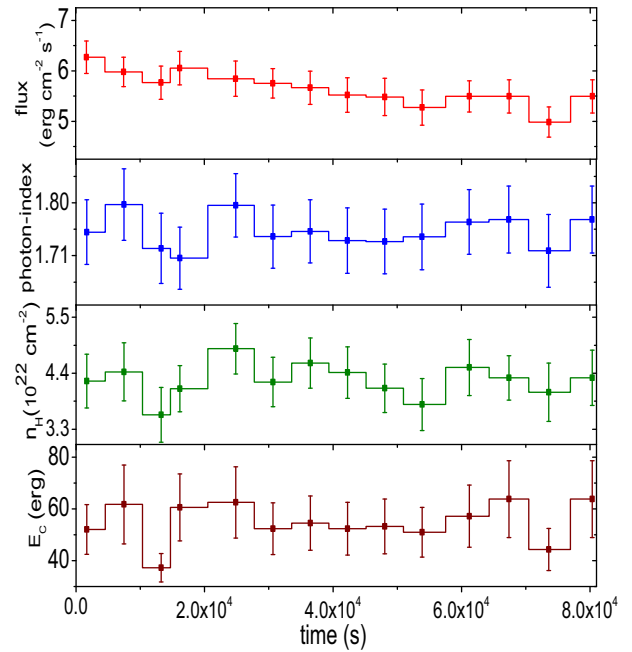


Figure 9. Variation of spectral parameters with time. The figure in red in the top panel is the flux on a scale of 10^{-10} . The bottom panel shows the variation of cut-off energy E_{c} . The variation of photon index α is shown in blue. The variation of n_{H} is shown in green. The time shown in the figure starts after 58216.358 MJD.

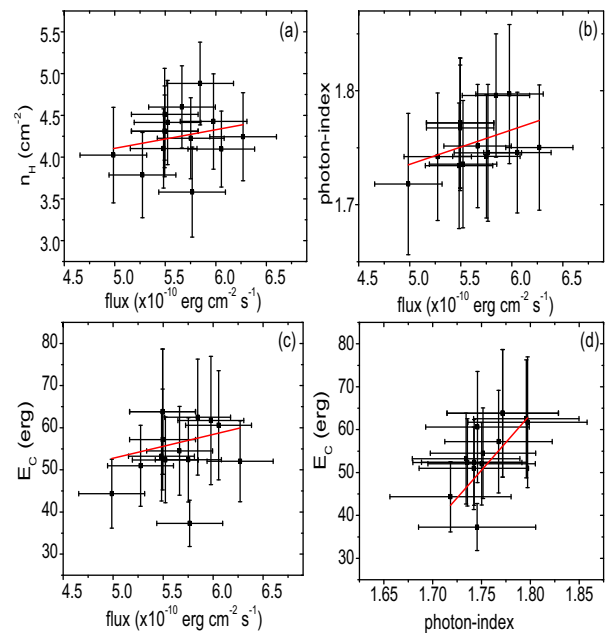


Figure 10. Variation of (a) n_{H} , (b) cut-off energy (E_{c}) and (c) photon index (α) with flux, respectively, obtained from time-resolved spectroscopy; the flux is on a scale of 10^{-10} . Panel (d) shows the variation of E_{c} with respect to α .

MJD and then decreases; at 58218.38 MJD, it was found to be 0.94. The flux increases between 58210.67 and 58216.77 MJD and then decreases in later observations, its maximum value being 14.96×10^{-11} at 58216.75. The spectrum is found to be softer as the flux increases, which we have observed in time-resolved spectroscopy of *NUSTAR* data of J1756.9.

4 DISCUSSION AND CONCLUSION

The outburst in AMXP J1756.9 was observed to decay very quickly, as a ~ 15 per cent decrease in count rate was observed in just 84.5 ks. We investigated in detail the change in the morphology of the pulse profile with energy. The 3–79 keV pulse profile of J1756.9 is found to deviate from a sinusoidal shape due to the presence of the second harmonic. Changes in the morphology of the pulse profile with energy can be seen: for 3–7, 7–17 and 17–35 keV, the pulse profile is non-sinusoidal, while the 35–79 keV pulse profile is found to be double-peaked. The normalized amplitudes of the first and second harmonics are found to increase and decrease with energy, respectively. A similar variation in the fractional amplitudes of the first and second harmonics of *Swift* J1756.9–2508 was observed by Patruno et al. (2010b) and Sanna et al. (2018b) using *NUSTAR* and *XMM-Newton* observations and Bult et al. (2018b) using NICER observations. Almost all AMXPs show a dependence of the pulse profile and fractional amplitude on energy (Patruno & Watts 2012): for example, the fractional amplitude of Aql X-1 (Casella et al. 2008), SAX J1748.9–202 (Patruno et al. 2009a) and IGR J17379–3747 (Bult et al. 2019) increases with energy. There are also some AMXPs with fractional amplitudes that decrease with energy, like XTE J0929–314 (Galloway et al. 2007) and HETE J1900.1–2455 (Galloway et al. 2007). Some AMXPs show a complex variation of fractional amplitude, where increases and decreases in its value are observed for different energies (see Patruno et al. 2010a; Falanga 2005). The increase in the pulse fraction with energy can be explained in terms of the toy model given by Alexander & Sergey (2008), according to which the X-ray-emitting region becomes smaller and smaller with increasing energy and hence become more pulsed. A similar explanation has been given by Patruno & Watts (2012) to explain the dependence of the fractional amplitude of AMXPs on energy. According to them, as the energy increases, the amplitude of pulsation of blackbody radiation emitted from hot spots also increases. We did not find any aperiodic signal or broadband noise in the power-density spectrum of J1756.9 at ~ 0.1 Hz, as reported by Linares et al. (2008) using *RXTE* data.

The 0.3–79.0 keV energy spectrum was found to be hard and flat with a cut-off energy of 74.58 keV, which may be due to Comptonization of low-energy photons. The hard state of J1756.9 with high cut-off energy during the 2018 outburst was reported by Sanna et al. (2018b). We studied in detail the spectrum of *Swift* J1756.9–2508 and performed phase-resolved and time-resolved spectroscopy using *NUSTAR* observations. It is noted that the spectral parameters show variation with pulse phase; the n_H value does not show a systematic variation with phase, whereas the photon index is found to decrease initially with phase, attain a minimum between 0.4 and 0.6 and then increase. The flux increases between 0.0 and 0.8 and then decreases abruptly during the end phase. The photon index is found to be maximum when the flux is minimum; this may be due to the absorption of X-rays during these phases. The variation of optical depth at different viewing angles can also account for the variation of photon index and flux with phase (Pravdo 1977). The variation in spectral parameters and flux for different pulse phases indicates the presence of anisotropy in the accretion column near the hotspot.

The variation of the photon index and column density with orbital phase were the same, but show some anticorrelation with flux, whereas E_c shows different variation with flux. From Fig. 8, it is observed that n_H and α decrease with increasing flux. The anticorrelation of α means that an increase in flux causes the spectrum to become hard. This may be due to an increase in optical depth with the increase in mass accretion during different orbital phases. No spectral softening is seen with time, but the spectral

parameters are correlated among themselves and with the flux. Thus, an increase in flux results in softening of the spectrum. A decrease in photon index and flux with time is also observed from *Swift*–XRT observations. The softening of the spectrum with increasing flux was observed in Aql X-1 by Zhang, Yu & Zhang (1998): according to them, this indicates the fact that the pulsar is in propeller phase. The cut-off energy E_c in both orbital phase and the time-resolved spectral analysis shows a positive correlation with flux. E_c is associated with the plasma temperature of the emission region (Soong et al. 1990) and plasma temperature increases with flux; hence E_c will increase with flux. It is also noted that no emission and absorption lines were seen in the spectra as observed by Sanna et al. (2018b); however, an emission line was observed in J1756.9 in the 6–7 keV energy range in the 2009 outburst by Patruno et al. (2010b), suggesting the presence of a possible iron line, but they were unable to constrain its line energy and width, due to the poor energy resolution of *RXTE*–PCA. Sanna et al. (2018b) estimated the upper limit of the non-detected iron line in the 2018 outburst to be 5 keV by assuming a line energy of 6.5 keV and a width of 0.23 keV. No emission lines or reflection features were observed in AMXP IGR J17379–3747 during the 2018 outbursts (Sanna et al. 2018a).

ACKNOWLEDGEMENTS

The research has made use of *NUSTAR* and *Swift* observations and the data were obtained from the NASA High Energy Astrophysics Science Archive Research Center (HEASARC), Goddard Space Flight Center. We thank the anonymous referee for suggestions to improve the quality of this article. The research is supported by SERB-DST research grant EMR/2016/005734.

REFERENCES

- Alexander L., Sergey T., 2008, *AIP Conference Proc.*, 1054, 191
 An H. et al., 2015, *ApJ*, 807, 1
 Arnaud K. A., 1996, *Astronomical Data Analysis Software and System V*, ASP Conference Series, Vol. 101, p. 17
 Bult P. M. et al., 2018a, *Astron. Tel.*, 11502, 1
 Bult P. et al., 2018b, *ApJ*, 864, 1
 Bult P. et al., 2019, *ApJ*, 877, 2
 Casella P., Altamirano D., Patruno A., Wijnands R., van der Klis M., 2008, *ApJ*, 674, L41
 Falanga M. et al., 2005, *A&A*, 444, 15
 Galloway D.K., Morgan E. H., Krauss M. I., Kaaret P., Chakrabarty D., 2007, *ApJ*, 654, L73
 Gonzalez M. E., Dib R., Kaspi V. M., Woods P. M., Tam C. R., Gavriil F. P., 2010, *ApJ*, 716, 1345
 Krimm H. A. et al., 2007a, *Astron. Tel.*, 1105, 1
 Krimm H. A. et al., 2007b, *ApJ*, 668, L147
 Linares M., Wijnands R., van der Klis M., Krimm H., Markwardt C. B., Chakrabarty D., 2008, *ApJ*, 677, 515
 Markwardt C. B., Krimm H. A., 2007, *Astron. Tel.*, 1114, 1
 Mereminskiy I. A., Grebenev S. A., Krivonos R. A., Sunyaev R. A., 2018, *Astron. Tel.*, 1497, 1
 Patruno A., Watts A. L., 2012, preprint ([arXiv:1206.2727v4](https://arxiv.org/abs/1206.2727v4))
 Patruno A., Altamirano D., Hessels J. W. T., Casella P., Wijnands R., van der Klis M., 2009a, *ApJ*, 690, 1856
 Patruno A., Markwardt C. B., Strohmayer T. E., Swank J. H., Smith S. E., Pereira D., 2009b, *Astron. Tel.*, 2130, 1
 Patruno A., Hartman J. M., Wijnands R., Chakrabarty D., van der Klis M., 2010a, *ApJ*, 717, 1253
 Patruno A., Altamirano D., Messenger C., 2010b, *MNRAS*, 403, 1426
 Pravdo S. H., Boldt E. A., Holt S. S., Serlemitsos P. J., 1977, *ApJ*, 216, L23
 Sanna A. et al., 2018a, *A&A*, 616, L17
 Sanna A. et al., 2018b, *MNRAS*, 481, 1658
 Sanna A. et al., 2019, *Astron. Tel.*, 12882, 1

- Soong Y., Gruber D. E., Peterson L. E., Rothschild R. E., 1990, *ApJ*, 348, 641
 Tendulkar S. P. et al., 2015, *ApJ*, 808, 32
 Wijnands R., van der Klis M., 1998, *Nature*, 394, 344
 Zhang S. N., Yu W., Zhang W., 1998, *ApJ*, 494, L71

APPENDIX A: VARIATION OF DIFFERENT SPECTRAL PARAMETERS WITH ORBITAL PHASE AND TIME

Table A1. Variation of spectral parameters with orbital phase, the time is offset by 58216.358 MJD. The flux is calculated between 3 and 79 keV and χ^2_{ν} is the reduced chi-square.

Phase	n_{H} (10^{22} cm^{-2})	Photon index (α)	E_{c} (erg)	Flux ($\times 10^{-10} \text{ erg cm}^{-2}$)	χ^2_{ν}
0.0–0.1	4.7 ± 0.4	1.79 ± 0.04	66.7 ± 11.4	5.77 ± 0.13	0.97
0.1–0.2	3.8 ± 0.3	1.74 ± 0.04	58.4 ± 8.6	5.91 ± 0.12	0.91
0.2–0.3	3.4 ± 0.4	1.67 ± 0.04	48.8 ± 6.4	5.70 ± 0.12	0.91
0.3–0.4	4.2 ± 0.4	1.68 ± 0.04	47.6 ± 6.1	5.89 ± 0.13	0.88
0.4–0.5	3.1 ± 0.4	1.64 ± 0.04	45.6 ± 5.8	5.78 ± 0.12	0.86
0.5–0.6	3.7 ± 0.4	1.67 ± 0.04	62.4 ± 10.8	5.99 ± 0.11	0.87
0.6–0.7	4.7 ± 0.4	1.77 ± 0.05	64.3 ± 12.6	5.82 ± 0.13	0.83
0.7–0.8	4.1 ± 0.4	1.69 ± 0.05	46.5 ± 7.2	5.61 ± 0.12	0.90
0.8–0.9	4.7 ± 0.4	1.78 ± 0.05	59.8 ± 11.0	5.56 ± 0.11	0.85
0.9–1.0	4.6 ± 0.4	1.76 ± 0.04	59.3 ± 10.1	5.70 ± 0.13	0.90

Table A2. Variation of spectral parameters with time, the time is offset by 58216.358 MJD. The flux is calculated between 3 and 79 keV and χ^2_{ν} is the reduced chi-square.

Time (ksec)	n_{H} (10^{22} cm^{-2})	Photon index (α)	E_{c} (erg)	Flux ($\times 10^{-10} \text{ erg cm}^{-2}$)	χ^2_{ν}
0–3.3	4.2 ± 0.5	1.70 ± 0.06	52.0 ± 9.6	6.27 ± 0.32	0.87
6–9	4.4 ± 0.6	1.80 ± 0.06	61.7 ± 15.2	5.98 ± 0.29	0.86
12–15	3.6 ± 0.5	1.63 ± 0.06	37.3 ± 5.5	5.76 ± 0.33	0.90
17–21	4.1 ± 0.4	1.74 ± 0.05	60.6 ± 12.9	6.05 ± 0.33	0.86
23–26	4.9 ± 0.5	1.79 ± 0.05	62.5 ± 13.7	5.84 ± 0.35	0.78
29–32	4.2 ± 0.5	1.74 ± 0.05	52.4 ± 10.0	5.75 ± 0.29	0.90
35–38	4.6 ± 0.5	1.75 ± 0.05	54.5 ± 10.5	5.66 ± 0.33	0.85
41–44	4.4 ± 0.5	1.74 ± 0.06	52.3 ± 10.2	5.52 ± 0.34	0.91
46–50	4.1 ± 0.5	1.73 ± 0.06	53.2 ± 10.6	5.48 ± 0.37	0.86
52–55	3.8 ± 0.5	1.74 ± 0.06	51.0 ± 9.6	5.27 ± 0.35	0.81
58–63	4.5 ± 0.6	1.77 ± 0.06	57.2 ± 12.0	5.49 ± 0.31	0.88
65–70	4.3 ± 0.4	1.77 ± 0.06	63.8 ± 14.9	5.49 ± 0.33	0.78
71–76	4.0 ± 0.6	1.72 ± 0.06	44.3 ± 8.2	4.99 ± 0.30	0.97
76–84	4.3 ± 0.5	1.77 ± 0.06	63.8 ± 14.9	5.49 ± 0.33	0.78

This paper has been typeset from a $\text{\TeX}/\text{\LaTeX}$ file prepared by the author.

Astrophysics and Space Science

Timing and spectral properties of Be/Xray pulsar 4U 1901+03 during 2019 outburst --Manuscript Draft--

Manuscript Number:	ASTR-D-20-00586R2
Full Title:	Timing and spectral properties of Be/Xray pulsar 4U 1901+03 during 2019 outburst
Article Type:	Original Article
Keywords:	star:neutron-- pulsar:general--X-ray:\\binaries -- X-rays:individual: 4U 1901+03--X-rays:bursts
Corresponding Author:	Bikash Chandra Paul, Ph.D. University of North Bengal Siliguri, West Bengal INDIA
Corresponding Author Secondary Information:	
Corresponding Author's Institution:	University of North Bengal
Corresponding Author's Secondary Institution:	
First Author:	binay rai, M.Sc
First Author Secondary Information:	
Order of Authors:	binay rai, M.Sc Bikash Chandra Paul, Ph.D.
Order of Authors Secondary Information:	
Funding Information:	
Abstract:	<p>We have studied the timing and spectral properties of the BeXB 4U 1901+03 during the 2019 outburst using NuSTAR, Swift, and NICER observations. Flares are in all observations and were of tens to hundreds of seconds duration. Pulse profiles were changing significantly with time and the luminosity of the source. An increase in the height of the peak of the pulse profiles was observed with energy. The pulse fraction increases with energy and at the end of the outburst. The variation of the pulse profile with time indicates the transition of the pulsar in different accretion regimes. The absorption like feature at 10 keV shows a positive correlation with the luminosity and along with other spectral parameters this feature was also pulse phase dependent. As the distance to the source is not precisely known hence we cannot confirm this feature to be CSRF and also cannot ignore other possible explanations of the feature. Another absorption like feature about 30 keV was observed in the spectra of the last two NuSTAR observations and has line energy of about 30.37 ± 0.55 and 30.23 ± 0.62 keV respectively. We have also studied the variation of the line energy, width, and optical depth of this feature with pulse phase. The soft ening of the spectrum along with the increase in pulse fraction at the end of the outburst and absence of pulsation after 58665.09 MJD suggest that pulsar has entered propeller phase, also abrupt decrease in Swift-XRT flux supports the fact.</p>
Response to Reviewers:	I would like to express the anonymous referee for his/her valuable comments and suggestions that helped me to improve the quality of this paper.

Timing and spectral properties of Be/Xray pulsar 4U 1901+03 during 2019 outburst

Binay Rai¹ • Bikash Chandra Paul¹

Abstract We have studied the timing and spectral properties of the BeXB 4U 1901+03 during the 2019 outburst using *NuSTAR*, *Swift*, and *NICER* observations. Flares are in all observations and were of tens to hundreds of seconds duration. Pulse profiles were changing significantly with time and the luminosity of the source. An increase in the height of the peak of the pulse profiles was observed with energy. The pulse fraction increases with energy and at the end of the outburst. The variation of the pulse profile with time indicates the transition of the pulsar in different accretion regimes. The absorption like feature at 10 keV shows a positive correlation with the luminosity and along with other spectral parameters this feature was also pulse phase dependent. As the distance to the source is not precisely known hence we cannot confirm this feature to be CSRF and also cannot ignore other possible explanations of the feature. Another absorption like feature about 30 keV was observed in the spectra of the last two *NuSTAR* observations and has line energy of about 30.37 ± 0.55 and 30.23 ± 0.62 keV respectively. We have also studied the variation of the line energy, width, and optical depth of this feature with pulse phase. The softening of the spectrum along with the increase in pulse fraction at the end of the outburst and absence of pulsation after 58665.09 MJD suggest that pulsar has entered propeller phase, also abrupt decrease in *Swift*-XRT flux supports the fact.

Keywords star:neutron– pulsar:general–X-ray:

Binay Rai

Bikash Chandra Paul

¹Department of Physics

North Bengal University

Raja rammohanpur, Darjeeling, W. B. -734013

E-mail:binayrai21@gmail.com (BR)

bc paul@associates.iucaa.in (BCP)

binaries – X-rays:individual: 4U 1901+03–X-rays:bursts

1 Introduction

X-ray binaries (XRB) falls under the broad class of binary stars. One of the component of X-ray binary is compact object (white dwarf, neutron star and black hole). Depending upon the mass of the companion star, X-ray binaries are classified into High Mass X-ray Binaries (HMXB) and Low Mass X-ray Binaries (LMXB). XRBs with neutron star is further classified into Be X-ray Binaries (BeXB) and Super Giant X-ray Binaries (SGXB) (Reig 2011). BeXBs consist of normal Be star along with the neutron star. They are mostly transient in nature and are observable during a bright outburst.

The X-ray source 4U 1901+03 is a BeXB which was first detected in 1970-1971 by Uhuru mission. The source was not observed for few decades but it was finally observed in 2003 when the source appeared again during a giant outburst (Galloway et al. 2005). The *Rossi X-ray Timing Explorer* observations of 2003 outburst revealed the source to be a pulsar with a pulse period of 2.763 s and orbital period of 22.58 days (Galloway et al. 2005). James et al. (2011) observed X-ray flares, broadening of pulse frequency and quasi-periodic oscillation (QPO) in the source. The flares were 100-300 s long lasting, stronger and more frequently observed during the peak of the outburst. The frequency of QPO is centered around ~ 0.135 Hz with the r.m.s. value of 18.5 ± 3.1 per cent.

The residue of the best fitted spectra of the source showed a significant deviation near 10 keV, this 10 keV feature were observed during 2003 by Reig & Milonaki (2016); Galloway et al. (2005) in the spectra of the pulsar. This feature was found to be dependent on the flux Reig & Milonaki (2016) and possibly be

a cyclotron line. The pulse profile of a pulsar varies throughout an outburst and indicates different accretion regimes (Basko & Sunyaev 1976; Becker et al. 2012; Mushtukov et al. 2015), the study of the pulse profiles of 4U 1901+03 predicted that the object passed through different accretion regimes during the outburst Reig & Milonaki (2016). These regimes are defined by a certain value of luminosity called critical luminosity (Basko & Sunyaev 1976; Becker et al. 2012; Mushtukov et al. 2015). The critical luminosity (L_{crit}) is defined as luminosity above which the radiation pressure is strong enough to stop the accreting matter at a certain distance above the neutron star. The super-critical regime is reached when the luminosity of the pulsar (L_X) is greater than L_{crit} . In this case radiation dominated shock wave is formed which moves up to few kilometers above the neutron star. However for sub-critical regime $L_X < L_{crit}$, accreting material are capable of reaching onto the surface of neutron star with heating it. In case of the super-critical regime X-ray photons escape from the side surface of the accretion column perpendicular to the magnetic field lines thus forming fan shaped beam but for sub-critical regime the emission is parallel to the magnetic field which come out as a pencil beam pattern consisting of pulsed component with simple pulse profile. The pulse profile associated with the fan shaped beam pattern is however complex in shape and in some cases mixture of fan and pencil shape beam pattern are also observed. The abrupt change in the correlation of the photon index with the flux also indicates the transition from super-critical regime to sub-critical regime (Reig & Nespoli 2013).

The recent outburst of the X-ray source 4U 1901+03 was detected on February 2019 by MAXI/GSC (Nakajima et al. 2019) and *Swift*/BAT (Kennea et al. 2019). Ji et al. (2020) using *Insight*-HXMT and *NICER* observations found dozens of flares during 2019 outburst of the pulsar which were 1.5 times brighter than the persistent emission of the object. The shape of the pulse profiles during flares were found different from that of the persistent emission. However, at a comparable luminosities pulse profiles were similar to that of the persistent emission which indicates that the accretion onto the neutron star is only dependent on the mass accretion rate. Lei et al. (2009) observed dependence of spectrum on phase and found that at beginning of the outburst the optical depth of Compton scattering was maximum near the major peak phase while during decay it was away from the main peak of the pulse profile. They observed that the flux of Fe emission line was independent of the phase suggesting the origin of this line to be accretion disk. Using torque models Tuo et al. (2020) studied the correlation between intrinsic spin

frequency derivative and bolometric flux. The authors also estimated the distance to the pulsar to be 12.4 ± 0.2 kpc. Nabizadeh et al. (2020) studied the spectral evolution of the source using *Insight*-HXMT and *NuSTAR* observations. They also studied the 10 keV feature of the source and also observed 30 keV feature in the *NuSTAR* data. Beri et al. (2020) showed that this feature has fulfilled all the necessary condition for being CRSF. The motivation of the present paper is to investigate the Be X-ray source 4U 1901+03 using *Swift*, *NuSTAR* and *NICER* observation during 2019 outburst. The bursts are different from the thermonuclear burst which is characterized by sharp rise and exponential decay. We estimated the average duration of flares and number of flares in each *NuSTAR* observation and also studied the variation of pulse profile and pulse fraction with time and energy. We have simultaneously fitted *NuSTAR* and *Swift*-XRT spectra in a broad 0.5-79 keV range and also performed phase resolved spectral analysis to study the variation of spectral parameters with phase. We have study the variation of the 10 keV feature with luminosity and phase. The phase variation of 30 keV feature in last two *NuSTAR* were studied.

2 Observation and Data reduction

During the recent outburst *Nuclear Spectroscopic Telescope Array* (*NuSTAR*) observed the source four times. *NuSTAR* consist of two co-aligned telescopes operating in the energy range 3-79 keV, each telescope has its own focal plane module consisting of a solid state CdZnTe detector (Harrison et al. 2013). Observed data reduction were carried on HEASOFT v6.26.1. We use clean event files obtained from unfiltered event files making use of the mission specific command NUPIPELINE. These cleaned event files were then used to extract light curves and spectra for analysis. We took a 90'' circular region around the bright region of the image as the source region and consider another region of the same size away from the bright region as background region. We use the above regions to extract light curves and the relevant spectra with the help of a tool NUPRODUCTS. The background subtraction of the light curves is done using LCMATH, and the light curves from two focal plane modules (FPMA & FPMB) are combined using the same tool. The barycentric correction of the light curves are done using *ftool* BARYCORR. All the spectra are fitted in XSPEC v12.10.1f (Arnaud 1996). From hereafter the four *NuSTAR* observations are referred as Obs1, Obs2, Obs3 and Obs4 respectively.

The standard screening and reprocessing of *Swift*-XRT unfiltered event files were done using XRT-

PIPELINE. For our analysis, we took *Swift*-XRT observations done in Windows Timing (WT) mode having good timing resolution. A circular region of 20 pixels around the optical position of 4U 1901+03 was considered as the source region, another region of the same area but away from the central region was taken as the background region. Using these region files we extracted light curves and spectra in XSELECT. An ancillary response (ARF) file was created using a XRTMKARF, whereas the response matrices file was obtained from the latest calibration database files. The background correction of the light curves was made with the help of LCMATH. Finally using XRTLCCORR we created light curves which is corrected from telescope vignetting and point spread function. After 58637.08 MJD *Swift*-XRT observations were made in Photon Counting (PC) mode and the source was only detected in one observation. So we used *NICER* observations made after 58637.08 to study the variation of pulse profile with time. The standard data screening and reduction were made using NICERL2. Light curves in 0.2-12 keV energy range and having a binning of 1 ms were extract from the *NICER* clean event files. We also applied a barycentric correction to the *Swift*-XRT and *NICER* light curves.

3 Analysis and Results

3.1 Light curves, pulse profiles and pulse fraction

The four different *NuSTAR* observations were taken during different stages of the outburst are depicted in the Fig.1. Light curves having time resolution of 4 s were plotted using *ftool lcurve*. The flares in the light curves of the pulsar are observed in all observations (Fig.2). The duration of these flare were tens to hundreds of seconds. The bursts were more frequent and longer enough during the peak period of the outburst (Ji et al. (2020), James et al. (2011)). Considering a flare on to a part of light curve having count rate 3σ level above the mean we estimated duration for first two observations for (5-6) per hour and for another two observations its was 3-4 per hour. The beginning and end of a flare is considered to be a lowest point of flare below the mean. The mean duration of burst for the first observation was ~ 135 s whereas for the second observation the means was found ~ 62.18 s. However, it is found that for the last two observations the mean burst duration were ~ 98.13 and 95.35 s.

A crude estimation of the pulse period of the pulsar can be obtained by a Fourier transformation of the light curve. Therefore, we consider *NuSTAR* light curves

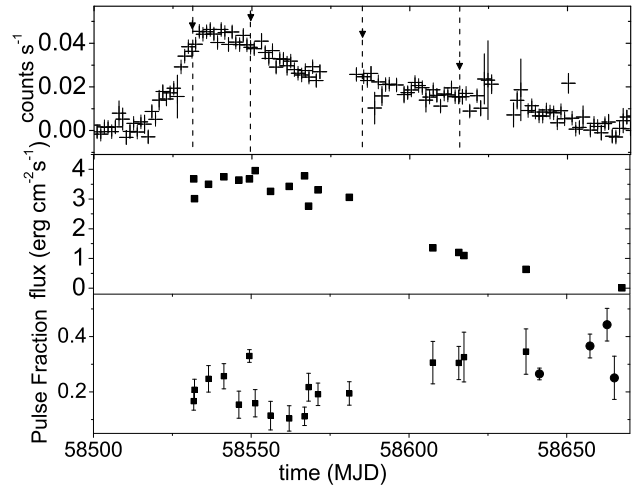


Fig. 1 Upper panel shows *Swift*-BAT light curves of 4U 1901+03 during 2019 outburst in 15-50 keV energy range. The down arrows and vertical lines indicates four *NuSTAR* observations. The middle panel shows variation of *Swift*-XRT flux in 0.5-10 keV energy range. Fluxes are in the order of 10^{-9} and obtained by using the command flux in XSPEC for *Swift*-XRT spectra fitted by POWERLAW model. Bottom panel represents change in Pulse fraction with time, the square and circle symbols are for *Swift*-XRT (0.5-10.0 keV) and *NICER* (0.2-12 keV) respectively.

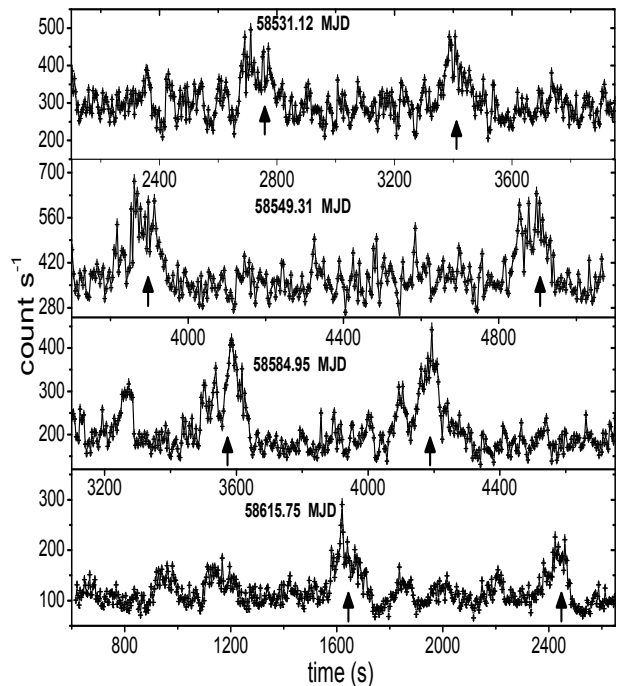


Fig. 2 Light curves showing some of the bursts observed in four *NuSTAR* observations. The burst present in the light curves is indicated by up arrow.

obsId	Date of Obs (MJD)	Exposure (ks)	P_s
90501305001	58531.121	17.85	2.76415 ± 0.00001
90502307002	58549.308	12.25	2.76152 ± 0.00002
90502307004	58584.946	21.45	2.76211 ± 0.00006
90501324002	58615.752	45.12	2.76054 ± 0.00001

Table 1 Table showing four *NuSTAR* observations indicated by their observation IDs along with the date of observation, exposure and the pulse period of pulsar. The pulse period is obtained using light curves in 3-79 keV energy range.

with binning of 1 ms to estimate the pulse period and to obtain the pulse profile. Final estimation of the pulse period was then obtained with the help of EFSEARCH using the initial estimated value. The pulse periods for the four *NuSTAR* observations is shown in table 1. The uncertainty associated with the pulse periods are estimated using the method described in Boldin et al. (2013). We can see from table 1 that the pulse period is not fixed but varies throughout the outburst. The evolution of the pulse period of an X-ray pulsar is caused by the transfer of the angular momentum from the accretion disk (Ghosh & Lamb 1979; Wang 1987). During an outburst large amount of matters are accreted onto the neutron star along with the transfer of angular momentum which causes an accelerating torque to act on the neutron star. This accelerating torque causes an increase in the intrinsic spin frequency or decrease in the spin period of the pulsar. Pulse profiles are obtained by folding light curves in 3-79 keV energy range about the pulse period of the pulsar using the tool EFOLD. For 0.5-10 keV *Swift*-XRT we extracted light curves having binning of 0.0018 s and pulse profiles were extracted using the above procedures. Pulse profiles were observed to be evolving with time. For *NuSTAR* pulse profile at 58531.12 MJD is sinusoidal in shape (Fig.3 first column) which later evolved into double peaked with one main peak at 58549.31 MJD (Fig. 3 second column). At about 58584.95 MJD the pulse profile was consist of a single peak (Fig. 3 third column) having a notch and finally at 58615.75 MJD pulse profile becomes broad with single peak (Fig. 3 fourth column) but the shape is found different from that of the first observation (Fig. 3). The variation of the pulse profile with time were also studied using *Swift*-XRT observations (Fig. 4). The pulse profile at 58532.03 MJD was two peaked with a strong primary peak. At 58541.33 MJD the second peak merged with the primary peak and at 58568.16 MJD the pulse profile was nearly single peaked with a notch. At 58581.05 MJD the pulse profile was a broad single peak. From 58607.54-58637.08 MJD pulse profiles were observed were almost the same and were having a broad single peak. The pulse profile at 58665.09 MJD is obtained by folding *NICER* light curve and consist of a single peak which sharp compared to

Swift-XRT pulse profiles in between 58607.54-58637.08 MJD. After 58665.09 MJD no further pulsation was observed in the source. In order to study the energy dependence of the pulse profile, we extract the light curves at different energy ranges using *NuSTAR* observations. For Obs1 the pulse profiles at different energy bands are almost sinusoidal in shape (Fig. 3). Pulse profiles in the energy bands 7-12 and 3-79 keV are almost the same and as we move in hard X-ray region above 12 keV an increase in the height of the peaks of the pulse profiles is observed. For Obs2 (Fig. 3), pulse profiles in 3-7, 7-12, 12-18 and 3-79 keV are double peaked whereas none significant second peak was observed in the energy band 18-24 and 24-32 keV however an increase in height of the primary peak is observed in these energy bands. The 3-7 and 3-79 keV pulse profiles for Obs3 (Fig. 3) were having nearly a single peak with a notch near ~ 0.5 , above 7 keV the pulse profiles were not so smooth and were associated with large errors. In the case of Obs4 the pulse profiles at different energy bands were almost sinusoidal in shape, pulse profiles in energy bands 7-12 and 3-79 keV are almost the same however above 18 keV large errors were associated with each the of normalized count rates.

We define a pulse fraction (PF) parameter as $PF = (p_{max} - p_{min}) / (p_{max} + p_{min})$, where p_{max} and p_{min} are the maximum and minimum intensities of a pulse profile. In Fig. 5, PF is plotted with respect to energy for four *NuSTAR* observations. The pulse fraction follows a complex variation with energy but there is an overall increase in its value with energy in all four observations. For Obs1 pulse fraction increases almost monotonically with energy (black). Pulse fractions in Obs2 increase slowly between 5-15 keV but above 15 keV pulse fraction increases rapidly (red). For the third observation (blue) pulse fractions increases slowly between 5-12 keV and remain almost constant between 12-21 keV and above 21 keV pulse fraction increases again. In the last observation there is overall increases in pulse fractions between 5-25 keV and above 25 keV the pulse fraction remained almost constant. It is evident Fig. 5 that the pulse fraction is steeper for the first two observations when the luminosity was higher than the last two observations. Thus the pulse fraction

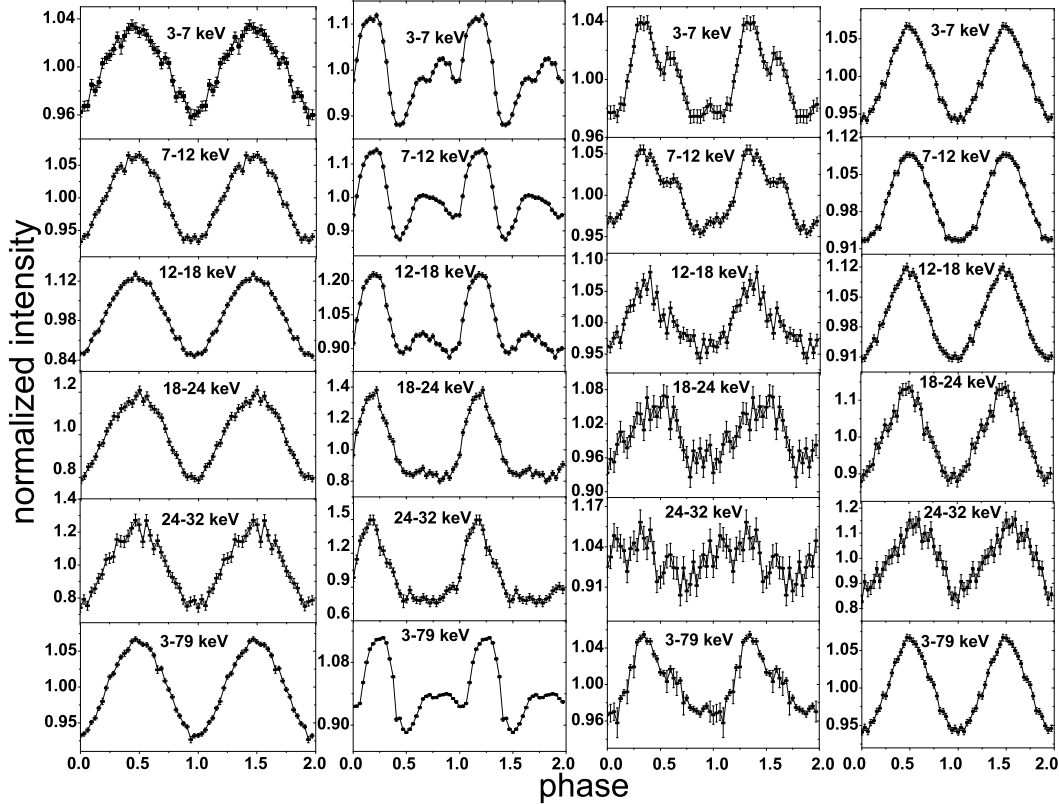


Fig. 3 Pulse profiles for different *NuSTAR* observations and variation of pulse profile with energies. Figures (a),(b),(c) and (d) are for the 58531.12, 58549.31, 58584.95 and 58615.75 MJD respectively.

in different energy ranges is high if the luminosity is high. The variation of the pulse fraction for different observations is also shown in table 2.

The variation of the pulse fraction with time and flux were studied using *Swift*-XRT observations. The pulse fraction was found to increase initially between 58531.77-58549.43 MJD from 0.17-0.33 and decreases to 0.16 at 58551.23 MJD and remain almost constant between 58556.14-58566.91 MJD. However in between 58568.16-58637.08 MJD the pulse fraction increases from 0.22 to 0.34 (bottom panel of fig 1). The variation of the pulse fraction with flux in 0.5-10 keV energy range is shown in bottom panel of figure 9. The pulse fraction decreases from 0.34-0.10 as flux increases from $0.64\text{-}3.43 \times 10^{-9}$ erg cm $^{-2}$ s $^{-1}$ and increases from 0.11 to 0.33 between $3.43\text{-}3.68 \times 10^{-9}$ erg cm $^{-2}$ s $^{-1}$ and abruptly decreases to 0.15 at 3.96×10^{-9} erg cm $^{-2}$ s $^{-1}$. Thus as we go below 3.43×10^{-9} erg cm $^{-2}$ s $^{-1}$ there is increase in pulse fractions. So as the outburst decays the pulse fraction increases.

3.2 Spectral Analysis

The three *NuSTAR* observations Obs1, Obs2 and Obs4 were close to three *Swift* observations having obsIds

00088846001, 00088849001 and 00088870001 respectively. So we fitted *Swift*-XRT and *NuSTAR* (FPMA & B) spectra simultaneously in 0.5-79.0 keV energy range, here *Swift* spectra were in 0.5-10 keV energy range and *NuSTAR* in 3-79 keV range. However, there is a slight mismatch between the *Swift*-XRT and *NuSTAR* data points while fitting their spectra simultaneously which has been reported earlier by Bellm et al. (2014). A CONSTANT model was used while fitting XRT and *NuSTAR* spectra simultaneously which take into accounts the instrumental uncertainties and also non-simultaneity of the observations. The spectra were fitted with two different combinations of models. First, we used the combination of CONSTANT, PHABS, BLACKBODY, CUTOFFPL and GAUSSIAN and in the second case we replaced the CUTOFFPL with the model COMPTT which describes the Comptonization of the soft photon in hot plasma. Let us define Model I to be CONSTANT*PHABS*(CUTOFFPL+GAUSSIAN) and Model II to be CONSTANT*PHABS*(COMPTT+GAUSSIAN). The cross section for the PHABS was chosen to be vern and the abundance was set to angr. The optical depth of the Comptonizing region in Model II was obtained using disk geometry. However, in both

Table 2 Variation of pulse fraction with energy four different observations.

Energy (keV)	Obs1	Obs2	Obs3	Obs4
5	3.85±0.15	11.92±0.02	3.22±0.01	6.28±0.01
8.5	5.89±0.01	12.98±0.34	5.13±0.01	10.08±0.03
9.5	6.63±0.01	13.32±0.03	5.01±0.01	8.01±0.02
12	10.14±0.02	14.83±0.05	6.42±0.03	12.92±0.02
15	14.60±0.06	15.81±0.03	6.75±0.03	10.62±0.02
17	17.97±0.09	20.11±0.06	6.59±0.11	14.79±0.07
21	21.12±0.17	26.67±0.02	7.20±0.01	12.70±0.01
23	22.25±0.22	28.86±0.03	8.41±0.01	17.12±0.02
26	26.40±0.46	36.56±0.66	12.28±0.25	16.54±0.03
28	26.34±0.40	32.89±0.51	11.78±0.23	16.54±0.25
30	30.24±0.82	34.44±1.00	14.27±0.52	17.8±0.51

Spectral parameters	Obs1+ <i>Swift</i>	Obs2+ <i>Swift</i>	Obs3	Obs4+ <i>Swift</i>
Model I				
n_H (cm ⁻²)	3.80±0.12	4.03±0.07	2.97±0.43	3.74±0.23
kT (keV)	0.20 ±0.04	0.23±0.02	0.31±0.05	0.15±0.07
α	0.51±0.02	0.46±0.02	0.34±0.01	0.80±0.02
E_H (keV)	7.26±0.12	6.82±0.02	6.21±0.08	6.87±0.02
E_{Fe} (keV)	6.52±0.03	6.52±0.07	6.49±0.02	6.61±0.08
σ_{Fe} (keV)	0.20±0.02	0.32±0.02	0.30±0.07	0.18±0.04
E_{gabs_1} (keV)	10.71±0.11	11.65±0.04	10.14±0.01	7.04±0.33
σ_{gabs_1} (keV)	4.32±0.12	2.49±0.09	4.12±0.14	6.54±0.23
τ_{gabs_1}	0.26±0.05	0.18±0.03	0.33±0.05	0.53±0.07
E_{gabs_2} (keV)	30.37±0.55	30.23±0.62
σ_{gabs_2} (keV)	1.79±0.34	1.04±0.35
τ_{gabs_2}	0.11±0.07	0.07±0.03
$flux$ (erg cm ⁻² s ⁻¹)	6.45 ^{+1.21} _{-0.61}	7.52 ^{+0.80} _{-0.74}	5.01 ^{+0.23} _{-0.1}	2.56 ^{0.90} _{-0.41}
χ^2_ν	1.02	1.11	0.98	1.01
Model II				
n_H (cm ⁻²)	2.32±0.02	2.40±0.05	2.70±0.13	3.75±0.45
kT (keV)	0.27 ±0.05	0.39±0.04	0.47±0.02	0.28±0.08
T_0 (keV)	1.27±0.07	1.08±0.08	1.33±0.17	0.75±0.11
kT (keV)	4.81±0.05	4.58±0.05	4.52±0.06	4.63±0.11
τ	4.94±0.05	4.89±0.13	4.81±0.07	4.56±0.15
E_{Fe} (keV)	6.52±0.07	6.45±0.02	6.61±0.07	6.56±0.50
σ_{Fe} (keV)	0.27±0.05	0.23±0.04	0.24±0.04	0.22±0.05
E_{gabs_1} (keV)	11.32±0.36	10.87±0.03	9.57±0.64	10.03±0.27
σ_{gabs_1} (keV)	2.01±0.15	1.57±0.21	3.54±0.50	3.68±0.12
τ_{gabs_1}	0.09±0.04	0.07±0.02	0.17±0.05	0.14±0.07
E_{gabs_2} (keV)	30.09±0.57	31.18±0.48
σ_{gabs_2} (keV)	2.10±0.55	4.04±0.25
τ_{gabs_2}	0.15±0.07	0.10±0.06
$flux$ (erg cm ⁻² s ⁻¹)	6.41 ^{+0.51} _{-0.54}	7.49 ^{+0.61} _{-0.67}	4.15 ^{+0.45} _{-0.70}	2.51 ^{0.51} _{-0.25}
χ^2_ν	1.01	1.11	1.00	0.99

Table 3 Best fitted spectral parameters of 4U 1901+03 for four different cases using Model I and Model II. α and E_H are photon index and highcut energy of the CUTOFFPL model. E_{gabs} and E_{Fe} are energy of absorption and Fe lines respectively. τ_{gabs} is the optical depth. σ_{gabs} and σ_{Fe} are the widths of absorption and Fe line. The subscript $gabs_1$ and $gabs_2$ are for two GABS models. The column density (n_H) and flux are in the scale of 10²² and 10⁻⁹ respectively. T_0 , kT and τ are the spectral parameters of the COMPTT model. Flux were calculated in 3-79 keV energy range. Errors quoted are within 90% confidence interval.

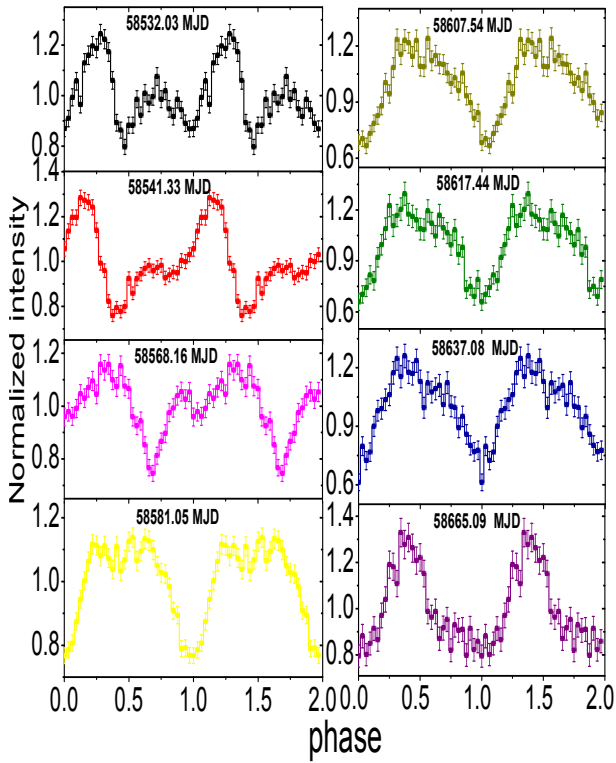


Fig. 4 Variation of Pulse profile with time. Pulse profiles from 58532.03 to 58637.08 MJD are obtained by folding *Swift*-XRT lightcurve. For *Swift*-XRT the significant level of pulse periods were greater than 3σ . The broadening of the *Swift*-XRT pulse profiles can be due to the short exposure time of the instrument so that there is not enough photons count rate to fold about the pulse period. The last pulse profile at 58665.09 MJD is obtained by folding *NICER* lightcurve in 0.2-12 keV energy range (ObsId. 2200570141).

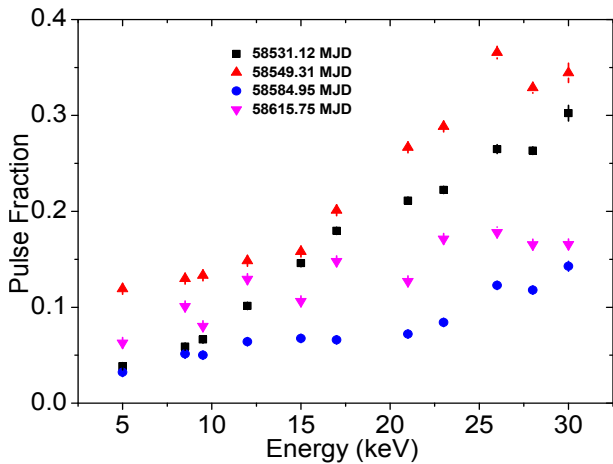


Fig. 5 Variation of the pulse fraction of the pulse profile with energy obtained using *NuSTAR* observations.

cases, large negative residuals were observed near 10 keV. So we incorporated the Gaussian absorption model GABS in both cases. However, the HIGHECUT model did not fit the spectra well and large residuals were observed near the cutoff energy of the model.

When Model I was used to fit Obs1 and Obs2 without GABS model a wave like a feature in the residuals between 3-30 keV energy range with large negative residuals near 10 keV were observed causing the fitting to be unacceptable (Fig. 6). An addition of GABS model fitted the spectra well. The reduced χ^2 were about 1.76 and 1.52 for the first two cases respectively before the addition of GABS model which is unacceptable and after the addition it's values were about 1.02 and 1.11 respectively.

In the case of *NuSTAR* Obs3 there were no *Swift* observations close to the *NuSTAR* observation, so we fitted 3-79 keV FPMA & B spectra. The spectra were fitted well with Model I along with the GABS. As observed by Coley et al. (2019) we too observed some negative residuals near 30 keV indicating another absorption like feature and possibly a Cyclotron Resonant Scattering Feature (CSRF). Fitting this absorption like feature with GABS model Coley et al. (2019) found the energy of the line to be 31 keV with width 3.1 keV and optical depth about 1.1. So we added another GABS model and searched for an absorption feature near 30 keV (see Fig. 7), the best fitted value of line energy was 30.37 keV. The width and the depth of this absorption line were 1.79 keV and 0.11 respectively.

The simultaneous fitting of *Swift*-XRT and *NuSTAR* Obs4 using Model I without GABS was not good as wave like feature was observed with large negative residuals near 10 keV. So we also used two GABS models one for 10 keV and another for 30 keV absorption like features, the spectra were fitted very well with reduced χ^2 of the fitting about 1.01. However, the first absorption like feature was observed at 7.04 keV which is much below what we have observed in three previous cases. The second feature was observed at 30.23 keV with width and optical depth about 1.04 keV and 0.07 respectively.

The spectra were also fitted well by Model II along with the GABS model. The column density is found to lie between 2.32 - $3.75 \times 10^{22} \text{ cm}^{-2}$ (Table 3). The input soft temperature (T_0) of COMPTT model varies between 0.75-1.33 keV. The plasma temperature (kT) and the plasma optical depth (τ) of this model are between 4.52-4.81 keV and 4.56-4.96 respectively. When the 10 keV feature was fitted with the absorption model the line energy was 11.32, 10.87, 9.57 and 10.03 keV for four *NuSTAR* observations respectively. The width and the optical depth of this feature are in the range of

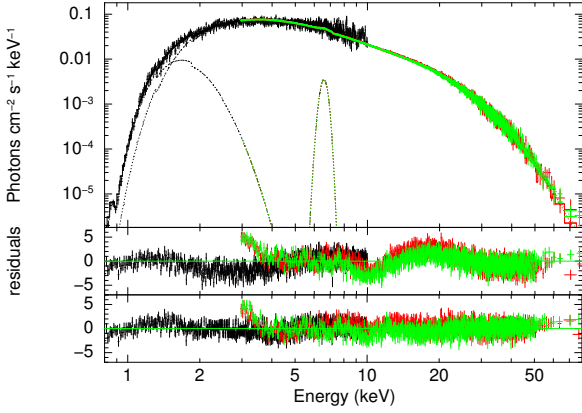


Fig. 6 Unfolded spectra of *NuSTAR* Obs1 and *Swift*-XRT observation fitted with Model I. The bottom and middle panels shows residuals after without and with the GABS model. Black indicates *Swift*-XRT spectra, red and green indicates *NuSTAR* FPMA & B spectra respectively.

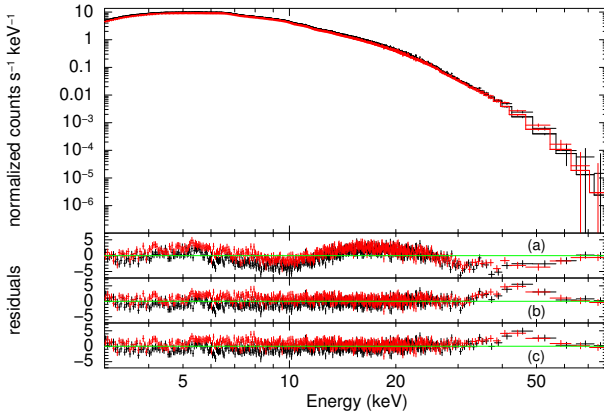


Fig. 7 Fitted spectra of *NuSTAR* Obs3 in 3-79 keV energy range. Panel (a) shows residuals for Model I where as panel (b) is residuals for Model I*GABS models and (c) shows residuals for Model I*GABS*GABS models.

1.57-4.02 keV and 0.07-0.17. An absorption like feature around 30 keV was also observed in Obs3 and Obs4, so we used another GABS model and found the line energy of this feature to be about 30.09 and 31.18 keV.

The spectral fitting by Model I estimated blackbody temperature was about 0.20-0.31 keV. The iron emission line was estimated to lie between 6.52-6.61 keV. For all four cases, the flux were estimated in 3-79 keV energy range. The best fitted spectral parameters are shown in table 3. The thermal component was also observed in the spectra fitted with Model II. The estimated flux were 6.45×10^{-9} , 7.52×10^{-9} , 5.01×10^{-9} and 2.56×10^{-9} erg cm $^{-2}$ s $^{-1}$ respectively. Thus the luminosity of the pulsar in 3-79 keV were $1.24 \times 10^{37} D_4^2$, $1.44 \times 10^{37} D_4^2$, $9.59 \times 10^{36} D_4^2$ and $4.89 \times 10^{36} D_4^2$ erg s $^{-1}$ for four the cases respectively. The 10 keV absorption like feature was dependent on flux or luminosity and thus increases or decreases with the increase or decrease in flux or luminosity, from table 3 we can note that as flux decreases from 7.52×10^{-9} to 2.56×10^{-9} erg cm $^{-2}$ s $^{-1}$ the line energy of the feature decreases from 11.65 to 7.04 keV. Thus the line energy of the feature shows a positive correlation with the source luminosity. The absorption feature near the 30 keV was only observed in the last two *NuSTAR* observations. This feature was also present in the spectra fitted with Model II. However, when the spectra were fitted with Model II the 10 keV feature does not show the same variation with flux or luminosity as seen in the case of spectral fitting with Model I but shows some positive correlation with flux or luminosity. The observed flux and E_{Fe} were almost the same in the two cases. In order to check whether the origin of the 30 keV absorption like feature in spectra of the last two *NuSTAR* observations was due to Compton reflection, we fitted these spectra with the Compton reflection models like PEXRAV, PEXRIV and PEXMON. However, these models were not consistent with the observed spectra of the pulsar. So we rejected the possible origin of this feature due to Compton reflection.

3.2.1 Fitting of *Swift*-BAT spectra

The 0.5-10 keV *Swift*-BAT spectra were fitted with PHABS and POWERLAW models. The power law model fitted the spectra well and no additional models was required. As the pulsar slowly fades the photon index increase or in other words with decrease in flux the photon index increases (Fig. 9). Thus the spectra were softer near the end of the outburst. As the flux varies between 0.13 - 39.60×10^{-10} erg cm $^{-1}$ s $^{-1}$ the photon index varies between 1.03-2.1. The column density was observed to lie between 3.20 - 4.31×10^{22} cm $^{-2}$. The softening of the spectra of the pulsar at the end of an outburst was also observed by Reig & Milonaki (2016).

3.2.2 Phase Resolved Spectral Analysis

In order to understand the variation of spectral parameters with pulse phase we performed phase resolved spectral analysis of the *NuSTAR* observations. For phase resolved spectral analysis we have divided each pulse into 10 equal segments (Fig. 8). For each segment, a good time interval (gti) is created using XSELECT and using this gti file FPMA & B spectra were produced. Each of the spectrum was fitted in 3-79 keV energy range with CONSTANT, PHABS, CUTOFFPL, GAUSSIAN and GABS models. Flux is estimated in the 3-79 keV energy range. Spectral parameters are found to vary significantly with the phases. From the phase-resolved spectroscopy of Obs1, the photon index (α) and the highcut energy (E_H) were observed to show some anti-correlation with the flux. The flux varies between $6.40-7.02 \times 10^{-9}$ erg cm $^{-2}$ s $^{-1}$ whereas α and E_H varies between 0.19-0.366 and 6.08-6.64 keV respectively. The column density lies between $0.80-1.54 \times 10^{22}$ cm $^{-2}$. The variation of the Fe emission line (E_{Fe}) follows a complex pattern, its value decreases from 6.56 to 6.44 keV and then increase from 6.52 to 6.6 keV in between phase 0.2 to 0.6 and then decreases again, however, an abrupt increase in its value is observed between 0.9-1.0. The absorption like feature (E_{gabs_1}) was also observed to show some anti-correlation with the flux and lies between 10.12-11.02 keV. However the width (σ_{gabs_1}) and optical depth (τ_{gabs_1}) of the line have two peak and also shows anti-correlation with the E_{1gabs} and lies between 3.23-5.08 keV and 0.15-0.34 respectively.

From phase-resolved spectral analysis of Obs2 the photon index and E_H have some positive correlation with flux. Flux in this case decreases in between 0.0-0.3 from 7.89×10^{-9} to 7.79×10^{-9} erg cm $^{-2}$ s $^{-1}$, in between 0.4-0.8 the flux increases reaching a maximum value 8.1×10^{-9} erg cm $^{-2}$ s $^{-1}$ at 0.7-0.8. The variation of the Fe line with the phase is complex. The absorption feature E_{gabs_1} in between phase interval 0.0-0.1 is 11.38 keV and reaches a maximum value of 11.6 keV in between 0.1-0.2 and then decreases reaching a minimum of 11.07 keV at 0.9-1.0. σ_{gabs_1} from 2.65 keV at 0.0-0.1 increases to reach a value of 3.12 keV after that it decreases reaching a minimum value of 2.06 keV in between phase 0.5-0.6 and increases then decreases again. The maximum value of σ_{gabs_1} is 3.50 keV and was observed at 0.7-0.8. The optical depth (τ_{gabs_1}) decreases from 0.15 at 0.0-0.1 to 0.10 at 0.6-0.7 and then increases abruptly to 0.17 and decreases again. The column density varies between $1.14-1.77 \times 10^{22}$ cm $^{-2}$.

In Obs3 the variation of flux with phase is such that it exhibits two peaks one in between the phase 0.2-0.3 and another in between 0.7-0.8. The photon index and

E_H follows the flux and have two peaks. The Fe line from 6.58 keV decreases to reach a minimum value 6.43 keV in the phase interval 0.2-0.3 and increases reaching a peak in the interval 0.5-0.6 after that it again decreases and increases to reach a maximum value of 6.61 keV in the interval 0.9-1.0. From Fig. 8, we can see that the variation in E_{gabs_1} is quite different from the two previous cases. The energy of the 10 keV feature E_{gabs_1} decrease from 9.87 keV in between 0.0-0.3 followed by an increase and decrease. In the interval 0.4-0.6 the value E_{gabs_1} increases again followed by a sharp decrease reaching 8.57 keV and after that, it increases again. As we can see from the figure the width of the line σ_{gabs_1} shows negative correlation with the E_{gabs_1} . The optical depth (τ_{gabs_1}) does not varies much in the phase interval 0.0-0.6, however its variation with phase is similar to that of the E_{gabs_1} and varies between 0.28-0.46. In this case the column density varies between $0.38-1.72 \times 10^{22}$ cm $^{-2}$.

From the phase-resolved spectral analysis of the fourth *NuSTAR* observation, we found that the flux lies between $2.53-2.72 \times 10^{-9}$ erg cm $^{-2}$ s $^{-1}$. The minimum value of photon index 0.39 was observed at phase interval 0.4-0.5 and the maximum value of 1.04 was observed at 0.5-0.6. The cutoff energy (E_H) was within 5.94-7.09 keV energy range. The value of column density (n_H) lies between $1.54-3.63 \times 10^{22}$ cm $^{-1}$. The iron fluorescence line was lying between 6.45-6.64 keV with its width in 21-380 eV energy range. The 10 keV feature was found to vary between 5.84-8.79 keV. The width and the optical depth of the feature were lying between 1.97-5.59 keV and 0.68-0.99 respectively.

The absorption like feature of about 30 keV in Obs3 was also found to depend on the pulse phase (Figure 10). The estimated line energy increases from 29.38 to 38.24 keV between the phase interval 0.0-0.4 and decreases to 33.38 keV, after that it increases to 33.88 keV and decreases again to 30.33 keV. In the phase interval 0.7-1.0 the line energy increases from 29.89-36.21 keV. The width σ_{gabs_2} and optical depth τ_{gabs_2} of the feature also varies with the pulse phase and was found to lie between 2.17-7.16 keV and 0.2-0.7 respectively. For the Obs4 the 30 keV feature was found to vary between 27.6-33.51 keV with its width lying between 3.29-6.41 keV and depth varying between 0.17-0.42.

We also fitted phase resolved spectra of Obs1 and Obs2 with GABS model in order to check the presence of 30 keV absorption like feature. For Obs1 the line energy and width of the feature varies between 31.24-38.76 keV and 0.75-6.15 keV respectively and in the phase interval 0.7-0.8 and 0.8-0.9 the feature was absent. In the case of Obs2 the energy of the feature is between 28.90-35.48 keV with a width lying between 0.77-6.06 keV.

1 However for phase intervals 0.5-0.6 and 0.8-0.9 of Obs2
 2 the value of σ_{gabs_2} and τ_{gabs_2} were unrealistic so we did
 3 not considered there values.
 4

5 4 Discussion

6 We present Be X-ray pulsar 4U 1901+03 analysis which
 7 has undergone short bursts of tens to hundreds of sec-
 8 onds. The burst of the X-ray pulsar can be due to
 9 instability in accretion disk burst (Taam et al. 1988;
 10 Lasota & Pelat 1991; Cannizzo 1996) similar to the
 11 burst observed in other sources namely, SMC X-1, GRO
 12 J1744-28 and MXB 1730-355 (Moon et al. 2003; Rai et
 13 al. 2018; Fishman et al. 1995; Lewin et al. 1976). Pulse
 14 profiles show variation with both time and flux and are
 15 similar to that observed by (Lei et al. 2009; Reig &
 16 Milonaki 2016; Ji et al. 2020). From the *NuSTAR*
 17 observations, we found that the pulse profile having a
 18 single peak evolved into a double peak with one main
 19 peak and once again became a single peak (Fig. 3).
 20 Similar variations were observed in *Swift*-XRT pulse
 21 profiles (Fig. 4). The height of the pulse profile peak
 22 increases with the increase in energy. Also, the double
 23 peaked pulse profile in Obs2 evolves into a single peaked
 24 at hard energy range. The pulse fraction is found to
 25 increase with the increase in energy and at the end of
 26 the outburst. As the X-ray emitting region gets smaller
 27 with an increase in energy and becomes more pulse as a
 28 result the pulse fraction increases (Alexander & Sergey
 29 2008).
 30

31 From the *NuSTAR* observations, we observed that
 32 pulse profile (Fig. 3) is sinusoidal in shape at a lu-
 33 minosity of $1.24 \times 10^{37} D_4^2$, which evolves into a double
 34 peak pulse profile with one main peak at $1.44 \times 10^{37} D_4^2$
 35 erg s^{-1} . The second peak of the pulse profile disappears
 36 and becomes a single-peak with a notch near ~ 0.5 when
 37 the luminosity of the pulsar becomes $9.59 \times 10^{36} D_4^2$
 38 erg s^{-1} . With the further decrease in luminosity, the notch
 39 disappears and the pulse profile becomes a single peak
 40 and this happens at $4.89 \times 10^{36} D_4^2$ erg s^{-1} . Similar
 41 variations were observed in *Swift*-XRT pulse profiles
 42 (Fig.4). Thus 4U 1901+03 shows luminosity dependent
 43 pulse profile having a double peak at high luminosity
 44 and a single peak at high luminosity. The complex
 45 variation of pulse profiles can be due to a change in
 46 emission beam pattern with luminosity (see section 1),
 47 which can be due to either fan and pencil beam pattern
 48 or mixture of these two beam pattern (Chen et al. 2008;
 49 Ji et al. 2020; Reig & Milonaki 2016). The fan shape
 50 beam pattern being dominated at the high luminosity
 51 whereas pencil beam pattern being dominating at the
 52 low luminosity states outburst (Chen et al. 2008; Reig &
 53

54 Milonaki 2016; Ji et al. 2020). The simple single peak
 55 pulse profile during Obs1 and Obs4 can be due to the
 56 source in the sub-critical region where the pencil shape
 57 beam pattern dominates the fan shape beam pattern.
 58 The significant variation of pulse profile in Obs2 and
 59 Obs3 from Obs1 and Obs4 can be due to the fan shape
 60 beam pattern or a mixture of fan and pencil shape beam
 61 pattern. We did not observe an abrupt change in the
 62 correlation between the flux and photon were seen sug-
 63 gesting the source was in which indicates that there
 64 was no transition between super-critical to sub-critical
 65 regimes. It might be possible that the source has not
 66 reached the pure super-critical regime during the out-
 67 burst (Chen et al. 2008; Reig & Milonaki 2016).

68 The 10 keV absorption like feature was observed in
 69 all four *NuSTAR* observations of the pulsar and was
 70 found to increase with the luminosity. Also, the width
 71 and optical depth of the feature varies for different ob-
 72 servations. The energy, width and optical depth of the
 73 feature is within the range observed by Reig & Milon-
 74 aki (2016). It was observed that accreting pulsars
 75 show a positive correlation of the cyclotron line energy
 76 with the luminosity in sub-critical regime and an ega-
 77 tive correlation in super-critical regime (Becker et al.
 78 2012; Mushtukov et al. 2015). If the pulsar was in sub-
 79 critical regime most of the time during the outburst as
 80 discussed above then the observed positive correlation
 81 of the 10 keV feature hints to be a cyclotron line. In
 82 addition to that the strong dependence of this feature
 83 on the viewing angle *i.e.* on pulse phase like cyclotron
 84 line which also show a strong dependence on the pulse
 85 phase (Isenberg et al. 1998; Heindl et al. 2004; Reig &
 86 Milonaki 2016) also support this feature to be a cy-
 87 clotron line. The width and optical depth of the 10
 88 keV features are within the range given by Coburn et
 89 al. (2002) for other pulsars. The 10 keV feature was
 90 observed in pulsars having CRSF or not at all and
 91 was found to depend on the pulse phase (Coburn et
 92 al. 2002). Considering the canonical value of neutron
 93 star parameters, the theoretically calculated value of
 94 critical luminosity was found by Becker et al. (2012) to
 95 be $L_{crit} \sim 1.49 \times 10^{37} B_{12}^{16/15}$, thus for this feature to
 96 be CRSF the critical luminosity must be $\sim 10^{37}$ erg
 97 s^{-1} . Assuming the distance of the source to be 3 kpc
 98 Bailer et al. (2018) observed luminosity lies between
 99 $2.69-8.04 \times 10^{36}$ erg s^{-1} which is below the critical lu-
 100 minosity. Reig & Milonaki (2016) noted that for the
 101 $L_{peak}/L_{crit} \sim 1$ the distance should not be larger than
 102 ~ 4 kpc. Thus for estimated luminosity to be less than
 103 the critical luminosity the distance of the source must
 104 be less than 4 kpc. However, Strader et al. (2019) noted
 105 that the distance of the object measured by the Bailer
 106 et al. (2018) was not a well constraint because the par-

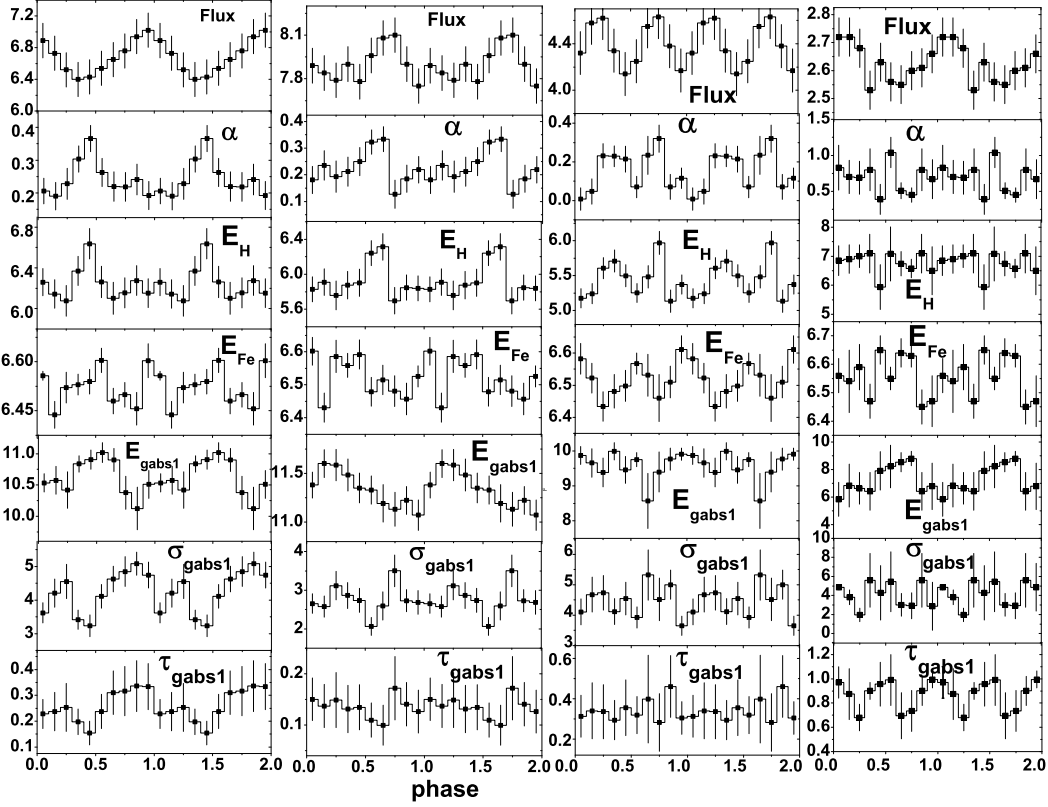


Fig. 8 Variation of Spectral parameters with phase for four *NuSTAR* observations. Figures in first, second and third columns are for Obs1, Obs2, Obs3 and Obs4 respectively. α and E_H are photon index and highcut of CUTOFFPL model. E_{Fe} is the energy of Fe line. E_{gabs1} , σ_{gabs1} and τ_{gabs1} are the line energy, width and optical depth of GABS model used for fitting 10 keV feature. The error associated with the spectral parameter is standard error within 90% confidence interval.

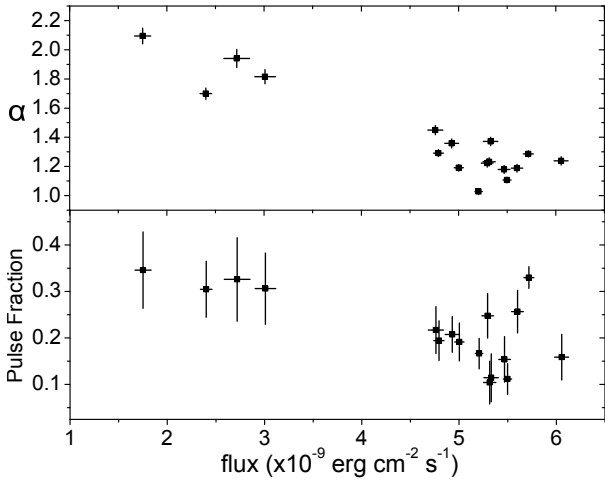


Fig. 9 Variation of photon index and pulse fraction with *Swift*-XRT flux in 0.5-10 keV energy range.

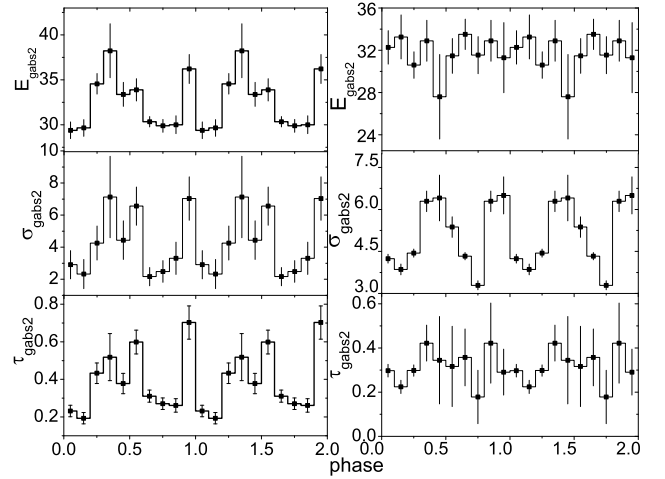


Fig. 10 Variation of 30 keV absorption feature with phase for Obs3 (first column) and Obs4 (second column). E_{gabs2} , σ_{gabs2} and τ_{gabs2} are the line energy, width and the optical depth of the feature.

allax of the star in Gaia DR2 was insignificant and considering PS1 reddening maps along the direction of the source (Green et al. 2018) concluded that the distance must be greater than 12 kpc. Recently Tuo et al. (2020) with the help of torque model and evolution of pulse profile during outburst estimated the distance of the source to be about 12.4 kpc. Assuming the distance of the source as 12.4 kpc the observed luminosity lies between $4.59\text{-}13.74 \times 10^{37} \text{ erg s}^{-1}$ which is close to or above the critical luminosity and raises doubt about this feature being CRSF. Mushtukov et al. (2015) showed that the critical luminosity is not a monotonic function of magnetic field and for pulsars having cyclotron energy about 10 keV the critical luminosity can reach a minimum value of few $10^{36} \text{ erg s}^{-1}$. If this is the case then even if the source is at a distance of 3 kpc the observed luminosity will be at or above the critical luminosity. In *NuSTAR* spectra weak residuals are observed around 10 keV due to tungsten L-edge of the *NuSTAR* optics (Madsen et al. 2015; Fürst et al. 2013). The 10 keV feature in other pulsars were present in the spectra of different instruments of different satellites (Coburn et al. (2002)) like in the case of 4U 1901+03 where this feature was observed by RXTE (Reig & Milonaki 2016) and *Insight*-HMXT (Nabizadeh et al. 2020), thus clearing doubt about the instrumental origin of the feature. We have also seen that the feature is present even if we used another continuum model COMPTT instead of CUTOFFPL. Nabizadeh et al. (2020) showed that when *NuSTAR* Obs3 spectra were fitted by a two components model consisting of two POWERLAW*HIGHECUT along with GAUSSIAN and PHABS models no residuals were left near 10 keV and also no additional absorption model around 10 keV was needed when this two component model was used to fit *Insight*-HMXT spectra. However, the authors also argued that transition from the typical cutoff power-law spectral shape to two-component spectral shape occurs at low luminosities about $10^{34\text{-}36} \text{ erg s}^{-1}$, which indicates that the source distance must be small. Thus without proper estimation of the distance, we cannot be sure about the feature to be CRSF. It is equally possible that this feature can be an inherent feature of the accreting X-rays pulsars or due to the departure of our phenomenological models used in fitting the spectra Coburn et al. (2002). The change in the hydrogen column density n_H for different *NuSTAR* observations or in phase-resolved spectral analysis can be as a result of absorption of photons by the interstellar medium.

As observed by Nabizadeh et al. (2020) and Coley et al. (2019) when Obs3 and Obs4+*Swift* spectra were fitted some negative residuals were observed near 30 keV and fitting the spectra with absorption model we

estimated the line energy about 30.37 and 30.23 keV for these observations respectively and were consistent with the value estimated by the authors. However, no negative residuals near 30 keV were observed in the first two *NuSTAR* spectra which were having higher flux compared to the last two observations. In Obs3 and Obs4 the line energy of the 30 keV feature shows pulse phase variation. Despite the fact that this feature was not observed in the phase-averaged spectra of Obs1 and Obs2 it was observed in the phase-resolved spectra of these observations. However, in Obs1 and Obs2 this feature was not observable in some phases. Beri et al. (2020) have given sufficient evidence for this feature to be cyclotron line by studying the variation of line energy with luminosity and pulse phase. The authors also observed an abrupt change in the pulse profiles around the line energy of the feature. In X-ray pulsars with a high mass accretion rate, the accretion columns will appear to be confined by the strong magnetic field of the neutron star and are supported by internal radiation pressure. Thus observed cyclotron line can thus be originated from accretion column (Schönherr et al. 2014) or due to X-rays reflected from the neutron star's atmosphere (Poutanen et al. 2013). The absence of the cyclotron line in some observed energy spectra of the XRBs' can possibly due to a large gradient of B-field strength over the visible column height or the latitude on the surface of a neutron star. The appearance of cyclotron line in certain pulse phases can be due to the partial eclipsing of the accretion column during which an observer is able to see some parts of the column (Molkov et al. 2019). In such a case, the magnetic field in the visible part of the accretion column is not so varied and we can observe cyclotron line in these phases like in the case of GRO J2058+42 (Molkov et al. 2019). This can also be due to the gravitational bending of light as it affects the visibility of both the accretion columns and neutron star (see eg. Mushtukov et al. (2018)).

When the magnetospheric radius r_m becomes greater than the co-rotational radius r_{co} then the centrifugal force will prevent the material from falling onto the neutron star this is known as Propeller Effect (Illarionov & Sunyaev 1975; Stella et al. 1986). As the propeller effect set in there is an abrupt decrease in the flux along with the absence of pulsation and even cause non-detection of the source. Here the co-rotational radius is defined as the radius where the keplerian angular velocity equals the spin angular velocity of the neutron star. The magnetospheric radius depends on the mass accretion rate, during a bright phase of an outburst the magnetospheric radius is less than the co-rotational radius so that matter can cross the magnetospheric radius and reach neutron star. As the mass accretion rate

decreases the magnetospheric radius increase and can reach a point when this radius will become equal to the co-rotational radius and at this stage propeller phase sets in. From the *NICER* observations, we found that the no pulsation was detected after 58665.09, also the flux abruptly decreases from 6.37×10^{-10} at 58637.08 MJD to 1.31×10^{-11} erg s $^{-1}$ at 58667.45 MJD which indicates that the pulsar has entered propeller phase. The increase in pulse fraction and the softening of the spectrum at the end of the outburst also support our argument (Tsygankov et al. 2016; Reig & Milonaki 2016; Zhang et al. 1998). As the accretion of matter onto the neutron star ceases when $r_m = r_{co}$ this implies that $B = 4.8 \times 10^{10} P^{7/6} \left(\frac{flux}{10^{-9} \text{ ergs}^{-1}} \right)^{1/2} \times \left(\frac{d}{1 \text{ kpc}} \right) \left(\frac{M}{1.4 M_{\odot}} \right)^{1/3} \left(\frac{R}{10^6 \text{ cm}} \right)^{-5/2}$ G (Cui 1997)), here *flux* is the minimum bolometric X-ray when the pulsation was still detectable and *d* is the distance to the source. Using *Swift*-XRT flux 6.37×10^{-10} erg cm $^{-2}$ s $^{-1}$ in 0.5-10.0 keV observed at 58637.08 MJD, which is the minimum flux estimated in *Swift*-XRT observations when the source was still pulsating and assuming the distance to the source to lie between 3-12.5 kpc the magnetic field of the neutron star lies 0.38-1.56 $\times 10^{12}$ G, assuming canonical values of mass and radius. However, the estimated magnetic field is associated with uncertainties as bolometric correction of the flux was not done and also the above minimum flux was not exactly known. Taking the cyclotron line energy to be 30 keV the estimated magnetic field of the neutron star will be about 2.59×10^{12} G and if it is so the distance to the source must be greater than 12.5 kpc.

Acknowledgments

The research has made use of *NuSTAR*, *Swift* and *NICER* observational data and were obtained from the NASA High Energy Astrophysics Science Archive Research Center (HEASARC), Goddard Space Flight Center. The research is supported by SERB-DST research grant EMR/2016/005734. BR is thankful to DST and IUCAA Center for Astronomy Research and Development (ICARD), Physics Dept, NBU for extending research facilities. BCP is thankful to DST, New Delhi for Project and IUCAA for Associateship program.

References

- Alexander L., Sergey T., arxiv:0808.2034
- Arnaud K. A. 1996, in *Astronomical Data Analysis Software and Systems V*, eds. G. H. Jacoby, & J. Barnes, ASP Conf. Ser., 101, 17
- Boldin P. A., Tsygankov S. S., Lutovinov A. A., 2013, *Astrophys. Let.*, 39, 375
- Bailer C. A. L., Rybizki J., Fouesneau M., Mantelet G., Andrae R., 2018, *AJ*, 156, 58
- Basko M. M., Sunyaev R. R., 1976, *MNRAS*, 175, 395
- Becker P. A. et al., 2012, *A&A*, 544, A123
- Bellm E. C., et al., 2014, *ApJ*, 792, 108
- Beri B., Girdhar T., Iyer N. Maitra C., 2020, *MNRAS*, 500, 1350
- Cannizzo J. K., 1996, *ApJ*, 466, L31
- Chen, W., Qu, J. l., Zhang, S., Zhang, F., & Zhang, G. B. ,2008, *caap*, 32, 241
- Coburn, W., Heindl, W. A., Rothschild, R. E., et al. 2002, *ApJ*, 580, 394
- Coley, J. B., et al., 2019, *Astronomers Telegram*, 12684
- Cui, W. 1997, *ApJ*, 482, L163
- Fishman, G. J., et al., 1995, *IAU Circ.*, No. 6290. 2
- Fürst F., et al., 2013, *ApJ*, 779, 1
- Galloway D. K., Wang Z., & Morgan E. H. 2005, *ApJ*, 635, 1217
- Ghosh, P. & Lamb, F. K. 1979, *ApJ*, 234, 296
- Green, G. M., Schlafly, E. F., Finkbeiner, D., et al. 2018, *MNRAS*, 478, 651
- Harrison F.A. et al. 2013, *ApJ*, 770, 103
- Heindl, W. A., Rothschild, R. E., Coburn, W., et al. 2004, in *X-ray Timing 2003: Rossi and Beyond*, eds. P. Kaaret, F. K. Lamb, & J. H. Swank, *AIP Conf. Ser.*, 714, 323
- James M., Paul B., Devasia J., Indulekha K., 2011, *MNRAS*, 410, 1489
- Ji L., et al., 2020, *MNRAS*, 493 ,5680
- Illarionov, A. F. & Sunyaev, R. A. 1975, *A&A*, 39, 185
- Isenberg, M., Lamb, D. Q., & Wang, J. C. L. 1998, *ApJ*, 505, 688
- Kennea J. A., Krimm H. A., Page K. L., Tohuvavohu A., 2019, *GRB Coordinates Network*, 23882, 1
- Lasota, J. -P., & Pelat, D. 1991, *A&A*, 249, 574. 11
- Lei Y.-J., Chen W., Qu J.-L., et al., 2009, *ApJ*, 707, 1016
- Lewin, W. H. G., et al. 1976, *ApJ*, 207, L95. 1, 2
- Lightman, A. P., & Eardley, D. M. 1974, *ApJ*, 187, L1
- Rai B., Pradhan P., & Paul B. C., 2018 , *RAA*, 18, 12
- Reig, P. 2008, *A&A*, 489, 725
- Reig, P., & Nespoli, E. 2013, *A&A*, 551, A1
- Reig P., 2011, *Ap&SS*, 332, 1-29
- Reig P., Milonaki F., 2016, *A&A*, 594, A45
- Madsen K. K., et al., 2015, *ApJS*, 220, 8
- Molkov S., Lutovinov A., Tsygankov S., Mereminskiy I., Mushtukov A., 2019, *ApJ*, 883, L11
- Moon D.-S., Eikenberry S. S., Wasserman I. M., 2003, *ApJ*, 582, L91
- Mushtukov A. A., Suleimanov V. F., Tsygankov S. S., Poutanen J., 2015, *MNRAS*, 1847
- Mushtukov, A. A., Verhagen, P. A., Tsygankov, S. S., et al. 2018, *MNRAS*, 474, 5425
- Nakajima M., et al., 2019, *The Astronomers' Telegram*, 12498, 1
- Nabizadeh A., et al., 2020, arxiv:2005.14555
- Poutanen, J., Mushtukov, A. A., Suleimanov, V. F., et al. 2013, *ApJ*, 777, 115
- Schönherr, G., Schwarm, F. W., Falkner, S., et al. 2014, *A&A*, 564, L8
- Stella, L., White, N. E., & Rosner, R. 1986, *ApJ*, 308, 669
- Strader, J., Chomiuk, L., Swihart, S., & Aydi, E. 2019, *The Astronomers' Telegram*, 12554, 1
- Tuo, Y. L. et al., 2020, *JHEP*, 27, 38-43
- Taam R. E., Fryxell B. A., Brown D. A., 1988, *ApJ*, 331, L117
- Tsygankov, S. S., Lutovinov, A. A., Doroshenko, V., Mushtukov, A. A., & Poutanen, J. 2016, *A&A*, 593, A16
- Wang, Y.-M., 1987, *A&A*, 183, 257
- Zhang S. N., Yu W., Zhang W., 1998, *ApJ*, 494, L71

Document Information

Analyzed document	Binay Rai_Physics.pdf (D109879460)
Submitted	6/29/2021 8:43:00 AM
Submitted by	University of North Bengal
Submitter email	nbuplg@nbu.ac.in
Similarity	2%
Analysis address	nbuplg.nbu@analysis.arkund.com

Sources included in the report

W	URL: https://ir.nbu.ac.in/bitstream/123456789/2748/22/Full%20thesis%20of%20Pragati%20Pradhan.pdf Fetched: 6/15/2021 1:06:47 AM	 10
J	Timing and Spectral Studies of Accretion Powered X ray Pulsars URL: ebe36546-236a-428b-add0-040e1577138b Fetched: 3/16/2019 1:08:25 PM	 11
W	URL: https://arxiv.org/pdf/1601.02348 Fetched: 6/15/2021 7:52:53 PM	 1
W	URL: http://arxiv.org/pdf/1106.3251 Fetched: 6/15/2021 7:53:07 PM	 1
W	URL: https://docplayer.org/154982801-Magnetic-fields-of-accreting-pulsars.html Fetched: 3/13/2021 4:41:51 AM	 2
W	URL: https://arxiv.org/pdf/1608.06118 Fetched: 12/18/2020 10:32:19 AM	 3
W	URL: https://iopscience.iop.org/article/10.3847/1538-4357/aae309 Fetched: 6/29/2021 8:44:00 AM	 1
W	URL: https://arxiv.org/pdf/2004.10452 Fetched: 6/24/2021 7:36:48 AM	 1
J	SPECTRAL AND TIMING NATURE OF THE SYMBIOTIC X-RAY BINARY 4U 1954+319: THE SLOWEST ROTATING NEUTRON STAR IN AN X-RAY BINARY SYSTEM URL: ecbbf36d-a643-418b-acc1-f0dca78c806c Fetched: 3/18/2019 11:17:06 PM	 1
W	URL: https://www.aanda.org/articles/aa/full_html/2016/10/aa29200-16/aa29200-16.html Fetched: 6/14/2020 2:26:18 PM	 3
W	URL: https://heasarc.gsfc.nasa.gov/xanadu/xspec/manual/node162.html Fetched: 6/29/2021 8:44:00 AM	 1

Binay Rai
02/05/2021

B. Baul
02/05/2021

Professor
Department of Physics
University of North Bengal